Optical harmonic generation at exciton resonances in GaAs, GaN, and Cu$_2$O semiconductors

Dissertation

presented to the Faculty of Physics of the
TU Dortmund University, Germany,
in partial fulfillment of the requirements
for the degree of

Dr. rer. nat.

by

David Samuel Brunne

technische universität
dortmund

Dortmund, May 2014

Accepted by the Faculty of Physics of the TU Dortmund University, Germany

Day of the oral examination: 13th June 2014

Examination board:
Prof. Dr. Dmitri R. Yakovlev
Prof. Dr. Metin Tolan
Prof. Dr. Bernhard Spaan
Dr. Bärbel Siegmann

Contents

1. Introduction

Physics would be dull and life most unfulfilling if all physical phenomena around us were linear. Fortunately, we are living in a nonlinear world. While linearization beautifies physics, nonlinearity provides excitement in physics.

Y. R. Shen in The Principles of Nonlinear Optics

The proof of second harmonic generation (SHG) in quartz with a pulsed ruby optical maser by Franken in 1961 [1] is usually considered to be the first observation of nonlinear optics. In nonlinear optics the response of a material on the light intensity is nonlinear, because the incident light changes the optical properties of the material [2, 3]. This leads to a variety of effects, for example, the saturation of light absorption from materials for high intensities [4]. The most prominent nonlinear optical effects are those which change the wavelength of laser light. It is possible to manipulate the wavelength and pulse duration of laser light with these effects by passing it through a suitable optical nonlinear medium. The wavelength can be shifted by Raman scattering [5] or multiplied by second and third harmonic generation (THG) [6]. The presence of multiple simultaneous wavelengths in a material leads to an even broader range of effects, such as sum frequency generation (SFG) and difference frequency generation (DFG) [7, 8]. The main focus of this thesis lies on SHG and THG in semiconductors. In SHG two photons from a fundamental light beam are annihilated and a single photon with twice the energy is created. In THG three photons are converted into a single photon with thrice the energy.

The first nonlinear optical experiments focused on the verification of proposed wavelength conversion effects. The possibility of changing the wavelength of laser light led to many applications, which are used in part in the experiments presented here. For fundamental research the inference from observed optical nonlinearities on material properties was very successful and finally led to its own field of research [1, 9, 10]. Spectroscopy with SHG proved to be a powerful tool for different material systems [11–15], including organic matter in biology [16–18]. SHG is one of the simplest optical nonlinearities and can be induced in every material with a laser. It offers certain advantages over the established linear optical investigations. Intense laser light can be tuned to the transparency region of a material, which is especially interesting for organic matter like cells, most of which would be influenced or even damaged by other techniques. The high number of photons interacting in this process offer more degrees of freedom, since their relative polarization, wave vector and frequency can be tuned [9]. The multi-photon transitions in nonlinear

optics obey other selection rules than the one-photon transitions in linear optics [19] and yield complementary information about energy levels in a system [20].

Besides the success in fundamental research, many of the nonlinear optical processes are exploited for technological applications. A well-known example is the green laser pointer. Its pump laser emits infrared light, which is converted into green light by a potassium titanyl phosphate (KTP) crystal through nonlinear optics. These diode pumped solid state frequency-doubled (DPSSFD) lasers gave the initial access to green and blue laser diodes, for which, only recently, direct solutions were realized by Osram [21]. Many more sophisticated laser systems exploit the strong optical nonlinearities over a broad spectral range of β barium borate (BBO) and monopotassium phosphate (KPD) to enhance the available spectral range. Optical parametric amplifiers (OPA) and optical parametric oscillators (OPO) [22, 23] control the nonlinearities of the crystals by temperature or angle tuning and allow a continuous wavelength tuning over a broad spectral range. Additional SHG and THG stages are also common tools to widen spectral ranges of various laser systems. Periodically poled materials are used to integrate such effects directly into fibers or optical chips [24, 25] and allow the integration of these techniques into optical communication technologies [26]. The application of such techniques in semiconductor spectroscopy is presented in the Experimental methods chapter.

Most of the reported SHG experiments on semiconductors were performed with optical harmonics in the transparency region of the material. The measurements are mostly done on a limited spectral range [27, 28], which can be provided by typical laser systems. Theoretical studies of SHG in semiconductors, on the contrary, often focus on first-principles calculations over the whole band structure for several eV [29, 30]. The role of excitons in the vicinity of the band gap in second harmonic generation is rather unexplored [31]. These bound electron-hole states play an important role in the interaction of light with semiconductors near the band gap. Their energy lies below the band gap and they are the main source of photoluminescence (PL) at low temperatures. Excitons lead to sharp resonances in SHG spectra, which are systematically influenced by magnetic fields, electric fields, strain, and temperature [32, 33]. The identified resonances have to be assigned to the specific crystal state while the microscopic reason for the nonlinearities has to be understood. In this thesis, several semiconductors are investigated in the vicinity of the band gap over a broad spectral range. Found resonances are assigned to crystal states and microscopic descriptions are derived. Appropriate nonlinear measurements such as SHG, THG, and multi-photon absorption combined with external perturbations are compared and the optimal technique for each case is identified. The investigated semiconductors GaAs, GaN, Cu_2O, and Si have important technological applications and are of interest for fundamental research. The important properties of these materials are summarized in Table 1.1.

In Chap. 4 measurements of the semiconductor gallium arsenide (GaAs) are presented. The material has a cubic crystal lattice and a band gap of $E_g = 1.420\,\text{eV}$ [34]. The zinc-blende lattice is not centrosymmetric and SHG in the electric dipole (ED) approximation is allowed.

Table 1.1. – List of investigated semiconductors. Additionally to the lattice type it is noted if the structure is centrosymmetric (CS) or not (not CS).

Material	$E_{\mathrm{g}}(T = 1.6\,\mathrm{K})$	$E_{\mathrm{g}}(T = 300\,\mathrm{K})$	lattice type	Exciton binding energy
GaAs	$1.519\,\mathrm{eV}$	$1.424\,\mathrm{eV}$	cubic (not CS)	$4.2\,\mathrm{meV}$
GaN	$3.50\,\mathrm{eV}$	$3.39\,\mathrm{eV}$	wurtzite (not CS)	$28\,\mathrm{meV}$
Cu_2O	$2.172\,\mathrm{eV}$	$2.137\,\mathrm{eV}$	cubic (CS)	$98\,\mathrm{meV}$
Si	$1.17\,\mathrm{eV}$	$1.12\,\mathrm{eV}$	cubic (CS)	$15\,\mathrm{meV}$
SiC (6H)	$3.00\,\mathrm{eV}$	$3.02\,\mathrm{eV}$	hexagonal (not CS)	

There are existing reports about SHG in the vicinity of the GaAs band gap [32, 35]. Non-resonant SHG was found over an energy range of more than $1\,\mathrm{eV}$. The spectrum showed no exciton features. The application of a magnetic field gave rise to resonances in the spectrum, which stem from magneto-excitons. The responsible susceptibilities were identified and a qualitative description of the magneto-exciton series was given.

In this thesis the influence of an electric field on SHG in GaAs in the spectral range of excitons is reported and compared to the magnetic-field-induced SHG. The excitons interact differently with an electric field than with a magnetic field and the influence of an electric field on exciton SHG has not been reported before. An electric field gives rise to exciton SHG, due to the mixing of different states by the Stark effect. Calculations of the exciton mixing allow a modeling of the resonance intensity and energy dependence on the external electric field. The polarization dependence is presented and modeled by a third order susceptibility.

In the next step the influence of crossed magnetic and electric fields on SHG in the exciton energy region is reported. The spectrum is dominated by the magneto-exciton resonances. The electric field acts differently on every other magneto-exciton resonance, which is shown by polarization dependent studies. This was not expected from the existing model of magneto-excitons, which predicts every resonance to act alike in an additional electric field.

THG spectra of GaAs are presented in the second part of the chapter. Most lasers for optical harmonics generation studies do not provide the necessary wavelength and these measurements are presented for the first time. Excitons lead to enhanced THG even without an external field. This way, the nonlinear interaction of excitons with a light field is observed, undisturbed by an external field.

Again, external fields are applied and their influence on the THG spectrum is investigated. This is compared to the proposed microscopic mechanisms for SHG in external fields. The influence of an external electric field is in accordance to the model from the SHG section. The application of a magnetic field is expected to give rise to a complex magneto-exciton series as in SHG, but only a single resonance from the $1s$ exciton is found. Its intensity increases by a factor of 175 in a magnetic field of $B^0 = 10\,\mathrm{T}$, which is an unusually strong influence of a magnetic field on THG.

In Chap. 5 SHG and THG spectra of gallium nitride (GaN) are presented and discussed. Although GaN is also a III-V semiconductor, it has different properties compared to GaAs. The most common crystal lattice of GaN is wurtzite, making it an uniaxial system. The band gap of $E_\mathrm{g} = 3.50\,\mathrm{eV}$ is much larger than in GaAs, and the exciton structure is more complicated. Three excitons series from different valence bands are within $30\,\mathrm{meV}$ below the band gap. The growth of this material is still problematic and important features, such as the band gap energy, vary between different samples, due to strain from lattice mismatch of GaN and the substrate material. In the past, THG and SHG from excitons in GaN were used to determine the energy of the $1s$ and $2p$ excitons from the A, B, and C exciton series [36]. A shift of the exciton resonances from strain within the material was found. In this thesis broad range THG spectra from $2.1\,\mathrm{eV}$ up to $3.55\,\mathrm{eV}$ are presented. The $1s$ excitons from all three valence bands are found. By comparison to existing studies, strain is verified in the material. Further resonances are found in the energy range below the excitons. They were not reported before, since the studies were confined to the region of excitons. For each resonance a responsible growth defect of GaN is proposed.

The SHG spectrum in GaN is similar to GaAs and is dominated by a broad range non-resonant SHG without exciton resonances. Measurements in a magnetic field are presented, but they do not reveal any contribution from excitons. This is attributed to the growth defects, because it was found that the quality of the sample has a strong influence on the intensity of exciton resonances in the SHG spectrum in GaAs.

In Chap. 6 SHG measurements in cuprous oxide (Cu_2O) are shown and discussed. Cu_2O is a very well investigated semiconductor and many effects on excitons were found in it for the first time [37]. It has a cubic crystal structure, but is centrosymmetric in contrast to GaAs. In centrosymmetric systems the electric-dipole SHG is forbidden and such systems are usually investigated by other methods [38]. Nevertheless, SHG of the $1s$ ortho exciton was reported and explained by electric-quadrupole (EQ) transitions [39]. Further measurements in other crystal directions and a magnetic field revealed SHG, which still lacks a microscopic description [33]. In chapter 6 extensive SHG measurements for three different crystal orientations with magnetic fields in Voigt and Faraday geometry are presented. Again SHG is found, which cannot be explained by EQ transitions. Polarization dependencies are compared to models of proposed mechanisms for the observed SHG. For further exciton states ($n > 1$ excitons, para excitons) an increase of SHG by a magnetic field is found. This is attributed to the mixing of exciton states by the external field.

In chapter A THG and SHG spectra of indirect band gap semiconductors, namely silicon (Si) and silicon carbide (SiC), are presented. The studies focus on the possibility of SHG and THG spectroscopy of indirect band gap semiconductors. Due to the indirect band gap, these materials are not very well suited for the interaction with light. Existing studies focus on SHG from interfaces or SHG in the reflection geometry. In this thesis SHG and THG from the bulk contribution in transmission geometry are investigated. In Si direct optical transitions from bands at the Γ point, which have a higher energy than the band gap, are investigated. In SiC on the other hand, SHG near the indirect band gap is investigated.

2. Theoretical background

At the beginning of this thesis a theoretical background for the measurements is given. The derivation of the nonlinear effects follows the books by Shen and Boyd [7, 8]. First, the fundamental equations for nonlinear optics based on the Maxwell equations will be presented. Especially the properties of SHG and THG will be discussed. A brief discussion of group theory allows to simplify the description of the processes and gives a useful tool for the prediction of polarization selection rules. Additionally, this theory is necessary to understand the frequency conversion of the laser system used in the experimental setup.

The second part introduces the main properties of semiconductors. Especially features of the electronic system, such as the band gap or excitons, are introduced. The interaction with light is the basis for the understanding of nonlinear optical phenomena within these systems. The most important symmetry features will be discussed. In the last part both will be combined for the understanding of theoretical aspects of the measurements.

2.1. Nonlinear optics

Nonlinear optics covers phenomena, which exceed the approximations of linear optics. Especially the manifold ways to convert the wavelength of light are in the focus of research. From everyday experience it is known that the approximations of linear optics are in good agreement with the observed effects. A high power density of light is necessary in order to give rise to nonlinear optics. This can only be achieved by intense laser light. The first observation of second harmonic generation was made soon after the invention of the laser [1]. The charges within a crystal do not react like a harmonic oscillator in strong light fields, but show a more complex behavior. Modern laser systems are strong enough to induce manifold high order nonlinear optical effects [40]. At first, the fundamental differences between linear and nonlinear optical effects and their origin are discussed.

2.1.1. Fundamentals of nonlinear optics

The Maxwell equations are a fundamental starting point for linear and nonlinear optics. They describe the relationship between the electromagnetic field and electric charges. A few manipulations of the equations lead to a macroscopic equation of light waves in a
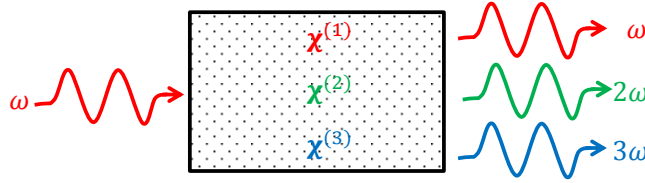
Figure 2.1. – The crystal can be considered to be a blackbox. The interaction with light is given by the susceptibilities. Each order of χ describes (among other effects) a specific harmonic generation.

solid-state material. A common representation of the Maxwell equations is [41]:

$$\nabla \cdot \mathbf{E} = \frac{\rho}{\epsilon_0} \tag{2.1a}$$

$$\nabla \cdot \mathbf{B} = 0 \tag{2.1b}$$

$$\nabla \times \mathbf{E} = -\frac{\partial \mathbf{B}}{\partial t} \tag{2.1c}$$

$$\nabla \times \mathbf{B} = \mu_0 \left(\mathbf{j} + \epsilon_0 \frac{\partial \mathbf{E}}{\partial t} \right) \tag{2.1d}$$

The electric field $\mathbf{E}$ and the magnetic field $\mathbf{B}$ are connected with the charge density ρ and the current density $\mathbf{j}$ by the electric constant ϵ_0 and the permeability μ_0. Since the fields depend on the derivative of each other, light waves are a possible solution. In order to get a wave equation for an electric field, the Grassmann identity is applied to Eq. (2.1c), then the other equations are plugged in. The current density $\mathbf{j}$ is expanded in a multipole expansion to identify different kinds of light matter interaction processes. This forms a wave equation for the electric field and the influences of the surrounding medium, which acts like an external driving force on the oscillating wave.

$$\Delta \mathbf{E} - \frac{1}{c^2} \frac{\partial^2 \mathbf{E}}{\partial t^2} = \mu_0 \frac{\partial^2 \mathbf{P}}{\partial t^2} + \mu_0 \frac{\partial}{\partial t} \nabla \times \mathbf{M} - \mu_0 \frac{\partial^2}{\partial t^2} \nabla \cdot \mathbf{Q} \tag{2.2}$$

The multipole elements $\mathbf{P}$, $\mathbf{M}$, and $\mathbf{Q}$ interact with the electric field of the light wave in this inhomogeneous wave equation. An external light field in a medium induces these multipole moments of charge distribution in the crystal. These react back on the light wave itself. Through this interaction an incident electric field creates high order frequencies within a material. These frequencies are emitted as light. A time dependent oscillating polarization $\mathbf{P}$ is an accelerated charge and radiates photons with the according frequency. Macroscopic calculations of a light field incident on oscillators allow for a basic understanding of this process and describe linear optical phenomena. Adding perturbations to harmonic oscillators reveals the influence of different symmetry situations and nonlinear optical processes.

The interaction of laser light with a crystal can best be understood by the introduction

of susceptibilities. The introduction of harmonic frequencies in the polarization by the electric field of the light wave is the strongest interaction and is presented first. The focus lies on the strong ED polarization, since it is the most important source of harmonic generation. Other multipole moments will be introduced when they are necessary and the effects from these can be considered in the same way as ED processes. The macroscopic equation

$$P_{\text{eff},i} = \epsilon_0 \chi_{ij}^{(1)} E_j + \epsilon_0 \chi_{ijk}^{(2)} E_j E_k + \epsilon_0 \chi_{ijkl}^{(3)} E_j E_k E_l + \dots \tag{2.3}$$

describes the polarization $\mathbf{P}_{\text{eff}}$ induced by incident electric fields $\mathbf{E}$. The first order susceptibility $\chi^{(1)}$ can be translated into the complex index of refraction $n' = n + i\kappa$, which describes the effects of linear optics. Higher order susceptibilities lead to nonlinear optical effects. These susceptibilities are usually much smaller than $\chi^{(1)}$. The electric field has to be strong enough to drive the oscillator away from the harmonic approximation. This can lead to harmonic conversion and other nonlinear optical effects.

In Fig. 2.1 the influence of the susceptibilities on the frequency conversion is shown schematically. Each susceptibility leads to a specific frequency conversion. From the susceptibilities one can derive the optical selection rules, which can be exploited to identify the contributions, or to selectively enhance or suppress them. The symmetry of a crystal gives much information about its susceptibilities. It reveals which components have to be zero and which components are independent from each other, but not oscillator strength or transition probabilities. For SHG it is necessary to know the second order susceptibility (which is a third rank tensor) of a certain system. For THG it is a fourth rank tensor. Many of the off diagonal terms of a susceptibility are zero for highly symmetrical systems. Crystals with the same symmetry therefore share many nonlinear optical properties, although a different band structure changes the details of the light matter interaction. Typical values for $\chi^{(2)} \approx 10^{-11} \frac{\text{cm}}{\text{V}}$ and $\chi^{(3)} \approx 10^{-17} \frac{\text{cm}^2}{\text{V}^2}$ are very small and therefore these effects are only observed under intense laser light.

The main focus of this thesis lies on second harmonic generation. A short calculation reveals the creation of harmonics due to the second order susceptibility. To calculate the expected results, the problem is reduced to one dimension and the incident wave is described as a plane wave:

$$E_x^\omega(t) = E^0 e^{(i\omega t)} + E^0 e^{(-i\omega t)} \tag{2.4a}$$

$$P_{\text{eff},x}^{2\omega}(t) = \epsilon_0 \chi_{xxx}^{\text{cryst}} \left(E_x^\omega(t)\right)^2 \tag{2.4b}$$

$$P_{\text{eff},x}^{2\omega}(t) = 2\epsilon_0 \chi_{xxx}^{\text{cryst}} E_x^\omega (E_x^\omega)^* + \epsilon_0 \left[\chi_{xxx}^{\text{cryst}} (E_x^\omega)^2 e^{(2i\omega t)} + \chi_{xxx}^{\text{cryst}} (E_x^\omega)^2 e^{(-2i\omega t)} \right] \tag{2.4c}$$

Equation (2.4a) describes the incident electric field of the light wave, which consists of an electric field amplitude E^0 and a complex e-function describing the oscillation. In Eq. (2.4b) an exemplary susceptibility connects the electric field to the effective second order polarization $P_x^{2\omega}(t)$ in the material. In Eq. (2.4c) the electric field is plugged into Eq. (2.4b) and the solution is sorted for different frequency components. The frequency independent part of the solution describes optical rectification. A strong light field can induce a constant electric field inside a crystal, which is exploited for certain applications [42].

The other part has the frequency 2ω. This time dependent polarization of second order emits a light wave with the frequency 2ω as it was discussed for Eq. (2.2). Other frequency conversions can be described with similar calculations. Besides sum effects, difference frequency processes are also possible. This leads to optical parametric oscillation, which is used in the experimental setup. This process splits a high frequency into two lower frequencies $\omega_0 = \omega_1 + \omega_2$.

The calculations (2.4) are specific for ED processes in which only the electric field of the light and the polarization in the material play a role. These calculations can be enhanced by also taking the magnetic field of light, its wave vector, and more multipole moments from (2.2) into account. This can be calculated like (2.4) and is necessary if the strongest ED contribution is forbidden. A complete set of possible transitions up to electric quadrupole is:

$$
\begin{pmatrix} \mathbf{P}^{2\omega} \\ \mathbf{M}^{2\omega} \\ \mathbf{Q}^{2\omega} \end{pmatrix} \propto \begin{pmatrix} \chi(\mathbf{P}^{2\omega}, \mathbf{E}^{\omega}, \mathbf{E}^{\omega}) & \chi(\mathbf{P}^{2\omega}, \mathbf{E}^{\omega}, \mathbf{H}^{\omega}) & \chi(\mathbf{P}^{2\omega}, \mathbf{H}^{\omega}, \mathbf{H}^{\omega}) \\ \chi(\mathbf{M}^{2\omega}, \mathbf{E}^{\omega}, \mathbf{E}^{\omega}) & \chi(\mathbf{M}^{2\omega}, \mathbf{E}^{\omega}, \mathbf{H}^{\omega}) & \chi(\mathbf{M}^{2\omega}, \mathbf{H}^{\omega}, \mathbf{H}^{\omega}) \\ \chi(\mathbf{Q}^{2\omega}, \mathbf{E}^{\omega}, \mathbf{E}^{\omega}) & \chi(\mathbf{Q}^{2\omega}, \mathbf{E}^{\omega}, \mathbf{H}^{\omega}) & \chi(\mathbf{Q}^{2\omega}, \mathbf{H}^{\omega}, \mathbf{H}^{\omega}) \end{pmatrix} \begin{pmatrix} \mathbf{E}^{\omega}\mathbf{E}^{\omega} \\ \mathbf{E}^{\omega}\mathbf{H}^{\omega} \\ \mathbf{H}^{\omega}\mathbf{H}^{\omega} \end{pmatrix}. \quad (2.5)
$$

In principle, it is possible to induce any multipole moment from Eq. (2.2) by any combination of the electric or magnetic field of the light wave. But each contribution, which is not of ED type ($\mathbf{E}^{\omega}$ of the light and the multipole moment $\mathbf{P}^{2\omega}$), substantially decreases the conversion efficiency. Susceptibilities which only connect polar vectors or an even number of axial vectors, are also called polar. The susceptibility is axial in case an odd number of axial vectors is involved. Typical polar vectors are the electric field of the fundamental light $\mathbf{E}^{\omega}$ or an externally electric field $\mathbf{E}^{0}$ applied to the sample. Typical axial vectors are the magnetic field of the light $\mathbf{H}^{\omega}$ or an external applied magnetic field $\mathbf{B}^{0}$.

There are two more effects which influence the conversion strength and do not play a big role in SHG spectroscopy. The first one is pump depletion. The loss of intensity in the incident light ω is not taken into account in the presented calculations, as the conversion strength in semiconductors is small enough to neglect this effect. In case SHG is used as a tool to convert the wavelength of a laser, high conversion efficiency is desired. In this case the depletion of the pump light intensity has to be taken into account.

The second effect stems from the phase difference between all the involved light waves. The electric field from the incident light does not have a fixed phase compared to the light field of SHG, because of the normal dispersion. This phase mismatch can decrease the efficiency of the conversion process, which was investigated by Maker et al. [43] shortly after the observation of SHG. It is possible to achieve phase matching between the fundamental light and the harmonics under certain conditions. By changing the temperature of the crystal or tuning the incident angle of the light, the phase matching conditions can be fine-tuned to enhance specific transitions. The optical parametric oscillator (OPO) in the experimental setup, which is described later, makes use of these techniques. For SHG spectroscopy the semiconductor sample is usually not optimized for phase matching. The incident angle of the light is chosen to match the symmetry conditions of electronic levels and the temperature is minimized to reduce phonon interactions. Therefore the measure-
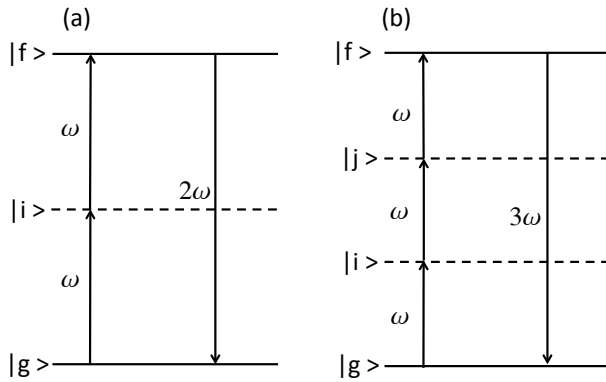
Figure 2.2 – (a) Transition scheme for SHG with a ground state $|g\rangle$, an excited state $|f\rangle$, and intermediate state $|i\rangle$. (b) QM transition scheme for THG with a second intermediate state $|j\rangle$.

ments are not enhanced by phase matching. In case an external magnetic field is applied to the sample, which influences the refractive index of the material, it is possible that the phase matching conditions are changed.

For SHG spectroscopy a more detailed connection between the eigenstates of the investigated semiconductors and the SHG has to be made, therefore requiring a microscopic description of light matter interaction leading to SHG.

2.1.2. Microscopic description of optical harmonic generation

The macroscopic description of harmonic generation made in Sec. 2.1.1 allows a basic understanding of the effects. However, the wavelength dependence of the susceptibility was not considered. The magnitude of a susceptibility is influenced by quasi-particles within a crystal. This can be exploited for the spectroscopy of these states. In order to calculate the wavelength dependent strength of harmonic generation, the transition has to be understood quantum mechanically (QM). In the QM description SHG is pictured as the conversion of two photons into a high energy one. In Fig. 2.2(a) the QM representation for this process is shown. The first photon makes a virtual transition between the ground state $|g\rangle$ and an intermediate state $|i\rangle$. The second photon completes the transition to the excited state $|f\rangle$. From the excited state the ground state is reached by emitting a photon with the frequency 2ω. In Fig. 2.2(b) the transitions for THG are presented. For THG three photons are converted into a high energy one of frequency 3ω. In this case another intermediate state $|j\rangle$ has to be taken into account. It is important to underline once more that the $|f\rangle$ state is not really existent, in the sense that is has a lifetime. It is possible to excite a quasi particle within a crystal with a two-photon process, but this is fundamentally different from SHG and will be considered later.

In the same way the Maxwell equations are the starting point for a classical description of optical effects, the Hamiltonian of a problem is the natural starting point for a QM

description. The Hamiltonian of the light, the electrons, and the interaction is:

$$\mathbf{H} = \sum_{e^-} \left[\left(\frac{\mathbf{p}^2}{2m_{\text{free,e}}} - e_0 V \right) + \left(\frac{e_0^2}{2m_{\text{free,e}}c^2} \mathbf{A}^2 + \frac{e_0}{m_{\text{free,e}}c} \mathbf{p}\mathbf{A} \right) \right] +$$
$$\frac{1}{8\pi} \int \left(\mathbf{E}^2 + \mathbf{B}^2 \right) \mathrm{d}^3 r \tag{2.6a}$$

$$\mathbf{H} = \mathbf{H}_{\text{e}} + \mathbf{H}_{\text{int}} + \mathbf{H}_{\text{light}} \tag{2.6b}$$

For the interaction between the light field and the charges the minimal coupling was chosen, which only includes the interaction of the charge distribution. Higher order contributions will be covered by introducing further mechanisms, like the interaction of light with the spin of the particle. The electron is characterized by its rest mass $m_{\text{free,e}}$, charge e_0, and momentum $\mathbf{p}$. The crystal structure is included through the periodic potential V. Especially the linear term in $\mathbf{A}$ is of interest for the interaction, as it describes the transition between different states. In order to identify different contributions to the interaction the vector potential of the light is expanded into a multipole series up to second order

$$\mathbf{A} = A_0 e_0 \mathrm{e}^{(\pm \mathrm{i}\mathbf{k}(\omega)\mathbf{r})} \simeq A_0 e_0 (1 \pm \mathrm{i}\mathbf{k}(\omega)\mathbf{r}) \tag{2.7}$$

With this expansion, the linear part of the interaction Hamiltonian can be divided in different transition elements, similar to the expanded current density in Eq. (2.2). The $\mathbf{k}$ independent part describes the so called electric dipole (ED) transition. The contributions linear in $\mathbf{k}$ are called magnetic dipole (MD) and electric quadrupole (EQ).

$$\langle \, \mathrm{f} \, | \, \mathbf{p} \, | \, \mathrm{g} \, \rangle : \mathbf{H}_{\text{ED}} = q\mathbf{E}\mathbf{r} \tag{2.8a}$$

$$\langle \, \mathrm{f} \, | \, \mathbf{pkr} \, | \, \mathrm{g} \, \rangle : \mathbf{H}_{\text{EQ}} = q\mathbf{k}\mathbf{E}\mathbf{r}^2 \tag{2.8b}$$

$$\langle \, \mathrm{f} \, | \, \mathbf{pkr} \, | \, \mathrm{g} \, \rangle : \mathbf{H}_{\text{MD}} = (\mathbf{L} + \mathbf{S})\mathbf{B} \tag{2.8c}$$

The ED transition is the strongest one and the other two only play a role if the ED is forbidden by the selection rules. For SHG to occur a two-photon transition and a one-photon transition to a specific resonance have to be allowed as shown in Fig. 2.2. The light intensity decreases rapidly for higher order processes and most of the three-photon transitions have to be of ED type to make SHG strong enough to be detected. The strongest SHG process only has ED contributions. This is usually the case for situations in which states are mixed by an external perturbation. In the unperturbed case a state is only allowed for one- or two-photon ED transitions, but not for both. In such a case it is possible to observe SHG by a two-photon ED and a one-photon EQ or MD transition. Processes with more than one transition of higher order than ED are very weak and seldom observed. For SHG spectroscopy of semiconductors this QM three-photon transition picture has to be combined with the susceptibility, which was introduced through wave equations. Through this combination it is possible to learn about the influence of eigenstates $| \, \mathrm{f} \, \rangle$ on $\chi^{(2)}$.

Up to now the wavelength dependence of $\chi^{(2)}$ was neglected. The susceptibility magnitude for each wavelength has to be derived from optical transition probabilities. In report

[31] the connection between the optical transition probabilities and the susceptibility is explained in detail with close relation to the measurement techniques used for this thesis. The equation

$$\chi_{lmn}(E_\mathrm{f},\mathbf{k}_\mathrm{f},\mathbf{B}^0,\mathbf{E}^0) \propto \sum_i \frac{\langle\, \mathrm{g}\,|\, \hat{V}_l^{2\omega}\,|\, \mathrm{f}\,\rangle\, \langle\, \mathrm{f}\,|\, \hat{V}_m^{\omega}\,|\, \mathrm{i}\,\rangle\, \langle\, \mathrm{i}\,|\, \hat{V}_n^{\omega}\,|\, \mathrm{g}\,\rangle}{(E_\mathrm{f} - 2\hbar\omega - i\Gamma_\mathrm{f})(E_\mathrm{i} - \hbar\omega)} \tag{2.9}$$

connects the susceptibility to the optical transitions by the eigenstates inside a medium. For the general description three arbitrary states have to be taken into account. For SHG spectroscopy of semiconductors each state has a specific role and will already be named according to that role. The states are the ground state $|\,\mathrm{g}\,\rangle$, the final state $|\,\mathrm{f}\,\rangle$, and the intermediate state $|\,\mathrm{i}\,\rangle$. These will get a more specific meaning in Sec. 2.2. The susceptibility in terms of energy, wave vector, and external perturbations is proportional to the transition strength for each of the three-photon processes and normalized by the energy difference between the photons and the eigenstates. The last two elements in the numerator describe a two-photon transition and the first element describes the creation of one photon of higher energy. The perturbations $\hat{V}$ represent the possible transitions described in (2.8). All possible intermediate states have to be taken into account within the sum. This is of course difficult for most real world applications. Therefore the sum has to be limited to the intermediate states which have the strongest contribution. The denominator takes the energy difference between the crystal states and the photons into account, including a damping factor Γ_f. Only states which are close to the photon energies have a noteworthy influence as the denominator grows with the energy mismatch. The responsible states within a semiconductor will be explained in the next chapter. The equation can be derived by perturbation theory. This is described in the appendix B, where the transition from the wavelength centered description to the focus on the crystal eigenstates is explained. The susceptibilities, which describe SHG and THG in a crystal without an external perturbation, are noted χ^cryst.

The exact calculation of the denominator of Eq. (2.9) is difficult, because the necessary eigenstates are hard to compute from first principles. It is often enough to understand what kind of perturbation leads to a non-zero denominator. This can be achieved by group theoretical calculations. The integral $\langle\,\mathrm{f}\,|\,\hat{V}\,|\,\mathrm{g}\,\rangle$ is only non-zero if $\Gamma_\mathrm{f} \subset \Gamma_\mathrm{V} \otimes \Gamma_\mathrm{g}$. The Γ_x represents the symmetry group of a crystal eigenstate or a perturbation. This will be covered in the next chapter, in which semiconductor crystals and the symmetry groups are explained.

2.2. Semiconductors

Semiconductors are a well known class of materials with manifold applications. Computer chips made from silicon are the most well-known application and have an unfathomable impact on technology in general. The name "semiconductor" already hints at the main property. The electronic structure lies between the isolators and the metals. Semiconductors do have a band gap in contrast to metals, but the magnitude is smaller compared to

isolators. The materials investigated in this thesis are well known semiconductors, which have technological applications and are of fundamental interest for research. The energy of the band gap is in the same range as that of photons in the visible or near infrared spectrum. This makes optical spectroscopy one of the main tools for the investigation of these materials.

2.2.1. Electronic band structure

The discrete energy levels of electrons in a shell of an atom change when they are located within the periodic structure of a crystal. An overlapping of the electronic orbitals leads to energy bands, the sum of which is called the band structure. It is impossible to calculate the solution of the full Hamiltonian of a crystal because of the huge amount of degrees of freedom such systems have.

The most interesting region for optical investigations is the band gap. Below the band gap all states are occupied and charge transport is impossible at low temperatures. Above the band gap, on the other hand, all states are empty. Electrons from the filled valence band can be excited into the empty conduction band. In order to understand the important properties for the interaction with light in this spectral range, simplifications of the complex many-body interactions are necessary.

First of all, the band structure is calculated for a single electron moving within an effective crystal potential. This potential accounts for all other ion cores and electrons, and has the same periodicity as the ion lattice. Interaction between the electrons will be taken into account as perturbations. These calculations reveal a band structure with energy bands labeled by the band index n and wave vector $\mathbf{k}$, which already allows for an understanding of the most important effects. Many properties of a crystal can be understood by calculating a single unit cell with periodic boundary conditions. The smallest unit cell in the $\mathbf{k}$ space is called Brillouin zone.

In order to calculate the band structure, theoretical tools like Bloch equations, the tight binding model and density functional theory are available [38, 44]. These calculations are complicated, because of the complexity of the situation. In order to understand important optical properties near the band gap, group theoretical analysis brings good insight into the situation.

The starting point for the group theoretical analysis are electron states in a free atom. The main quantum number has no direct influence on the symmetry conditions as it mainly influences the Bohr radius. The orbital angular momentum quantum number has the biggest influence and defines the transformations under which the system is invariant. Comparing the spherical s states to the bar-bell shaped p states makes the differences in symmetry obvious. The p states have a main symmetry axis whereas the s states have no preferred direction. All the eigenvalues of operations under which a state is invariant are collected in groups which are labeled from $D_0^{\pm}$ to $D_{\frac{13}{2}}^{\pm}$. Among these operations are rotations by a certain angle C_i, reflections at a plane σ_i and the identity E, for example.

The next step is to identify how the eigenvalues change if the state is within a crystal, which has a reduced symmetry compared to the full rotation group. Most semiconductors

have similar valence and conduction bands in this sense. The fully occupied p orbitals of the negatively charged kation form the valence bands. The empty s orbitals of the anion form the conduction band. However, there are important deviations from this scheme as will be discussed for Cu_2O.

A p type valence band has three bands, which are each two-fold spin degenerated. The four $J_h = 3/2$ states are split from the $J_h = 1/2$ by spin-orbit coupling. The sign of the spin-orbit energy Δ_{SO} determines, which of the states is the top valence band. The four $J_h = 3/2$ states are either degenerated at the center of the Brillouin zone or split in the crystal field, depending on the structure of the semiconductor. Away from the center of the Brillouin zone, the $J_h = 3/2$ are separated into two bands with different effective mass due to their different angular momentum projection $J_z = 1/2$ and $J_z = 3/2$. The dispersion of states near the center of the Brillouin zone is approximated by a parabola. The curvature of the parabola is described by an effective mass

$$\left(\frac{1}{m_{e,h}}\right)_{ij} = \frac{1}{\hbar^2}\frac{\partial^2 E_{e,h}(k)}{\partial k_i \partial k_j}, \tag{2.10}$$

which depends on the second derivative of the energy of an electron in the conduction band $E_e(k)$ or a hole in the valence band $E_h(k)$ near the center of the Brillouin zone. The effective mass $m_{e,h}$ replaces the free electron mass $m_{e,free}$ in the dispersion $E_{e,free}(k) = \frac{\hbar^2 k^2}{2m_{e,free}} \rightarrow E_{e,h}(k) = \frac{\hbar^2 k^2}{2m_{e,h}}$. The effective mass is important for the interaction with external electric or magnetic fields.

Optical transitions from the valence band to the conduction band can be calculated according to Eq. (2.9). The selection rules can be derived with group theory alone. The correct symmetries have to be plugged into the transition probability $\langle f | \hat{V} | g \rangle$. The ground state is the valence band and the final state is the conduction band. The perturbation is replaced by the appropriate symmetry of an ED, EQ or MD perturbation. Transitions induced by photons are practically vertical in the band structure, since they only have a small momentum. The details of this for SHG are explained in Sec. 2.3.

An electron excited into the conduction band can enter a bound state, called exciton, with a hole in the valence band. Excitons have many interesting properties, which are an active topic in optical investigations of semiconductors and are the main focus of this thesis. In the next section these particles are described in detail.

2.2.2. Excitons and polaritons

Excitons play a major role in the interaction between light and semiconductors, especially in the vicinity of the band gap. It turns out that photons with a smaller energy than the band gap can still excite electrons. Electrons which stay close to the created residual hole have a lowered energy due to the attractive Coulomb interaction between them. The binding energy can be as big as several hundred meV. The electron hole pair can be treated as a quasi-particle with its own wave function. There are two different kinds of excitons and they are classified by the Bohr radius of the two particle system. Frenkel

[45] excitons are very small and mainly confined to a single lattice site. Wannier excitons [46] extend over multiple lattice constants, and are the main type of excitons in the materials considered in this thesis. In semiconductors with several relevant valence bands or conduction bands, different excitons can be formed depending on the bands involved. The excitons are grouped in series which might be labeled A, B and C (in GaN) or yellow, green, and blue (in Cu_2O) for example. The energy of exciton series is described in analogy to the Rydberg series of an atom.

$$E_{\text{exc}}^n(k_{\text{exc}}) = E_{\text{g}} - \frac{R_{\text{exc}}}{n^2} + \frac{\hbar^2 k_{\text{exc}}^2}{2m_{\text{exc}}} \tag{2.11}$$

E_{g} is the energy of the band gap. The exciton energy lies below the band gap, due to the Coulomb attraction between the electron and the hole. This is expressed by the Rydberg energy of the exciton $R_{\text{exc}} = \hbar^2/2\mu_{\text{exc}}a_{\text{B}}$. An exciton also has excited states with reduced binding energy, which are labeled by the main quantum number n in E^n. Like the hydrogen series the exciton binding energy decreases with $1/n^2$ for the main quantum number[47]. The exciton Bohr radius is $a_B = 4\pi\epsilon\hbar^2/\mu_{\text{exc}}e_0^2$. The influence of screening effects can be described by the dielectric constant ϵ, since the Bohr radius of the investigated excitons is big enough for this averaging technique. The Rydberg energy and Bohr radius of the exciton depend on its reduced mass $\mu_{\text{exc}} = \frac{m_{\text{e}}m_{\text{h}}}{m_{\text{e}}+m_{\text{h}}}$, whereas the slope of the dispersion depends on the exciton mass $m_{\text{exc}} = m_{\text{e}} + m_{\text{h}}$. The effective electron m_{e} and hole mass m_{h} was defined in Sec. 2.2.1. The unit charge is $e_0 = 1.6 \cdot 10^{-19}$ C.

The wave function of an exciton does not solely depend on the valence and conduction band, but an additional envelope of the two particle wave function has to be considered. Since the electron hole pair can be treated in analogy to the hydrogen atomic model the envelopes are called $1s$, $2s$, $2p$, $3s$, $3p$, $3d$ etc. The calculation of these wave functions strongly depends on the knowledge of the wave functions of the energy bands in the crystal. The different angular momentum states are typically not degenerated and the influence of the angular momentum on the binding energy has to be considered in each individual case.

For the presented measurements a group theoretical approach will be made. The symmetry of such an exciton state is calculated by multiplying the valence band symmetry Γ_{vb} with the conduction band symmetry Γ_{cb} and an envelope Γ_{env}. The according ground state in selection rule calculations is the crystal in its undisturbed state and therefore always of Γ_1 symmetry.

$$\Gamma_{\text{exc}} = \Gamma_{\text{cb}} \otimes \Gamma_{\text{vb}} \otimes \Gamma_{\text{env}} \tag{2.12}$$

The conduction and valence band symmetry product usually leads to several excitons with different spin structures. Some of the excitons can be spin forbidden for optical transitions and are called dark excitons. For the bright excitons the envelope determines if the optical transition is allowed for one- or two-photon transitions. Usually only one or the other is allowed for the strong ED transition due to parity constraints. The remaining ones usually need at least an electric quadrupole transition and are much weaker.

Excitons, which couple to the electric field via the electric dipole operator, strongly interact with the light field. This interaction can be described by a quasi particle called
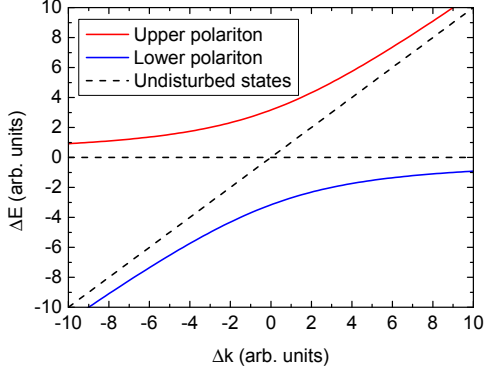
Figure 2.3 – Plotted solution to the polariton Hamiltonian. Black lines are the unperturbed photon and exciton. The red and blue line represent the upper and lower polariton branch respectively.

exciton-polariton [48, 49]. In fact, the light can couple strongly to different kinds of quasiparticles. All the coupled states are called polariton. Only exciton-polaritons play a role in this thesis and are addressed as polaritons.

In a simplified picture a polariton can be understood as the subsequent absorption of a photon to create an exciton and the emission of a photon by annihilation of an exciton over and over again. Stronger coupling of the exciton to the light field and a shorter lifetime of the exciton lead to more pronounced polariton effects. The biggest flaw of this picture is the time separation of the two particles, as they are in fact coexistent. Understanding polaritons as coupled oscillators is still a simple picture, but qualitatively reveals all its important properties. Therefore a Hamiltonian of coupled oscillators for a photon and an exciton is investigated. [49, 50]

$$\mathbf{H}_{\text{exc}-\text{p}} = \begin{pmatrix} E_{\text{p}}(k) & \frac{1}{2}\hbar\Omega_R \\ \frac{1}{2}\hbar\Omega_R & E_{\text{exc}}(k_{\text{exc}}) \end{pmatrix} \tag{2.13}$$

The energies $E_{\text{p}}(k)$ and $E_{\text{exc}}(k_{\text{exc}})$ are the k dependent energies of the photon and exciton, respectively. The off-diagonal entries are Rabi energies, which describe the coupling strength between the two particles in a crystal [51]. Diagonalization of the Hamiltonian (2.13) reveals the eigenvalues and eigenenergies of new quasiparticles.

$$E_{\text{Pol}} = \frac{E_{\text{p}}(k) + E_{\text{exc}}(k_{\text{exc}})}{2} \pm \sqrt{\left(\frac{E_{\text{p}}(k) + E_{\text{exc}}(k_{\text{exc}})}{2}\right)^2 + \left(\frac{\hbar\Omega_R}{2}\right)} \tag{2.14}$$

Plotting Eq. (2.14) around the crossing energy $E_{\text{p}}(k) = E_{\text{exc}}(k_{\text{exc}})$ reveals an anticrossing between the two states as presented in Fig. 2.3. The new quasi particles are the upper and lower polariton. In a semiconductor usually several different excitons contribute to polaritons. If this is the case then all the other exciton states in the vicinity have to be taken into account. In the Sellmeyer presentation the effect of multiple excitons can be expressed by the equation [49]

$$\epsilon(\omega) = \left(\frac{ck}{\omega}\right)^2 = \epsilon_\text{B} + \sum_i \frac{F_i}{T_i^2 - (\hbar\omega)^2}. \tag{2.15}$$

In Eq. (2.15) the effect of the polaritons on the dielectric constant $\epsilon = \epsilon_\text{r}\epsilon_0$ of the semiconductor is expressed, which can also be separated into the fundamental electric constant ϵ_0 and the material dependent relative permittivity ϵ_r. If only a specific energy range $\hbar\Delta\omega$ is of interest then only exciton states in the vicinity of this energy range need to be taken into account. The influence of the other exciton states is summarized in a background dielectric constant ϵ_B. Solving the equation for $\omega(k)$ reveals all allowed polariton states. The oscillator strength of the excitons F_i and the energy of transverse excitons T_i determine the strength of the interaction. The polariton picture is especially important for ED allowed transitions, because of the influence of the oscillator strength. The effects are much smaller for EQ transitions. States which are neglected in the summation are included in the background constant ϵ_B. The more convenient Kurosawa representation [52] is chosen for the actual calculations:

$$\epsilon(\omega) = \left(\frac{ck}{\omega}\right)^2 = \epsilon_\text{B} \prod_i \frac{L_i^2 - (\hbar\omega)^2}{T_i^2 - (\hbar\omega)^2} \tag{2.16}$$

This representation is equivalent to the Sellmeyer representation, but expresses ϵ in terms of the longitudinal and transverse exciton energies, which are well-known through spectroscopic studies in many cases. In contrast to the vacuum light wave there are excitons with longitudinal oscillations for the dispersion $\epsilon(\omega) = 0$, which are called longitudinal excitons. For uniaxial crystals the two different dielectric constants $\epsilon_\parallel$ and $\epsilon_\perp$ have to be considered separately. In case of light with polarization components for both the ordinary and the extraordinary axis, so called mixed-mode polaritons have to be taken into account. They are angle dependent on the k vector.

2.2.3. Band structure and exciton series of the investigated materials

In Secs. 2.2.1 and 2.2.2 general properties of semiconductors were introduced. In this section the materials investigated in this thesis are discussed in more detail and band structures for the investigated materials are presented. The important symmetries Γ_X and energies are noted. Every valence band has a maximum at the center of the Brillouin zone. The minimum of the conduction band depends on the specific material. Si and SiC are indirect semiconductors, as the global minimum of their conduction band is not at the Γ point. Other materials studied in this thesis are direct band gap semiconductors.

GaAs

In Fig. 2.4 the band structure of GaAs is presented. GaAs has a direct band gap with an energy of $E_\text{g}(T = 1\,\text{K}) \approx 1.52\,\text{eV}$ [34] at cryogenic temperatures. The band gap energy of
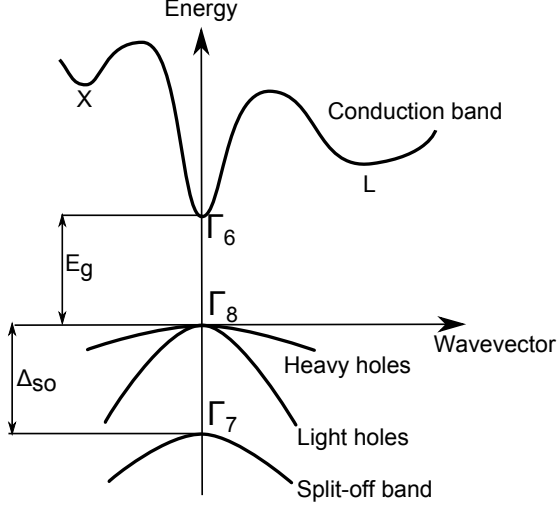
Figure 2.4 – Band structure of GaAs in the center of the Brillouin zone. The band gap E_g is at the Γ point, which makes it a direct semiconductor. The two valence bands, with angular momentum $3/2$, are degenerate at the Γ point and are called heavy-hole band and light-hole band according to their curvature. The valence band with angular momentum $1/2$ is separated by the energy Δ_{SO}. Each of the presented bands is two-fold spin degenerated.

GaAs decreases for higher temperatures and can be calculated by [34]

$$E_g(T) = 1.519 \, [\text{eV}] - \frac{0.0005405 \, T^2}{204 \, [\text{K}] + T} \left[\frac{\text{eV}}{\text{K}} \right] \tag{2.17}$$

The p type valence band is two-fold degenerated for the angular momentum $J_h = 1/2$ states and four-fold degenerated for the $J_h = 3/2$ states at the Γ point. The angular momentum $J_h = 1/2$ states have a reduced energy $\Delta_{SO} = 340 \, \text{meV}$ due to spin-orbit interaction and are called split-off band. The four angular momentum $J_h = 3/2$ states are degenerated at the Γ point and are called heavy hole $m_{hh} = 0.51 \, \text{m}_{\text{e,free}}$ and light hole $m_{lh} = 0.044 \, \text{m}_{\text{e,free}}$ [53] band according to their effective mass. The heavy holes are important for the observed excitons because the flat dispersion leads to a higher density of states. At the center of the Brillouin zone the upper valence bands have the symmetry Γ_8. The s type conduction band with $m_e = 0.067 \, \text{m}_{\text{e,free}}$ is two-fold spin degenerated and has the symmetry Γ_6.

Excitons with a binding energy of $R_{exc} = 4.2 \, \text{meV}$ are located below the band gap. The s excitons have the symmetry $\Gamma_{1s} = \Gamma_6 \otimes \Gamma_8 \otimes \Gamma_1 = \Gamma_3 \oplus \Gamma_4 \oplus \Gamma_5$. Only the Γ_5 states with spin $S = 1$ are allowed for one-photon transitions, which also have Γ_5 symmetry. The other exciton states with spin $S = 0$ are called dark excitons. The p excitons have a Γ_5 envelope and are only allowed for two-photon transitions. The important energies for the measurements are $E_{1s} = 1.5152 \, \text{eV}$, $E_{2s} = 1.5183 \, \text{eV}$, and $E_{2p} = 1.5189 \, \text{eV}$ [54, 55].

Excitons from the split-off band are neglected. Due to the strong spin-orbit coupling they are about $340 \, \text{meV}$ above the band gap and do not interact with the excitons from the Γ_8 band.

It is not expected to observe SHG from the excitons in GaAs. No exciton state is allowed for one- and two-photon transitions at the same time. Only mixed states created by external fields lead to resonant enhanced SHG. For THG it is expected to observe the s excitons. They are allowed for one- and three-photon transitions, which have similar selection rules. The important symmetries are summarized in Table 2.1. Although GaAs

Table 2.1. – Symmetry considerations for GaAs

state	symmetry	parity
valence band	$\Gamma_8 \oplus \Gamma_8 \oplus \Gamma_7$	$-$
conduction band	Γ_6	$+$
one photon	Γ_5	$-$
two photons	$\Gamma_1 \oplus \Gamma_3 \oplus \Gamma_4 \oplus \Gamma_5$	$+$
three photons	$\Gamma_1 \oplus \Gamma_2 \oplus \Gamma_3 \oplus \Gamma_4 \oplus \Gamma_5$	$-$
$1s$ exciton	$\Gamma_3 \oplus \Gamma_4 \oplus \Gamma_5$	$-$
$2p$ exciton	$\Gamma_1 \oplus \Gamma_3 \oplus \Gamma_4 \oplus \Gamma_5$	$+$

Figure 2.5 – Band structure of GaN in the center of the Brillouin zone. The band gap E_g is at the Γ point, which makes it a direct semiconductor. The two valence bands, with angular momentum $3/2$ are called A and B band. The valence band with angular momentum $1/2$ is separated by the energy Δ_SO and is called C band. Each of the presented bands is two-fold spin degenerated.
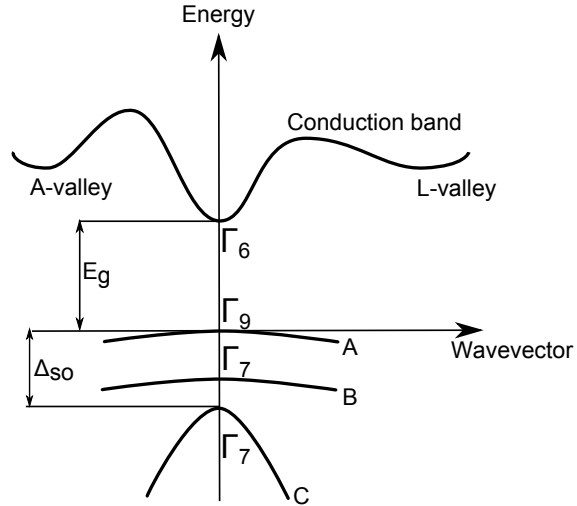
is not centrosymmetric, parity conservation is a good approximation at the center of the Brillouin zone and the parity approximations are also given in Table 2.1.

GaN

GaN has two different stable crystal lattices. The growth parameters determine if the more common wurtzite structure or a cubic structure emerges. In this thesis only the wurtzite structure is investigated and its band structure is discussed in detail.

In Fig. 2.5 the band structure of GaN is presented. It has a direct band gap like GaAs, but a much higher band gap energy of $E_\mathrm{g}(T = 1\,\mathrm{K}) \approx 3.50\,\mathrm{eV}$. The exact band gap value depends on the thickness of the GaN sample and the substrate it is grown on. The temperature dependence of the band gap is [56]

$$E_\mathrm{g}(\mathrm{T}) = 3.47\,[\mathrm{eV}] - 7.7 \cdot 10^{-4} \frac{T^2}{600\,[\mathrm{K}] - T} \left[\frac{\mathrm{eV}}{\mathrm{K}}\right]. \tag{2.18}$$

The conduction band is formed by the Ga $3d$ states and has Γ_6 symmetry. The valence band is formed by the N $2p$ states. The C band stems from the $J_\mathrm{h} = 1/2$ states with Γ_7 symmetry and has a reduced energy of about $\Delta_\mathrm{SO} \approx 24\,\mathrm{meV}$ [57]. In contrast to GaAs

Table 2.2. – Symmetry considerations for GaN. For the excitons the symmetry component governing the interactions with photons are noted and secondary components are in brackets.

state	symmetry
valence band	$\Gamma_9 \oplus \Gamma_7 \oplus \Gamma_7$
conduction band	Γ_6
photon $\parallel c$ axis	Γ_1
photon $\perp c$ axis	Γ_5
$A1s/B1s$ exciton	$\Gamma_5(\oplus \Gamma_1)$
$C1s$ exciton	$\Gamma_1(\oplus \Gamma_5 \oplus \Gamma_2)$

the $J_{\mathrm{h}} = 3/2$ are not degenerated at the Γ point because the hexagonal crystal field lifts the degeneracy of p_z and $p_{x,y}$ orbitals. The highest band has Γ_9 symmetry and the lower one has Γ_7 symmetry.

There are more exciton series to differentiate compared to GaAs. First of all, the splitting between the three valence bands is of the same order as the exciton binding energy. The excitons from the lower valence bands have to be taken into account. The three exciton series are called A, B, and C according to the involved hole. Additionally, the uni-axial structure leads to a splitting of exciton states polarized parallel or perpendicular to the c axis. All the different exciton states can be derived from the band symmetries, but only a few states have the necessary oscillator strength to be observed. Polarization (of excitons and photons) along the c axis has Γ_1 symmetry and polarization perpendicular to the c axis has Γ_5 symmetry. This is also used to identify the most important component of an exciton state for its interaction with light. In a tilted geometry, light has both symmetry components and multi-photon transitions are possible to many different states. An overview of the important symmetries is given in Table 2.2.

The resulting $A1s$ excitons $\Gamma_9 \otimes \Gamma_7 \otimes \Gamma_1 = \Gamma_5 \oplus \Gamma_6$ and $B1s$ excitons $\Gamma_7 \otimes \Gamma_7 \otimes \Gamma_1 = \Gamma_5 \oplus \Gamma_1 \oplus \Gamma_2$ have the same main symmetry component Γ_5, because the valence band functions are mainly polarized perpendicular to the c axis, although their overall symmetry is different. The $C1s$ excitons $\Gamma_7 \otimes \Gamma_7 \otimes \Gamma_1 = \Gamma_1 \oplus \Gamma_5 \oplus \Gamma_2$ are mainly of Γ_1 symmetry as they are polarized mainly along the c axis. The Γ_6 and Γ_2 states are optical forbidden paraexcitons.

The p excitons aligned along the c axis have an additional Γ_1 envelope contribution. Perpendicular to the c axis the p excitons have a Γ_5 envelope. The additional Γ_5 contribution from the p envelope enhances the Γ_5 component of the $C2p$ exciton.

Cu$_2$O

In Fig. 2.6 the band structure of Cu$_2$O is presented. Cu$_2$O is a centrosymmetric material. Parity is a good quantum number and parity conservation is a strict selection rule. The highest valence band from the Cu $3d$ electrons is split into three states by the crystal field and spin-orbit interaction. The d type valence band leads to different optical selection rules of the excitons, compared to the more common p type valence band, which is found in

Figure 2.6 – Band structure of Cu$_2$O in the center of the Brillouin zone. The band gap E_g is at the Γ point, which makes it a direct semiconductor. Each of the presented bands is two-fold spin degenerated.
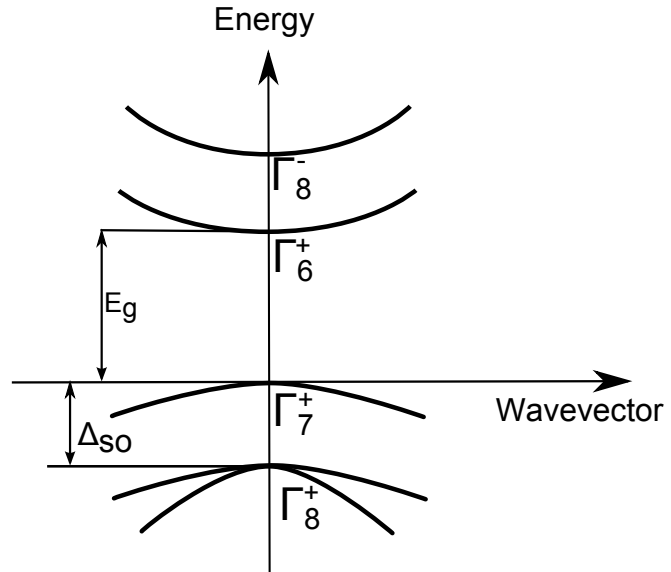
GaAs and GaN. Additionally, the spin-orbit splitting of the valence band $\Delta_{SO} = -0.13\mathrm{eV}$ [58] has a negative energy in Cu$_2$O. Therefore the the angular momentum $J_\mathrm{h} = 1/2$ band is the highest one and has symmetry Γ_7^+. The four-fold degenerate $J_\mathrm{h} = 3/2$ band is the lower lying one and is of Γ_8^+ symmetry. The lowest lying conduction band from the Cu $4s$ states has Γ_6^+ symmetry. A Γ_8^- band about $\Delta E \approx 0.5\,\mathrm{eV}$ above the conduction band from the Cu $4p$ is not investigated in this thesis. The band gap of Cu$_2$O is $E_\mathrm{g} = 2.172\,\mathrm{eV}$ [59].

Between all different valence and conduction bands exciton series are formed. The series of lowest energy is between the Γ_7^+ valence band and the Γ_6^+ conduction band. It is called yellow series, due to its emission wavelength. The green series is formed between the lower lying Γ_8^+ valence band and the same Γ_6^+ conduction band. Both series have similar selection rules, because they stem from bands with the same positive parity. The two valence bands form the blue and violet series together with the Γ_8^- conduction band. The blue $E_{\mathrm{g,blue}} = 2.624\,\mathrm{eV}$ and violet $E_{\mathrm{g,indigo}} = 2.755\,\mathrm{eV}$ band-band transitions [60] have an energy which lies well above the band gap. They are not investigated in this thesis and the interaction of the blue and indigo exciton series with the other two exciton series can be neglected. The yellow and green series have a smaller energy than the band gap and are discussed in more detail. They belong to the band-band transitions with $E_{\mathrm{g,yellow}} = E_\mathrm{g} = 2.172\,\mathrm{eV}$ and $E_{\mathrm{g,green}} = 2.304\,\mathrm{eV}$ [61].

The yellow exciton series has been investigated up to $n = 12$. The symmetry of the s type excitons is $\Gamma_7^+ \otimes \Gamma_6^+ \otimes \Gamma_1^+ = \Gamma_5^+ \oplus \Gamma_2^+$. The Γ_2^+ exciton is the optically forbidden paraexciton, which has an angular momentum of $J_\mathrm{exc} = 0$. The Γ_5^+ s excitons have $J_\mathrm{exc} = 1$ and are allowed for one-photon EQ transitions and two-photon ED transitions. The p excitons of this series are allowed for one-photon ED transitions. The yellow exciton series is described with the binding energy $R_\mathrm{exc} = 98\,\mathrm{meV}$. The yellow $1s$ exciton has

Table 2.3. – Symmetry considerations for Cu_2O. The Γ_5^+ states of the $1s$ exciton are orthoexcitons and the Γ_2^+ states are the optically forbidden paraexcitons.

state	symmetry
valence band	$\Gamma_7^+ \oplus \Gamma_7^+ \oplus \Gamma_8^+$
conduction band	$\Gamma_6^+ \oplus \Gamma_8^-$
$1s$ yellow exciton	$\Gamma_5^+ \oplus \Gamma_2^+$
photon	Γ_4^-

an exceptionally small Bohr radius $a_B = 0.8\,\text{nm}$ [62] compared to the lattice constant $a = 0.42\,\text{meV}$ of Cu_2O. This leads to an enhanced binding energy of $R_{1s,\text{exc}} = 150\,\text{meV}$, due to central cell corrections, specifically for the $1s$ exciton. For $n > 2$ these corrections only play a minor role, because the Bohr radius increases quadratically with n. The $1s$ orthoexciton has an increased energy compared to the paraexciton $\varepsilon = 12.1\,\text{meV}$, because of isotropic short range interactions of the electron and hole, which only affects the orthoexciton states [63]. The symmetry and parity values are given in Table 2.3. The important energies for the measurements are summarized in Table 2.4.

**Table 2.4.** – Energies of the yellow exciton series taken from [59, 64]

yellow excitons	$1s$ (ortho)	$1s$ (para)	$2s$	$2p$	$3s$	$3p$	$3d$
Energy (eV)	2.0330	2.0212	2.1544	2.1473	2.1603	2.1609	2.1630

The green exciton series is not directly observed in the measurements presented in Sec. 6, but the green $1s$ exciton $E_{\text{green},1s} = 2.1378\,\text{eV}$ [64] lies in between the $1s$ and $2s$ states from the yellow series. It is admixed to the yellow $1s$ and $2s$ states, but this does not change the selection rules, because it stems from bands with the same symmetry as the yellow excitons. Due to the admixture, the oscillator strength of the $1s$ green exciton is very small [64] and is not expected to be observed in the SHG spectra.

Si and SiC

The semiconductors Si and SiC are both indirect semiconductors in contrast to the other semiconductors investigated in this thesis. The minimum of the conduction band of Si and SiC is not at the center of the Brillouin zone, but at another point in the k-space. The valence band, on the other hand, is similar to the other semiconductors. In Fig. 2.7 the band structure of Si is presented. The valence band splitting is similar to GaAs, but the minimum of the conduction band is near the X point. The temperature dependency

Figure 2.7 – Band structure of Si and SiC. The conduction band minimum is at the X-valley for Si and cubic SiC. Other SiC structures have the conduction band minimum at other points (e.g. M-valley), but never at the Γ point. The exemplary valence band structure fits to Si and cubic SiC. Other SiC structures have the typical three-fold splitting of hexagonal structure (e.g. like GaN presented in Fig. 2.5).
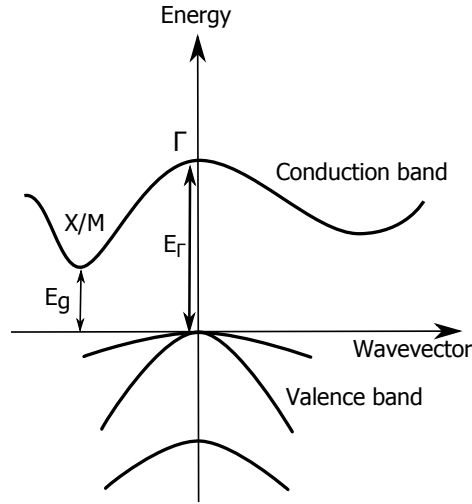
of the band gap [65] is

$$E_{\mathrm{g}}(T) = 1.1700\,[\mathrm{eV}] + T \cdot 1.059 \cdot 10^{-5} \left[\frac{\mathrm{eV}}{\mathrm{K}}\right] - T^2 \cdot 6.05 \cdot 10^{-7} \left[\frac{\mathrm{eV}}{\mathrm{K}^2}\right]$$
$$\text{for } 0\,\mathrm{K} < T < 190\,\mathrm{K}, \qquad (2.19\mathrm{a})$$

$$E_{\mathrm{g}}(T) = 1.1785\,[\mathrm{eV}] - T \cdot 9.025 \cdot 10^{-5} \left[\frac{\mathrm{eV}}{\mathrm{K}}\right] - T^2 \cdot 3.05 \cdot 10^{-7} \left[\frac{\mathrm{eV}}{\mathrm{K}^2}\right]$$
$$\text{for } 150\,\mathrm{K} < T < 300\,\mathrm{K}, \qquad (2.19\mathrm{b})$$

which results in $E_{\mathrm{g}}(T = 0\,\mathrm{K}) = 1.170\,\mathrm{eV}$. The direct transition at the Γ-point has the energy $E_{\Gamma}(T = 300\,\mathrm{K}) = 3.4\,\mathrm{eV}$. The temperature dependence of E_{Γ} is not reported, but the shift of the direct transition at $T = 0\,\mathrm{K}$ should be of the same order as the shift of E_{g}.

SiC is also an indirect band gap semiconductor. There are many stable lattice phases for SiC. In this thesis the hexagonal 6H and 4H are investigated, which are the most common stable phases along with the cubic 3C phase. Hexagonal SiC has a minimum of the conduction band in the M-valley with $E_{\mathrm{g,4H}}(T = 300\,\mathrm{K}) = 3.23\,\mathrm{eV}$, $E_{\mathrm{g,6H}}(T = 300\,\mathrm{K}) = 3.0\,\mathrm{eV}$ and $E_{\mathrm{g,4H}}(T = 0\,\mathrm{K}) = 3.26\,\mathrm{eV}$, $E_{\mathrm{g,6H}}(T = 0\,\mathrm{K}) = 3.02\,\mathrm{eV}$ [66–68]. The band structure in Fig. 2.7 matches the cubic phase of SiC. The hexagonal phase has three nondegenerated valence bands like hexagonal GaN, which is presented in Fig. 2.5. The direct band-band transition for any type of SiC is bigger than $E_{\Gamma} \geq 5\,\mathrm{eV}$ at the Γ point and is not accessible by the experimental setup.

2.2.4. Influence of electric and magnetic fields on excitons

An important part of the investigations in this thesis are external fields applied to semiconductors. Therefore the main interactions of excitons with external magnetic or electric fields are described. An external field has two influences on the SHG and THG spectra. On the one hand, the exciton energy is influenced, which leads to a shift of exciton res-

onances in the spectrum. On the other hand, the intensity of SHG and THG is changed by the influence of an external field on the wave function of excitons. This can lead to an intensity enhancement of a resonance (even from a forbidden resonance in zero field) or to a decrease of intensity in an external field.

Small external fields are treated as a perturbation of the excitons. In this context, an electric field is termed as "small" when it does not ionize the exciton into a free electron and hole. This would lead to an electrical current, since the electrons and holes move in opposite directions due to the electric field. The applied voltage breaks down and a current flows, since the resistance of the semiconductor is reduced. The limit is reached when $\frac{E^0}{\epsilon} e_0 a_{\mathrm{B}} \geq R_{\mathrm{exc}}$, which is about $E^0 \approx 4 \, \frac{\mathrm{kV}}{\mathrm{cm}}$ for the excitons in GaAs. A small electric field is treated as an odd parity perturbation of the excitons, the Stark effect, which is known from the influence of an electric field on the lines in an optical spectrum of atoms.

A magnetic field is termed "small" when its influence lies mostly on the exciton itself and the effect on the band structure can be neglected. When the exciton binding energy R_{exc} is bigger than the cyclotron energy $\hbar\omega_{\mathrm{c}} = \hbar\frac{e_0 B^0}{\mu_{\mathrm{exc}}}$, the magnetic field can be treated as a perturbation of the undisturbed exciton system. In this case the exciton energy changes because of the diamagnetic shift and the degeneracy of orbital and spin angular momentum is lifted. The Landau quantization of the electron bands is the dominant effect in high magnetic fields.
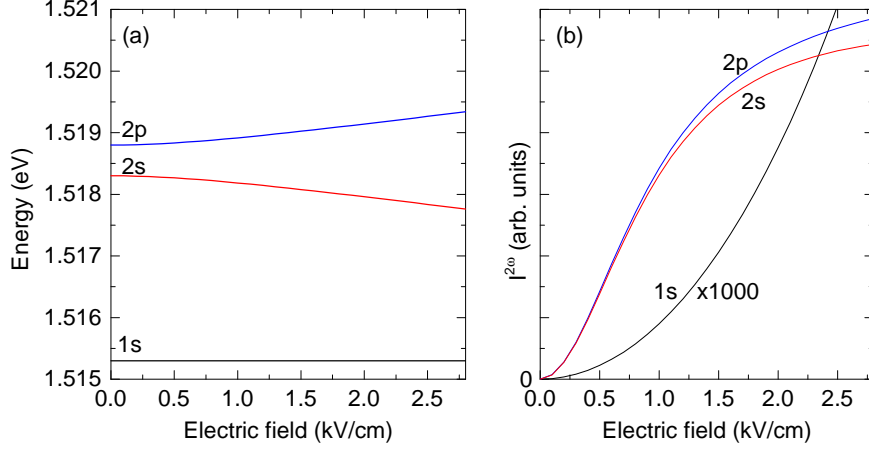
Stark effect

Measurements for GaAs are made in an electric field. The application of an electric field to a semiconductor leads to the mixing of exciton states with opposite parity. The electric field also influences the whole electron band structure, but the influence is small considering the field strength used in the experiments. The shift of the GaAs band gap is well below the $200 \, \mu\mathrm{eV}$ resolution of the experimental setup for the maximum applied field of $2.8 \, \frac{\mathrm{kV}}{\mathrm{cm}}$ [69].

The influence of the electric field on the exciton ground state E_{1s} and the first two excited states E_{2s} and E_{2p} is described by the Hamiltonian

$$H(E^0) = \begin{pmatrix} E_{1s} & 0 & \xi\frac{E^0}{\epsilon}e_0 a_{\mathrm{B}} \\ 0 & E_{2s} & \frac{E^0}{\epsilon}e_0 a_{\mathrm{B}} \\ \xi\frac{E^0}{\epsilon}e_0 a_{\mathrm{B}} & \frac{E^0}{\epsilon}e_0 a_{\mathrm{B}} & E_{2p} \end{pmatrix}. \tag{2.20}$$

On the main diagonal are the energies of the undisturbed $1s$ exciton $E_{1s} = 1.5152\,\mathrm{eV}$, $2s$ exciton $E_{2\mathrm{s}} = 1.5183\,\mathrm{eV}$, and the $2p$ exciton $E_{2\mathrm{p}} = 1.5189\,\mathrm{eV}$ at $T = 5\,\mathrm{K}$ [55]. The off-diagonal elements describe the mixing of these states through the electric field. The Stark effect depends on the external field strength E^0, the exciton Bohr radius $a_B = 15\,\mathrm{nm}$ [70] and the elementary charge $e_0 = 1.6 \cdot 10^{-19}\,\mathrm{C}$. The external field is reduced by the DC dielectric constant of GaAs $\epsilon = 12.9$ [71]. The higher oscillator strength between $2s$ and $2p$ states over the $1s$ and $2p$ states is accounted for by ξ. The interaction of the $1s$ and

$2p$ is reduced by $\xi = \frac{1}{\sqrt{2}}(\frac{2}{3})^8 \approx 0.28$. It is the relative magnitude of the orbital overlap solutions $\xi = \frac{S_{1s/2p}}{S_{2s/2p}}$.

Figure 2.8. – (a) Eigenenergy solutions of the Stark effect Hamiltonian for excitons in GaAs. The shift of the $1s$ exciton is small $\Delta_{1s} << 10\,\mu\text{eV}$. The $2s$ and $2p$ excitons shift each $\Delta_{\text{Sta}} \approx 0.5\,\text{meV}$ away from each other. (b) The expected increase of SHG for $\mathbf{k} \parallel [001]$ at the $1s$, $2s$, and $2p$ exciton resonance. The EFISH at the $1s$ grows quadratic, whereas the other two states show a saturation for high field strength. The growth of the $1s$ is magnified by 1000.

The Stark effect Hamiltonian is diagonalized to calculate the modified eigenstates and eigenenergies. In Fig. 2.8(a) the modified eigenenergies, which depend on the external field strength, are plotted. The $1s$ state has a negligible small shift even for maximal field strength. The $2s$ and $2p$ states undergo a repulsion and shift about $\Delta_{\text{Sta}} \approx 0.5\,\text{meV}$ down ($2s$) or up ($2p$).

The eigenvectors of the Hamiltonian describe the admixture of the undisturbed states to the wave function of the modified states in an electric field. Both the s excitons and the p excitons are forbidden for SHG, but the new wave function of the mixed states are allowed for SHG. There is a detailed explanation in Sec. 2.3.1. The new wave functions Ψ' are given by

$$\Psi'_{1s,\text{mix}} = C_{1s}^{1s}(E^0)\Psi_{1s} + C_{2s}^{1s}(E^0)\Psi_{2s} + C_{2p}^{1s}(E^0)\Psi_{2p} \tag{2.21a}$$

$$\Psi'_{2s,\text{mix}} = C_{1s}^{2s}(E^0)\Psi_{1s} + C_{2s}^{2s}(E^0)\Psi_{2s} + C_{2p}^{2s}(E^0)\Psi_{2p} \tag{2.21b}$$

$$\Psi'_{2p,\text{mix}} = C_{1s}^{2p}(E^0)\Psi_{1s} + C_{2s}^{2p}(E^0)\Psi_{2s} + C_{2p}^{2p}(E^0)\Psi_{2p} \tag{2.21c}$$

The coefficients $C_B^A(E^0)$ describe the fraction of the undisturbed wave function Ψ_B to the new mixed state $\Psi'_{A,\text{mix}}$ depending on the electric field strength E^0. In Sec. 2.3.1 it is explained how the SHG intensity is calculated from the coefficients $C_B^A(E^0)$. The solution of these calculations reveals the intensity

$$I_X^{2\omega} \propto \left(\chi^{(3)}\right)^2 \propto C_{2p}^X(C_{1s}^X + \frac{1}{\sqrt{8}}C_{2s}^X) \tag{2.22}$$

for each of the exciton resonances $X \hat{=} 1s$, $2s$, or $2p$. The $\frac{1}{\sqrt{8}}$ factor accounts for the reduced oscillator strength of the undisturbed $2s$ compared to the $1s$ exciton. The solutions are plotted in Fig. 2.8. For the $1s$ exciton a quadratic increase of intensity is expected. For the $2s$ and $2p$ an increase up to a saturation is expected. The increase of intensity at the $1s$ resonance is smaller by a factor of 1000, because it has a bigger energy distance to the other states and a smaller wave function overlap with them.

It is important to remember, that the threshold of $E^0 \approx 4\,\frac{\text{kV}}{\text{cm}}$ for ionization was calculated for the binding energy of the $1s$ state. The other two states might not turn up in the spectra, because of their reduced binding energy of $\frac{R_{\text{exc}}}{n^2} \approx 1\,\text{meV}$. These states are ionized even below $E^0 \approx 1\,\frac{\text{kV}}{\text{cm}}$.

Diamagnetic shift

Every exciton experiences the diamagnetic shift in an external magnetic field. It is the compression of the Bohr radius a_B of the excitons through the Lorentz force, which the particles experience in the magnetic field. It leads to a quadratic shift of the exciton energy

$$\Delta E_{\text{dia}}(B^0) = \left[B^0\right]^2 \alpha_{\text{dia}}. \tag{2.23}$$

The constant α_{dia} has to be measured or calculated for each exciton state. Excitons with a higher Bohr radius experience a stronger diamagnetic shift $\alpha_{\text{dia}} \propto a_\text{B}^2$. For the yellow $1s$ orthoexciton in Cu_2O, for example, the diamagnetic shift can be neglected, because it has a very small Bohr radius of $a_\text{B} = 0.8\,\text{nm}$. It is the main mechanism for the blue shift in a magnetic field for the $1s$ exciton in GaAs.

The diamagnetic shift is smaller than the other magnetic field influences on the excitons, which will be presented next, but it is always present and has to be taken into account. The diamagnetic shift leads to a shift of exciton resonances in SHG and THG spectra. It appears, for example, in measurements on the $1s$ exciton of GaAs in Sec. 4.3.3.

Zeeman effect

The Zeeman effect describes the interaction of the exciton angular momentum with an external magnetic field. This angular momentum stems from the spin of an exciton or its envelope function.

The spin Zeeman effect splits the degenerated spin states of an exciton

$$\Delta E_{\text{SpinZee}} = \pm \frac{1}{2} g_\text{x} \mu_\text{B} B^0 \tag{2.24}$$

The energy shift is proportional to the magnetic field B^0 and the g_x factor of the exciton. The g_x factor of an exciton stems from the hole and the electron contribution $g = g_\text{h} + g_\text{e}$. The g_x factor has to be determined for the exciton. The factor $\mu_\text{B} = \frac{e_0}{2m_\text{e}}\hbar$ is the Bohr magneton. The Zeeman effect can be observed in the splitting of the $1s$ exciton in Cu_2O presented in Sec. 6.2.2.

The splitting of degenerated states in a magnetic field due to their orbital angular momentum is described by

$$\Delta E_{\text{OrbZee}} = \pm g_{\text{orb}} \mu_{\text{B}} B^0 \tag{2.25}$$

In this case, the energy shift is also linear in B^0 and depends on the g factor of the envelope.

A magnetic field also leads to a mixing of exciton states through these effects. In contrast to an electric field, a magnetic field can only mix states with the same parity, since the magnetic field is of even parity. The Zeeman effect is very important for the influence of a magnetic field on the $1s$ orthoexciton and paraexciton states when investigating Cu_2O in Sec. 6.
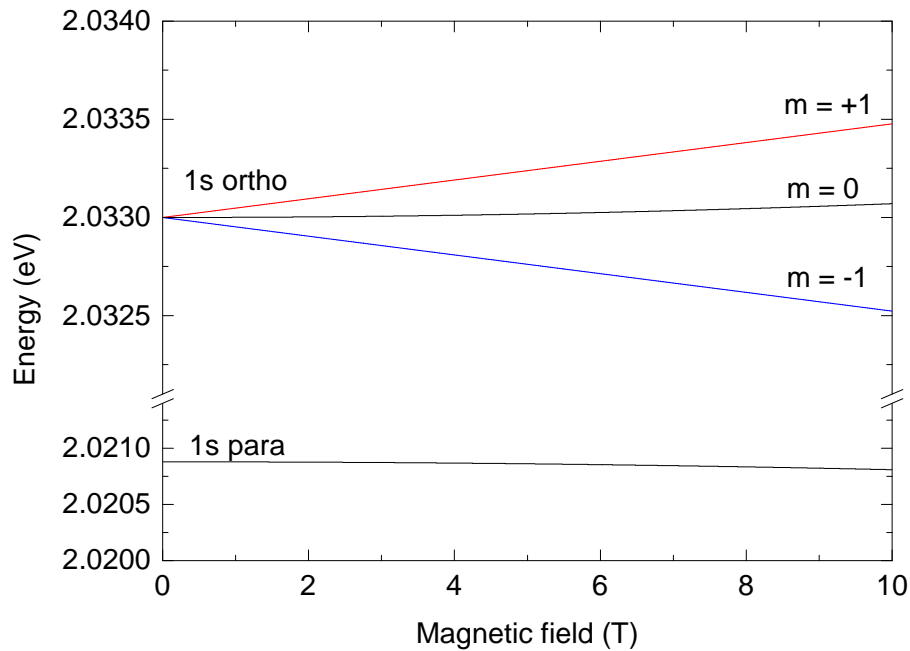
Figure 2.9. – Eigenenergy solutions of the Zeeman Hamiltonian for $1s$ orthoexcitons in Cu_2O. The three degenerated ortho exciton states are splitted into three new eigenstates $m = \pm 1, 0$. The $m = 0$ and paraexciton exhibit repulsion leading to a small shift of $\Delta < 0.1\,\text{meV}$ for both states.

In Sec. 2.2.3 the band structure of Cu_2O was introduced. There are four states of the yellow $1s$ exciton. There are three almost degenerated orthoexciton states Γ_{5x}^+, Γ_{5y}^+, Γ_{5z}^+, and one paraexciton state Γ_2^+, which has a reduced energy $\varepsilon = 12.12\,\text{meV}$. The Zeeman Hamilton for the four exciton states is

$$H(B^0) = \begin{pmatrix} -\varepsilon & i\alpha_{\mathrm{op}}\mathbf{B}_x^0 & i\alpha_{\mathrm{op}}\mathbf{B}_y^0 & i\alpha_{\mathrm{op}}\mathbf{B}_z^0 \\ -i\alpha_{\mathrm{op}}\mathbf{B}_x^0 & 0 & -i\alpha_{\mathrm{oo}}\mathbf{B}_z^0 & -i\alpha_{\mathrm{oo}}\mathbf{B}_y^0 \\ -i\alpha_{\mathrm{op}}\mathbf{B}_y^0 & i\alpha_{\mathrm{oo}}\mathbf{B}_z^0 & 0 & -i\alpha_{\mathrm{oo}}\mathbf{B}_x^0 \\ -i\alpha_{\mathrm{op}}\mathbf{B}_z^0 & i\alpha_{\mathrm{oo}}\mathbf{B}_y^0 & i\alpha_{\mathrm{oo}}\mathbf{B}_x^0 & 0 \end{pmatrix}. \tag{2.26}$$

The interaction between orthoexciton and paraexciton states is described by the Zeeman parameter $\alpha_{\mathrm{op}} = 92.5\,\frac{\mu\mathrm{eV}}{\mathrm{T}}$ and the interaction between two orthoexciton states is described by the Zeeman parameter $\alpha_{\mathrm{oo}} = 47.7\,\frac{\mu\mathrm{eV}}{\mathrm{T}}$ [72]. A diagonalization of the Hamilton reveals three new eigenstates of the orthoexciton in a magnetic field, which are shown in Fig. 2.9. They are labeled by $m = \pm 1, 0$. The $m = \pm 1$ states exhibit the typical Zeeman splitting. The $m = 0$ state is shifted to higher energies in a magnetic field, due to a repulsion with the paraexciton, which is shifted to smaller energies due to the repulsion. The paraexciton shift and $m = 0$ orthoexciton shift both lie below the resolution of the experimental setup. The admixture of the $m = 0$ state and the paraexciton also leads to a transfer of oscillator strength from the orthoexciton to the paraexciton, which can be expressed by the admixture coefficient [73, 74]

$$u = \frac{\alpha_{\mathrm{op}} B^0}{\sqrt{(\alpha_{\mathrm{op}} B^0)^2 + \varepsilon^2}} \approx \frac{\alpha_{\mathrm{op}} B^0}{\varepsilon}. \tag{2.27}$$

At $B^0 = 10\,\mathrm{T}$ only 0.6 % of the $1s$ orthoexciton oscillator strength is transferred to the paraexciton.

Landau Levels

In high magnetic fields the electron bands itself are influenced by the magnetic field and a complicated series of magneto-excitons has to be considered. This is important for measurements in GaAs in which the high field regime starts at $\hbar\omega_{\mathrm{C}}(2.7\,\mathrm{T}) \approx R_{\mathrm{exc}} = 4.2\,\mathrm{meV}$, because of the small binding energy of the excitons. The maximum magnetic field of $B^0 = \pm 10\,\mathrm{T}$ used in the experiments is still in the regime of small perturbation for the other investigated materials. A basic model to describe the magneto-exciton series in GaAs is proposed in [75]. First, the Landau quantization of the conduction and valence band is calculated. The energy distance between any valence and conduction band level is

$$E_{\mathrm{N_e-N_h}} = E_{\mathrm{g}} + \frac{e\hbar}{c} \left[\frac{1/2 + N_{\mathrm{e}}}{m_{\mathrm{e}}} + \frac{1/2 + N_{\mathrm{h}}}{m_{\mathrm{h}}} \right] B^0. \tag{2.28}$$

The different Landau levels are addressed by $N_{\mathrm{e}} = 0, 1, 2, \ldots$ for the conduction band and $N_{\mathrm{h}} = 0, 1, 2, \ldots$ for the valence band. The distance between the Landau levels increases linearly with B^0 depending on the effective mass of the conduction band m_{e} and valence band m_{h}. The effective mass of the conduction band in GaAs is smaller $m_{\mathrm{e}}/m_{\mathrm{h}} \approx 0.13$ than the heavy holes and dominates the shift of energy. Details of the effective masses

and the valence band are given in Sec. 2.2.3.

For each combination of Landau levels $N_e - N_h$ an exciton series is assumed. Each exciton series has $1s$, $2s$, $2p$, etc. states, which are observed in the magnetic-field-induced SHG (MFISH) spectrum.

Magneto-Stark effect

The Magneto-Stark effect influences excitons with a finite momentum $\hbar \mathbf{k}_{exc}$. In the classical picture the movement of the exciton through a magnetic field leads to the Lorentz force, acting on the negatively charged electrons and positively charged holes in the opposite direction and forcing them apart. In the center of mass system of the exciton this force is the same as an effective electric field. The effective field

$$E_{eff}^0 = \frac{\hbar}{m_{exc}} \left(\mathbf{k}_{exc} \times \mathbf{B}^0 \right) \tag{2.29}$$

is calculated by the cross product of the wave vector $\mathbf{k}$exc of the exciton and the magnetic field $\mathbf{B}^0$. The effective field E_{eff}^0 then leads to the Stark effect. The Magneto-Stark effect is usually much smaller than other effects from a magnetic field in terms of an energy shift of the resonance, but it is the only way a magnetic field can lead to an admixture of excitons with a different parity. The Magneto-Stark effect was shown to increase SHG from excitons in ZnO [31], since SHG is very sensitive to the admixture of different parity excitons.

2.3. Nonlinear optical properties of semiconductors

2.3.1. Nonlinear optical spectroscopy of semiconductors

The optical phenomena presented in Sec. 2.1 are a powerful spectroscopy tool for the investigation of semiconductors. Since their discovery in the 1960s, the investigations keep revealing interesting insights about nonlinear interactions up to today. One of the applications is the investigation of energy levels which are forbidden in linear optics. Some effects only manifest in linear optics as a small change on a strong background signal. In nonlinear optics it is often possible to create a situation in which the effect gives rise to a signal from a zero measurement. This is usually more sensitive and reliable in comparison to small changes in the absorption coefficient, for example. In many cases linear and nonlinear optical spectroscopy are complementary in the investigation of semiconductors and their interaction with light.

A typical SHG spectrum reveals non-resonant broad band SHG. It can be calculated by taking all the electronic bands into account [28]. It stretches over several eV and has a smooth wavelength dependence, without any resonances. In case ED SHG is allowed it is often found in the transparency region of semiconductors. The SHG intensity is often much smaller above the band gap, although the calculated second order susceptibility can be bigger than in the transparency region. This is attributed to a reabsorption of the SHG

light by an excitation of electron band-band transitions and a reduced coherence length for the SHG process [8, 76].

Although the intensity of SHG is reduced by reabsorption for energies above the band gap, it is still possible to use SHG spectroscopy in this energy region. As long as the fundamental light is in the transparency region, it passes the whole sample and SHG occurs along the whole path throughout the crystal. The SHG at the entrance region of the fundamental light will be reabsorbed on its way to the end of the sample. The SHG at the end of the sample only has a short way to couple out of the material. In this case SHG light couples out of the crystal without being reabsorbed. This is especially important for samples which are grown on a substrate. In this case, the sample is aligned so that the fundamental light passes the substrate first and the material of interest last. The SHG created in the material is coupled out and is not influenced by the substrate. This is less important for materials grown on a substrate with a much higher band gap, since SHG is well within the transparency region of the substrate. This is the case, for GaN ($E_\mathrm{g} \approx 3.5\,\mathrm{eV}$) grown on sapphire ($E_\mathrm{g} \approx 8.8\,\mathrm{eV}$), for example.

In certain cases an oscillation of the SHG intensity for different wavelengths in the transparency region is detected. A feature such as this is attributed to reflections of the fundamental light, which lead to interference. This is especially the case for semiconductors with a high index of refraction like GaAs ($n > 3$), because it leads to reflections at the sample-air interface. The wavelength distance of two maximums of intensity is estimated by assuming a Fabry-Perot interference.

$$\Delta\lambda \approx \frac{\lambda_c^2}{2nl\cos\theta_{\mathrm{FP}}} \tag{2.30}$$

Since such a feature is observed in the GaAs measurements presented in Sec. 4.2.1, the expected wavelength splitting is calculated for these measurements. The central wavelength is $\lambda_c = 1936\,\mathrm{nm}$, which is the laser wavelength. The refractive index is $n(2000\,\mathrm{nm}) = 3.36$ in the transparency region [77]. For the thickness $l \approx 400\,\mu\mathrm{m}$ the epitaxy layer and the GaAs substrate are taken into account, since the reflection between the GaAs layers should be minimal and the GaAs-Air interface dominates the process. The angle $\approx 13.6°$ is defined by the experimental geometry. The calculated splitting between intensity maxima is $\Delta\lambda \approx 1.4\,\mathrm{nm}$. This approximation could be improved by also taking the reflection of the SHG light and a wavelength dependent refractive index into account. The oscillations should be suppressed above the band gap, because the absorption of light does not allow for many round trips of the light, which is like a small quality factor of the Fabry-Perot-Interferometer.

The fundamental idea of SHG and THG spectroscopy is the enhancement of the conversion efficiency when the light is in resonance with crystallographic eigenstates. For SHG and THG spectroscopy it is therefore necessary to understand the influence of certain eigenstates on the susceptibilities. It is possible to learn about the states by measuring the wavelength and rotational anisotropy of the susceptibility. For this understanding it is necessary to bring the findings of Sec. 2.2 and 2.1 together. In Sec. 2.2 the symmetry of

the states was discussed. The interaction between light and crystal states depends on the symmetry of the wave vector and the electric light field. In the case of a uniaxial material the parallel and perpendicular component to the extraordinary axis have to be differentiated. For the ED case the calculation is straight forward. If the transition $\langle\, f \,|\, \hat{\mathbf{V}}_{ED} \,|\, g \,\rangle$ is non-zero, the symmetry of the final $|\, f \,\rangle$ state has to be a part of the symmetry of the operator $\hat{\mathbf{V}}_{ED}$ acting on the ground state $|\, g \,\rangle$

$$\langle\, \Gamma_f \,|\, \Gamma_{ED} \,|\, \Gamma_i \,\rangle \neq 0 \Leftrightarrow \Gamma_f \subseteq \Gamma_{ED} \otimes \Gamma_g \tag{2.31}$$

For band-band transitions the initial state is one of the valence bands and the final state is the conduction band. In the case of excitons the initial state is the unperturbed crystal which is noted as Γ_1 in any symmetry group. The final state possesses the symmetry of the whole exciton wave function. To the very same state, a two-photon transition has to be allowed. The projection of two photons Γ_p onto the final state has to be calculated for a two-photon process. With a two-photon transition only specific states of an exciton level are accessed, in contrast to the one-photon ED transition in which every component is excited. This can be important for EQ transitions which also couple to specific components of a state. In the case of Cu_2O this fact is important and specific calculations are made. The EQ transition is treated in a similar way to the two-photon transition, because the projection of the wave vector symmetry and the electric field symmetry on the state are taken into account.

For SHG it is often the case that no exciton state is allowed for one- and two-photon transitions at the same time in the ED approximation. For many semiconductor structures parity conservation is a good approximation at the center of the Brillouin zone, where the optical transitions in the measurements take place. For example one-photon transitions are only allowed for s excitons and two-photon transitions are only allowed for p excitons (or the other way around). None of the excitons are allowed for both. If they lead to SHG, it has to stem from higher order transitions like EQ, as it is the case for Cu_2O. Usually these transitions are too weak to be detected in the experiments. This situation is presented in Fig. 2.10(a,c). Neither the $1s$ or the $2p$ exciton is allowed for the complete SHG transition.

In Sec. 2.2.2 the mixing of exciton states by external fields is described. Such a mixing can create a state with mixed parity, which would be allowed for a one- and two-photon transition in the ED regime at the same time. This is presented in Fig. 2.10 (b). The mixed $1s/2p$ state is allowed for both transitions and leads to resonant enhanced SHG. The SHG intensity depends on the mixing of the states and each individual oscillator strength. If the microscopic mechanism of the mixing is understood, then it is possible to calculate the increase of the SHG intensity from the admixture coefficients. In this example the new wave function $\Psi'_{1s/2p} = C_{1s}\Psi_{1s} \cdot C_{2p}\Psi_{2p}$ in an external electric or magnetic field leads to SHG intensity $I^{2\omega} \propto (\chi)^2 \propto C_{1s} \cdot C_{1p}$. The expected increase in SHG intensity can be compared to the measured data to verify the proposed mixing mechanism.

It is possible that the resonance from an energy level interferes with crystallographic broad band SHG. This interference leads to a Fano resonance [78]. The phase of crystallo-
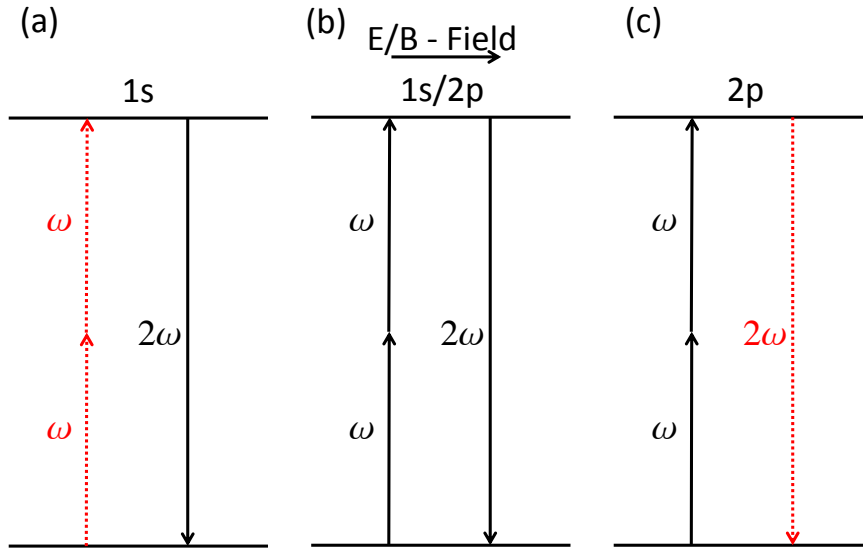
Figure 2.10. – Exemplary exciton states and optical transitions from the ground state to excitons. Black lines represent allowed transitions and red dotted lines forbidden transitions in the ED approximation. (a) $1s$ exciton, which is allowed for one-photon transitions and forbidden for two-photon transitions. (c) $2p$ exciton, which is allowed for two-photon transitions and forbidden for one-photon transitions. (b) Mixed $1s/2p$ exciton state through the interaction with an external electric or magnetic field. The two-photon transition is allowed from the $2p$ fraction and the one-photon transitions is allowed for the $1s$ fraction. Only this mixed state leads to resonant enhanced SHG.

graphic SHG only shows small changes over a wavelength region lying a few meV around the resonance. The phase of resonant SHG, on the other hand, changes by 2π over the width of the resonance. This leads to a constructive and destructive interference between these two SHG light waves for different points on the resonance. The line shape of a resonance is distorted by this process. Typical for a Fano resonance is a local minimum on one side of the resonance where the interference is destructive. On the other side of the resonance the interference is constructive, which leads to a tail of the resonance. In case the crystallographic SHG is as intense as the resonance, it is necessary to correct the energy of the resonance since the peak energy is shifted by the interference. This is not the case in any of the presented measurements.

Still, it is important to recognize Fano resonances. If SHG is induced by an external field, the growth of intensity with increasing field strength is also influenced by the interference with crystallographic SHG. The phase of induced SHG differs depending on the external field direction, even when the intensity growth is the same. This leads to an asymmetry between positive and negative field strength through the interference with crystallographic SHG. The field direction, which leads to induced SHG with a phase close

Figure 2.11 – (a) Schematics of a three photon SHG process between the ground state $|g\rangle$ and the final state $|f2\rangle$. (b) Schematics of a two photon absorption exciting state $|f2\rangle$. Through interactions it relaxes to the lower state $|f1\rangle$ and emits a photon of wavelength ω_2.
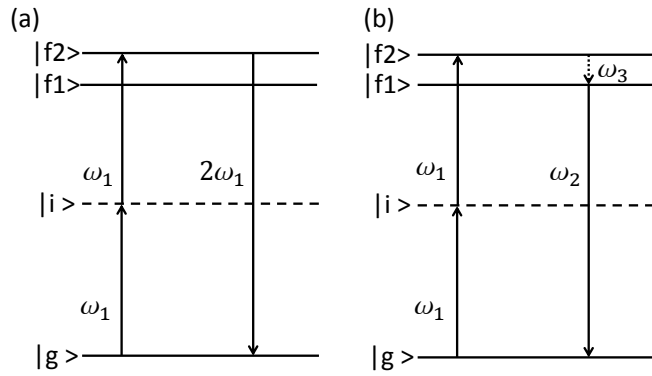
to the crystallographic one, results in a higher induced intensity compared to the field direction, which leads to destructive interference. Such an effect has to be recognized so as to avoid a wrong interpretation of the observed asymmetry of induced intensity.

The main influence of the sample temperature in the SHG and THG measurements is a shift of the band gap. The expansion of the crystal volume leads to a higher lattice constant. Due to the smaller wave function overlap of the electrons, the band gap is decreased at high temperatures. Observed exciton resonances shift together with the band gap. Another effect is the increase of the exciton resonance linewidth and the decrease of the exciton resonance intensity. This is treated differently than in linear optics, since no photon is involved in the coherent SHG or THG process. The influence of the phonons stems from the thermal movement of the atoms on the crystal lattice, which can be treated similarly to the Debye-Waller factor in x-ray imaging.

2.3.2. Harmonics generation versus multi-photon absorption

Intense light, at twice the wavelength of a resonance, also leads to another process. Instead of a parametric upconversion of the light by SHG, two photons can be absorbed and a crystal state is excited. This was predicted in 1931 by Göppert-Mayer [79] and experimentally verified by Hopfield [80] and is called two-photon absorption (TPA). The selection rules for this optical transition are similar to the two photon part of SHG [81]. After such a state (e.g. exciton) is excited, it has a lifetime after which it relaxes to the ground state. This can lead to confusion with SHG depending on the specific decay channel. In Fig. 2.11 this process is compared to SHG. In Fig. 2.11(a) the SHG process is shown, in which the state $|f2\rangle$ leads to SHG at $2\omega_1$. In Fig. 2.11(b) the same incident light ω_1 leads to the excitations of the state $|f2\rangle$. There are several different possibilities for this state $|f2\rangle$ to reach the ground state. Usually the first step is to reach the lowest lying excited state $|f1\rangle$ by emitting photons or phonons. For most semiconductors the splittings of the excited states are so small that the photons are far away from the visible regime and play no role in the studies presented. The ground state is reached by sending out a photon from the lowest excited state. So two-photon-absorption photoluminescence (TPA-PL) is the subsequent absorption of two photons and the creation of another photon. This

can interfere with SHG under certain circumstances. From a standpoint of energy and momentum conservation these processes are similar, since the same number of photons take part in them. For SHG spectroscopy a state has to be two- and one-photon allowed, which makes TPA-PL also possible. This tends to be no problem for excitons with $n \geq 2$ as the main mechanism for excited states is to relax to the $1s$ state without sending out a photon with twice the energy of the incident light, like SHG. Only light which cannot be distinguished by the energy resolution of the experimental setup could be confused with SHG. After relaxation the photons have a different energy and can be suppressed by the spectrometer. This can cause problems for the $1s$ exciton only, as shown in the Cu_2O chapter. The process also limits the maximum intensity of the fundamental light, since energy is deposited in the crystal, which can heat the sample up or even damage it.

The TPA can be described by perturbation theory. The resulting selection rules are different from SHG, because the created photon is not an inherent part of the process, which changes the situation. Most notably it can occur in centrosymmetric systems in which SHG is forbidden. It has the same square dependence on incident intensity. The photons from the relaxation process are not directed like SHG, because all information about the wave vector is lost in the interactions with the crystal. In most cases they relax through an ED process, which is allowed for all wave vector directions and the intensity in the same direction as SHG is small.

In a similar process three photons can be absorbed to create an excited state. This is called a three-photon-absorption (3PA). After the excited state is created it behaves the same way as described for TPA. The selection rules of 3PA are similar to one-photon absorption.

2.3.3. Modeling of the SHG/THG rotational anisotropy

In Sec. 2.1.1 the important role of the susceptibility for the description of SHG was presented. In this section the influence of the crystal structure on the susceptibility is introduced and the modeling of rotational anisotropies is described.

The rotational anisotropies are described by an expression like

$$\mathbf{P}_i^{(2\omega)} = \chi_{ijk}^{(2)} \mathbf{E}_j^\omega \mathbf{E}_k^\omega, \tag{2.32}$$

which can be compared to the measurements. Therefore the experimental geometry has to be taken into account by defining the $\mathbf{k}$ vector and the possible electric fields of the laser light. A detailed description of the experimental geometry is given in Sec. 3.2.1. In order to model the rotation of laser light polarization for 2π about the $\mathbf{k}$ vector during the measurements, a rotation matrix for rotations about the $\mathbf{k}$ axis is applied to the electric field $\mathbf{E}^\omega$. The general rotation matrix about an arbitrary vector $\mathbf{k} = (k_1, k_2, k_3)^\intercal$ (transposed) is

$$\mathbf{E}^\omega(\varphi) = \overline{\mathbf{R_k}}(\varphi) \cdot \mathbf{E}^\omega(0\,^\circ) = \mathbf{k}(\mathbf{k} \cdot \mathbf{E}^\omega) + \cos(\varphi)(\mathbf{k} \times \mathbf{E}^\omega) \times \mathbf{k} + \sin(\varphi)(\mathbf{k} \times \mathbf{E}^\omega). \tag{2.33}$$

Applying the rotation to the electric field vector of the light wave $\mathbf{E}^\omega$ introduces φ as the

angle between the electric field vector and the laboratory y axis. This can be plugged in the equation for the polarization

$$\mathbf{P}^{2\omega}_{\text{eff}}(\mathbf{E}^\omega) = \begin{pmatrix} \sum\limits_{j,k} \chi_{xjk} E^\omega_j E^\omega_k \\ \sum\limits_{j,k} \chi_{yjk} E^\omega_j E^\omega_k \\ \sum\limits_{j,k} \chi_{zjk} E^\omega_j E^\omega_k \end{pmatrix} \tag{2.34}$$

which gives the effective polarization $\mathbf{P}^{2\omega}_{\text{eff}}$ induced by the incident light field $\mathbf{E}^\omega$. The effective polarization leads to the radiation of a light field with the same $\mathbf{k}$ vector as the incident light and a polarization $\mathbf{E}^{2\omega} \parallel \mathbf{P}^{2\omega}_{\text{eff}}$. The optical harmonic light passes a polarization filter before it is detected. For this polarization filter only two configurations are chosen. It transmits the optical harmonic light with a polarization which is either parallel or perpendicular to the incident polarization $\mathbf{E}^\omega$. To model the polarization filter the effective polarization $\mathbf{P}^{2\omega}_{\text{eff}}$ is projected on a vector $\mathbf{F}$ parallel to the transmitted polarization of the filter. For the parallel configuration $\mathbf{F}$ is parallel to the incident polarization $\mathbf{F}(\varphi) = \frac{\mathbf{E}^\omega(\varphi)}{|\mathbf{E}^\omega|}$ resulting in an effective polarization $\mathbf{P}^{2\omega}_{\parallel,\text{eff}}(\varphi) = \mathbf{P}^{2\omega}_{\text{eff}}(\varphi) \cdot \mathbf{F}(\varphi)$. For the crossed configuration the filter is $90°$ ahead of the incident polarization $\mathbf{P}^{2\omega}_{\perp,\text{eff}}(\varphi) = \mathbf{P}^{2\omega}_{\text{eff}}(\varphi) \cdot \mathbf{F}(\varphi + 90°)$. The intensity of the optical harmonic light is detected in the experiments. The intensity depends quadratically on the electric light field

$$I^{(2\omega)} = \frac{cn\epsilon_0}{2}|\mathbf{E}^{2\omega}|^2, \tag{2.35}$$

and linearly on the refractive index n. The speed of light c and the electric constant ϵ_0 also have to be taken into account. The electric field of the light wave $\mathbf{E}^{2\omega}$ is proportional to the polarization $\mathbf{P}^{2\omega}_{\text{eff}}$, as shown in Sec. 2.1.1. For the two main configurations the resulting intensity is calculated by

$$I^{2\omega}_\parallel \propto \left(\mathbf{P}^{2\omega}_{\parallel,\text{eff}}(\varphi)\right)^2 \tag{2.36a}$$

$$I^{2\omega}_\perp \propto \left(\mathbf{P}^{2\omega}_{\perp,\text{eff}}(\varphi)\right)^2 \tag{2.36b}$$

The factors c, n, and ϵ_0 are not taken into account, since no absolute values are measured or calculated. The right susceptibility for the observed transition has to be used for an actual modeling of the anisotropies. In order to find the susceptibility for a certain process it is necessary to know the microscopical mechanism responsible for the transition. The susceptibilities for ED, MD or EQ transitions differ from each other and the correct one has to be chosen. In case this information is not available, it is possible to check all possible transition types and compare which one best fits the measured anisotropy.

The known tensor components for the crystal symmetry and transition type are taken from the tables of Birss or Popov [82, 83]. Some components have to be zero for a certain symmetry group. The symmetry groups of the semiconductors investigated in this thesis usually have only a few non-zero components, which reduces the complexity of the

problem. Another reduction of the parameters stems from the linear dependencies of the tensor components. The calculations can be explained with a simple example. At the end of this section the expected anisotropies for the main measurements of this thesis are given. All non-zero components are grouped into several dependent components for a given point group. The second order electric dipole susceptibility $\chi^{(2)}$ of GaAs, for example, is expressed as

$$\underline{\chi_{xyz}} = \chi_{zxy} = \chi_{yzx}. \tag{2.37}$$

The underlined component is arbitrarily chosen to represent the value of the dependent components. In this case the 27 independent components of the generalized susceptibility are reduced to one independent component, which appears in three different positions within the susceptibility. Such a susceptibility is plugged into Eq. (2.34) and the resulting intensities are calculated by Eq. (2.36).

The anisotropies $I_\parallel^{2\omega}$ and $I_\perp^{2\omega}$, calculated in this way, are then fitted to the observed data from the measurements. This reveals the relative magnitude of the independent tensor components. In some cases it is necessary to include sample tilting angles in the calculations. The angles are introduced in detail in Sec. 3.2.1. This allows one to fit the direction of the light polarization within the sample to the measurements. It is necessary to choose starting angles which are close to the experimental alignment to avoid wrong results of the fit.

2.3.4. Expected rotational anisotropies for the investigated materials

GaAs

The semiconductor GaAs belongs to the symmetry group T_d. This is a cubic structure which is not centrosymmetric. The independent tensor components of the second order ED susceptibility $\chi^{(\text{cryst})}$ are

$$\underline{\chi_{xyz}} = \chi_{zxy} = \chi_{yzx}. \tag{2.38}$$

It is clear that for $\mathbf{k} \parallel [001]$ no ED SHG is allowed, since no polarization is possible along the z axis ([001]). The resulting intensities from the calculations are

$$I_\parallel^{2\omega}(\varphi) = 9\chi_{xyz}^2 \cos(\beta)^2 \cos(\gamma - \varphi) \left[\cos(\gamma - \varphi)\sin(\theta)\sin(\beta) - \cos(\theta)\sin(\gamma - \varphi)\right]^2$$
$$\left[\cos(\theta)\cos(\gamma - \varphi)\sin(\beta) + \sin(\theta)\sin(\gamma - \varphi))\right]^2 \tag{2.39}$$

$$I_\perp^{2\omega}(\varphi) = \frac{1}{1024}\chi_{xyz}^2 \sin(2\beta)^2 \left[4\cos(2\theta)\left\{\cos(\gamma - \varphi) + 3\cos(3(\gamma - \varphi))\right\} + \right.$$
$$\sin(2\theta)\left\{-1\left(\cos(\beta) + 12\cos(3\beta)\cos(\gamma - \varphi)^2\right)\sin(\gamma - \varphi) + \right.$$
$$\left. 15\cos(\beta)\sin(3(\gamma - \varphi))\right\}\big]^2 \tag{2.40}$$

In this case all three possible tilting angles θ (around the y axis), β (around the x axis), and γ (around the z axis) are taken into account. These tilting angles are explained in detail in Sec. 3.2.1. For $\mathbf{k} \parallel [001]$ all angles are zero, which results in the expected zero intensity. In Fig. 2.12(a) the expected anisotropy for $\mathbf{k} \parallel [111]$ is plotted. It has a typical
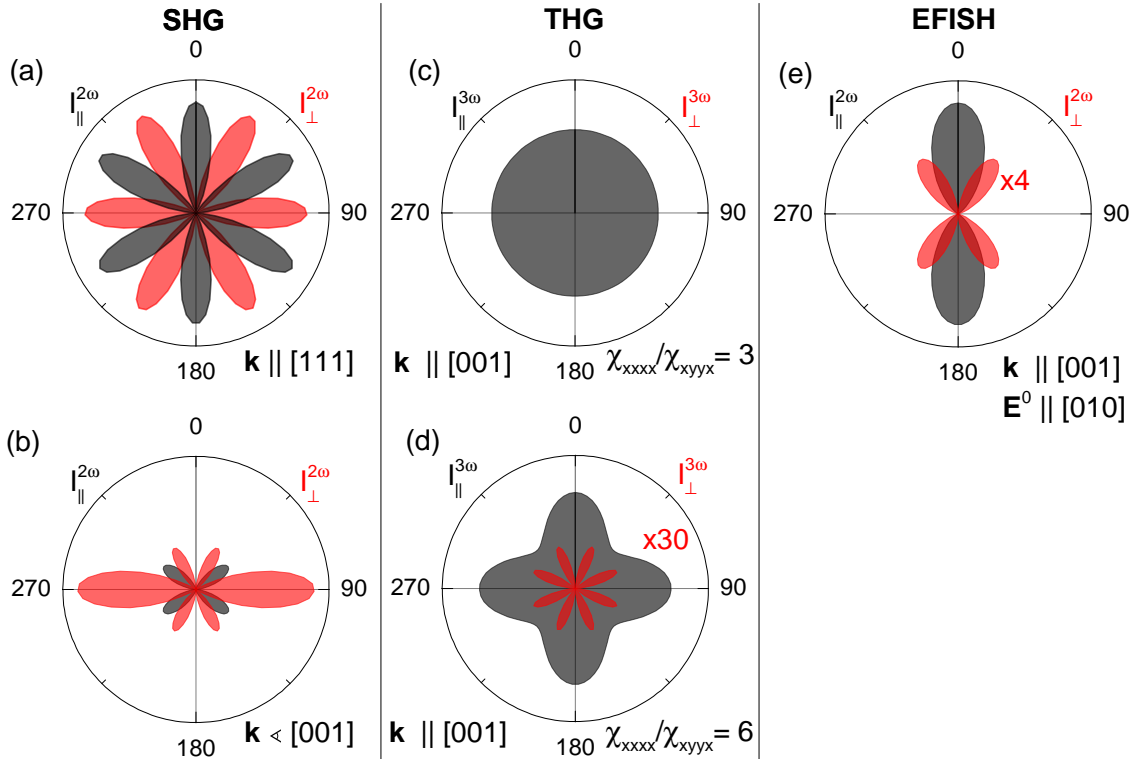
Figure 2.12. – Model calculations for expected rotational anisotropies of SHG and THG signals in GaAs. (a,b) Parallel $I_{\parallel}^{2\omega}$ (black) and crossed $I_{\perp}^{2\omega}$ (red) anisotropy of crystallographic SHG in GaAs for different **k** directions. (c,d) Model anisotropies of crystallographic THG in the **k** $\parallel$ [001] configuration for different ratios $\frac{\chi_{xxxx}}{\chi_{xyyx}}$. (e) Expected anisotropy for EFISH in the **k** $\parallel$ [001] and **E**^{0} $\parallel$ [010] configuration.

six-fold shape for the parallel $I_{\parallel}^{2\omega}$ and crossed $I_{\perp}^{2\omega}$ anisotropy, which reflects the symmetry of the crystal lattice along this direction. For the model calculation the $[1\bar{1}0]$ direction is at $\varphi = 0\,^\circ$, other alignments would just rotate the presented anisotropy. Other directions for **k** lead to a reduction of some of the maxima. For $\theta = 10\,^\circ$ the expected anisotropy is plotted in Fig. 2.12(b). Compared to (a), the maxima of the parallel anisotropy at $\varphi = 30\,^\circ$ and $\varphi = 150\,^\circ$ are reduced. The maximum at $\varphi = 90\,^\circ$ is reduced to zero for the crossed anisotropy. For $\theta = 0\,^\circ$ and $\beta = 10\,^\circ$ (tilting about the x axis) the same shape rotated by $90\,^\circ$ is expected.

Since there is only one independent tensor component for χ^{cryst}, the anisotropy is solely determined by the direction of **k** in the crystal. The shape of the anisotropy in a certain experimental geometry does not change with wavelength or temperature, although the overall intensity might be different.

The application of an electric field leads to the mixing of exciton states and a resonant enhancement of SHG. Independent from the microscopical mechanisms, the anisotropy of

such a resonance is described by

$$P_{\text{eff},i}^{2\omega} = \epsilon_0 \chi_{ijmn}^{(3)} E_j^\omega E_m^\omega E_n^0, \tag{2.41}$$

as long as it is in the ED approximation. The independent tensor components of the third order polar susceptibility in T_d are

$$\begin{aligned}
&\underline{\chi_{\text{xxxx}}} = \chi_{\text{yyyy}} = \chi_{\text{zzzz}} \\
&\underline{\chi_{\text{xyyx}}} = \chi_{\text{yxxy}} = \chi_{\text{xzzx}} = \chi_{\text{zxxz}} = \chi_{\text{yzzy}} = \chi_{\text{zyyz}} = \\
&\chi_{\text{xxyy}} = \chi_{\text{xxzz}} = \chi_{\text{yyzz}} = \chi_{\text{zxzx}} = \chi_{\text{zyzy}} = \chi_{\text{yxyx}}
\end{aligned} \tag{2.42}$$

In the experiments the electric field is applied along the y axis $\mathbf{E}^0 = (0, E^0, 0)^\intercal$ and only components with y as the fourth index are taken into account. The increased amount of independent tensor components leads to several different shapes, depending on the relative magnitude of the components. Typically the χ_{yyyy} is strongest for an electric field along the y axis, but fitting model calculations to actual measurements allows to determine the relative magnitude of the tensor components. The resulting anisotropy for $\underline{\chi_{\text{xxxx}}} >> \underline{\chi_{\text{xyyx}}}$ is plotted in Fig. 2.12(e). For the parallel configuration the EFISH is only expected to be parallel to the external field along the y axis. The crossed anisotropy for EFISH has a four-fold shape.

The MFISH anisotropy is discussed in detail in [75]. In the ED approximation the expected anisotropy is similar to the EFISH one. For a Voigt magnetic field the maximum intensity is typically found perpendicular to the field direction, which is also $\varphi = 0\,^\circ$ as in the parallel EFISH anisotropy. The actual measurements of MFISH anisotropy in [75] can only be explained when taking magneto-spatial dispersion ($\mathbf{k}$ dependence) into account. For this effect a fifth rank axial tensor

$$P_{\text{eff},i}^{2\omega} = \epsilon_0 \chi_{ijmno}^{(4)} E_j^\omega E_m^\omega k_n B_o^0 \tag{2.43}$$

is responsible, which has four independent tensor components and overall 60 non-zero components. Many rotational anisotropy shapes emerge from different ratios of the tensor components, which are wavelength dependent.

For THG the same susceptibility as for EFISH is used

$$P_{\text{eff},i}^{3\omega} = \epsilon_0 \chi_{ijmn}^{(3)} E_j^\omega E_m^\omega E_n^\omega. \tag{2.44}$$

only in this case three incident light fields E^ω are taken into account. The resulting intensities for $\mathbf{k} \parallel [001]$ are

$$I_\parallel^{3\omega} = \frac{1}{16} \left[3\chi_{xxxx} + \chi_{xyyx} + (\chi_{xxxx} - 3\chi_{xyyx}) \cos(4\varphi) \right]^2 \tag{2.45}$$

$$I_\perp^{3\omega} = \frac{1}{16} (-\chi_{xxxx} + 3\chi_{xyyx})^2 \sin^2(4\varphi). \tag{2.46}$$

The shape of the anisotropy depends on the relation $\frac{\chi_{xxxx}}{\chi_{xyyx}}$. In contrast to EFISH there is

no expected relation between the independent tensor components, and the relation could change with the wavelength or other parameters. In the case of $\frac{\chi_{xxxx}}{\chi_{xyyx}} = 3$ the crossed anisotropy is zero and the parallel one is constant, which is presented in Fig. 2.12(c). For other values both anisotropies have an angular dependence. In Fig. 2.12(d) the anisotropy for $\frac{\chi_{xxxx}}{\chi_{xyyx}} = 6$ is plotted, in which case the crossed anisotropy is four-fold and the parallel is not φ independent anymore.

For magnetic-field-induced THG in the ED approximation the susceptibility

$$P^{2\omega}_{\text{eff},i} = \epsilon_0 \chi^{(5)}_{ijmno} E^\omega_j E^\omega_m E^\omega_n B^0_o \tag{2.47}$$

only has non-zero tensor elements, which have at least one z component. Again, there are many possible shapes from the 60 non-zero components. In case an anisotropy for $\mathbf{k} \parallel [001]$ and a Voigt magnetic field is found, a higher order susceptibility is necessary. It is plausible that for THG magneto-spatial dispersion also has to be included. In this case at least the fifth order axial susceptibility $\chi^{(6)}$ is needed, which has a large number of non-zero components. It is no longer listed in the common susceptibility tables. Experience shows that the main intensity is found at $\varphi = 0\,^\circ$ in the parallel configuration, because this is often the case for magnetic field induced harmonics in semiconductors.

GaN

The independent tensor components of the ED susceptibility $\chi^{(2)}$ in $C_{6\text{v}}$ are

$$\begin{aligned} &\underline{\chi_{zzz}} \\ &\underline{\chi_{xxz}} = \chi_{xzx} = \chi_{zxx} = \chi_{yyz} = \chi_{yzy} = \chi_{zyy} \end{aligned} \tag{2.48}$$

The uniaxial structure is reflected by the important role of the z axis in the susceptibility. The expected intensity is calculated with a tilting angle θ around the x axis as a parameter. The resulting intensities

$$\begin{aligned} I^{2\omega}_{\parallel}(\varphi) = \sin^2(\theta)\sin^2(\varphi) \cdot \\ \left(3\chi_{\text{xxz}}\cos^2(\varphi) + \left(3\chi_{\text{xxz}}\cos^2(\theta) + \chi_{\text{zzz}}\sin^2(\theta)\right)\sin^2(\varphi)\right)^2 \end{aligned} \tag{2.49}$$

$$\begin{aligned} I^{2\omega}_{\perp}(\varphi) = \sin^2(\theta)\cos^2(\varphi) \cdot \\ \left(\chi_{\text{xxz}}\cos^2(\varphi) + \left(-2\chi_{\text{xxz}} + 3\chi_{\text{xxz}}\cos^2(\theta) + \chi_{\text{zzz}}\sin^2(\theta)\right)\sin^2(\varphi)\right)^2 \end{aligned} \tag{2.50}$$

depend on the fundamental light polarization φ and the tilting angle θ. Without tilting SHG is forbidden, since the $\sin^2(\theta)$ terms in both configurations are zero. Therefore crystallographic SHG should only be detected for the tilted sample configuration, which is shown in Fig. 2.13(a). For a tilting about the y axis ($\theta \neq 0$) the parallel intensity has a maximum at $\varphi = 90\,^\circ$. For this angle the electric field of light has the strongest component along the z axis. The shape is the same for most relations of the tensor components, only the crossed intensity changes, which is always very small. In the experiments only $I^{2\omega}_{\text{both}} = I^{2\omega}_{\parallel} + I^{2\omega}_{\perp}$ is detected. It mainly looks like $I^{2\omega}_{\parallel}$, because $I^{2\omega}_{\perp}$ is rather small.
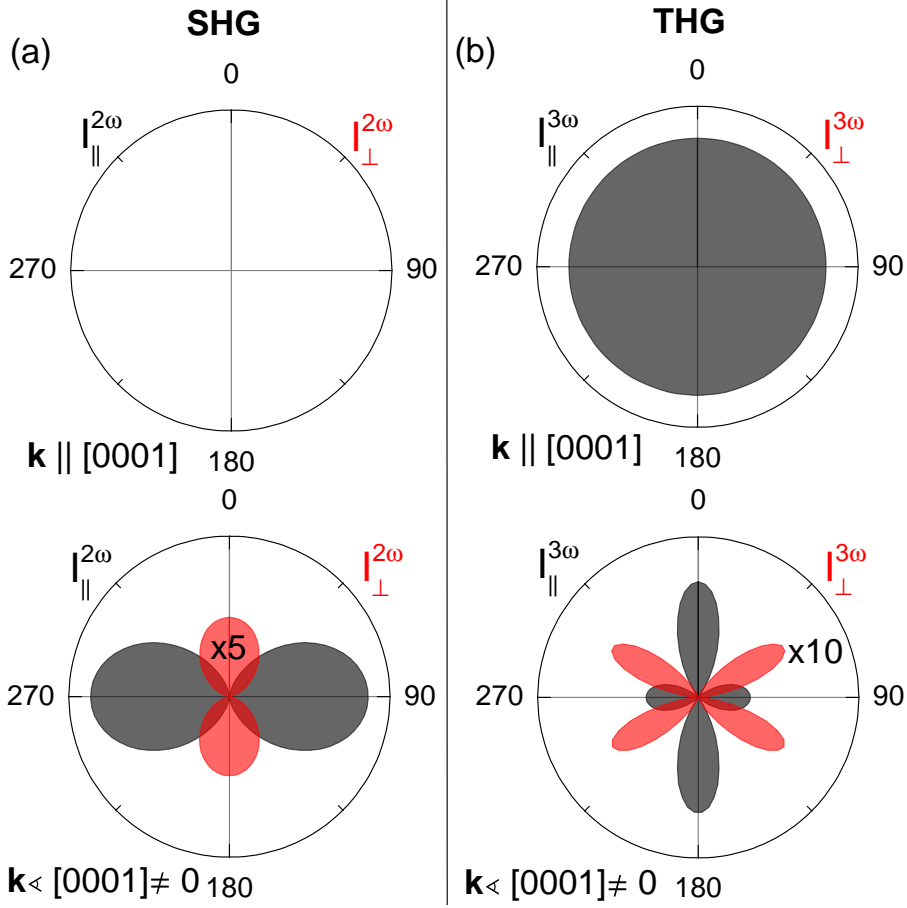
Figure 2.13. – Model calculations for expected $I_\parallel$ parallel and $I_\perp$ crossed rotational anisotropies of SHG and THG signals in GaN. For the tilted configuration always a tilting about the y axis ($\theta \neq 0$) is assumed. (a) There is no ED SHG allowed for $\mathbf{k} \parallel [0001]$. For $\mathbf{k}\measuredangle[0001] \neq 0$ mainly in the parallel configuration at $\varphi = 90°$ the SHG intensity has a maximum. (b) For $\mathbf{k} \parallel [0001]$ THG in the parallel configuration is constant and the crossed configuration is forbidden. For $\mathbf{k}\measuredangle[0001] \neq 0$ various shapes of the THG anisotropy can emerge and an exemplary one is plotted.

The anisotropies for crystallographic THG are modeled with the third order susceptibility $\chi^{(3)}$ of C_{6v}, which has the independent tensor components

$$\chi_{xxxx} = \chi_{yyyy} = 3\underline{\chi_{xxyy}}$$

$$\underline{\chi_{zzzz}}$$

$$\underline{\chi_{xxyy}} = \chi_{xyxy} = \chi_{xyyx} = \chi_{yyxx} = \chi_{yxyx} = \chi_{yxxy}$$

$$\underline{\chi_{xxzz}} = \chi_{xzxz} = \chi_{xzzx} = \chi_{zzxx} = \chi_{zxzx} = \chi_{zxxz}$$

$$\underline{\chi_{zzxx}} = \chi_{zxzx} = \chi_{zxxz} = \chi_{xxzz} = \chi_{xzxz} = \chi_{xzzx}. \tag{2.51}$$

The biggest difference to SHG is the occurrence of tensor components which have no z

component. Therefore it is possible to measure them in the **k** ∥ [0001] configuration. The only independent tensor component which remains in this configuration is χ_{xxyy}, as all other tensor components have a z component. The calculated intensities for **k** ∥ [0001] are

$$I_{\parallel}^{(3\omega)} = 9 * \chi_{xxyy}^2 \tag{2.52}$$

$$I_{\perp}^{(3\omega)} = 0. \tag{2.53}$$

All the rotational anisotropies for ED transitions of different resonances have to be constant for the parallel configuration and zero for the crossed configuration, since only one independent tensor component influences the anisotropy. The anisotropy is shown in Fig. 2.13(b). The more general results for tilted incidence $\theta \neq 0$ are

$$
\begin{aligned}
I_{\parallel}^{(3\omega)} = \big(&3\chi_{xxyy}\cos(\varphi)^4 + 3\cos(\varphi)^2\big(2\chi_{xxyy}\cos(\theta)^2 + \\
&\sin(\varphi)^2(\chi_{xxzz} + \chi_{zzxx})\sin(\theta)^2\big) + \sin(\varphi)^4\big(3\chi_{xxyy}\cos(\theta)^4 + \\
&3(\chi_{xxzz} + \chi_{zzxx})\cos(\theta)^2\sin(\theta)^2 + \chi_{zzzz}\sin(\theta)^4\big)\big)^2
\end{aligned}
\tag{2.54}
$$

$$
\begin{aligned}
I_{\perp}^{(3\omega)} = \frac{1}{4}\sin(\theta)^4 \big(&6(\chi_{xxyy} - \chi_{zzxx})\cos(\varphi)^3\sin(\varphi) + \\
&\cos(\varphi)\sin(\varphi)^3\big(3(\chi_{xxyy} + \chi_{xxzz} - \chi_{zzxx}) - \chi_{zzzz} + \\
&\cos(2\theta)(3\chi_{xxyy} - 3(\chi_{xxzz} + \chi_{zzxx}) + \chi_{zzzz})\big)\big)^2.
\end{aligned}
\tag{2.55}
$$

In this case various two-fold or four-fold shapes can emerge, depending on the relation of the tensor components. In Fig. 2.13(b) an exemplary shape for $\chi_{zzzz} = 5$; $\chi_{xxyy} = -2$; $\chi_{xxzz} = 5$; $\chi_{zzxx} = -2$; $\theta = 45\,^\circ$ is plotted. In contrast to SHG, the main intensity is not necessarily pointed in the direction of the z axis. The crossed intensity is smaller than the parallel one for most tensor component relations.

The measurements on GaN showed no influence of a magnetic field and the anisotropies did not change in an external magnetic field. Therefore the calculations of magnetic field induced SHG and THG are omitted. All Voigt magnetic field induced SHG in GaN is anisotropic and is non-zero for the crossed configuration. It can easily be recognized for **k** ∥ [0001], because of the strong difference to the crystallographic SHG and THG.

Cu₂O

Since Cu$_2$O is a centrosymmetric material, ED SHG is forbidden in it. The polar susceptibility $\chi^{(2)}$ is zero for all components. Still it was shown by Shen that it is possible to observe SHG from the yellow $1s$ exciton [39]. The optical selection rules for ED transitions allow two-photon transitions to the $1s$ exciton from the ground state, but a one-photon transition is forbidden. The one-photon part of the SHG transitions is an EQ transition. The excitation of an EQ moment by a two-photon excitation in the crystal is described by the third order susceptibility

$$Q_{ij}^{2\omega} = \chi_{ijnm}^{(3)} E_n^\omega E_m^\omega. \tag{2.56}$$
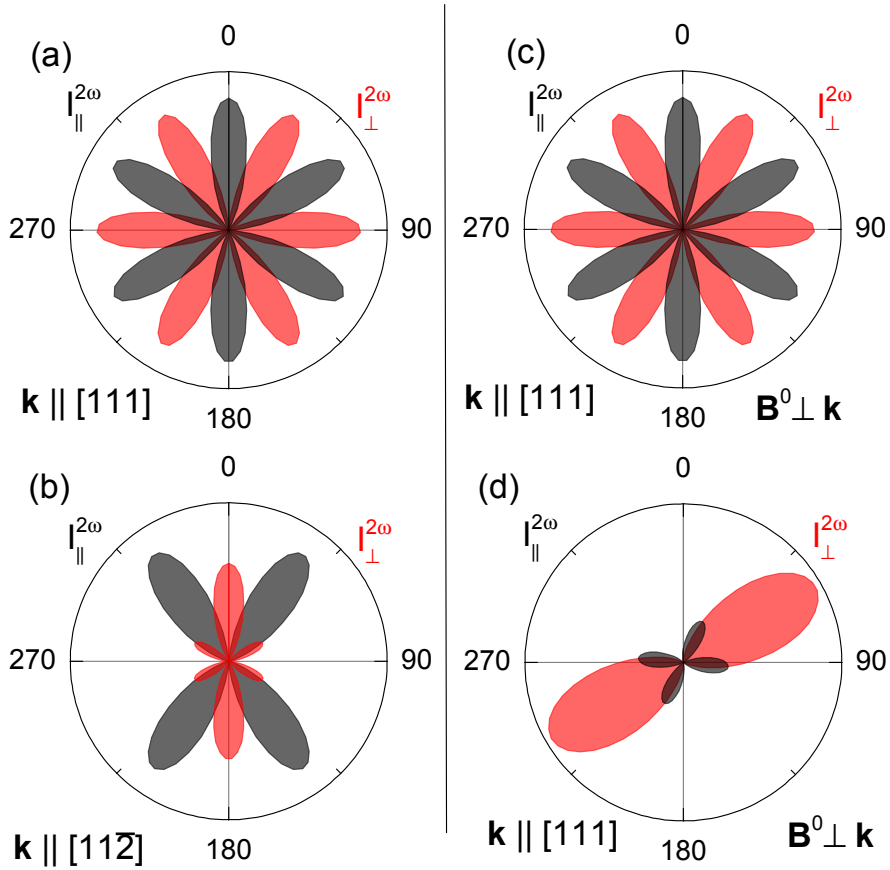
Figure 2.14. – Model calculations for various expected anisotropies in Cu_2O. (a) Parallel $I_\parallel^{2\omega}$ and crossed $I_\perp^{2\omega}$ anisotropy of EQ SHG in the $\mathbf{k} \parallel [111]$ direction. It has the typical six-fold shape of an anisotropy of SHG in this direction in cubic structures. (b) Expected anisotropy for $\mathbf{k} \parallel [11\bar{2}]$ direction. The parallel anisotropy is four-fold and the crossed six-fold. (c,d) Exemplary anisotropies for EQ SHG in a Voigt magnetic field and $\mathbf{k} \parallel [111]$. There are numerous possible shapes from different magnitudes of tensor components. Most notably the same six-fold shape as in (a) can emerge.

The resulting quadrupole moment leads to light emission with an intensity depending on the wave vector:

$$I^{2\omega} \propto |-i\mathbf{k}\mathbf{Q}^{2\omega}|^2 \tag{2.57}$$

The anisotropies can be modeled in the same way as in ED SHG. In the direction $\mathbf{k} \parallel [111]$ the described quadrupole process is allowed. The independent tensor components for $\chi^{(3)}$

in the O_h group are

$$
\begin{aligned}
\underline{\chi_{xxxx}} &= \chi_{yyyy} = \chi_{zzzz} \\
\underline{\chi_{xyyx}} &= \chi_{xzzx} = \chi_{yxxy} = \chi_{yzzy} = \chi_{zxxz} = \chi_{zyyz} = \\
\chi_{xxyy} &= \chi_{xxzz} = \chi_{yyxx} = \chi_{yyzz} = \chi_{zzxx} = \chi_{zzyy} = \\
\chi_{xyxy} &= \chi_{xzxz} = \chi_{yxyx} = \chi_{yzyz} = \chi_{zxzx} = \chi_{zyzy}.
\end{aligned}
\tag{2.58}
$$

Calculating the expected anisotropy for **k** $\parallel$ [001] and **k** $\parallel$ [1$\bar{1}$0] reveals zero intensity for the parallel and crossed configuration. EQ SHG is allowed in other directions. In Fig. 2.14(a) the expected anisotropy for **k** $\parallel$ [111] is plotted. Both configurations have a six-fold shape with the same intensity. The calculated intensities are

$$
I_\parallel^{2\omega}(\varphi) = (\chi_{xxxx} - 3\chi_{xxyy})^2 \cos^2(3\varphi)
\tag{2.59}
$$
$$
I_\perp^{2\omega}(\varphi) = (\chi_{xxxx} - 3\chi_{xxyy})^2 \sin^2(3\varphi)
\tag{2.60}
$$

This is the same expected anisotropy as ED SHG in GaAs for **k** $\parallel$ [111]. Although the susceptibility has two independent tensor components, only the difference between them turns up and every resonance has the same shape. It reflects the structure of cubic materials in this direction, which is similar to a hexagonal structure. The **k** $\parallel$ [11$\bar{2}$] direction is shown in Fig. 2.14(b). The equations for this direction are

$$
I_\parallel^{2\omega}(\varphi) = (\chi_{xxxx} - 3\chi_{xxyy})^2 \cos^4(\varphi) \sin^2(\varphi)
\tag{2.61}
$$
$$
I_\perp^{2\omega}(\varphi) = \frac{1}{144}(\chi_{xxxx} - 3\chi_{xxyy})^2 (\cos(\varphi) + 3\cos(3\varphi))
\tag{2.62}
$$

Again, only one shape for every resonance is expected. The intensity for the parallel configuration is much higher and shows a four-fold symmetry. In the next step, the EQ SHG in a magnetic field is calculated.

The expected EQ SHG in a magnetic field is calculated from the axial susceptibility $\chi^{(4)}$ with the tensor components

$$
\begin{aligned}
\underline{\chi_{zyxx}} &= \chi_{xzyyy} = \chi_{yxzzz} = -\chi_{yzxxx} = -\chi_{zxyyy} = -\chi_{xyzzz} \\
\underline{\chi_{zyxy}} &= \chi_{xzyzz} = \chi_{yxxzx} = -\chi_{zxxyx} = -\chi_{yzxzz} = -\chi_{xyyzy} \\
\underline{\chi_{zyxzz}} &= \chi_{xzxyx} = \chi_{yxyzy} = -\chi_{zxyzz} = -\chi_{yzxyy} = -\chi_{xyxzx} \\
\underline{\chi_{zyyyx}} &= \chi_{xzzzy} = \chi_{yxxxz} = -\chi_{zxxxy} = -\chi_{yzzzx} = -\chi_{xyyyz} \\
\underline{\chi_{zyzzx}} &= \chi_{xzxxy} = \chi_{yxyyz} = -\chi_{zxzzy} = -\chi_{yzyyx} = -\chi_{xyxxz} \\
\underline{\chi_{zzyzx}} &= \chi_{xxxzy} = \chi_{yyxyz} = -\chi_{zzxzy} = -\chi_{yyyzx} = -\chi_{xxxyz}
\end{aligned}
\tag{2.63}
$$

The high number of independent tensor components allows for many different anisotropy shapes, which can depend on the wavelength. For **k** $\parallel$ [111] and $\mathbf{B}^0 \perp \mathbf{k}$ the resulting

intensities are

$$
\begin{aligned}
I_{\parallel}^{2\omega}(\varphi) = (&3(\chi_{zyxxx} + \chi_{zyxyy} + \chi_{zyxzz} - \chi_{zyyyx} - \chi_{zzyzx})\cos(\varphi) \\
&+ 3(\chi_{zyxyy} + \chi_{zyxzz} - \chi_{zzyzx})\cos(3\varphi) \\
&+ \sqrt{3}((\chi_{zyxxx} + \chi_{zyxyy} + \chi_{zyxzz} - \chi_{zyyyx} - \chi_{zzyzx})\sin(\varphi) \\
&+ (-2\chi_{zyxxx} + \chi_{zyxyy} + \chi_{zyxzz} + 2\chi_{zyyyx} - \chi_{zzyzx})\sin(3\varphi)))^2
\end{aligned}
\tag{2.64}
$$

$$
\begin{aligned}
I_{\perp}^{2\omega}(\varphi) = (&-\sqrt{3}(3\chi_{zyxxx} + \chi_{zyxyy} + 5\chi_{zyxzz} + \chi_{zyyyx} + 2\chi_{zyzzx} + 3\chi_{zzyzx})\cos(\varphi) \\
&+ \sqrt{3}(2\chi_{zyxxx} - \chi_{zyxyy} - \chi_{zyxzz} - 2\chi_{zyyyx} + \chi_{zzyzx})\cos(3\varphi) \\
&+ 3(3\chi_{zyxxx} + \chi_{zyxyy} + \chi_{zyxzz} + \chi_{zyyyx} + 2\chi_{zyzzx} - \chi_{zzyzx})\sin(\varphi) \\
&+ 3(\chi_{zyxyy} + \chi_{zyxzz} - \chi_{zzyzx})\sin(3\varphi))^2
\end{aligned}
\tag{2.65}
$$

Among the various possible anisotropies there is also a six-fold shape like the zero field anisotropy, which is shown in Fig. 2.14(c). Another possible shape is shown in Fig. 2.14(d). In this case the crossed anisotropy is stronger and only two-fold. Without a more detailed understanding of the independent tensor components the measurement of the anisotropy in a magnetic field does not reveal much information about the process, since many possible shapes can be fitted by Eq. (2.65).

In Sec. 6 it is shown that SHG is observed in the EQ forbidden directions $\mathbf{k} \parallel [001]$ and $\mathbf{k} \parallel [1\bar{1}0]$ in Cu$_2$O. It is therefore interesting to investigate the responsible selection rules for these directions in more detail. In the $\mathbf{k} \parallel [1\bar{1}0]$ direction the calculated intensity from a quadrupole is zero and cannot explain the observed resonance. Another possibility for a higher order SHG process is an MD transition. This is described by the susceptibility

$$
P_{\mathrm{i}}^{2\omega} = \chi_{\mathrm{ijn}}^{(2)} E_{\mathrm{j}}^{\omega} H_{\mathrm{n}}^{\omega}
\tag{2.66}
$$

which calculates the resulting polarization from a transition in which the magnetic field of the light is involved. It turns out that this polarization is also zero for $[1\bar{1}0]$.

In order to find out more about the selection rules for the EQ transition, the symmetries of the transitions at the Γ point are investigated. This leads to more information than the general susceptibility calculations. The crystal is cut in such a way that the directions $[1\bar{1}0]$, $[11\bar{2}]$ and $[111]$ are fundamental faces and a good starting point for a basis of the involved states. The set of basis vectors

$$
\mathbf{E}_{(111)} = \frac{1}{\sqrt{3}}\begin{pmatrix} 1 \\ 1 \\ 1 \end{pmatrix} \quad \mathbf{E}_{(11\bar{2})} = \frac{1}{\sqrt{6}}\begin{pmatrix} 1 \\ 1 \\ -2 \end{pmatrix} \quad \mathbf{k}_{(1\bar{1}0)} = \frac{1}{\sqrt{2}}\begin{pmatrix} 1 \\ -1 \\ 0 \end{pmatrix}
\tag{2.67}
$$

is used for these calculations. The subscript defines the direction of the vector. The $\mathbf{E}$ vectors are the polarizations of the light wave and the $\mathbf{k}$ vector is the wave vector. A two-photon ED transition to the $1s$ exciton is described by the projection of two Γ_4^- photons

on the Γ_5^+ exciton

$$\mathbf{A}(\mathbf{E}) = \begin{pmatrix} e_y e_z \\ e_x e_z \\ e_y e_x \end{pmatrix} \tag{2.68}$$

and depends on the direction of the light polarization $\mathbf{E}$. The quadrupole transition is described by the symmetric vector product of $\mathbf{E}$ and $\mathbf{k}$.

$$\mathbf{Q} = \begin{pmatrix} e_y k_z + e_z k_y \\ e_x k_z + e_z k_x \\ e_y k_x + e_x k_y \end{pmatrix} \tag{2.69}$$

For SHG the two-photon ED and the one-photon EQ transition have to be allowed for the same state of the three $1s$ exciton states. Therefore the transitions are calculated for both polarizations of light with $\mathbf{k} \parallel [1\bar{1}0]$, which are $\mathbf{E} \parallel [111]$ and $\mathbf{E} \parallel [11\bar{2}]$. In the following calculations the $\mathbf{S}$ vector describes the excited crystal state. They are normalized after they are calculated from the polarization and wave vectors.

$$\mathbf{Q}(\mathbf{k}_{(1\bar{1}0)}, \mathbf{E}_{(111)}) \quad = \frac{1}{\sqrt{6}} \begin{pmatrix} -1 + 0 \\ 0 + 1 \\ 1 - 1 \end{pmatrix} \quad \hookrightarrow \mathbf{S}_{(1\bar{1}0)} \tag{2.70a}$$

$$\mathbf{Q}(\mathbf{k}_{(1\bar{1}0)}, \mathbf{E}_{(11\bar{2})}) \quad = \frac{1}{2\sqrt{3}} \begin{pmatrix} 2 + 0 \\ 0 - 2 \\ 1 - 1 \end{pmatrix} \quad \hookrightarrow \mathbf{S}_{(1\bar{1}0)} \tag{2.70b}$$

$$\mathbf{A}(\mathbf{E}_{(111)}) \quad = \frac{1}{3} \begin{pmatrix} 1 \\ 1 \\ 1 \end{pmatrix} \quad \hookrightarrow \mathbf{S}_{(111)} \tag{2.70c}$$

$$\mathbf{A}(\mathbf{E}_{(11\bar{2})}) \quad = \frac{1}{6} \begin{pmatrix} -2 \\ -2 \\ 1 \end{pmatrix} \quad \hookrightarrow \mathbf{S}_{(\bar{2}\bar{2}1)} = -(\mathbf{S}_{(111)} + \mathbf{S}_{(11\bar{2})}) \tag{2.70d}$$

The EQ transition is only allowed for the $\mathbf{S}_{(1\bar{1}0)}$ state, which lies in the direction of the wave vector. The two-photon ED transition, on the other hand, is only allowed for the states perpendicular to $\mathbf{S}_{(1\bar{1}0)}$. No state is allowed for both, which is the reason for the vanishing susceptibility for SHG in this direction.

The presented calculations reveal that the observed signal in $\mathbf{k} \parallel [1\bar{1}0]$ direction could be TPA-PL (and the same argument can be used for the forbidden $\mathbf{k} \parallel [001]$ direction as shown by Kono [33]). SHG is only forbidden because the one- and two-photon transitions are not allowed to the same state. Since all three $1s$ exciton states $\mathbf{S}_{(111)}$, $\mathbf{S}_{(1\bar{1}0)}$, and $\mathbf{S}_{(\bar{2}\bar{2}1)}$ are degenerated (except for the tiny $\mathbf{k}^2$ splitting) a transition between the states is possible. First, a two-photon absorption process creates the exciton. Depending on the polarization it is either the $\mathbf{S}_{(111)}$ or the $\mathbf{S}_{(11\bar{2})}$ state. During its lifetime it can convert into another state through means of interaction with other quasiparticles [84]. Once it is

in the $\mathbf{S}_{(1\bar{1}0)}$ state it can emit a photon in the $[1\bar{1}0]$ direction via an EQ process.

The calculations for the $\mathbf{k} \parallel [1\bar{1}0]$ direction were done relative to the crystal faces of the sample. The same calculations are done with the basis $[1\bar{1}0]$, $[001]$, and $[110]$ which includes the fundamental $\mathbf{E} \parallel [001]$ direction. The resulting selection rules are

$$\mathbf{Q}(\mathbf{k}_{(1\bar{1}0)}, \mathbf{E}_{(001)}) \qquad = \frac{1}{\sqrt{2}} \begin{pmatrix} -1+0 \\ 0+1 \\ 0 \end{pmatrix} \qquad \hookrightarrow -\mathbf{S}_{(1\bar{1}0)} \qquad (2.71\mathrm{a})$$

$$\mathbf{Q}(\mathbf{k}_{(1\bar{1}0)}, \mathbf{E}_{(110)}) \qquad = \begin{pmatrix} 0 \\ 0 \\ 0 \end{pmatrix} \qquad \hookrightarrow \text{forbidden} \qquad (2.71\mathrm{b})$$

$$\mathbf{A}(\mathbf{E}_{(001)}) \qquad = \begin{pmatrix} 0 \\ 0 \\ 0 \end{pmatrix} \qquad \hookrightarrow \text{forbidden} \qquad (2.71\mathrm{c})$$

$$\mathbf{A}(\mathbf{E}_{(110)}) \qquad = \begin{pmatrix} 0 \\ 0 \\ 1 \end{pmatrix} \qquad \hookrightarrow \mathbf{S}_{(001)} \qquad (2.71\mathrm{d})$$

The selection rules are simpler with this basis. The incident ED two-photon transition is only allowed for the light polarization $\mathbf{E} \parallel [110]$ and the EQ transition is only allowed for $\mathbf{E} \parallel [001]$. This can be compared to measurements in which only the fundamental or the SHG polarization are turned separately.

Si and SiC

For the measurements of Si and SiC it is sufficient to briefly summarize the important features of the according susceptibility. It is only used to verify that a detected signal is in fact SHG or THG and does not belong to another type of transition.

Si belongs to the symmetry group O_h like Cu_2O. Most importantly, ED SHG is forbidden in the centrosymmetric structure. The rotational anisotropy for THG is described by the third order susceptibility $\chi^{(3)}$ of O_h. The independent tensor components for $\chi^{(3)}$ are given in (2.58). For $\mathbf{k} \parallel [111]$ a constant intensity of the parallel configuration is expected, as is a four-fold shape for the crossed intensity.

Hexagonal SiC belongs to the symmetry group C_{6v}. A thorough analysis of the rotational anisotropy in this group is given in [31]. For the rotational anisotropy of SHG in the $\mathbf{k} \parallel [0001]$ configuration, a six-fold shape is expected, which reflects the crystal structure in this direction. For a tilted configuration $\Theta \neq 0\,^\circ$ a two-fold parallel anisotropy with a maximum at $\varphi = 90\,^\circ$ is expected.

3. Experimental methods

In this chapter the experimental methods to investigate nonlinear light matter interactions are introduced. A general optical setup consist of a light source, a sample mounting, and light detection. The specific devices in the setup are optimized for SHG and THG spectroscopy of semiconductors over a broad spectral range. In Sec. 3.1 "Components" these devices are described. The setup allows for manifold measurement routines, which lead to complementary information. The most important measurement routines for the thesis are described in Sec. 3.2 "Measurement techniques".

3.1. Components
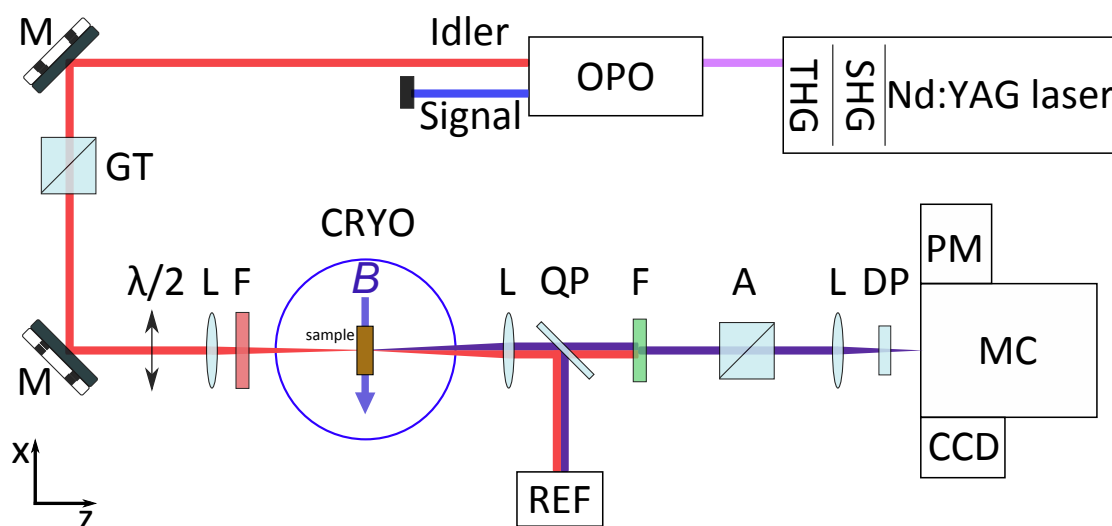
SHG/THG - second/third harmonic | OPO - optical parametric oscillator | GT - Glan-Thompson prism
λ/2 - half-wave plate | F - filter | REF - reference (photo diode) | A - analyzer (foil/GT) | DP - depolarizer
MC - monochromator | CCD - charged-coupled-device camera | PM - photomultiplier | M - mirror
CRYO - split coil cryostat | L - lense | QP - fused quartz plate

Figure 3.1. – Sketch of the experimental setup. For the presented measurements only the idler beam of the OPO is used. The analyzer of linear polarized light is either a Glan-Thompson prism or a polarization foil.

A sketch of the experimental setup is shown in Fig. 3.1 and a 3D image in Fig. 3.2. The main parts are the laser system, the cryostat, a detection system and optical components.

The whole setup is controlled by a custom LabView program running on a PC. It controls the different components and also handles the timing of measurements. The samples are mounted within a split-coil cryostat to control the temperature and external magnetic or electric fields. The laser system allows a variation of the power and wavelength of the incident light. The optical components can adjust and filter the light polarization and wavelength. The optical axis is defined as the z axis, so that z is parallel to the wave vector of the laser light. The x axis is parallel to the optical table and the y axis is perpendicular to the table.

3.1.1. Laser system
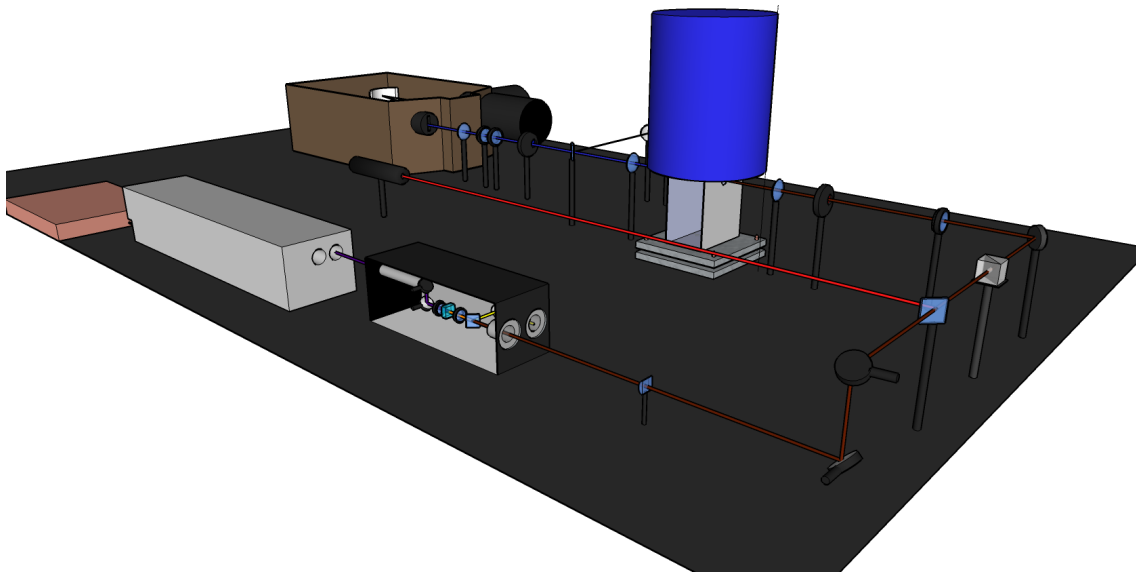
Figure 3.2. – 3D image of the experimental setup.

A "SpitLight 600" laser by Innolas is used to pump a "VisIR2" OPO by GWU. The SpitLight 600 is a seeded neodymium-doped yttrium aluminum garnet (Nd:YAG) laser with optical pumping by flash lamps and an amplifier crystal, which is pumped by the same flash lamps. The flash lamps work at a repetition rate of 10 Hz. A Pockels cell is used as a Q-switch for maximum population inversion in the medium before the lasing is started. Integrated SHG and THG stages convert the typical Nd:YAG wavelength (1024 nm) down to 532 nm and 355 nm respectively. The fundamental light is separated from the 355 nm by short-pass mirrors. The pulse duration is 7 ns with a pulse energy of about 180 mJ. The light from the Nd:YAG laser is used to operate an optic parametric oscillator (OPO). This allows a tuning of the laser wavelength by parametric down conversion. Angle tuning of a BBO crystal allows one to convert the pump frequency w_p into two new frequencies w_s and w_i. The short wavelength is called "signal" and the long one "idler". They have the relationship $w_s + w_i = w_p$, because of energy conservation. In each transition one photon of each wavelength is created. This leads to an uneven distribution of energy in the signal and idler beam. Angle tuning of the BBO crystals allows to create different
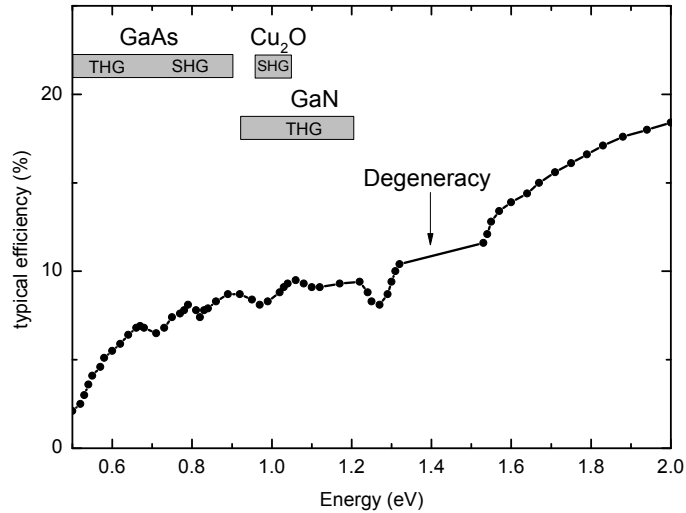
Figure 3.3. – Typical conversion efficiency (black line) of the OPO taken from the manual [85] and x axis converted to eV from nm. The gap around the point of degeneracy can actually be avoided by correct adjustment of the OPO. Also the energy range for the fundamental light of the measurements are marked (gray areas).
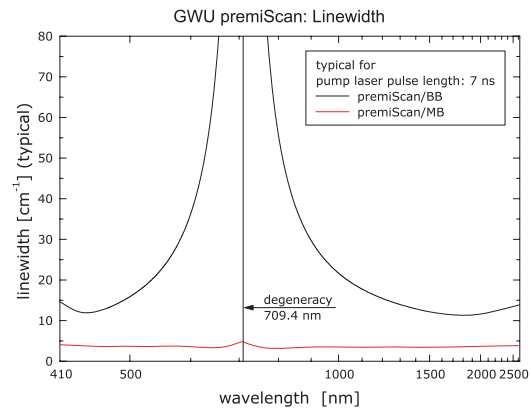
Figure 3.4 – Typical linewidth of the OPO taken from the manual [85]. The linewidth of the premiScan/MB used in the experiment is almost constant $5\,\mathrm{cm}^{-1}$ over the whole spectral range and only increases to $6\,\mathrm{cm}^{-1}$ at the degeneracy point $\lambda_\mathrm{D} = 709\,\mathrm{nm}$.

phase matching conditions to favor one specific signal (and therefore also idler) frequency. In order to get access to as much angles as possible two different BBO crystals are mounted on top of each other, which have a different starting angle relative to the laser light. The conversion process is started by ambient photons which accidentally match the frequency of the signal or idler. To achieve a high conversion of up to 20 %, the crystals are mounted within an optical resonator for the idler. The OPO gives access to the wavelength region between 400 nm ($3.098\,\mathrm{eV}$) and 2500 nm ($0.496\,\mathrm{eV}$). In Fig. 3.3 the conversion efficiency depending on the wavelength is shown. The wavelength regions covered in this thesis are marked by gray bars. An energy of 2 mJ up to 6 mJ per pulse is reached after the OPO. This is more than sufficient and has to be reduced by optical gray filters in most cases to avoid a damaging of samples.

The laser linewidth is about $5\,\mathrm{cm}^{-1}$ as shown in Fig. 3.4. The linewidth increases

only slightly near the degeneracy point at $710\,\mathrm{nm}$ to $6\,\mathrm{cm}^{-1}$, because the premiScan/MB (MidBand) OPO is used. The premiScan/MB is a type-II OPO, which allows for a small linewidth compared to type-I OPOs. The OPO linewidth is the main limiting factor for the resolution of energy, as the detection offers a higher resolution.

The 10 pulses of $7\,\mathrm{ns}$ lead to $70\,\mathrm{ns}$ laser action time during a second. This is a duty cycle of 1.4×10^{-11}. Most measurements were performed using an energy per pulse between $0.2\,\mathrm{mJ}$ and $3\,\mathrm{mJ}$, depending on the damage threshold of the investigated crystal. For $1\,\mathrm{mJ}$ per pulse the system has an average power of $10\,\mathrm{mW}$. Taking only the time during one pulse into account, a power of about $150\,\mathrm{kW}$ is reached. A typical spot size of $300 \times 300\,\mu\mathrm{m}^2 = 9 \cdot 10^{-8}\,\mathrm{m}^2$ can be achieved at the the sample. The irradiance of $15\,\frac{\mathrm{TW}}{\mathrm{m}^2}$ for the focused beam is sufficient to induce nonlinearities in most materials.

The linear polarization of the laser light can be turned by a half-wave plate, called "polarizer". This allows the measurement of the polarization anisotropy of SHG and is an important part of SHG spectroscopy. In Sec. 3.2.3 "SHG/THG rotational anisotropy" the measurement routines involving polarization dependence are explained. The uniaxial material for a wave plate has strong nonlinear optical properties and leads to SHG, although the laser light passes it unfocussed. This SHG is filtered by a long pass optical filter in front of the sample.

3.1.2. Cryostat and sample holder

Most of the experiments were performed with an Oxford Spectromag system. It is isolated by a vacuum $P_\mathrm{V} \approx 10^{-6}\,\mathrm{mbar}$ and a nitrogen shield. It includes a superconducting split-coil magnet, which can reach magnetic fields up to $11\,\mathrm{T}$ in the Faraday and Voigt geometry, which are explained in Sec. 3.2.1. By controlling helium flow with a pump, the temperature of the sample can be regulated between $T = 1.5\,\mathrm{K}$ (superfluid helium) and $300\,\mathrm{K}$ (warm helium gas). The superfluid helium phase is reached by reducing the pressure in the cryostat down to $40\,\mathrm{mbar}$ with a pump. The sample can be investigated optically through quartz windows on each side. The sample is mounted on a holder within the cryostat.

Three different sample holders are used for the measurements. The main sample holder allows the attachment of up to four samples simultaneously and is equipped with a cernox diode to measure the temperature precisely. This is presented in Fig. 3.5(Top). A second sample holder allows a rotation of the crystal around the optical axis. In this way the external magnetic field can be applied along different crystal axis.

A custom-made sample holder was designed, as shown in Fig.3.5(Bottom), for the application of an electric field. The main structure is made from nylon, which has a low coefficient of thermal expansion $\alpha \approx 80 \cdot 10^{-6}\,\mathrm{K}^{-1}$ and is an insulator. Within this structure there are two brass blocks, which are used as a capacitor. These blocks have rounded off edges so as to avoid voltage spikes. The sample rests on the lower brass block while the upper one presses against the sample. The pressure is adjusted by three springs to a value, which secures the sample, but also avoids strain or even damage. A comparison between measurements with this sample holder and measurements with other sample holders reveals, that the strain is negligible and does not change the obtained SHG spectrum.
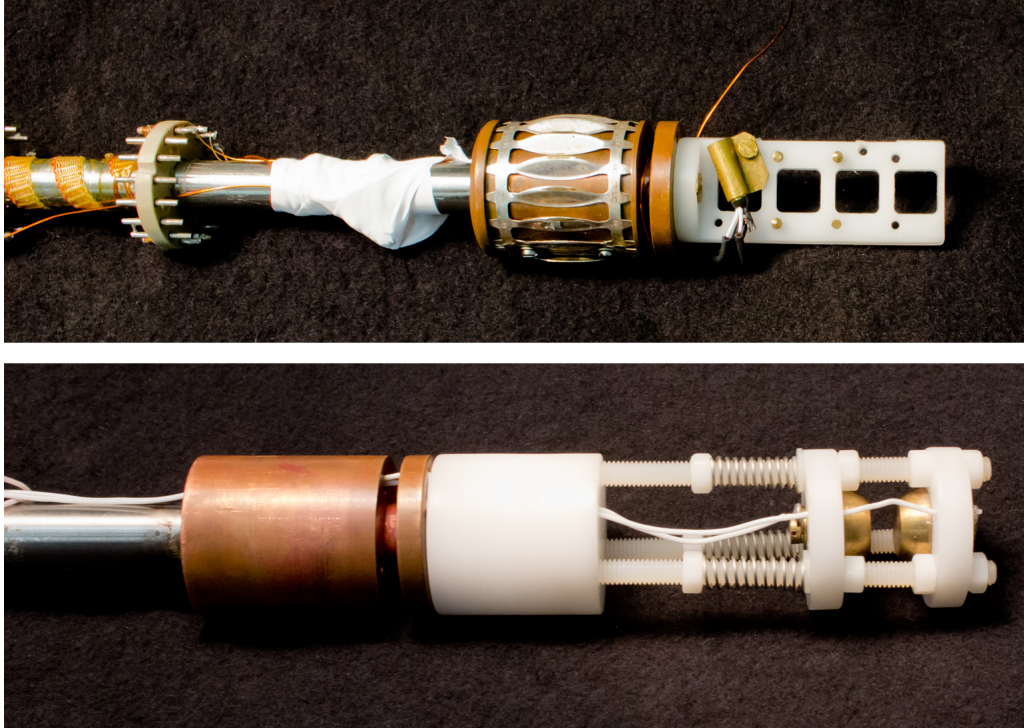
Figure 3.5. – (Top) The main sample holder allows to attach several samples at once. A cernox diode makes temperature measurements close to the samples possible. (Bottom) The custom designed electric field sample holder. The main structure is made from nylon for good electric isolation. Two rounded brass plates are connected to a power source. In between the brass plates the sample is fixed by pressure from springs.

A drawback of this sample holder is, that the sample orientation cannot be adjusted as well as in the other holders. The sample position can change due to vibrations during the insertion or adjusting process. This leads to a small tilting of the adjusted position of about $\Theta < 3°$. This is taken into account for model calculations.

The brass capacitor is connected to a power supply with two cables. The voltage and current limitations are set separately. With the measurements the influence of an electric field of up to $2\,\text{kV}$ on SHG is investigated. Even small currents lead to an undesired heating of the sample and have to be avoided. The current limitation is set to about $2\,\text{mA}$. Then the maximum possible voltage is checked with the laser wavelength tuned to a resonance of the sample. Absorption of the laser light induces photo currents, which lead to smaller possible voltages before the current limit is reached. The highest possible voltage decreases over time. Especially after a few current spikes the maximum voltage has to be reduced. Taking the sample out of the cryostat and cleaning the surface makes higher voltages possible again. The currents are probably conducted via the surface, which seems to collect impurities.

It is not possible to reach $T = 1.5\,\text{K}$ when voltages over $500\,\text{V}$ are applied with this sample holder. The connector between the cables in the cryostat to the brass capacitor
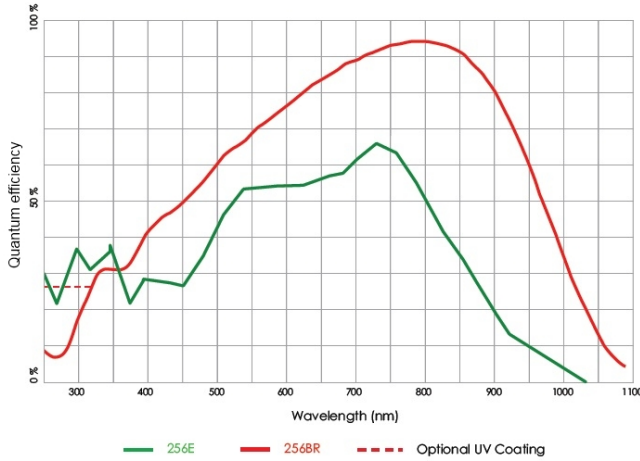
Figure 3.6 – Quantum efficiency of the CCD [86]. In the experimental setup the model Pixis 256E from Princeton Instruments is used.

and the external power supply is in the low pressure He gas at the top of the cryostat when the He pump is used. He gas at low pressure has a smaller breakthrough voltage threshold than He at normal pressure according to Paschen's law and spark-overs happen for voltages above $500\,\text{V}$. All measurements with this sample holder are performed at $T = 5\,\text{K}$, which is sufficient to avoid a broadening of resonances from phonon interactions.

For the presentation of the experimental data the actual applied voltage is always given. For theory calculations the electric field strength is the important quantity. The voltage V is converted into electric field strength. For the GaAs 239 sample with a height of $0.7\,\text{cm}$ parallel to the electric field it is calculated by $E^0 \approx \frac{V}{0.7\,\text{cm}}$. The actual field strength could be smaller due to losses at the sample capacitor interface.

3.1.3. Detection

For SHG spectroscopy light is probed for its properties after it passes through the sample. The polarization, wavelength, intensity and, in specific cases, duration of the pulse can be measured. The SHG light coincides in time and space with the laser light and the two have to be separated. A short-pass filter absorbs the laser light and transmits the SHG light behind the sample. Different filters are available to cover all wavelengths. With a Glan-Thompson filter, called "analyzer", specific linear polarizations of the SHG light are selected for detection. The relative position of the polarizer and the analyzer is an important tool for SHG spectroscopy and the measurements based on these components are explained in Sec. 3.2.3.

A spectrometer is used to center a specific wavelength on a charged-coupled device (CCD) camera. The spectrometer is a Jobin Yvon HR460 with two switchable gratings. The relative efficiency of the gratings is presented in Fig. 3.7. To avoid the different efficiency for transverse electric (TE) and transverse magnetic (TM) light, the SHG passes a depolarizer before it is focused on the spectrometer slit. Therefore only the unpolarized efficiency (blue line) is of importance. Grating 53028 is blazed with $1200\,^{\text{lines}}/_{\text{mm}}$ and Grating 53018 is blazed with $1800\,^{\text{lines}}/_{\text{mm}}$. Both have an edge length of $l_{\text{Mo}} = 10\,\text{cm}$. The gratings are chosen according to better efficiency for the SHG wavelength.
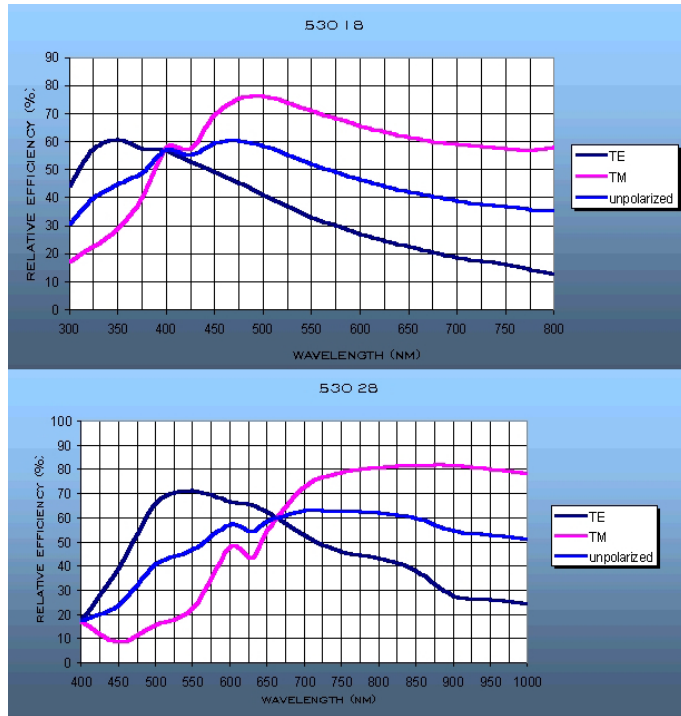
Figure 3.7 – Relative efficiency of the two gratings used in the spectrometer [87]. The efficiency for unpolarized light (blue line) is important for the measurements, because any light is depolarized before it is focused into the spectrometer.

The CCD chip has 256×1024 pixels. The columns are binned to increase the signal because no spatial resolution is necessary. Each column corresponds to a wavelength and the center column 512 is the selected wavelength of the spectrometer. The whole spectral range over the CCD is evaluated for PL measurements. For resonant SHG measurements only a few columns around the central wavelength are summed up and stored as the relative intensity.

3.2. Measurement techniques

3.2.1. Experimental geometry

The angles between the sample, the incident light, the detected light, and possible external perturbations have to be taken into account in the experimental studies. The sensitivity of SHG on the symmetry conditions makes the understanding of the geometry especially important. Therefore the angles describing the experiment are introduced.
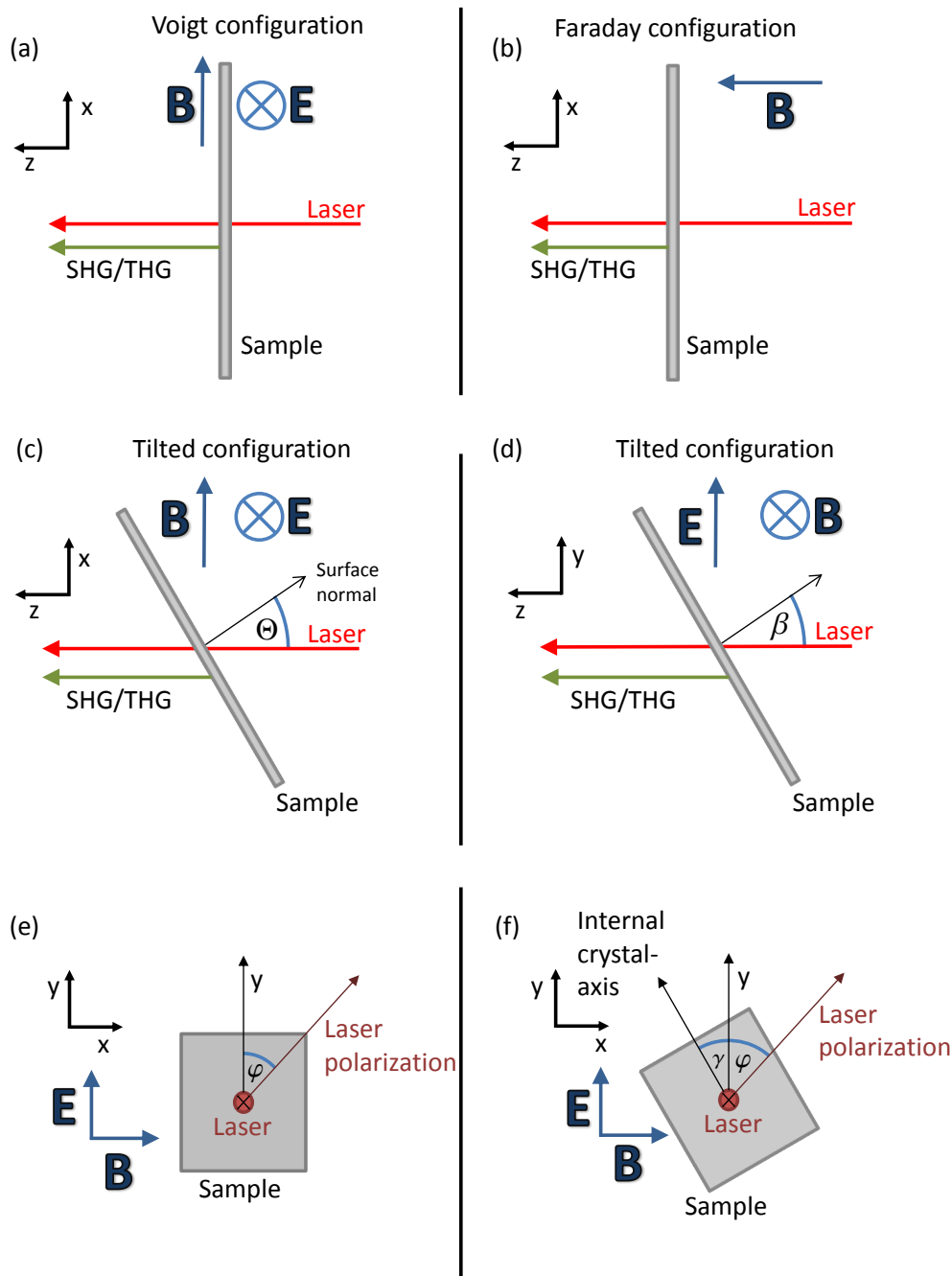
Figure 3.8. – Configurations used in the experiments. (a) Voigt configuration for normal incidence and electric field perpendicular to the magnetic field. (b) Faraday configuration for normal incidence. (c,d) tilted samples described by Θ and β. (e,f) Polarization geometries.

The measurement geometries are presented in Fig. 3.8. The optical axis of the laser is always the z axis of the laboratory system. The x axis is parallel to the optical table and

the y axis is perpendicular to it. In Fig. 3.8(a) the most frequently used measurement geometry is presented. The sample surface is perpendicular to the incident laser and this sample configuration is called "normal incidence". The magnetic field lies along the x axis, which is called "Voigt geometry". An electric field is applied along the y axis. This configuration is always chosen for crossed magnetic and electric fields. The geometry in Fig. 3.8(b) is still "normal incidence", but in contrast to (a) the magnetic field is in Faraday configuration, in which case the magnetic field is parallel to the laser light. In Fig. 3.8(c) the laser light and external fields face in the same direction as in (a), but the sample surface is tilted around the y axis. The tilting is described by the angle Θ, between the surface normal of the sample and the laser light. This tilting is used for $\mathbf{k}$ dependent studies and is controlled by the rotation of the sample holder. In Fig. 3.8(d) a sample tilting around the x axis is presented. The angle β is defined between the surface normal of the sample and the laser light. Such a tilting can happen in the electric field sample holder as explained in Sec. 3.1. The geometry presented in Fig. 3.8(e) is the same as in (a), but viewed along the z axis. The angle φ is defined between the y axis and the polarization for the laser light. It is used for polarization dependent modeling of the harmonics generation. Both the polarization after the polarizer and the polarization selection by the analyzer are described by this angle. In the crossed configuration $\mathbf{E}^{2\omega} \perp \mathbf{E}^{\omega}$ the analyzer is set to $\varphi + 90\,°$. In Fig. 3.8(f) the angle γ, which describes a rotation of the sample around the z axis, is presented. It is defined between an internal crystal axis and the y axis. For $\mathbf{k} \parallel [001]$ it is the angle between the y axis and the [010] crystal direction. For $\gamma = 45\,°$ (similar to Fig. 3.8(f)) the [110] is parallel to the y axis. This is important for the comparison of model calculations and measured anisotropies. It can be understood as a correction of the $\varphi = 0\,°$ polarization direction.

3.2.2. SHG and THG spectroscopy

SHG spectroscopy is the standard technique used for the measurements. For this measurement the OPO is tuned over a wavelength region of interest. This is a region in which the photons have half the energy compared to the energy levels of interest. This way the states can lead to resonantly enhanced SHG. The spectrometer acts as a last filter for the light and centers the SHG on the CCD camera. Therefore it is set to exactly half the wavelength of the OPO, so a wavelength region is scanned, step by step, for SHG. In such a measurement the linewidth of the observed peaks is the convolution of the laser linewidth and the broadening of the state itself.

3.2.3. SHG/THG rotational anisotropy

For a polarization dependence (rotational anisotropy) the OPO and spectrometer wavelength are fixed and the polarization optics, which lie before and behind the sample, are changed. Thereby the light intensity for every combination of incident and emitted polarization can be obtained. Typical measurements are a parallel turning of the incident and the detected polarization about $360\,°$, which is called $I_{\parallel}^{2\omega}$, or the detected polarization is

turned ahead by $90\,^{\circ}$, which is called $I_{\perp}^{2\omega}$. These two measurements are compared to the expected anisotropy of the nonlinear optical susceptibility.

In some cases a specific crystal direction, e.g. a direction along an external field or along a specific crystal axis, is important. In this case either the polarizer or analyzer are held fixed at a specific polarization, whereas the other one is turned about $360\,^{\circ}$ starting from $\varphi = 0\,^{\circ}$. In case the polarizer is held fixed the resulting intensity is I_{Out}, since the emitted polarization is measured for a fixed fundamental polarization. In case the analyzer is held fixed the intensity is I_{In}.

If the intensity of the optical harmonic light is low, it is necessary to remove the analyzer from the setup to detect the intensity $I_{\mathrm{both}}^{2\omega}$ of both light polarization configurations $\mathbf{E}^{2\omega} \parallel \mathbf{E}^{\omega} + \mathbf{E}^{2\omega} \parallel \mathbf{E}^{\omega}$ at the same time. Such a measurement does not reveal as much about the tensor components as $I_{\parallel}^{2\omega}$ and $I_{\perp}^{2\omega}$, but it is still enough to distinguish SHG from other processes, which show no rotational anisotropy at all.

3.2.4. Multi-photon absorption photoluminescence spectroscopy

In Sec. 2.3.2 TPA-PL and 3PA-PL were introduced. These are used to investigate the multi-photon absorption of excitons. Directly measuring the loss of laser intensity by the absorption process in the sample is not possible with the presented experimental components. The relative change in intensity is usually much smaller than the 5% intensity fluctuation of the laser system. Therefore a PL of the electrons excited by TPA is detected.

First, it is necessary to find the strongest source of PL in a sample for these measurements. This is done by using a laser with $\hbar\omega_1 > E_{\mathrm{g}}$, which leads to hot electron-hole pairs from band-band transitions. For example a HeNe laser is used for GaAs, since $\hbar\omega_{\mathrm{HeNe}} \approx 1.\,96\,\mathrm{eV} > E_{\mathrm{g,GaAs}}(5\,\mathrm{K}) \approx 1.\,5\,\mathrm{eV}$. The energy region below the band gap is scanned for the strongest source of PL with the spectrometer and CCD camera. For the actual measurements the spectrometer and CCD camera are kept at this wavelength. Similar to the SHG measurements only a small part of the CCD pixels are evaluated so as to integrate only the PL light.

Then the TPA-PL measurements are performed by tuning the laser light with the OPO over the wavelength region of half the exciton energy. For each wavelength step in the laser light the PL intensity is detected. In case no resonance leads to enhanced TPA, no PL intensity is detected. A strong PL intensity indicates that there is a resonance for TPA at the laser wavelength. The detected intensity at the fixed wavelength is plotted for each wavelength step of the OPO.

These measurements are performed in a reflection geometry, which is presented in Fig. 3.9. The laser light enters the cryostat from the side windows, perpendicular to the detection direction. The sample is aligned, so that the specular reflection of the laser light is dumped within the cryostat. PL has no specific wave vector direction in contrast to SHG and all the light leaving the cryostat through the windows is captured by a lens and focused on the spectrometer. In order to suppress the small amount of diffuse reflected laser light a Glan-Thompson prism is used, which only transmits light polarized perpendicular to the laser light. The PL is not polarized and 50% are transmitted through

Figure 3.9 – Geometry for TPA-PL and 3PA-PL measurements. The laser is directed along the x axis and illuminates the sample under an angle. The specular reflection is dumped within the cryostat. The PL from the sample is undirected. The PL light, which leaves the cryostat along the z axis is collected with a lens. The magnetic field is along the x axis and is also tilted compared to the sample axis.
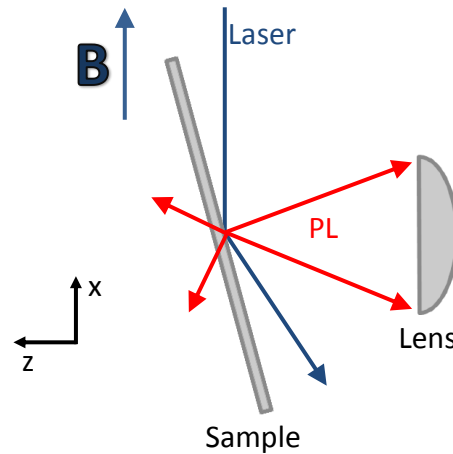
the Glan-Thompson prism in any case.

Another way of measuring TPA-PL is keeping the spectrometer and OPO wavelength fixed. Then the whole CCD is evaluated and the pixel number is converted into a certain wavelength, according to the spectrometer specifications. Again it is possible to observe SHG (or resonant TPA-PL) at the CCD pixel which are illuminated by the wavelength 2ω. In addition to this wavelength 2ω further wavelengths at other positions of the CCD can be evaluated. This enables an investigation of the relaxation process leading to PL, in addition to the SHG measurements. In this way several decay channels of an excited state can be observed at once.

It is possible to perform measurements similar to TPA-PL and 3PA-PL with the laser directly resonant to the excitons, so as to measure the one-photon absorption. This technique is called photoluminescence spectroscopy (PLE). This was, for example, performed on GaAs, but it turns out that impurities in the substrate overpower the signal of the excitons from the high quality epitaxy-layer. For TPA-PL and 3PA-PL this is not big problem, because the nonlinear interaction of the impurities is small. A different technique is used to investigate the one-photon absorption.

In order to investigate the one-photon transition to crystal states, white light reflection measurements can be made. The used light source is a common lamp. The light is collimated and focused on the sample through the same cryostat window, which is also used for the detection. It is possible to make measurements in the normal incidence geometry via a polarizing beam splitter and waveplates, which is described in detail in [88]. The reflected light is focused on the spectrometer and detected with the CCD camera. In this way the intensity of the reflected light for a certain wavelength region can be investigated.

An advantage of this method is, that only a shallow depth of the sample is probed, which can be used to investigate only the high quality side of a sample and avoid contributions from a substrate. With this method it is possible to observe excitons, because they lead to a minimum in the reflection spectra in case they are one-photon allowed and absorb some

of the light. Since most optical measurements are done in the linear regime the white light reflection method is helpful when comparing an investigated sample to known results.

3.3. Samples

Table 3.1. – List of samples used in the experiments.

Material	Name	Growth method	Thickness	Crystal face
GaAs	239	gas-phase-epitaxy	$10\,\mu$m	(001)
GaAs	PDI-M4_2601	molecular-beam-epitaxy	$3\,\mu$m	(111)
GaAs	S01	Bridgman	$245\,\mu$m	(001)
GaN	BS2887	MOVPE Layer	$4.5\,\mu$m	(0001)
Cu_2O	H28	natural growth	$5\,$mm	$(111)/(1\bar{1}0)$
Si	Si01	Czochralski	$500\,\mu$m	(001)
SiC	SiC4H	Lely	$500\,\mu$m	(0001)
SiC	SiC6H	Lely	$500\,\mu$m	(0001)

GaAs samples

In Ch. 4 measurements on GaAs are presented in which several samples are investigated. Most of these measurements are performed with the sample GaAs 239. It was used before for MFISH measurements on GaAs by Sänger et al. [75], in which different GaAs samples were compared. In each sample the resonance energies were the same, but it was found that the quality of the sample has a strong influence on SHG intensity, resonance linewidth, and rotational anisotropy. The sample 239 has the smallest linewidth for exciton resonances and is also used for the measurements in Ch. 4.

Sample 239 is a $10\,\mu$m thick layer of gas-phase-epitaxy grown GaAs on a semi-insulating GaAs substrate. The main face of the sample is (001) and, for normal incidence, the [001] direction lies on the optical axis. The sample has a low defect density of $10^{14}\,\mathrm{cm}^{-3}$, which leads to a good optical quality and a high resistance. The sample has a resistivity of $R(300\,\mathrm{K}) = 20\,\mathrm{M}\Omega$ at room temperature along the [010] direction, which increases beyond $R(5\,\mathrm{K}) = 30\,\mathrm{M}\Omega$ at $T = 5\,\mathrm{K}$. Voltages up to $V = 2\,\mathrm{kV}$ can be applied at $T = 5\,\mathrm{K}$. This sample is also used for the magnetic field induced SHG and THG measurements. Measurements in crossed magnetic and electric fields show the same spectrum as measurements in a magnetic field. The maximum voltage is probably not high enough to influence the MFISH spectrum. Therefore sample S01 is used for the measurements in crossed fields.

Sample PDI-M4_2601 is a $3\,\mu$m layer of GaAs on a GaAs substrate. It is used for the investigation of non-resonant SHG in the $\mathbf{k} \parallel [111]$ direction. The other two faces of the crystal are $(0\bar{1}1)$ and $(2\bar{1}\bar{1})$.

The GaAs substrate S01 sample is used for measurements in crossed electric and magnetic fields. A comparison of MFISH spectra to sample 239 revealed a low SHG intensity

and a higher linewidth of the resonances in the substrate, as is expected due to the lower optical quality of a substrate. Nevertheless, it is better suited for the measurements in crossed fields. The maximum possible voltage is only 800 V, but it leads to much stronger EFISH effects. The external voltage is better coupled to the electronic system of this GaAs sample. Because of the thickness of this sample, it has a higher surface area for the connection to the brass contacts. This could lead to a better connection and lower losses of field strength at the sample-brass connection.

Every GaAs epitaxy-layer is grown on a GaAs substrate. For every measurement the laser first passes the substrate and then the epitaxy-layer. This way the SHG is coupled out of the epitaxy-layer and does not interact with the substrate.

GaN samples

The GaN sample is a $4.5\,\mu$m thick layer of hetero-epitaxial (MOVPE) grown GaN on a sapphire substrate, which is investigated by SHG and THG spectroscopy and labeled "GaN BS2887".

The growth of GaN is not as well controlled as GaAs and reaching a high optical quality of samples is necessary for the observation of excitons. Several samples were available, but only BS2887 allowed the observation of excitons by THG spectroscopy. GaN BS2887 is grown on a sapphire substrate. Sapphire has a band gap of over $E_g > 8\,$eV [89], which is much higher than the band gap of GaN. The influence of the sapphire on optical harmonics generation should be minimal, because the wavelengths of the fundamental light and the harmonic light are both well within the transparency region of sapphire. However, sapphire has a direct influence on the band gap energy of GaN.

Growing GaN on sapphire usually results in a bigger band gap. The difference in the thermal expansion coefficient between GaN and sapphire leads to a compressed GaN lattice at the interface after the sample is cooled down to room temperature from the hot growth environment. This effect might be enhanced when the sample is further cooled down to cryogenic temperatures. The lattice structure relaxes to a strain free state away from the interface. Depending on the thickness of the GaN layer the properties are governed by the compressed interface region, or by the relaxed bulk contribution. The compression of the unit cell enhances the band gap in a semiconductor, as the electron shells of the ions are closer and experience a stronger repulsion. This was compared to samples, which exhibit tensile strain lowering the band gap [90], since they are grown on SiC, which leads to the opposite effect of a sapphire substrate. The binding energy of the excitons is not influenced by the compression, and therefore they shift along with the band gap. For comparison of the results from this thesis to other reports, it is necessary to consider the substrate and sample thickness.

Measurements revealed a very low damage threshold of the available GaN samples, including GaN BS2887. Typically any sample investigated is tested for its damage threshold by carefully increasing the fundamental light intensity until sample damage is suspected. This value is used as a threshold. For GaN BS2887 the maximum energy per pulse for THG has to be below $E_{\text{pulse}} < 200\,\mu$J. For SHG it is even lower than THG and can hardly

be picked up by the energy meter. Other investigated structures like Cu_2O $E_{pulse} \approx 1\,mJ$ and GaAs $E_{pulse} \geq 1\,mJ$ are much less sensitive to the light intensity. The low damage threshold of the GaN is probably due to the absorption of fundamental light from energy levels deep within the band gap. Since the fundamental wavelength for THG is higher than for SHG, it is absorbed by fewer energy levels.

Cu_2O

In Sec. 6 measurements on Cu_2O are presented. The investigated sample H28 was cut from a high quality natural crystal, which was found in the Tsumeb mine in Namibia. Several cube shaped samples were cut from the big crystal. The sample H28 showed the strongest SHG intensity and smallest linewidth. It is cut along the faces (111), $(1\bar{1}0)$, and $(11\bar{2})$ with a thickness of $5\,mm$ in each direction. Due to the high optical quality of the crystal it is possible to use laser pulses with an energy of about $1\,mJ$.

Si and SiC

In Sec. A measurements on Si and SiC are presented. The investigated Si sample is cut from a $500\,\mu m$ thick waver. The main crystal face is (111).

Two samples are investigated for SiC. Both are bulk samples with $500\,\mu m$ thickness. The sample SiC4H is grown in the 4H phase of SiC and the SiC6H sample is grown in the 6H phase. In both samples the c axis is perpendicular to the surface.
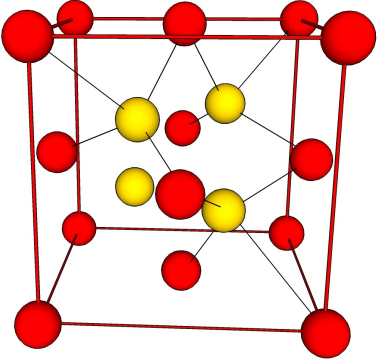
4. Gallium Arsenide (GaAs)

4.1. Introduction

GaAs is a direct band gap III-V semiconductor. It crystallizes in the cubic point group T_d ($\overline{4}3m$), which is zincblende structure [53]. The Gallium Ga^{+3} and Arsenide As^{-3} atoms are each located on a face-centered cubic (FCC) lattice. These lattices are shifted along the [111] axis, which is not a centrosymmetric structure and therefore ED SHG is allowed. Furthermore, basic parameters of GaAs are given in Table 4.1.

Table 4.1. – Basic parameters of GaAs and a sketch of the crystal lattice.

	GaAs
Symmetry	T_d ($4\overline{3}m$)
Crystal lattice	FCC
Centrosymmetric	No
Band gap ($T = 0\,\mathrm{K}$)	$1.519\,\mathrm{eV}$
Band gap ($T = 300\,\mathrm{K}$)	$1.424\,\mathrm{eV}$
Exciton binding energy	$4.2\,\mathrm{meV}$
Dielectric constant ϵ ($\omega = 0$)	12.9
Refractive index ($T = 5\,\mathrm{K}$)	$n(1.5\,\mathrm{eV}) \approx 3.66, \quad n(0.7\,\mathrm{eV}) \approx 3.38$
Samples	Homo-epitaxy layer (001) and (111)
Measurements	SHG, THG, TPA-PL, 3PA-PL, Reflection

GaAs is of high interest for fundamental physics and has important technological applications. A high electron mobility [91] makes it favorable in specialized high speed computation applications. An advantage for optical applications is the direct band gap. Typical applications in optical technology are LEDs, laser diodes, and photovoltaic technology.

The second order susceptibility $\chi^{(2)}$ of T_d has only one independent component and it is possible to choose experimental geometries in which SHG is either forbidden or allowed, which is an advantage for SHG spectroscopy. Although the system is spin compensated
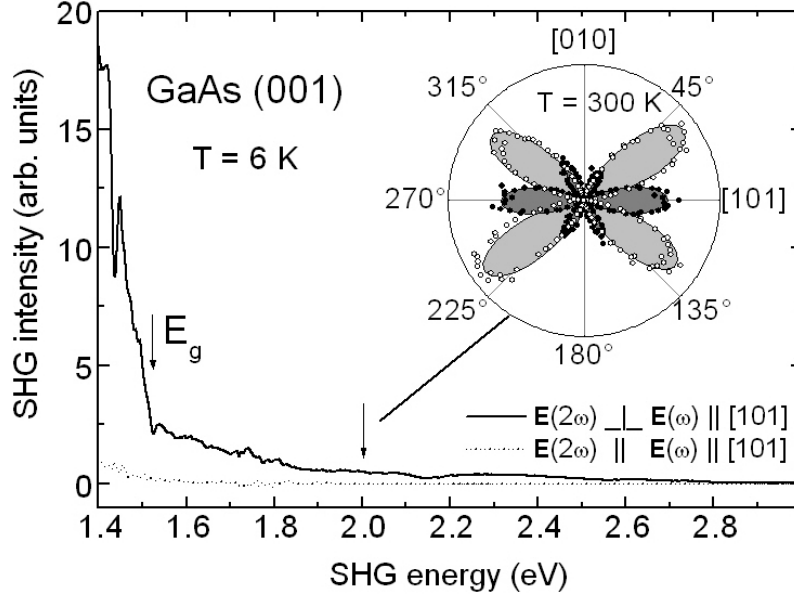
Figure 4.1. – SHG spectrum of GaAs for $\mathbf{k} \parallel [10\bar{1}]$ taken from [32]. The spectrum shows non-resonant SHG below and above the band gap. The inset shows the anisotropy, which is fitted by the ED susceptibility (shaded area).

and has diamagnetic properties, the application of an external magnetic field reveals a rich spectrum of magneto-excitons in SHG [32]. For GaAs there are reports about crystallographic SHG and MFISH [75], which are related to the presented measurements, and these are briefly summarized first.

In Fig. 4.1 SHG spectra at $T = 6\,\mathrm{K}$ from Sänger et al. [32] are presented. Non-resonant SHG was found over a broad range in a tilted geometry (black line). The SHG is most intense in the transparency region and is weaker above the band gap. This was attributed to the reabsorption of the SHG and a reduction of the coherence length, because the refractive index increases at the band gap. The anisotropy is modeled by the ED susceptibility $\chi_{\mathrm{ED}}^{(2)}$. For this susceptibility SHG is forbidden in the $\mathbf{k} \parallel [001]$ direction and it was used for MFISH spectroscopy, since non-resonant SHG is suppressed and does not interfere with the resonances.

In Fig. 4.2 the main result of the MFISH spectroscopy from [32] is presented. In the $\mathbf{k} \parallel [001]$ configuration the application of a magnetic field in Voigt direction revealed a complex spectrum with magneto-exciton resonances. In Fig. 4.2(a) the spectra up to $B^0 = 11\,\mathrm{T}$ are presented. Resonant SHG appears in a magnetic field close to the $1s$ exciton at $E_{1s} = 1.5152\,\mathrm{eV}$. For increasing field strength the intensity increases and the line is blue shifted. In addition to this resonance, further peaks appear in a regular distance. The anisotropies and increase of SHG intensity are described by $\chi^{(4)} E^\omega E^\omega k B^0$, which takes magneto-spatial dispersion into account. The microscopic mechanism for the increase of SHG intensity is unclear. In Fig. 4.2(b) the peak energies are plotted together with calculated Landau levels of the electronic bands. The blue shift of the resonances is in accordance with the calculated Landau bands. A group of resonances can be assigned
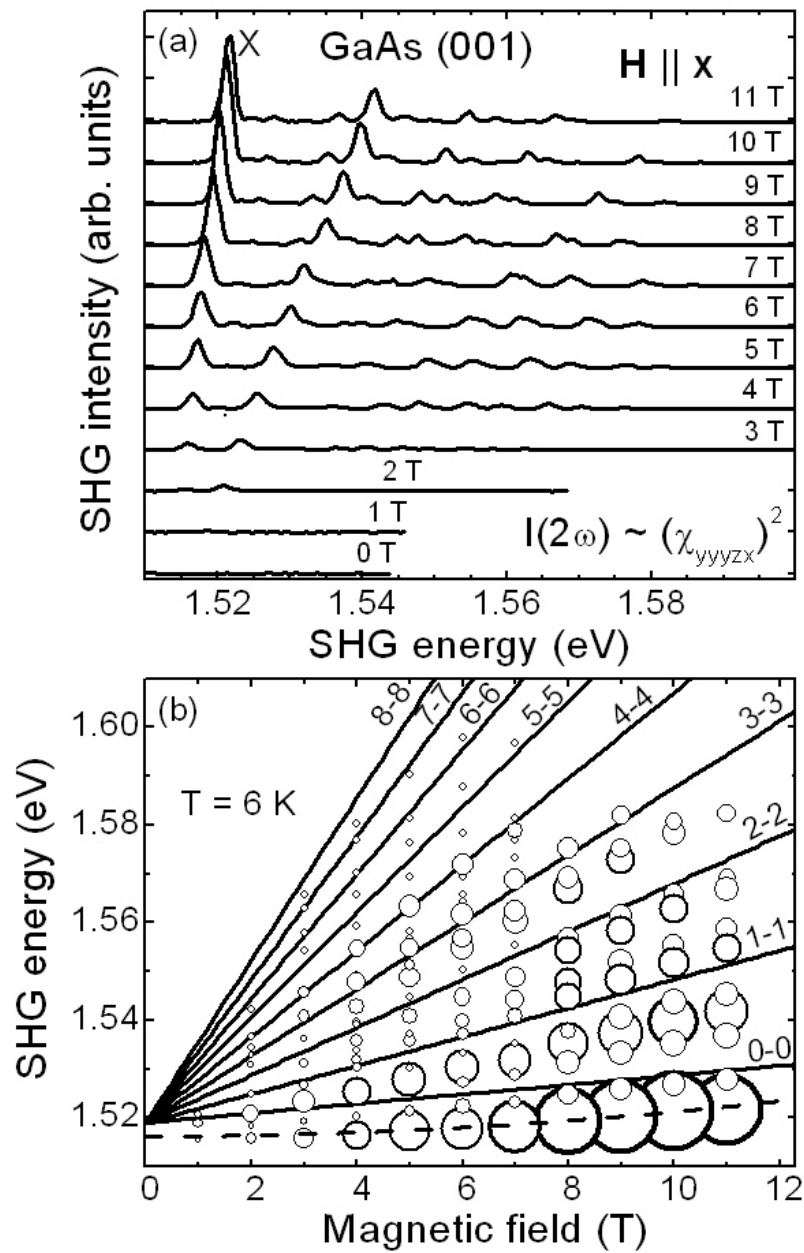
Figure 4.2. – (a) MFISH spectra for **k** ∥ (001) taken from [32]. In a magnetic field the 1*s* exciton (marked by X) and a series of magneto-exciton lead to enhanced SHG. (b) Calculated Landau level fan chart (black lines) and found resonances (dots: radius scaled to intensity).

to each Landau level. This is explained by an exciton series below each Landau level.

Further measurements are presented in the next sections based on these findings. The wavelength range of the laser system allows the measurement of SHG and THG on GaAs. First, SHG spectra without a perturbation are presented and compared to the exciting results. Then the influence of an electric field on SHG from exciton resonances is investigated. The application of an electric field is expected to give rise to exciton resonances in the SHG spectrum, because of the mixing of exciton states with opposite parity by the Stark effect. This is also applied to the magneto-exciton series, which are measured in crossed electric and magnetic fields.

For THG a wavelength of up to $\lambda \approx 2.5\,\mu$m is needed and such measurements have not been reported before. Without an external field the s excitons are expected to lead to resonant enhanced THG. This should not be increased by an external electric field, because the admixture of p excitons, which are forbidden for THG, is not beneficial for THG. Measurements in a magnetic field are also presented. For an external magnetic field it is unclear what to expect besides a shift of the resonance, since the microscopic mechanism for the enhanced SHG is unknown.

4.2. SHG: Enhanced resonant SHG by external fields

4.2.1. Crystallographic non-resonant SHG

At first, the spectral dependence of SHG efficiency in transmission geometry is investigated at low temperatures. Sample GaAs 239 was used for these measurements. Measurements of non-resonant SHG in GaAs at low temperatures are presented in Fig. 4.3. All measurements on GaAs were performed at $T = 5\,$K. In Fig. 4.3(a) measurements for a tilted sample $\theta = 45°$ about the y axis (black dots) and for $\mathbf{k} \parallel [001]$ are presented. Due to the high index of refraction $n = 3.38$ the internal angle is about $k \sphericalangle [001] \approx 13.6\,°$. The polarization is set to a parallel configuration $E^{2\omega} \parallel E^{\omega} \parallel [100]$, which is a maximum in the anisotropy as presented later in Fig. 4.4. In the tilted configuration non-resonant SHG over a broad spectral range is observed. The band gap $E_{\mathrm{g}}(5\,\mathrm{K}) = 1.519\,$eV [92] is marked by a red arrow. No pronounced exciton resonances are in the spectrum as shown in Fig. 4.3(c). Below the band gap the intensity of the SHG is oscillating. This oscillation is presented in Fig. 4.3(b). At the same tilting angle and polarization as 4.3(a) a spectrum with smaller wavelength steps is presented. The mean period of the oscillation is $\lambda_{osci} = 3.36\,$nm. They are attributed to interference from reflections in the sample, which is discussed in Sec. 4.2.4

Measurements for $\mathbf{k} \parallel [001]$ have the same polarization directions as the tilted geometry. In this direction no SHG is observed as expected from the ED susceptibility. Next, the anisotropy measurements are presented.
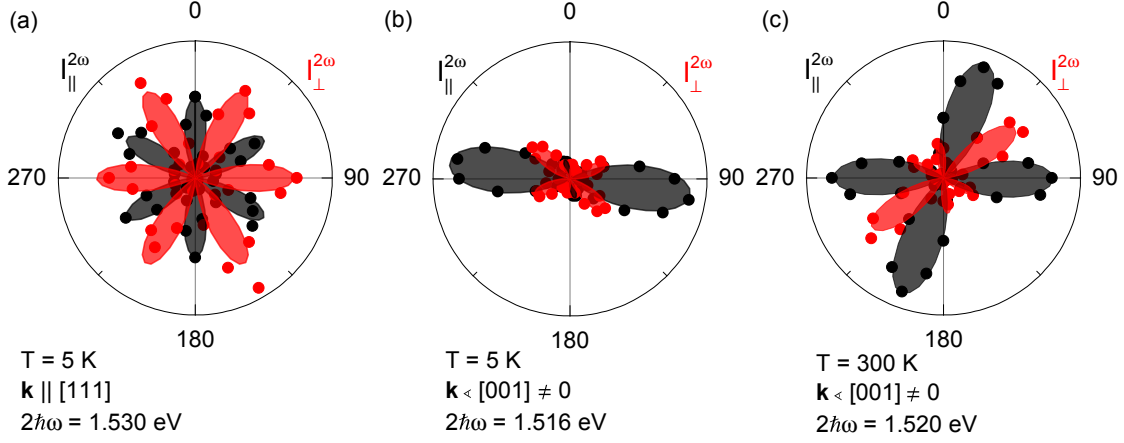
In Fig. 4.4 anisotropies for different parameters on different samples are shown. Each measurement was performed in the parallel $I_{\parallel}^{2\omega}$ (black dots) and crossed $I_{\perp}^{2\omega}$ (red dots) configuration. Model calculations of the anisotropies with the second order ED susceptibility $\chi_{\mathrm{ED}}^{(2)}$ of T_{d} are fitted to the data and are represented by shaded areas.
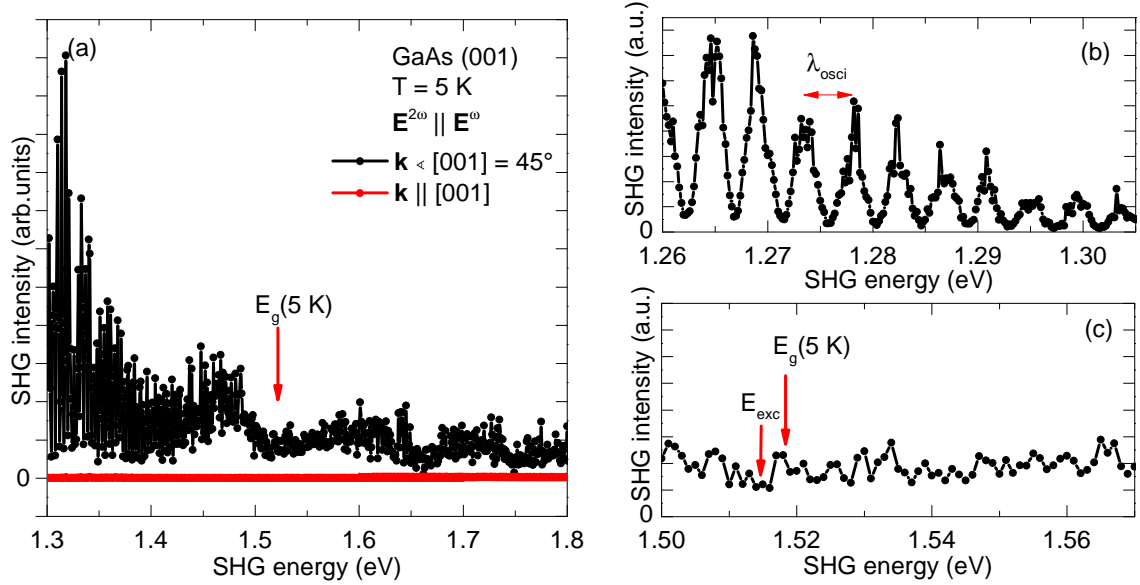
Figure 4.3. – (a) SHG spectrum of GaAs 239 for $\Theta \approx 45\,^\circ$ (black dots) over a broad spectral range from $1.3\,\mathrm{eV}$ up to $1.8\,\mathrm{eV}$ including the band gap $E_\mathrm{g}(5\,\mathrm{K}) = 1.519\,\mathrm{eV}$. The SHG intensity is maximal at small energies and decreases near the band gap. No SHG is detected in the $\mathbf{k} \parallel [001]$ geometry (red dots) as is expected from ED model calculations. (b) Spectrum in the transparency region for the same geometry as (a). The oscillation period is marked by λ_osci. (c) Magnified spectrum in the vicinity of the band gap. No resonant SHG is observed at the energy of the $1s$ exciton.

In Fig. 4.4 (a) measurements on sample PDI-M4_2601 are presented. On this sample the geometry $\mathbf{k} \parallel [111]$ is normal incidence of the laser light on the surface. The anisotropy was measured at $2\hbar\omega = 1.53\,\mathrm{eV}$ at $T = 5\,\mathrm{K}$, which is just above the band gap. The parallel anisotropy (black dots) has a six-fold shape with the first resonance at $0\,^\circ$. The crossed anisotropy (red dots) has the same shape, but is shifted by $30\,^\circ$. The six-fold shape and a shift between parallel and crossed configuration is predicted by the ED susceptibility model calculations. The model fit to the data results in calculated tilting angles of $\Theta \approx \theta \approx \gamma < 1\,^\circ$ between the optical axis and the [111] direction of the crystal, which is in good agreement with the experimental geometry. The crystal direction parallel to the laboratory y axis is $[1\bar{1}0]$ according to the fit, which is in agreement with the internal crystal axis.

In Fig. 4.4 (b) measurements on sample GaAs 239 at $T = 5\,\mathrm{K}$ and $2\hbar\omega = 1.516\,\mathrm{eV}$ are presented. The energy position is chosen, because the measurements in an electric field presented in Sec. 4.2.3 show an exciton resonance at this energy. The shape of the parallel configuration $I_\parallel^{2\omega}$ is mainly two-fold with a maximum at $95\,^\circ$. The crossed configuration is four-fold with $60\,^\circ$ and $120\,^\circ$ between the maximum intensities. The data is fitted by ED susceptibility model calculations. The resulting fitting angles are $\Theta \simeq -3.2\,^\circ$, $\beta \simeq 2.2\,^\circ$ and $\gamma \simeq 50.0\,^\circ$. This is in good agreement with the experimental geometry, which was

Figure 4.4. – Measured rotational anisotropies for different geometries and parameters. Shaded areas are fitted model calculations based on the ED susceptibility. (a) Measured on the (111) face of sample GaAs PDI-M4_2601 with **k** ∥ [111]. (b) Measured on the (001) face of sample GaAs 239 with a small tilting of **k** relative to the principle crystal axis. (c) Room temperature measurement of sample GaAs 239 for energies higher than the band gap.

adjusted close to **k** ∥ [001] direction.

In Fig. 4.4 (c) measurements on sample 239 at room temperature with an energy of $2\hbar\omega = 1.520\,\mathrm{eV}$ are presented. At room temperature the band gap of GaAs is $E(300\,\mathrm{K}) = 1.42\,\mathrm{eV}$ and the anisotropy is measured far above the band gap. In this case the parallel intensity has a four-fold shape. The crossed measurement shows a six-fold shape, with a global maximum at about $60\,^\circ$ and two local maximum intensities at $0\,^\circ$ and $120\,^\circ$. Fitting the ED susceptibility model to the data results in the angles $\Theta \simeq 11.2\,^\circ$, $\beta \simeq 0.5\,^\circ$, and $\gamma \simeq 34\,^\circ$.

All the anisotropies are in good agreement with the ED susceptibility model and independent from parameters as temperature or wavelength. For **k** ∥ [001] no signal was detected as it is expected from the model.

4.2.2. Electric-field-induced SHG

In this section the influence of an electric field on SHG in the spectral vicinity of exciton states is investigated. The application of an external electric field influences the electrons within the sample. Excitons are influenced more strongly than the band-band transitions, because of their low binding energy and dipole character. Therefore measurements in an external electric field were suspected to reveal resonant SHG from perturbation of excitons. This electric-field-induced SHG (EFISH) is a powerful tool to investigate excitons and their interaction in an electric field. The results from the last section are used to suppress non-resonant SHG by choosing the geometry **k** ∥ [001].

In Fig. 4.5(a,b) the results for EFISH spectroscopy in the **k** ∥ [001] configuration are presented. In the measurements with zero voltage (black dots) only a small background of
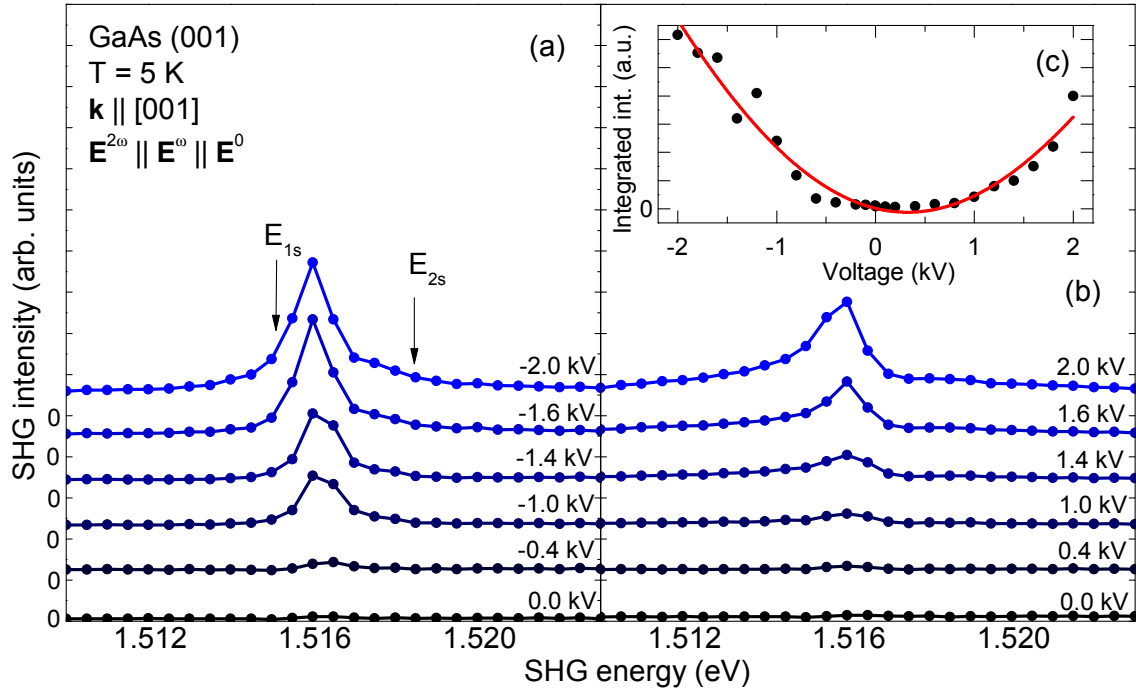
Figure 4.5. – (a,b) SHG spectra of sample GaAs 239 for voltages up to $E^0 = \pm 2\,\mathrm{kV}$ in $\mathbf{E}^{2\omega} \parallel \mathbf{E}^\omega \parallel \mathbf{E}^0 \parallel [010]$ and $\mathbf{k} \parallel [001]$ geometry for the exciton region. With increasing voltage a resonance in the spectrum appears and the maximum intensity of it increases. The energy of the $1s$ exciton E_{1s} and $2s$ exciton E_{2s} near the resonance are marked by arrows. (c) Integrated intensity of the spectra versus the applied voltage, fitted by a polynomial function of fourth order (red line)

SHG is present, which has about 1% intensity compared to the maximum induced SHG, as it is expected for this geometry from the results of the last Sec. 4.2.1. The polarization $\mathbf{E}^{2\omega} \parallel \mathbf{E}^\omega \parallel \mathbf{E}^0 \parallel [010]$ is expected to have the strongest EFISH intensity from calculations with $\chi^{(3)}$ in Sec. 2.3.3. Spectra with an external voltage have a resonance at $E = 1.516\,\mathrm{eV}$ with a FWHM of $\Delta_{\mathrm{FWHM}} \approx 1\,\mathrm{meV}$, which is close to the marked energy of the $1s$ exciton $E = 1.5152\,\mathrm{eV}$. The integrated intensity for each spectrum is presented in Fig. 4.5(c) (black dots). For both field directions the intensity increases and it fitted by a fourth-order polynomial $I(V) = A_0 + A_1 V + A_2 V^2 + A_3 V^3 + A_4 V^4$. The resulting coefficients are: $A_0 = 160$, $A_1 = 1050\,\mathrm{V}^{-1}$, $A_2 = 1\,\mathrm{V}^{-2}$, $A_3 = 7 \cdot 10^{-5}\,\mathrm{V}^{-3}$, and $A_4 = 7 \cdot 10^{-8}\,\mathrm{V}^{-4}$. In fact, the coefficients A_3 and A_4 are so small, that a quadratic function alone is a good fit. The sum of least squares is only 6% higher for a polynomial of second order compared to the polynomial of fourth order. The 30% difference between the integrated intensities at $V = \pm 2\,\mathrm{kV}$ and the offset of the minimum point of the fit function is not expected. The difference in maximum intensity (not integrated) between the $V = \pm 2\,\mathrm{kV}$ spectra is only 12%. The point group of GaAs is symmetric for [100] and [$\bar{1}$00]. Electric fields parallel to these directions should lead to the same action, except for a different phase of SHG light. The interference of the resonantly enhanced SHG with the underground is a

possible explanation for the asymmetry and is investigated in further measurements.
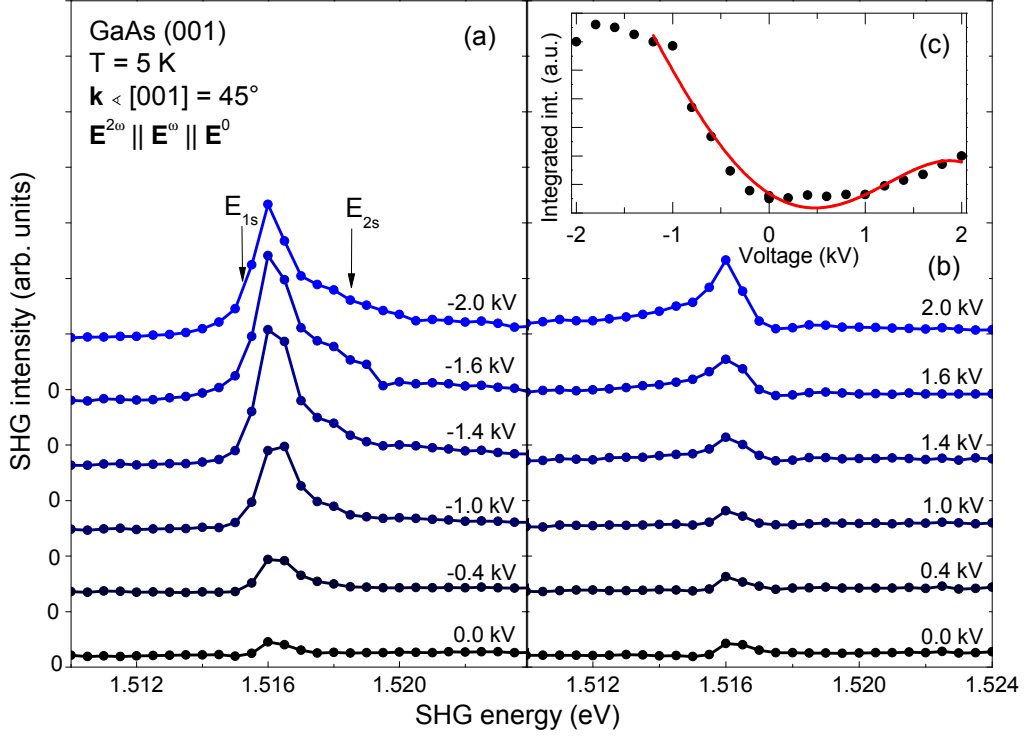
Figure 4.6. – (a,b) SHG spectra of sample GaAs 239 for voltages of up to $E^0 = \pm 2\,\mathrm{kV}$ in $\mathbf{E}^{2\omega} \parallel \mathbf{E}^{\omega} \parallel \mathbf{E}^0 \parallel [010]$ and $\mathbf{k}\angle[001] \approx 45\,^\circ$ geometry for the exciton region. With increasing voltage a resonance in the spectrum appears and its maximum intensity increases. The energy of the 1s exciton E_{1s} and 2s exciton E_{2s} near the resonance are marked by arrows. (c) Integrated intensity of the spectra versus the applied Voltage, fitted by a polynomial function of fourth order (red line).

In Fig. 4.6(a,b) the results for EFISH spectroscopy in a tilted sample geometry are presented. Every parameter is the same as in Fig. 4.5 except for the wave vector direction in the sample $\mathbf{k}\angle[001] \approx 45\,^\circ$. For zero voltage a much more intense SHG is found in contrast to Fig. 4.5. This is expected, because crystallographic SHG from χ^{cryst} is allowed in the tilted geometry. SHG spectra with an applied voltage show a resonance at $E = 1.516\,\mathrm{eV}$. The interference of the SHG background with the EFISH signal leads to a Fano shape of the resonance. For negative voltages presented in Fig. 4.6(b) the intensity on the low energy side of the resonance is higher than on the high energy side. It is the other way around for positive voltages as shown in Fig. 4.6(a). The integrated intensity of each spectrum is shown in inset (c). The fitting parameters for the fourth order polynomial (red line) are $A_0 = 3163$, $A_1 = -777\,\mathrm{V}^{-1}$, $A_2 = 1\,\mathrm{V}^{-2}$, $A_3 = -18 \cdot 10^{-5}\,\mathrm{V}^{-3}$, and $A_4 = -2 \cdot 10^{-8}\,\mathrm{V}^{-4}$. The difference in maximum intensity between $\pm 2\,\mathrm{kV}$ is 70%, which is more than for the $\mathbf{k} \parallel [001]$ measurements.

In Fig. 4.7 the results from rotational anisotropy measurements of the observed resonance in the EFISH spectrum are presented. In Fig. 4.7(b) measurements of the parallel
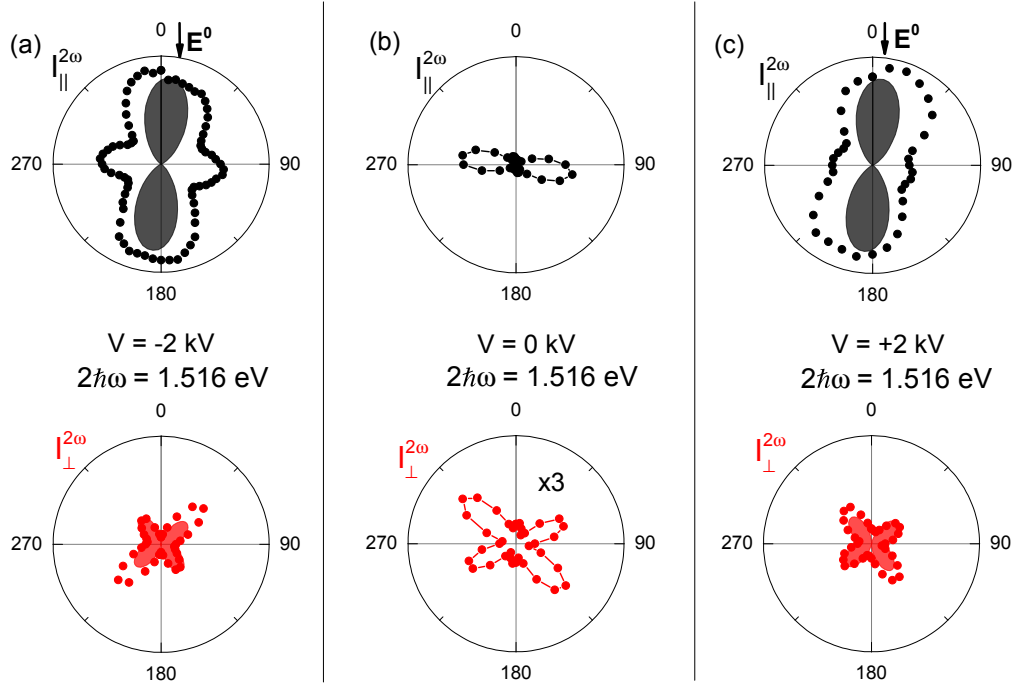
Figure 4.7. – SHG rotational anisotropies of sample GaAs 239 for **k** ∥ [001] at $2\hbar\omega = 1.516\,\text{eV}$ and $T = 5\,\text{K}$. (b) Zero field measurements. For this geometry the ED susceptibility predicts no intensity. Only by taking an angle between **k** and [001] from misalignment into account, the anisotropy observed can be modeled by χ^{cryst}. (a) Anisotropies for $V = -2\,\text{kV}$ in the $\mathbf{E}_0 \parallel$ [100] direction. In the parallel configuration (black dots) a strong increase of SHG at $\varphi \approx 0\,°$ is found. The crossed anisotropy has a four-fold shape, with a maximum intensity at $\varphi = 45\,°$ (c) $V = +2\,\text{kV}$ in the $\mathbf{E}_0 \parallel$ [100] direction. The parallel anisotropy is similar to (a). The crossed anisotropy is also four-fold, but has maximum intensity at $\varphi = 135\,°$. The shaded areas represent the ED $\chi^{(3)}$ model fitted to the data.

$I_\parallel^{(2\omega)}$ (black dots) and crossed $I_\parallel^{(2\omega)}$ (red dots) anisotropy are presented. The observed SHG is not expected for the geometry **k** ∥ [001], because SHG from χ^{cryst} is forbidden. Either it stems from strain, due to the sample holder, or misalignment gives rise to SHG from χ^{cryst}. In Fig. 4.7 (a) anisotropies at the energy of the resonance with an applied voltage of $+2\,\text{kV}$ are presented. The shaded areas are model calculations of $\chi_{\text{ED}}^{(3)}$ with $\mathbf{E}^0 \parallel$ [010]. An increase of intensity for $\mathbf{E}^{2\omega} \parallel \mathbf{E}^\omega \parallel$ [010] ($\varphi = 0\,°$ in $I_\parallel^{(2\omega)}$) is predicted by the model and observed in the measurements. The intensity in the [100] direction ($\varphi = 90\,°$ in $I_\parallel^{(2\omega)}$) is not predicted by the EFISH model. It has the same magnitude as the parallel anisotropy for zero voltage (b) in this direction and is not field induced. The crossed anisotropy (a) has a four-fold shape, which is predicted by the ED model. According to the model calculations all peaks have the same intensity. The measurements show an enhanced intensity at $\varphi = 45\,°$ compared to $\varphi = 135\,°$. This could stem from an interference with the zero field crossed contributions shown in (b). Again, the intensity in (c) is not predicted for $\varphi = 90\,°$ and might stem from misalignment. The crossed anisotropy for

voltage applied in the positive direction (c) has a higher intensity at $\varphi = 135°$ compared to $\varphi = 45°$, which is the other way around for negative voltages. This is a typical sign for an interference with crystallographic SHG.

## 4.2.3. SHG in crossed electric and magnetic fields
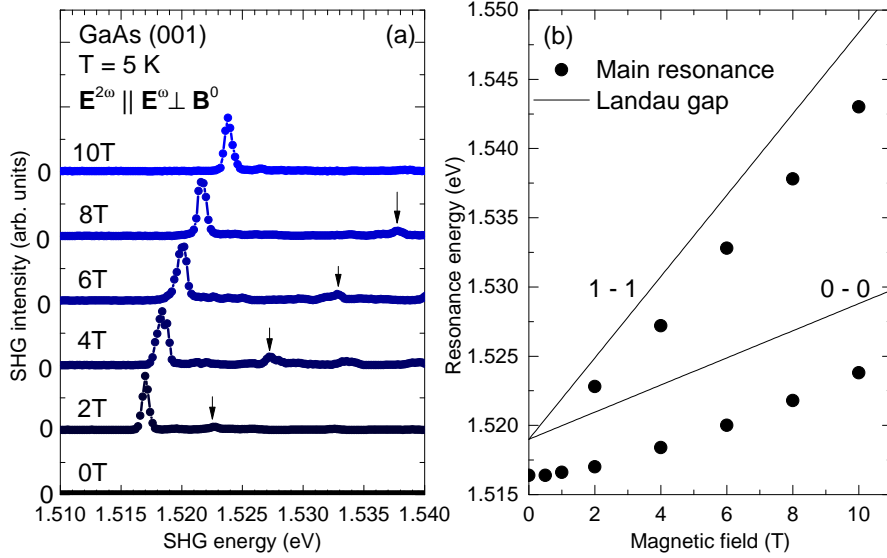
Figure 4.8. – (a) MFISH spectra of sample GaAs 239 in $\mathbf{k} \parallel [001]$ geometry normalized on maximum peak intensity. Additional maxima are marked by a black arrow. (b) The energy of the first two intense resonances (black dots) for different magnetic fields compared to the first two energy gaps of the Landau bands 0-0 and 1-1 (black lines).

In this section the influence of crossed electric and magnetic fields on SHG is investigated in a broad spectral range. The results for MFISH in GaAs are known, as it was shown in the introduction. The aim of the measurements in crossed fields is the investigation of the influence of an electric field on the complex magneto-exciton structure in MFISH spectra. In Fig. 4.8(a) MFISH spectra in Voigt geometry for sample GaAs 239 are presented. The spectrum is in good agreement with the reported results. The main difference to the reported spectra is that the first resonance is more intense compared to the smaller resonances. Since no absolute susceptibilities are calculated, it remains unclear if the first resonance is more intense or the other resonances are less intense than in the reported studies. In Fig. 4.8(b) the energy position of the peaks is compared to the Landau levels of the electron bands. Below each Landau level a strong resonance is present in the spectrum (black dots). The resonances have a distance of about $\Delta E \approx 4\,\text{meV}$ to the direct transition between the Landau levels (black lines), which is close to the binding energy of the excitons $R_{\text{exc}} = 4.2\,\text{meV}$. The value close to zero magnetic field is taken from a spectrum at $B^0 = 0.2\,\text{T}$. The energy of this resonance $E(0.2\,\text{T}) = 1.516\,\text{eV}$ is the same as the energy of the EFISH resonance. Besides the strong resonances, further features

are found in the spectrum when it is magnified. A resonance shape can be recognized for some features, but they are too small for clear assignments. In the previous studies these are assigned to excited states $n \geq 2$ of the excitons of each Landau level.

For sample GaAs 239 the additional application of an electric field did not influence the spectrum. Only on the GaAs substrate S01 were the measurements successful in crossed fields as discussed in Sec. 3.3.
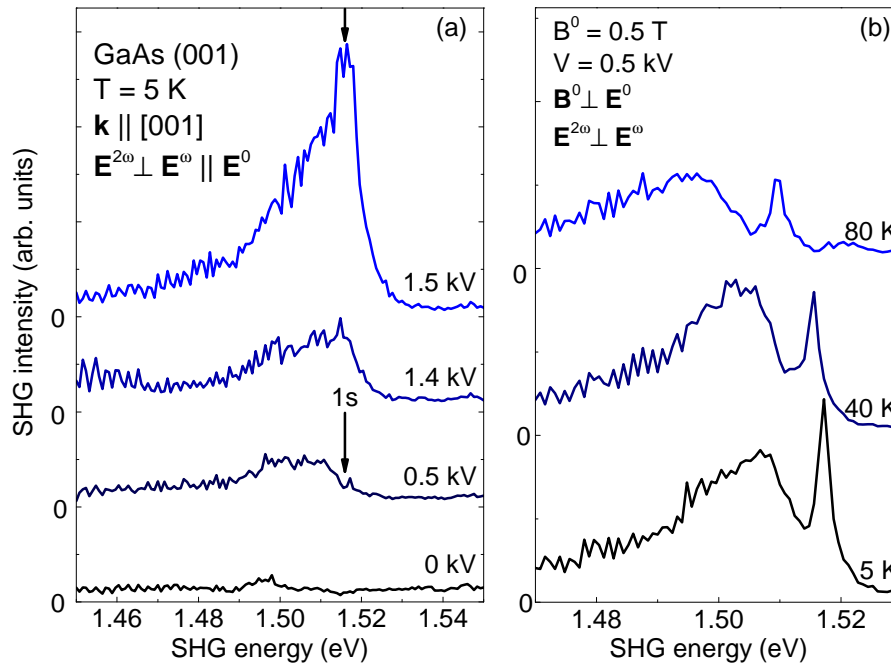
Figure 4.9. – (a) EFISH spectra of GaAs S01 for different values of externally applied voltage in the $\mathbf{E}^0 \parallel (100)$ direction. The $1s$ exciton energy $E_{1s} = 1.5152\,\mathrm{eV}$ is marked by a black arrow. (b) Temperature dependence of SHG spectra for crossed electric and magnetic fields in the $\mathbf{B}^0 \perp \mathbf{E}^0$ configuration.

First, the EFISH spectra are shown, because they are different than in the high quality GaAs 239 epitaxy layer. In Fig. 4.9(a) EFISH spectra for the GaAs substrate sample S01 are presented. A resonance close to the $1s$ exciton is in the spectrum for $V = 1.5\,\mathrm{kV}$. In contrast to the epitaxy layer samples, the resonance is accompanied by a broad tail on the low energy side, which stretches down to $E = 1.48\,\mathrm{eV}$ below the energy of the bound exciton states at $E = 1.489\,\mathrm{eV}$. There is no shift of the resonance in an electric field, which is the same as the EFISH measurements on the epitaxy layer samples. For small voltages the resonance is less intense. At $V = 0.5\,\mathrm{kV}$ mostly a broad feature around $E = 1.5\,\mathrm{eV}$ is left and the resonance is much less intense . In Fig. 4.9(b) spectra for crossed fields are presented. At $T = 5\,\mathrm{K}$, $B^0 = 0.5\,\mathrm{T}$, and $V = 0.5\,\mathrm{kV}$ (black line) both the broad electric field feature and an additional magnetic field induced resonance is observed. The MFISH resonance has a FWHM of $\Delta_{\mathrm{FWHM}} \approx 3\,\mathrm{meV}$. Both resonances can be observed up to $T = 80\,\mathrm{K}$. Above the $1s$ resonance further resonances from the Landau levels are found. The influence of an electric field on these resonances is presented next.
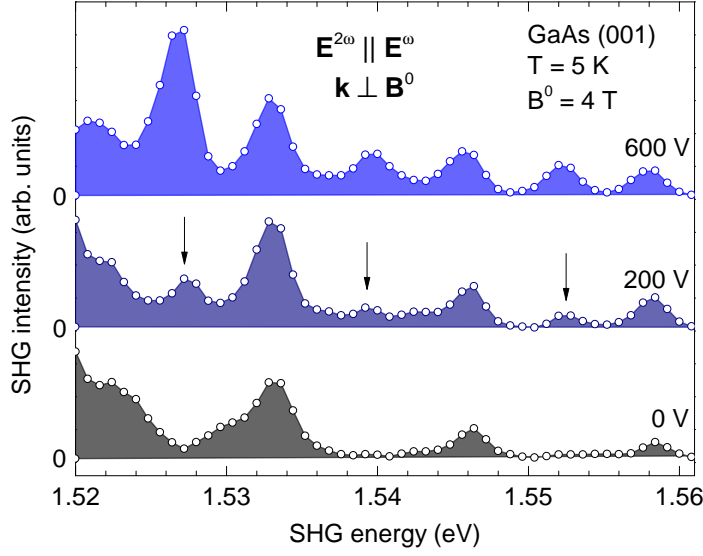
Figure 4.10. – Spectra of GaAs S01 in a magnetic field of $B^0 = 4\,\mathrm{T}$ with different additional electric fields $\mathbf{E}^0 \perp \mathbf{B}^0$. The polarization of $\mathbf{E}^{2\omega} \parallel \mathbf{E}^\omega \measuredangle (100) = 40\,^\circ$ is chosen, because in this configuration maximum intensity is found in the anisotropies presented later. The application of an electric field leads to a strong increase of additional resonances in between those which are present without the additional electric field.

In Fig. 4.10 measurements in crossed external fields are presented. The presented spectra start at $2\hbar\omega = 1.52\,\mathrm{eV}$, so that the resonances beyond the $1s$ exciton are visible. The measurement with only a Voigt magnetic field of $B^0 = 4\,\mathrm{T}$ (black line) has magneto-exciton resonances at $1.533\,\mathrm{eV}$, $1.546\,\mathrm{eV}$, and $1.559\,\mathrm{eV}$. The distance between the resonances $\Delta_{2\hbar\omega} = 13\,\mathrm{meV}$ is about twice the distance of $\Delta_L \approx 7\,\mathrm{meV}$ in between the Landau levels at $B^0 = 4\,\mathrm{T}$. With an additional electric field in the $\mathbf{E}^0 \perp \mathbf{B}^0 \wedge \mathbf{E}^0 \perp \mathbf{k}^0$ configuration additional resonances at $1.527\,\mathrm{eV}$, $1.540\,\mathrm{eV}$, and $1.554\,\mathrm{eV}$ occure in the spectrum (blue line). In this case a resonance for each expected Landau level is in the spectrum.

In Fig. 4.11 anisotropies for the resonances at $2\hbar\omega = 1.533\,\mathrm{eV}$ and $2\hbar\omega = 1.540\,\mathrm{eV}$ are compared with (blue dots) and without ($I^{2\omega}_{\parallel}$:black dots, $I^{2\omega}_{\perp}$:red dots) the additional electric field. Both resonances are present in the spectra in Fig. 4.10, which was measured with parallel light polarization at $\varphi = 40\,^\circ$ where both MFISH anisotropies have maximum intensity. The parallel anisotropies $I^{2\omega}_{\parallel}$ without the electric field have a four-fold shape with maximums at $\varphi = 40\,^\circ$ and $\varphi = 140\,^\circ$. Besides the intensity there is also a difference in the shape between the two resonances. The resonance (b) has a minimum at $\varphi = 90\,^\circ$, whereas the resonance (a) has a shoulder (or small maximum) at this angle. The additional electric field increases the two maxima of (b), whereas the intensity of the parallel anisotropy (a) is only enhanced at $\varphi = 90\,^\circ$. This is why it does not increase in the spectra in Fig. 4.10,
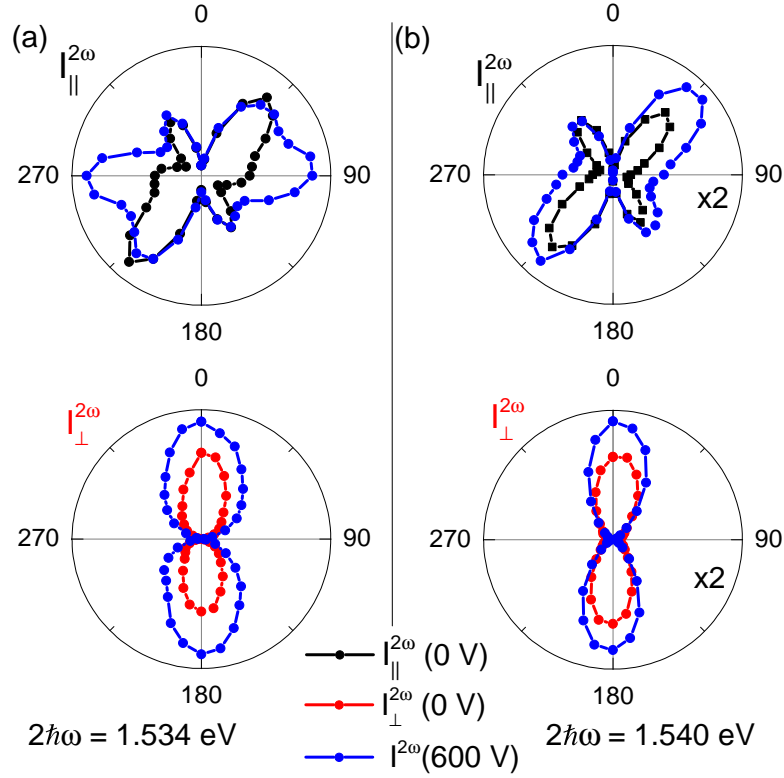
Figure 4.11. – Parallel $I_{\parallel}^{2\omega}$ (black dots) and crossed $I_{\perp}^{2\omega}$ (red dots) anisotropies of GaAs S01 in a Voigt magnetic field and also each anisotropy in crossed $\mathbf{E}^0 \perp \mathbf{B}^0 \perp \mathbf{k}$ fields (blue dots). (a) The parallel anisotropy at $2\hbar\omega = 1.533\,\mathrm{eV}$ has mainly a four-fold shape with a small shoulder at $\varphi = 90\,^\circ$. An additional voltage $V = 600\,\mathrm{V}$ leads to an enhancement of SHG at $\varphi = 90\,^\circ$. (b) The parallel anisotropy at $2\hbar\omega = 1.546\,\mathrm{eV}$ has a similar four-fold shape, but has no shoulder at $\varphi = 90\,^\circ$. An additional voltage leads to increased intensity at $\varphi = 40\,^\circ$ and $\varphi = 140\,^\circ$. Both crossed anisotropies have a two-fold shape, which is enhanced by the additional voltage.

because they were measured at $\varphi = 40\,^\circ$. Both crossed anisotropies are two-fold and an additional electric field only enhances the intensity. A small difference between the two is, that the anisotropy (b) only increases at $\varphi = 0\,^\circ$, whereas (a) also grows at $\varphi = 45\,^\circ$ and $\varphi = 135\,^\circ$.

The anisotropies have to be modeled with an axial susceptibility of at least fifth order

$$I^{2\omega} \propto \left(P_i^{2\omega}\right)^2 \propto \left(\chi_{ijklmn}^{(5)} E_j^\omega E_k^\omega k_l B_m^0 E_n^0\right)^2, \tag{4.1}$$

because it was reported before that the MFISH resonances have to be described by a fourth order susceptibility [32], which includes the $\mathbf{k}$ dependence from the magneto-spatial dispersion. The relative magnitude of the tensor components changes for different wavelength, since the anisotropies in Fig. 4.11 are different. This is not surprising, as it was found

before that the anisotropy of MFISH alone depends on the wavelength [75], which was attributed to magneto-spatial dispersion. It is interesting that the electric field has an influence in the [100] ($\varphi = 90°$) direction, because this was not found in the EFISH measurements in Sec. 4.2.2. The main influence of the electric field on the SHG intensity is expected along its own direction [010]. The interaction of the magneto-excitons formed from Landau levels has to be more complex than the mixing in the EFISH measurements.

There are too many non-zero tensor components of $\chi^{(5)}_{ijklmn}$ for a model fit without more detailed information about the responsible microscopic mechanism as explained in Sec. 2.3.

4.2.4. Discussion

Crystallographic SHG

The measurements of crystallographic SHG are in good agreement with the previous results from Sänger et al. [32], which are discussed in Sec. 4.2. The main features are verified by the presented measurements in this thesis. The polarization selection rules are determined by the ED $\chi^{(2)}$ susceptibility. For a tilted GaAs sample there is strong non-resonant SHG in the transparency region. The oscillations of intensity in Fig. 4.3 have not been observed before. They are attributed to reflections within the sample in these measurements, which lead to interference effects. The spectral width of the oscillations are $\lambda_{osci} = 3.36$ nm, which is close to the expected value of $\lambda^{\text{theory}}_{\text{osci}} \approx 1.4$ nm. The expected value is calculated by a Fabry-Perot model presented in Sec. 2.3.1. The parameters for the Fabry-Perot model are $\Theta_{\text{FP}} \approx 13.6°$ (including diffraction at the sample surface), $l \approx 400\,\mu$m (sample and substrate width), and $n(2000\,\text{nm}) = 3.36$ (at the fundamental wavelength for SHG). The decrease in intensity at the band gap is similar to the existing results, and is attributed to reabsorption of SHG and decrease of coherence length near the band gap [75], which is explained in Sec. 2.3.1. No exciton resonance is found for normal and tilted incidence in the SHG spectrum, which is expected from the selection rules, since the two-photon transition part of SHG is forbidden for the s excitons and the one-photon transition part is forbidden for p excitons.

EFISH

Spectra with an external voltage presented in Fig. 4.5 lead to a resonance in the spectrum, which is attributed to the $1s$ exciton. The resonance appears within 1 meV of the energy of the undisturbed $1s$ exciton and the intensity grows quadratically. As presented in Sec. 2.2.4 the $1s$ intensity should grow quadratically and the energy should not change. This behavior is measured for the observed resonance. The offset of 1 meV to the $1s$ exciton was also observed by Sänger et al. [75], by the extrapolation of MFISH data to the zero field energy of the $1s$ state. It could stem from polariton effects, as the $1s$ state couples to the light in the ED approximation.

The observed difference between positive and negative field strength probably stems from the interference with crystallographic SHG. This is verified by measurements for a tilted geometry presented in Fig. 4.6 in which the difference in intensity for positive

and negative field directions is enhanced, because of the stronger crystallographic SHG. The anisotropies for the EFISH measurements revealed crystallographic SHG even in the normal incidence configuration. This could stem from a small misalignment or strain from the electrodes of the electric field sample holder. The main intensity of the crystallographic SHG is perpendicular to the direction of EFISH. The alignment of the sample geometry was focused on the suppression of crystallographic SHG in the direction of EFISH for the measurements. This could explain a misalignment in the direction perpendicular to it, which would also lead to a small crystallographic SHG contribution in the EFISH direction.

The mixing of states by the Stark effect predicts SHG for all $1s$,$2s$,$2p$, ... exciton states. These are not observed in the measurements. The $2s$ and $2p$ excitons should show a saturation of intensity near $V \approx 1.5\,\mathrm{kV}$ and a shift of about $\Delta E \approx 0.5\,\mathrm{eV}$. Both are not observed for the EFISH resonance and these states are ruled out. As already mentioned in Sec. 2.2.4, this is probably due to the small binding energy $R_{\mathrm{exc}} = 4.2\,\mathrm{meV}$ of the excitons. The states above the $1s$ exciton are within $\frac{R_{\mathrm{exc}}}{2^2} \approx 1\,\mathrm{meV}$ band gap and are easily ionized (complete separation of electron and hole) by the electric field, which explains the lack of the according resonances in the spectrum. In fact, the $2s$ and higher exciton states are very sensitive to sample quality and can only be observed in very high quality samples. The next section about THG will show, that the $2s$ exciton is not observed, even without external perturbation, although it is allowed by selection rules. In white light reflection measurements presented in Sec. 4.4.2 also only the $1s$ state is observed.

MFISH

The results in Sec. 4.2.3 are in good agreement with reported results. The energy of the first resonance in the MFISH spectrum presented in Fig. 4.8 extrapolated to zero external field is $2\hbar\omega \approx 1.516\,\mathrm{eV}$. This is the same energy as the EFISH resonance and therefore the first resonance is assigned to the $1s$ exciton as it was done in the reported studies [75]. The microscopic mechanism for the increase is still unclear and has not been discussed before.

There are two possible mechanisms, which not only explain the observed MFISH resonances, but are also in agreement with the THG, TPA-PL, and 3PA-PL measurements presented in this thesis. The first one is an admixture of excitons in the magnetic field. In order to fulfill the ED SHG selection rules the odd parity $1s$ exciton has to be mixed with an even parity p exciton. The fulfillment of the SHG selection rules by the admixture of two different exciton states, which are each forbidden in ED SHG, is discussed in Sec. 2.3.1. However, a magnetic field has even parity and should only mix states of the same parity. The admixture of the $1s$ and $2p$ states could be due to the Magneto-Stark effect, which is introduced in Sec. 2.2.4. The Magneto-Stark effect describes that the magnetic field acts like an electric field on excitons in certain cases. This effective electric field would then mix the $1s$ and $2p$ exciton, just as in the presented EFISH measurements. It was shown, that it leads to enhanced SHG in ZnO [31]. However, this mechanism is ruled out by THG measurements presented in the next section.

The influence of a magnetic field on the polariton dispersion is another possible mechanism. Through the change of the polariton dispersion, the phase-matching conditions for

SHG and THG can be improved. This would lead to the observed increase of intensity and is in line with all the measurements. Measurements of the polariton dispersion are necessary in order to further verify this mechanism.

Crossed electric and magnetic fields

The analysis of the spectra in crossed fields is limited by the fact that only the GaAs substrate S01 with lower optical quality could be used. In the epitaxial layer sample GaAs 239 the influence of an additional electric field, in addition to the magnetic field, is too small to be detected by the experiment. In the bulk sample S01 the Landau level resonances are less intense and broader than in the high quality samples.

Adding an electric field along the y axis perpendicular to a Voigt magnetic field leads to a different influence on each resonance as presented in Fig. 4.10. Some resonances are influenced more than others. This is surprising, since it was expected that the magneto-excitons for each Landau level have similar properties.

In contrast to EFISH, the increase of SHG intensity is not for a parallel light polarization to the external field $\mathbf{E}^\omega \parallel \mathbf{E}^0$, but perpendicular to it $\mathbf{E}^\omega \perp \mathbf{E}^0$. This is a clear sign that in crossed fields not only both fields lead to their own separable effects, but interact in a more complex way.

The analysis of the microscopic mechanism is limited by the understanding of the MFISH resonances. Once a microscopic model of the MFISH mechanism is available it is possible to understand the influence of an additional electric field on the resonances.

4.3. THG: Influence of external fields on resonant THG

In this section the spectral dependence of THG in transmission geometry is investigated. All presented THG measurements are made with the sample GaAs 239. In contrast to SHG, there is no existing data on THG spectroscopy of the excitons in GaAs. In Sec. 2.3.4 the third order susceptibility of T_d is presented and the resulting rotational anisotropies are shown in Fig. 2.12(c,d). Since a three-photon transition has the same parity as a one-photon transition, it is expected to observe the $1s$ exciton even without an external perturbation by an electric or magnetic field. The question is if broad non-resonant ED THG can be observed (similar to SHG in tilted geometry), since ED THG $\chi_\mathrm{ED}^{(3)}$ is allowed even for $\mathbf{k} \parallel [001]$ in contrast to SHG. The influence of magnetic and electric fields on the THG efficiency in the vicinity of excitons is also presented and compared to the results of SHG spectroscopy.

For SHG it was found that the mixing of excitons with different envelopes by the Stark effect leads to EFISH. The situation is different for THG. The mixing of the allowed $1s$ exciton resonances with the forbidden $2p$ excitons should not lead to enhanced THG. Measurements of the THG spectrum in an external magnetic field will be compared to the complex magneto-exciton series found in the MFISH spectra.

4.3.1. Resonant THG on excitons
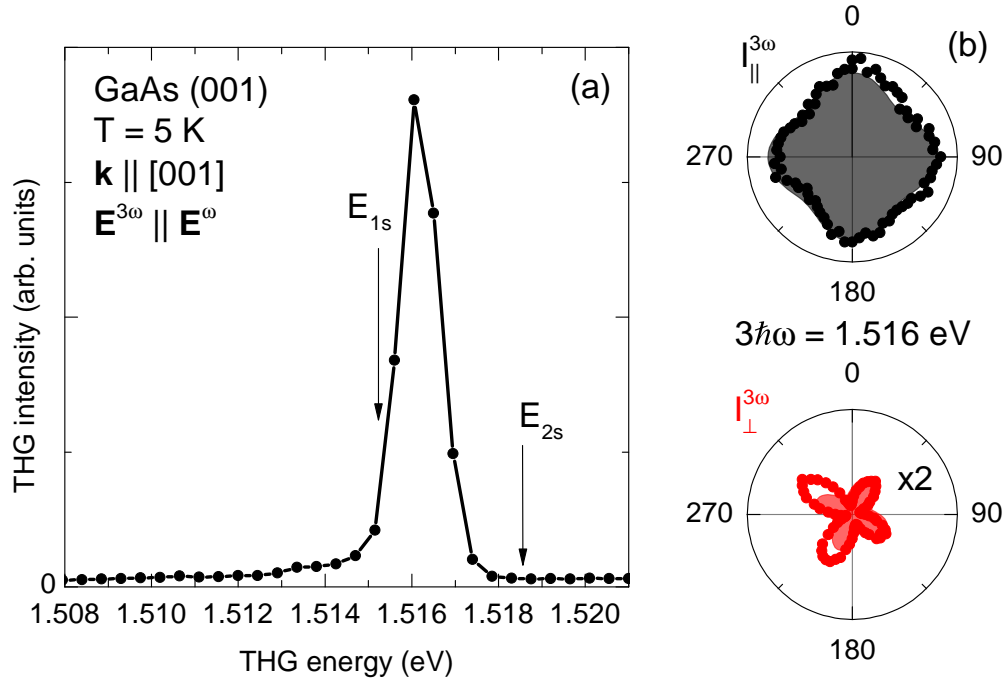
Figure 4.12. – (a) THG spectrum of sample GaAs 239 near the band gap for $\mathbf{k} \parallel [001]$. A resonance is near the $1s$ exciton and the crystallographic THG is less than 1% of the peak intensity. (b) Anisotropies at $3\hbar\omega = 1.516\,\text{eV}$. They are fitted by a $\chi^{(3)}$ model.

In Fig. 4.12(a) the THG spectrum for $\mathbf{k} \parallel [001]$ and $\mathbf{E}^{3\omega} \parallel \mathbf{E}^{\omega}$ is presented. There is a peak in the spectrum at $3\hbar\omega = 1.5162\,\text{eV}$ with a FWHM of about $\Delta_{\text{FWHM}} = 1\,\text{meV}$ in the vicinity of the band gap. Only about 1% of the peak intensity is non-resonant THG. The parallel anisotropy shown in inset (a) has the expected round shape of $\chi^{(3)}$ calculations. The crossed anisotropy has a four-fold shape, but the intensity is very small. It cannot be modeled by $\chi^{(3)}$ alone, because an eight-fold shape is predicted. The four-fold shape is found only for a tilting of at least $\Theta \geq 20°$ or for taking a background intensity into account, which is about 1% of the parallel intensity. It is improbable that the tilting angle is solely responsible, because the sample was aligned for normal incidence. The background intensity could stem from higher order processes, or a small admixture of parallel intensity to the crossed one in the detection.

For the specific ratio $\frac{\chi_{xxxx}}{\chi_{xyyx}} = 3$ of $\chi^{(3)}$ tensor components the parallel anisotropy is constant and the crossed anisotropy is zero as shown in Fig. 2.12. The model fit to the parallel data results in a ratio of $\frac{\chi_{xxxx}}{\chi_{xyyx}} \approx 1.4$. In case a small misalignment is taken into account the ratio changes by a small amount.

The resonance of the $1s$ exciton is expected from the selection rules. Both one- and three-photon transitions have odd parity and are allowed for the $1s$ exciton state. Resonances for $n \geq 2$ are not observed in the spectrum, although every odd parity state is allowed by

the selection rules.

The absence of non-resonant THG is an advantage for the observation of the exciton resonances in contrast to SHG. There are no theoretical studies about non-resonant THG in this energy region of GaAs, but THG has different selection rules than SHG, which can explain the big difference between the two.

4.3.2. Suppression of THG from excitons in an electric field
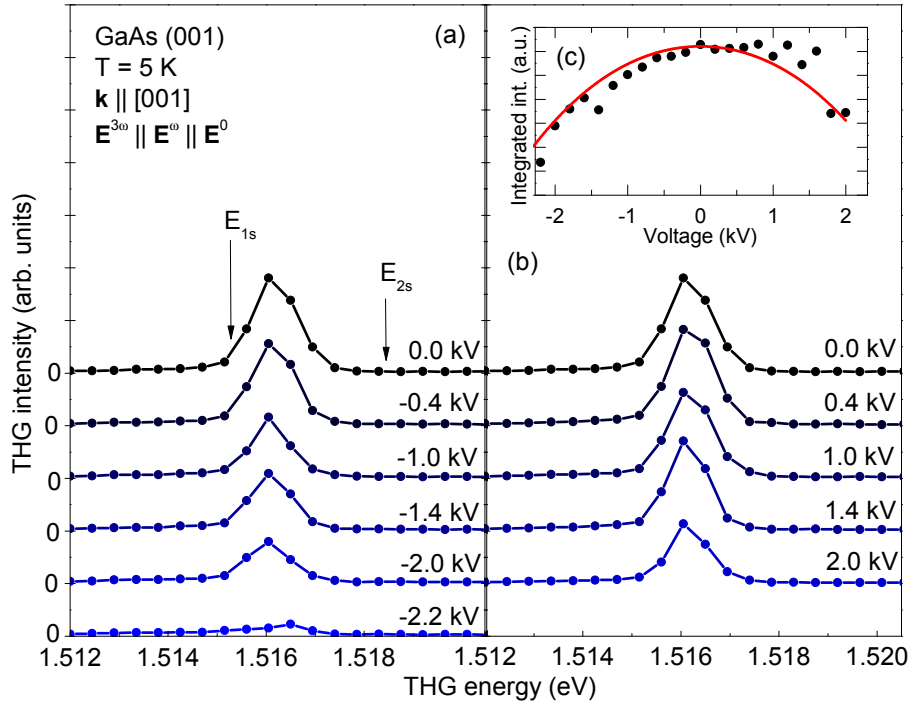
Figure 4.13. – (a,b) Electric field dependent THG spectra of sample GaAs 239 for $\mathbf{E}^{3\omega} \parallel \mathbf{E}^{\omega} \parallel \mathbf{E}^{0}$ and $\mathbf{k} \parallel [001]$. The electric field is applied in the [010] direction. No shift of the resonance is observed, but the maximum intensity decreases in an external electric field. (c) Integrated intensity of the THG spectra versus the applied voltage fitted by a fourth order polynomial.

In Fig. 4.13(a,b) THG spectra for different applied voltages are presented, including a spectrum for zero voltage. The experimental geometry $\mathbf{k} \parallel [001]$ and $\mathbf{E}^{3\omega} \parallel \mathbf{E}^{\omega} \parallel \mathbf{E}^{0} \parallel [010]$ is the same as for the EFISH measurements.

The external voltage leads to a suppression of the THG resonance. At $V = -2.2\,\text{kV}$ the integrated intensity of the THG spectrum is 22% of the spectrum for zero voltage. The integrated intensity for each spectrum is presented in Fig. 4.13 (c). It is fitted by a fourth order polynomial function with the resulting values: $A_0 = 9.94$, $A_1 = 1.25\,\text{V}^{-1}$, $A_2 = -1\,\text{V}^{-2}$, $A_3 = -0.024\,\text{V}^{-3}$, and $A_4 = -0.06\,\text{V}^{-4}$.

In Fig. 4.14 anisotropies of the THG resonance at $1.5162\,\text{eV}$ are presented for $V = \pm 2\,\text{kV}$. The anisotropies with an external voltage applied to the sample have the same
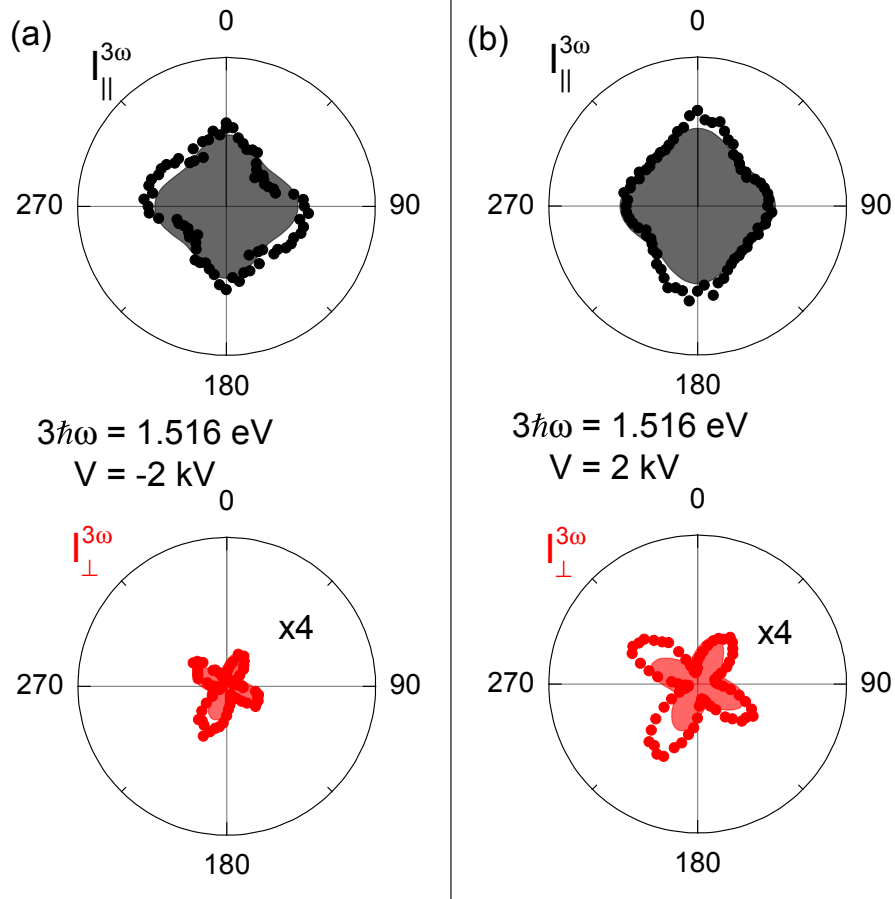
Figure 4.14. – THG Anisotropies of sample GaAs 239 for $\mathbf{k} \parallel [001]$ at the resonance $3\hbar\omega = 1.5162\,\text{eV}$. (a) anisotropies for $V = -2\,\text{kV}$ in the $\mathbf{E}^0 \parallel [100]$ direction. (b) $V = +2\,\text{kV}$ in the $\mathbf{E}^0 \parallel [100]$ direction. All anisotropies have the same shape with and without electric field. Shaded areas are fits with $\chi(3)$.

shape as the $V = 0\,\text{kV}$ anisotropies presented in Fig. 4.13, only the intensity for $I_{\parallel}^{(3\omega)}$ and $I_{\perp}^{(3\omega)}$ is reduced. They are also modeled with the $\chi_{\text{ED}}^{(3)}$ susceptibility.

4.3.3. Magnetic-field-induced THG on excitons

In this section the influence of a magnetic field on THG in the exciton region is investigated. In Fig. 4.15(a,b) THG spectra for magnetic fields applied in the Voigt configuration are presented. The light polarization is chosen, because the main action of the magnetic field on THG is in the polarization direction $\mathbf{E}^{3\omega} \parallel \mathbf{E}^\omega \perp \mathbf{B}^0 \parallel [010]$ as will be shown by the anisotropy in Fig. 4.18. The magnetic field shifts the observed resonance to a higher energy of up to $3\hbar\omega = 1.5232\,\text{eV}$ for $B^0 = \pm 10\,\text{T}$ and the integrated intensity grows up to a factor of 175 for $B^0 = \pm 10\,\text{T}$, compared to the zero field integrated intensity. The energy shift and increase of intensity are presented in Fig. 4.17. Also, the shape of the resonance is changed in the magnetic field. The resonance without a magnetic field has a Gaussian
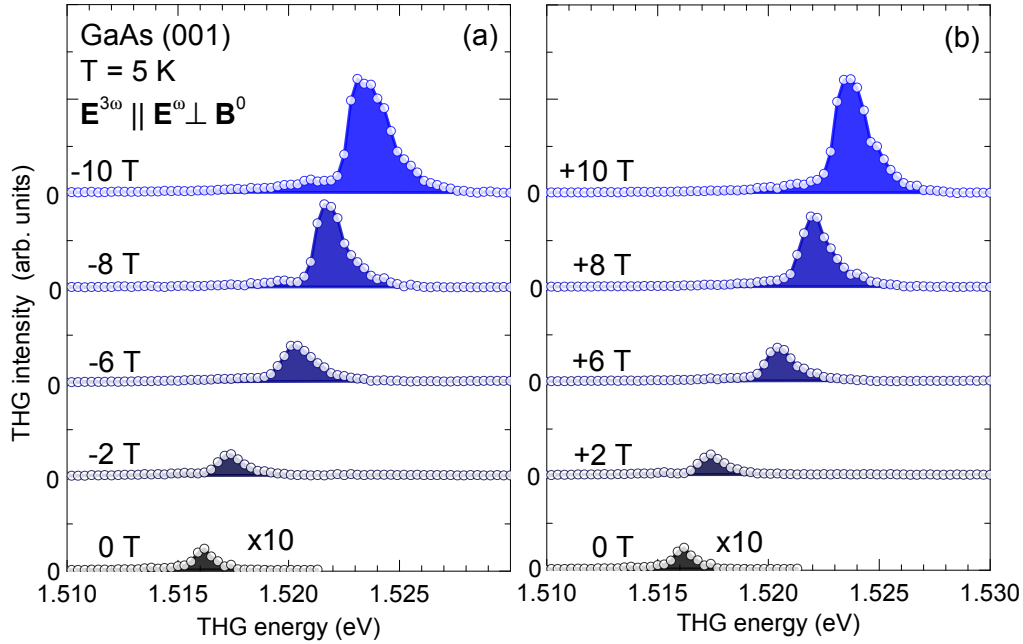
Figure 4.15. – Magnetic field dependence of the THG spectrum of sample GaAs 239 near the band gap for $\mathbf{k} \parallel [001]$. (a) Negative magnetic field strength up to $B^0 = -10\,\text{T}$. (b) Positive magnetic field strength up to $B^0 = +10\,\text{T}$. In both cases the line shifts to higher energies and the intensity increases.

shape as shown in Sec. 4.3.1. For $B^0 = \pm 10\,\text{T}$ the shape of the resonance is not Gaussian anymore. There are additional small features on the high and low energy side of the peak. The MFISH spectrum has shown many resonances from magneto-excitons. In Fig. 4.16 a THG spectrum at $B^0 = 10\,\text{T}$ in the range from $3\hbar\omega = 1.5\,\text{eV}$ up to $3\hbar\omega = 1.6\,\text{eV}$ is presented. No resonances, besides the one at $3\hbar\omega = 1.5235\,\text{eV}$, are observed. This is surprising, since the Landau level model predicts an s magneto-exciton for each Landau level. The measurement shows, that no state besides the lowest $1s$ exciton leads to a THG resonance or other resonances are at least much weaker than the $1s$ exciton.

Two changes of the resonance become obvious for rising field strength. The resonance is shifted and its intensity is increased. In Fig. 4.17 these changes are plotted and fitted.
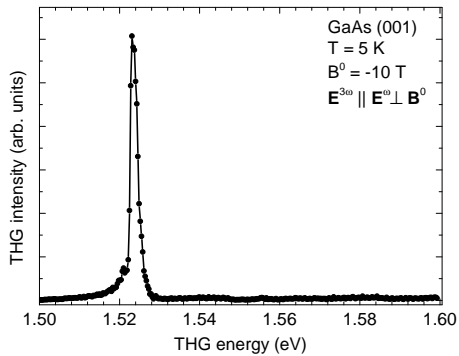
Figure 4.16 – THG spectrum in a broad spectral range at $B^0 = -10\,\text{T}$ with high integration time. No magneto-excitons from higher Landau levels are detected.
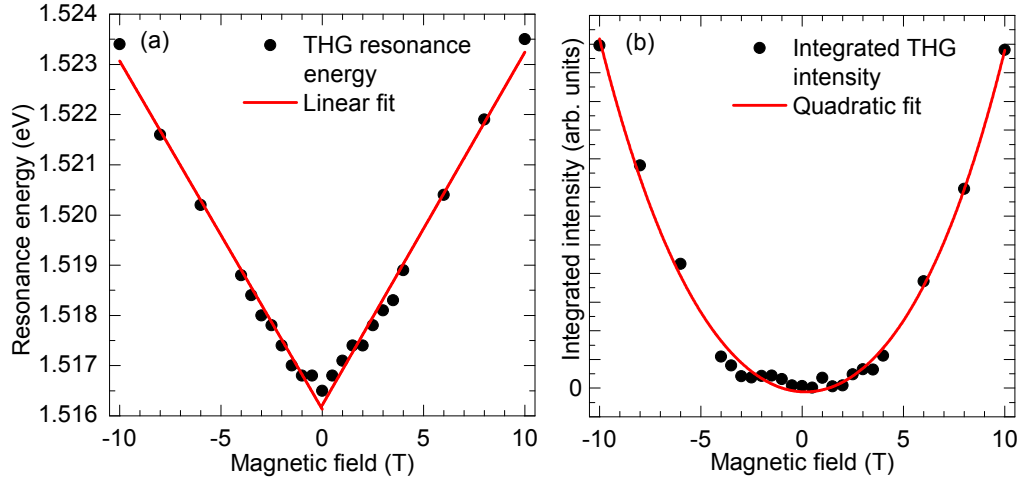
Figure 4.17. – Intensity and energy shift of the THG resonance presented in Fig. 4.15 with $T = 5\,\text{K}$ and a Voigt magnetic field. (a) Magnetic field dependent shift of the THG resonance and a linear fit function (red line). (b) Magnetic field dependent integrated intensity of the THG spectra (black dots) and a quadratic fit function (red line).

In 4.17 (a) the shift of the peak energy is plotted against the applied magnetic field. The slope of the shift is about $0.7\,\frac{\text{meV}}{\text{T}}$. The slope is a bit smaller than the estimated Landau shift, but much bigger than the expected diamagnetic shift of $\Delta_{\text{Dia}}(10\,\text{T}) \approx 0.34\,\text{meV}$. It shows the same behavior as the SHG resonance at this energy, except that the THG resonance can be observed in zero field. In Fig. 4.17 (b) the integrated intensity is plotted against the magnetic field. It is fitted with a polynomial of fourth order $I^{(3\omega)}_{\text{Integr}}(B) = A_0 + A_1 B + A_2 B^2 + A_3 B^3 + A_4 B^4$. The resulting coefficients are $A_0 = 0.0$, $A_1 = -81.9\,\text{T}^{-1}$, $A_2 = 249.9\,\text{T}^{-2}$, $A_3 = 0.3\,\text{T}^{-3}$, and $A_4 = 0.5\,\text{T}^{-4}$.

In Fig. 4.18 anisotropy measurements of the exciton resonance are presented. With increasing magnetic field strength the constant intensity of the anisotropy without a magnetic field changes into a two fold-shape. In Fig. 4.18(a) measurements at $B^0 = 4\,\text{T}$ are presented. At this field strength the anisotropy is just in between being dominated by the (nearly) constant zero-field contribution and magnetic field induced THG. The parallel anisotropy already has a two-fold shape from magnetic field induced THG, but the remaining constant term can still be observed. In the crossed configuration a four-fold shape is observed. Both the zero-field contribution and the field induced contribution have the same four-fold shape. The increased intensity at $140\,^{\circ}$ compared to $50\,^{\circ}$ could stem from an interference between the two contributions, as each of their maximums are expected to have the same intensity.

In Fig. 4.18(b) the anisotropies for $B^0 = 10\,\text{T}$ on the resonance at $3\hbar\omega = 1.523\,\text{eV}$ are presented. For this field strength the anisotropy is dominated by the magnetic field induced THG. The anisotropy can only be modeled with $\chi^{(4)} E^{\omega} E^{\omega} E^{\omega} B^0$ by taking a small misalignment into account. The non-zero tensor elements of $\chi^{(4)}$ all have at least one z component. A small tilting could explain the observed anisotropy shape, but it is unlikely
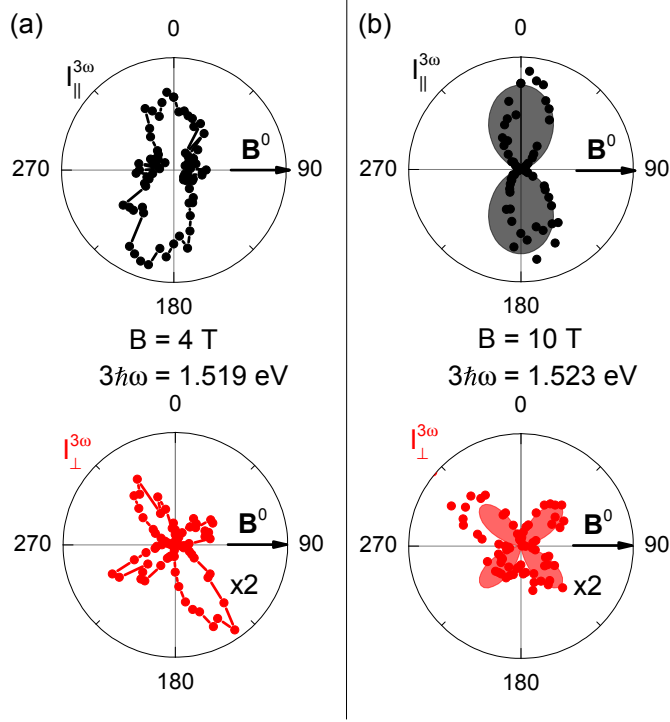
Figure 4.18. – THG anisotropies on the resonance in the spectra presented in Fig. 4.15. (a) parallel and crossed anisotropy at $3\hbar\omega = 1.519\,\text{eV}$ in a Voigt field of $B^0 = 4\,\text{T}$. The shape is a mixture of the (nearly) constant $\chi^{(3)}$ contribution and a two-fold magnetic field induced anisotropy. The intensity parallel to the magnetic field at $90°$ is the intensity of the remaining $\chi^{(3)}$ contribution. (b) parallel and crossed anisotropy at $3\hbar\omega = 1.523\,\text{eV}$ in a Voigt field of $B^0 = 10\,\text{T}$. The parallel anisotropy is dominated by the two-fold shape of the magnetic field induced THG. The expected crossed magnetic field induced anisotropy is eight-fold and cannot be explained by $\chi^{(4)}$ alone.

that such a strong increase of THG is observed in this case, because a small tilting only leads to a small z component of the polarization. Since it is necessary to include magneto-spatial dispersion effects for the modeling of SHG anisotropies, it is probable that this is also necessary for THG. In this case the anisotropy is described by $\chi^{(5)} E^\omega E^\omega E^\omega k B^0$, which also leads to the presented shape even without tilting.

4.3.4. Discussion

Crystallographic THG

The THG spectrum without a magnetic field presented in Fig. 4.12 is as expected. The $1s$ exciton is allowed for ED THG and the resonance at $E = 1.5162\,\text{eV}$ is assigned to this state. Both one- and three-photon transitions have odd parity and couple to the odd parity $1s$ exciton. Again a small redshift of the resonance to the reported value of $E_{1s} = 1.5152\,\text{eV}$ is found, which is similar to the SHG measurements. In contrast to

SHG, the resonance is observed without an external perturbation, which was not possible in the SHG studies. Even without an external electric field, which could ionize excited states, resonances for $n \geq 2$ excitons are not observed, although all odd parity states are allowed for THG. Most probably these states are not observed because they are distorted by defects in the sample.

THG in an electric field

An external electric field decreases the intensity of the resonance. This is in accordance to the explanation of enhanced SHG by an electric field in Sec. 4.2.4. The admixture of the even parity $2p$ exciton to the $1s$ exciton leads to a decreased oscillator strength for the new mixed state. In contrast to the odd parity $1s$ exciton, the even parity $2p$ exciton is forbidden for one- and three-photon transitions. The quadratic decrease of intensity for increased electric field strength is in accordance with the increased admixture of the $2p$ wave function to the $1s$ exciton, which was found to be in a linear regime up to $E^0 \approx 2.5\,\text{kV}$ in Sec. 2.2.4.

The macroscopic description cannot have the typical form

$$I^{3\omega} \propto \left[\chi^{(4)}\, E^\omega E^\omega E^\omega E^0 \right]^2 , \qquad (4.2)$$

because this only describes an increase of intensity with increasing E^0. The influence of the electric field on the third order susceptibility is not linear and cannot be factored out of the susceptibility as it is done in (4.2). It is described by

$$I^{3\omega} \propto \left[\chi^{(3)}(E^0)\, E^\omega E^\omega E^\omega \right]^2 , \qquad (4.3)$$

and the influence of E^0 on the susceptibility has to be derived microscopically. The value for $\chi^{(3)}$, which is responsible for the zero field THG resonance, decreases in an electric field.

Magnetic field influence on THG

A Voigt magnetic field increases the THG intensity for about a factor of 175. It is surprising that the magnetic field leads to enhanced SHG and THG at the same time. In Sec. 4.2.4 the magneto-Stark effect was proposed as one of the possible explanations for an increase of SHG in a magnetic field. The admixture of p states to the $1s$ exciton due to the magneto-Stark effect would lead to a suppression of THG, and not an increase, as it can be seen in the THG measurements with an electric field. Another possibility for SHG and THG to increase in a magnetic field is an increase of oscillator strength for one of the involved optical transitions. However, in Sec. 4.4 it is shown that neither the one-, two-, or three-photon oscillator strengths grow in a magnetic field. This leaves mainly polariton effects as an explanation for increased SHG and THG. These are discussed in Sec. 4.2.4.

4.4. Comparison of multi-photon absorption and harmonics

The measurement technique for TPA-PL and 3PA-PL is described in Sec. 3.2.4. At first it is necessary to find the brightest source of PL in the investigated sample. The sample was illuminated by a HeNe laser to generate hot electron hole pairs. The hot electrons relax down to the exciton states and lead to PL from these states. The strongest source of PL is $\hbar\omega = 1.489\,\text{eV}$ in the sample GaAs 239. This is well below the exciton energy $E_{1s} = 1.5152\,\text{eV}$. It stems from bound exciton states at impurities, which are well known in GaAs [55]. The PL from these states is used as a measure of absorption from resonances at the free exciton energy for TPA-PL and 3PA-PL as explained in Sec. 2.3.2.

4.4.1. Measurements of TPA-PL and 3PA-PL
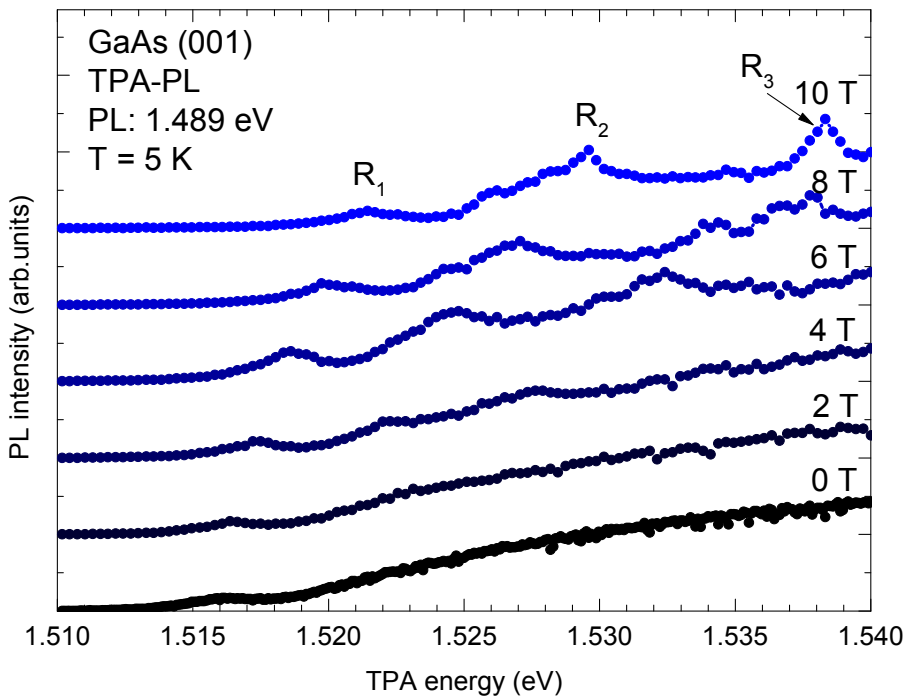
Figure 4.19. – TPA-PL measurements in a magnetic field up to $B^0 = 10\,\text{T}$ of sample GaAs 239. The electrons are excited by two-photon absorption on the epitaxial layer and the PL was detected on the same side with an angle of about $90\,^\circ$ between the excitation and detection. The detailed geometry is described in Sec. 3.2.1. The PL stems from bound excitons at impurities with photon energies of $\hbar\omega = 1.489\,\text{eV}$.

In Fig. 4.19 TPA-PL measurements on GaAs are presented. The geometrical configuration of the setup is explained in Sec. 3.2.1. For $B^0 = 0\,\text{T}$ (black dots) the spectrum has one resonance R_1 at $2\hbar\omega = 1.516\,\text{eV}$. This is close to the $1s$ exciton, which is forbidden for ED TPA. The unexpected observation of this resonance can be explained by a reabsorption of SHG, which is described in the discussion. The absorption increases at the

band gap with a square root dependence on the wavelength. The TPA for the band-band transition at the band gap is also forbidden by the ED selection rules, but higher order transitions can lead to absorption. The square root dependence is in accordance with the density of states of the conduction band.

In a magnetic field two more resonances R_2 at $2\hbar\omega = 1.530\,\text{eV}$ and R_3 at $2\hbar\omega = 1.539\,\text{eV}$ appear in the spectrum. Both are close to the second and third Landau level resonance in the MFISH spectrum. Besides these resonances, further small features can be found in the spectrum, which are too broad to be assigned to a specific energy. Those states could be related to the many small features in the MFISH spectrum.
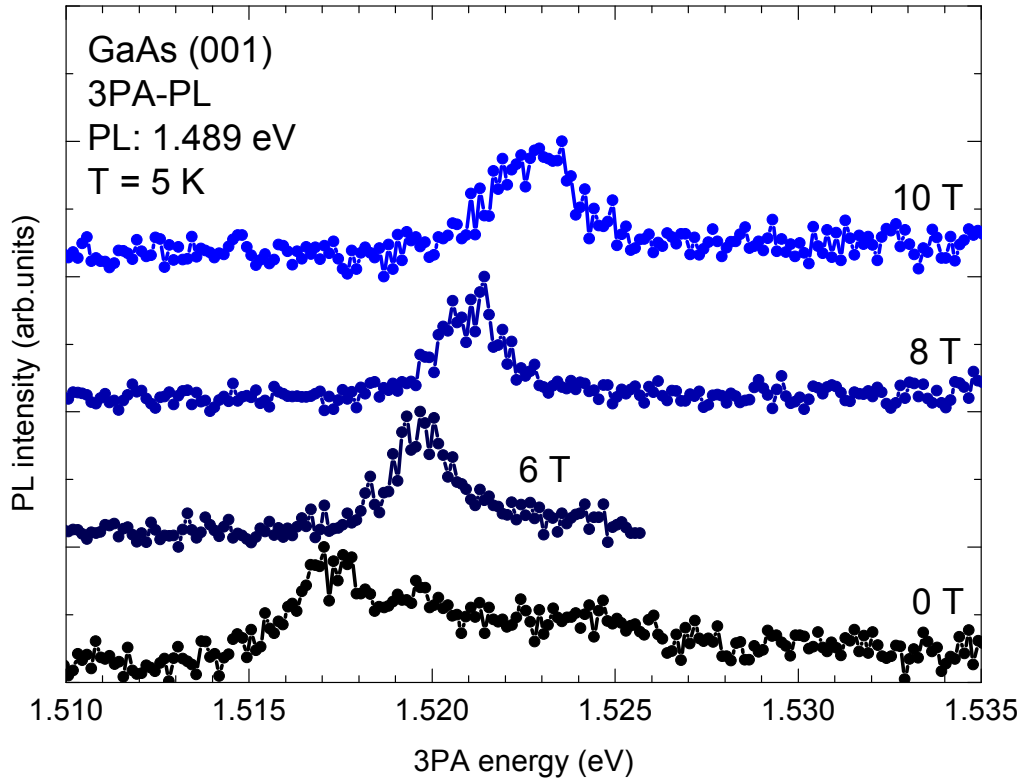
Figure 4.20. – 3PA-PL in reflection geometry on the epitaxy layer side of sample GaAs 239. The PL intensity of the bound excitons is detected at $\hbar\omega = 1.489\,\text{eV}$. The detailed experimental geometry is described in Sec. 3.2.1. The 3PA energy is varied in the region of magneto-excitons in GaAs.

In Fig. 4.20 3PA-PL measurements are presented. For $B^0 = 0\,\text{T}$ there is a single resonance at $3\hbar\omega(0\,\text{T}) = 1.517\,\text{eV}$ in the spectrum. On the high energy side the resonance has a tail of up to $3\hbar\omega = 1.528\,\text{eV}$. Since 3PA has the same parity conditions as one-photon absorption, it is expected to observe the same resonance as in the THG measurements. The blue-shift of $\Delta E = 1.8\,\text{meV}$ could be due to the unclear assignment of the resonance energy, since the line-shape is distorted and not Gaussian.

The resonance in the spectrum shifts to higher energies in a magnetic field. At $B^0 = 10\,\text{T}$ the resonance is at $3\hbar\omega(10\,\text{T}) = 1.523\,\text{eV}$. In a magnetic field the line-shape of the

resonance is more symmetric than for zero field and the energies can be assigned more precisely. The energy of the 3PA-PL resonance in a magnetic field is close to the resonance energy for THG spectra in a magnetic field.

4.4.2. White light reflection

In the measurements presented in this chapter the exciton resonance was investigated by various nonlinear optical methods and an unexpected difference between the $1s$ exciton energy and the resonances in the spectra was found. In order to find out if the energy difference is a sample property or connected to the nonlinear transitions, additional linear optical measurements are presented.
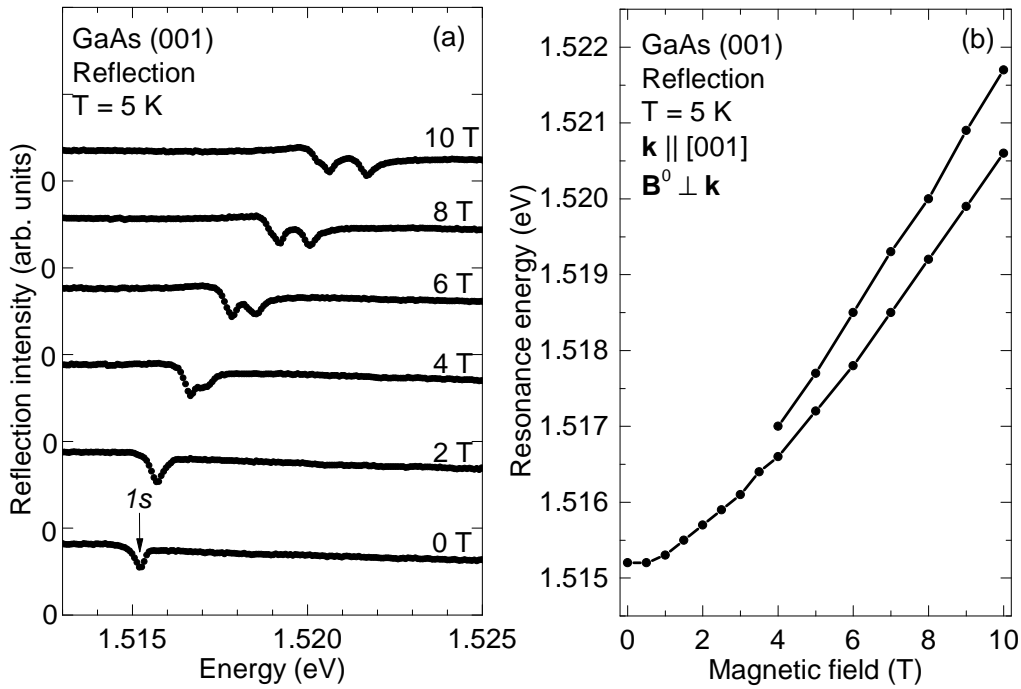
Figure 4.21. – White light reflection measurements of sample GaAs 239 in normal incidence configuration $\mathbf{k} \parallel [001]$ and with a magnetic field in Voigt direction. (a) Reflection spectra in the vicinity of the $1s$ exciton energy (black arrow) for different magnetic fields. At the energy of the $1s$ exciton is an intensity minimum, which is shifted and splitted in a magnetic field. (b) Plot of the magnetic field dependent resonance energy in the spectra.

In Fig. 4.21 white light reflection measurements are presented. The experimental setup is described in Sec. 3.2.4. The light was focused on the epitaxy-layer side of sample GaAs 239 in the normal incidence configuration. There is a minimum of intensity at the known $1s$ exciton energy $E_{1s} = 1.5152\,\text{eV}$ in the reflection spectrum. At the minimum there is about 14% less light intensity compared to the region before the resonance. It is not shifted to high energies in contrast to the nonlinear optical measurements. In a Voigt magnetic field of up to $B^0 = 10\,\text{T}$ the resonance is shifted to high energies and splits into

two separate resonances. Each of the minima in the $B^0 = 10\,\mathrm{T}$ spectrum has a reduced intensity of about 6%. The one-photon oscillator strength of the exciton seems not to be enhanced by the magnetic field. The energy of the minimum in the reflection spectrum, depending on the magnetic field, is shown in Fig. 4.21(b).

4.4.3. Discussion

The results of the multi-photon absorption spectroscopy are surprising. Reported TPA studies of GaAs revealed resonances for the p excitons and a small increase of absorption at the band gap from higher order processes, which is in agreement with the two-photon ED selection rules [93]. There are no studies for the comparison of the 3PA spectra, but from parity selection rules they should be similar to reported one-photon absorption studies, which showed resonances of the s excitons and band-band transitions at the band gap [94]. Neither of the expected results is found in the measurements presented in this section.

The TPA-PL measurements presented in this section have a resonance close to the $1s$ exciton, although s excitons are forbidden in the ED approximation for TPA. For energies above the band gap the absorption from band-band transitions increases beyond the absorption of the resonances. In previous reported studies the resonances are more intense than band-band transitions, since two-photon ED band-band transitions are forbidden. It is possible that the observed $1s$ resonance stems from a reabsorption of SHG [54]. Strong non-resonant SHG is expected in the tilted experimental geometry, which could be reabsorbed by a one-photon transition. The lack of $2p$ exciton resonances could be due to defects in the sample. The $2p$ excitons have a very small binding energy of $0.1\,\mathrm{meV}$ and it is known that they can only be observed in samples of very high quality.

The 3PA-PL spectra presented in this section have a single resonance close to the $1s$ state. No further resonances from the expected s type magneto-excitons are found. This is in line with the single exciton resonance observed in THG, which is presented in Fig. 4.16. There is no specific data on 3PA in the exciton region, as it was mainly investigated on a much broader wavelength scale in relation to THz lasing [95].

In addition to TPA-PL and 3PA-PL measurements photoluminescence-excitation (PLE) spectroscopy was also performed to investigate the behavior of one-photon absorption of the $1s$ exciton in a magnetic field. A PLE measurement is similar to TPA-PL, the only difference is that the laser light energy is directly resonant to the investigated states. Again the PL from bound states at $\hbar\omega = 1.489\,\mathrm{eV}$ are used to measure the absorption. No exciton feature was observed in the measurements. For any laser energy above $\hbar\omega > 1.489\,\mathrm{eV}$ an intense PL from the bound states was found, which did not change at characteristic energies like the $1s$ exciton or the band gap. It is possible that one-photon absorption from impurities in the substrate of the sample overpowers the exciton signal from the epitaxy layer. Another experiment was performed in order to investigate the one-photon absorption of the $1s$ exciton.

The white light reflection measurements in Fig. 4.21 have a resonance at the known $1s$ exciton energy of $E_{1s} = 1.5152\,\mathrm{eV}$. This rules out a shift of the exciton energy in the sample and verifies that the found energy shift in the nonlinear measurements stems from

the interaction of the exciton with the light. On the other hand, the shift of the exciton resonance in the reflection measurements is very similar to the other measurements, which shows that in all the measurements the 1s exciton is in fact observed. The 14% drop of intensity at the exciton in the reflection measurements proves a high quality of the epitaxial-layer. In a magnetic field the resonance splits into two separate minima and is shifted, but the drop of intensity is not increased. This rules out an increase of one-photon oscillator strength of the 1s exciton in a magnetic field. Additional white light absorption measurements in transmission geometry show a strong absorption of light above $\hbar\omega > 1.50\,\text{eV}$, which makes the observation of excitons impossible. It is not surprising that impurities in the substrate lead to an absorption of light below the band gap. This could be the reason that it was not possible to observe the excitons in the PLE measurements, because the substrate can lead to a strong one-photon absorption even below the exciton energy.
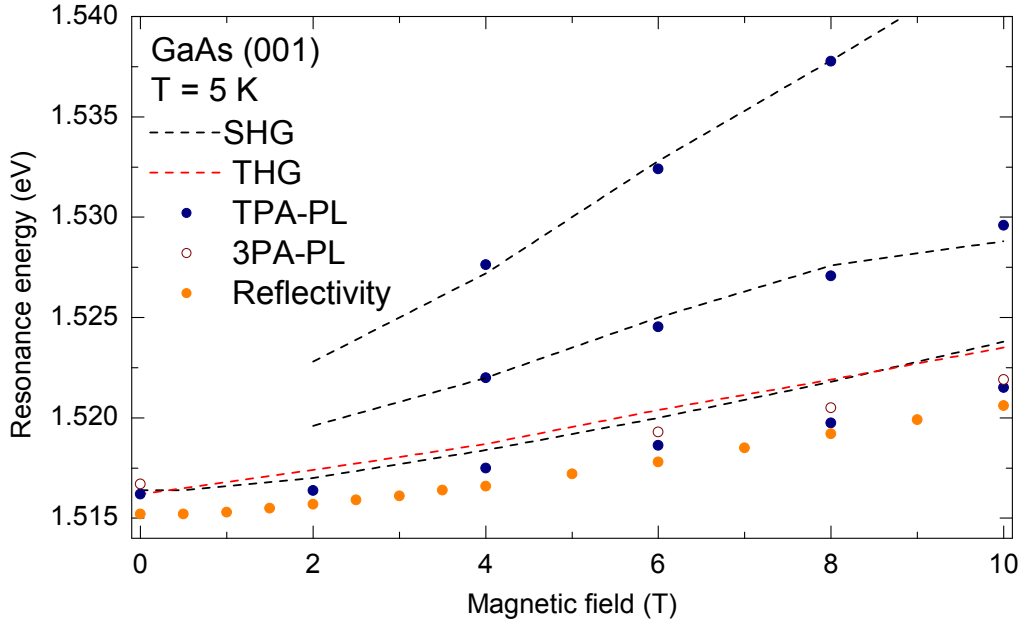
Figure 4.22. – Comparison of the multi-photon absorption measurements (TPA-PL: blue dots, 3PA-PL: open brown dots), reflectivity measurements (orange dots), and the harmonic generation spectra in the last sections (SHG: black dashed line, THG: red dashed line). For each measurement the energy of the exciton resonance in a magnetic field is presented.

In Fig. 4.22 the results of this section are compared to the harmonic generation spectra from the last sections. The average energy of the two resonances in a magnetic field is shown for the reflectivity measurements. The first three resonances of the TPA-PL spectra are close to the first three resonances in the MFISH spectra.

The 1s resonances from both absorption measurements deviate to lower energies at $B^0 = 10\,\text{T}$ by $\Delta E = 2\,\text{meV}$ compared to the harmonic generation measurements. There are two possible explanations for this. First, the transition to the observed states is the

same for harmonic generation and absorption, but the detected transitions are different. For harmonic generation the detected light is coherently generated from the incident light and one-photon ED allowed states. This leads to polariton effects, which shift the energy of the resonance as explained in Sec. 2.2.2. In the absorption measurements the light stems from bound excitons after several phonon interactions and no polaritons are involved. Second, the relaxation of excitons to the lowest states needs different energies of phonons in a magnetic field, since the exciton energy is shifted in relation to the bound states. It is possible, that the low energy side of the absorption line has a better coupling to the PL of the bound states at $\hbar\omega = 1.489\,\text{eV}$.

A significant increase of absorption in a magnetic field is found in none of the absorption measurements. This rules out the increase of one-, two- and three photon transition probability in a magnetic field as the explanation for increasing SHG and THG. It only leaves polariton effects as the source of strong intensity increase in the SHG and THG measurements.

4.5. Summary
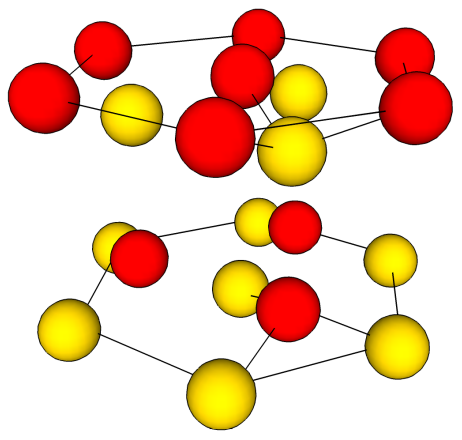
As shown in the introduction for GaAs there are already extensive studies about crystallographic and magnetic-field-induced SHG. The MFISH spectra show many resonances from the complicated magneto-exciton series. The energy of the resonances could be explained by a Landau level model. It remained unclear how a magnetic field actually leads to enhanced SHG, because it should not mix s and p excitons, which is needed for the complicated SHG selection rules. The magnetic-field-induced THG measurements in Sec. 4.3.3 help to exclude a mixing of s and p excitons as the responsible mechanism. The measurements in Sec. 4.4 rule out the increase of one-, two-, and three-photon oscillator strength. This leaves only polariton effects as the reason for an increase. The change of polariton dispersion in a magnetic field could simultaneously improve the resonance or phase-matching condition for SHG and THG. It is necessary to investigate the polariton dispersion in a magnetic field in more detail to verify such a mechanism.

An electric field is expected to mix the $1s$ and $2p$ exciton in contrast to a magnetic field. It is shown that this leads to the expected influence on SHG and THG. The admixture of states with different parity enhances SHG and suppresses THG. Both SHG and THG are explained by the Stark effect model calculations presented in Sec. 2.2.4.

5. Gallium Nitride (GaN)

5.1. Introduction

Table 5.1. – Basic parameters of GaN and a sketch of the crystal lattice.

	GaN
Symmetry	$C_{6v}(6mm)$
Crystal lattice	wurtzite
Centrosymmetric	No
Band gap ($T = 0\,\mathrm{K}$)	$3.50\,\mathrm{eV}$
Band gap ($T = 300\,\mathrm{K}$)	$3.40\,\mathrm{eV}$
Exciton binding energy	$28\,\mathrm{meV}$
Refractive index ($T = 330\,\mathrm{K}$)	$n_{\mathrm{o}}(1.17\,\mathrm{eV}) \approx 2.33, n_{\mathrm{e}}(1.17\,\mathrm{eV}) \approx 2.30$
Samples	$4.5\,\mu\mathrm{m}$ MOVPE epitaxy-layer
Measurements	SHG and THG

GaN is a direct wide band gap III-V semiconductor with a wurtzite structure and the symmetry group C_{6v} [53]. The wurtzite structure is the most stable and common phase of GaN. The ions are ordered in a hexagonal structure with the lattice constants $a = 3.19\,\text{Å}$ and $c = 5.19\,\text{Å}$. In this uni-axial structure the lattice directions are noted with four parameters (a_1, a_2, a_3, c). The third parameter a_3 is expressed in terms of the first two $a_3 = -(a_1 + a_2)$.

The interest in GaN for broad range harmonics spectroscopy arose due to similarities of the exciton series to the one in ZnO. Several different exciton series are close to each other and the p_z and $p_{x,y}$ are not degenerated. Such a rich exciton series enables the investigation of many different interactions. The exciton binding energy is also higher than in GaAs, which allows the identification of exciton states by their energy alone, because the resolution of the experimental setup is high enough to resolve the states. In ZnO SHG measurements proved to be a powerful tool for the investigation of excitons.

Especially different mixing mechanisms in an external magnetic field were observed and an extensive study revealed interesting effects, for example, the magneto-Stark effect [31].

In contrast to ZnO, the valence band order of GaN is typical for a hexagonal structure, which makes it an interesting model structure for other semiconductors [57, 96]. Theoretical calculations for SHG are available, but concentrate on the crystallographic response from 0 to 8 eV [97] and do not take sharp exciton resonances into account.

5.2. SHG spectroscopy

5.2.1. Crystallographic SHG

As explained in Sec. 3.3 the growth of GaN is still problematic and the samples are easily damaged by the fundamental light due to absorption. To enhance the signal in spite of the small energy per pulse of $E_{\mathrm{pulse}} \ll 200\,\mu\mathrm{J}$, the Glan-Thompson prism is removed from the setup for some measurements. This way the parallel and crossed SHG is picked up at the same time $\mathbf{E}^{2\omega} \parallel \mathbf{E}^{\omega} + \mathbf{E}^{2\omega} \perp \mathbf{E}^{\omega}$ enhancing the signal intensity.

First, crystallographic SHG in GaN is investigated near the band gap. In Fig. 5.1(a) the SHG spectrum is presented. A tilted geometry $\mathbf{k}\angle[0001] \approx 20\,^{\circ}$ is used, so that the light polarization has components in all three crystal directions and reveals most about crystallographic SHG. Measurements are made with the light passing the substrate first (black line) or passing the GaN layer first (red line). There is only a small difference between the two spectra around $2\hbar\omega = 3.4\,\mathrm{eV}$. Measurements in which the laser enters the sample on the GaN side show a slight decrease of intensity in this energy region. Both spectra display a strong decrease of intensity around $2\hbar\omega = 3.42\,\mathrm{eV}$, which is close to the band gap $E_{\mathrm{g}} \approx 3.50\,\mathrm{eV}$. At higher energies the intensity decreases gradually.

In Fig. 5.1(b) the anisotropy for $I_{\mathrm{both}}^{2\omega}$ is presented. For $I_{\mathrm{both}}^{2\omega}$ only the incident polarization $\mathbf{E}^{\omega}$ is rotated and every emitted polarization 2ω is detected without the analyzer as introduced in Sec. 3.2.3. The anisotropy has a two-fold shape with a maximum at $\varphi \approx 90\,^{\circ}$. The light intensity was too small to detect $I_{\parallel}^{2\omega}$ and $I_{\perp}^{2\omega}$ separately, but $I_{\mathrm{both}}^{2\omega}$ is enough to distinguish SHG from TPA-PL, which is expected to be anisotropic. The maximum SHG intensity is found at $\varphi \approx 90\,^{\circ}$ as is expected from the model calculations in Sec. 2.3.4. When pointed in this direction, the light polarization is in between the c axis and one of the other axis, which leads to the largest number of allowed susceptibility components.

5.2.2. Discussion

The observed spectra presented in Fig. 5.1 are similar to crystallographic SHG in GaAs. There is crystallographic SHG, which is reabsorbed at the band gap, leading to reduced SHG intensity for energies above the band gap. The exact position of the band gap is unclear, because it is shifted due to strain, but it is close to $E_{\mathrm{g}} \approx 3.50\,\mathrm{eV}$ as will be shown in the THG measurements. In this sample there are no oscillations of non resonant SHG for different wavelengths as in GaAs. The properties of the sample do not favor
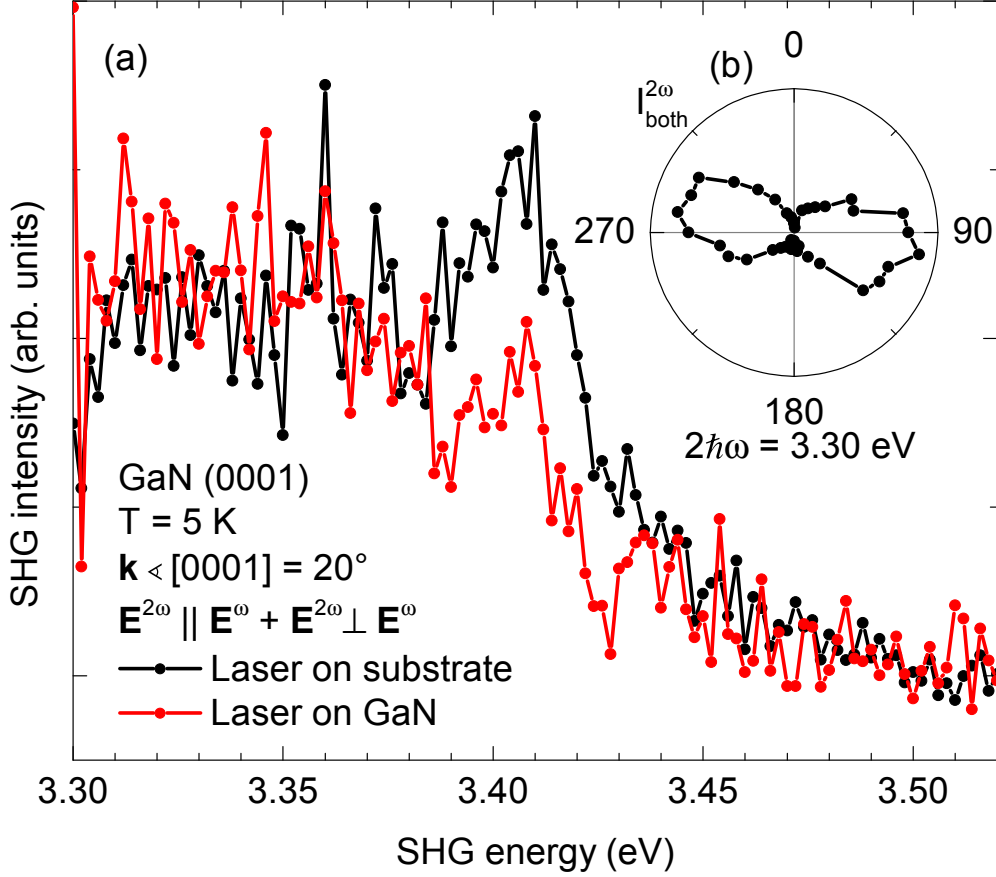
Figure 5.1. – (a) SHG spectra of GaN for tilted incidence. Comparison between light passing through the substrate first (black line) and passing through the sample first reveals no big difference, especially in the region of excitons, which is expected from the sample GaN BS2887, because of the sapphire substrate. (b) Anisotropy $I_{\text{both}}^{2\omega}$ at $2\hbar\omega = 3.30\,\text{eV}$. The two-fold shape verifies SHG as the source of detected light and maximum intensity at $\varphi \approx 90\,^\circ$ in which direction the light has the highest projection on the c axis.

the responsible reflections. The refractive index of sapphire is $n_{\text{Sa}} = 1.75$, which is much less than in GaAs. The reflections are smaller on the sapphire side and do not lead to interference.

The selection rules only allow the $2p$ excitons to be observed in SHG. They are very close to the band gap and have a small oscillator strength [36], which makes them difficult to observe. The application of an external magnetic field in the normal incidence configuration revealed no difference to measurements without a magnetic field so they are not presented. In contrast to GaAs, no resonances from mixed exciton states are found.

At the energy $2\hbar\omega = 3.41\,\text{eV}$ the intensity increases slightly. It is the only region of the spectrum in which the "correct" experimental configuration, where the laser passes the substrate first, leads to stronger SHG. It is therefore possible that the sapphire substrate has an influence in this energy region. Although it has a much higher band gap there

could be surface or interface effects, which reduce the energy in this region and also lead to the feature in the spectrum.

The number of SHG measurements on this sample was limited by the fact that the sample was damaged over time despite the low laser intensity of $E_{\text{Pulse}} \ll 200\,\mu\text{eV}$. Therefore the two different geometries were tested for less damage, with the laser either on the substrate or the sample, although it is expected to make no difference as explained in Sec. 3.3. Both directions were similarly prone to damage.

5.3. THG spectroscopy

In this section the results from the THG spectra in a broad wavelength range are presented. It is possible to choose a higher energy per pulse than in the SHG measurements. The laser wavelength is much higher for THG than for SHG and less energy levels absorb the photons. This allows shorter integration times and more extensive measurements.

5.3.1. Resonant THG

In Fig. 5.2 THG spectra in two different geometries are presented. The black dots are measured for $\mathbf{k} \parallel [0001]$. In the region of excitons several resonances are visible in the spectrum, labeled from X_1 to X_4. They are listed in Table 5.2. The energy of the resonance is compared to known results in the Discussion, which allows an identification of the excitons. Although the exciton energies depend on the specific sample, no exciton resonance is expected below $3\hbar\omega < 3.477\,\text{eV}$ as explained in the discussion. Therefore the observed resonances $3\hbar\omega \approx 3.459\,\text{eV}$ (R_1), $3\hbar\omega \approx 3.435\,\text{eV}$ (R_2), and $3\hbar\omega \approx 3.400\,\text{eV}$ (R_3) are not expected and the lower energy region is investigated in more detail in Fig. 5.3.

The measurements in a tilted geometry $\mathbf{k}\angle[0001] = 45°$ (red dots) lead to similar spectra as the normal incidence measurements. In contrast to SHG, no crystallographic background arises in the tilted geometry, which is similar to THG in GaAs. The exciton resonances are the main contribution to the spectrum. The intensity of the resonances between the two measurements cannot be compared like this, because a turning of the sample leads to the laser hitting another spot on the sample. Different regions of the sample showed different intensities, but the same spectral dependence.

Table 5.2. – Energies of the GaN THG resonances in the vicinity of the band gap.

THG Resonance	X_1	X_2	X_3	X_4
Energy (eV)	3.4884	3.4965	3.5010	3.5190

Because of the unexpected resonances R_n the lower energy region of GaN is investigated in more detail. In Fig. 5.3 broad range THG spectra from $3\hbar\omega = 2.1\,\text{eV}$ up to $3.33\,\text{eV}$ are presented. It turns out that there are resonances as low as $3\hbar\omega = 2.4\,\text{eV}$. In the $\mathbf{k} \parallel [0001]$ configuration the resonances are most intense and feature rich. Again, different sample positions are probed for different $\mathbf{k}$ directions, because turning the sample also shifts its
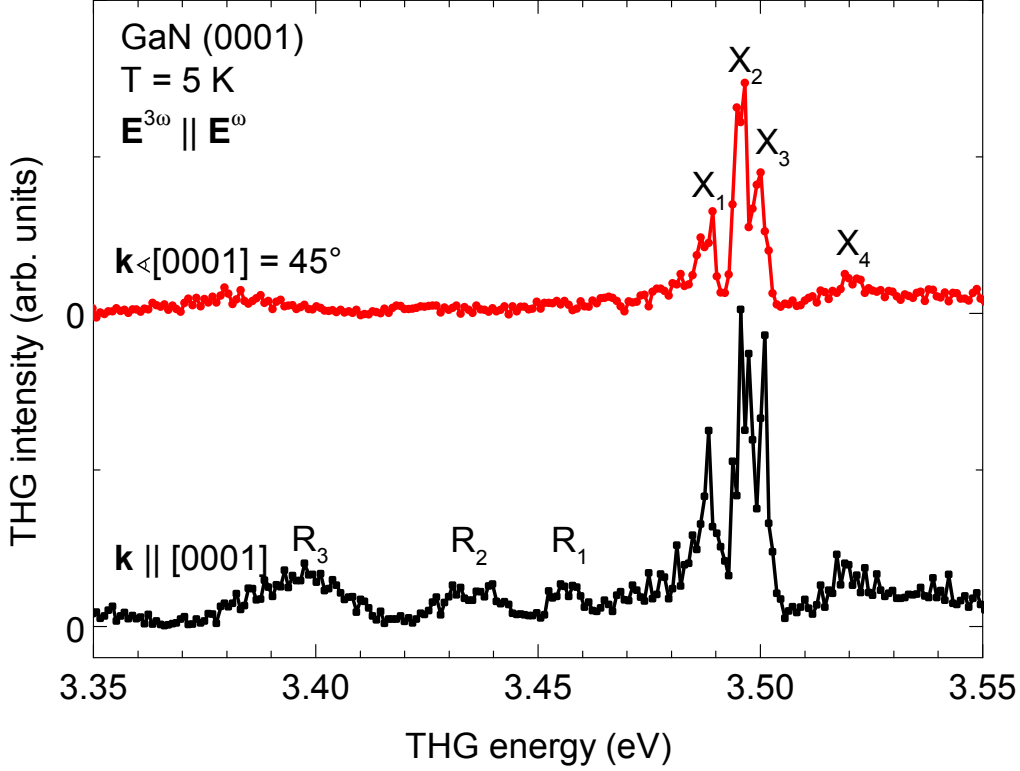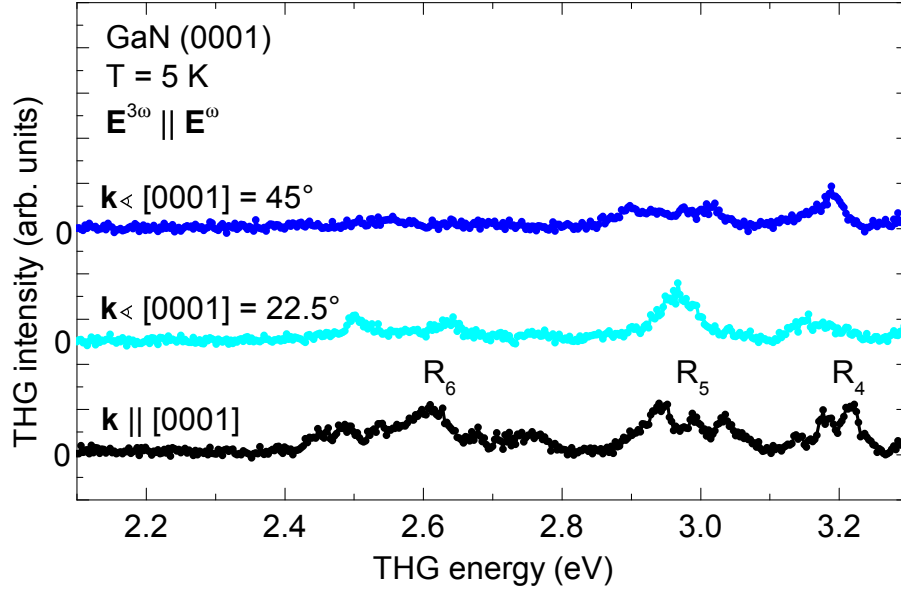
Figure 5.2. – THG spectra for different geometries in the vicinity of the band gap. The parallel polarization was set to $\varphi = 0\,°$ where the anisotropy has maximum intensity for both configurations as presented in Fig. 5.4. Several sharp resonances are present at exciton energies, which are marked by X_n. Below $3\hbar\omega < 3.46\,\text{eV}$ further broad resonances are in the spectrum, which cannot stem from excitons because their energy is too small and they are marked by R_n. They are more intense for $\mathbf{k} \parallel [0001]$.

position. For each measurement the position which lead to the strongest signal was chosen. The resonances R_4 to R_6 are very broad with a FWHM of up to $\Delta_{\text{FWHM}} \approx 100\,\text{meV}$. In the discussion different impurities and defects of GaN are proposed as a source of the resonances R_n. The resonances change their shape for a tilted sample geometry. The decrease in intensity might be due to enhanced reflection of the laser light for tilted incidence or due to $\mathbf{k}$ dependent selection rules. The energy of all the resonances R_n are listed in Table 5.3.

Table 5.3. – Energies of the GaN THG resonances, which cannot be attributed to excitons, because their energy is too small.

THG Resonance	R_1	R_2	R_3	R_4	R_5	R_6
Energy (eV)	3.455	3.435	3.400	3.200	3.000	2.610

In Fig. 5.4 rotational anisotropies of THG in GaN are presented. For the geometry $\mathbf{k} \parallel [0001]$ the same anisotropy can be found for every resonance. This is expected, since

Figure 5.3. – Wide range THG spectra of GaN for different geometries with the parallel polarization at $\varphi = 0\,^\circ$. For $\mathbf{k} \parallel [0001]$ the resonances R$_4$ to R$_6$ are most intense and feature rich.
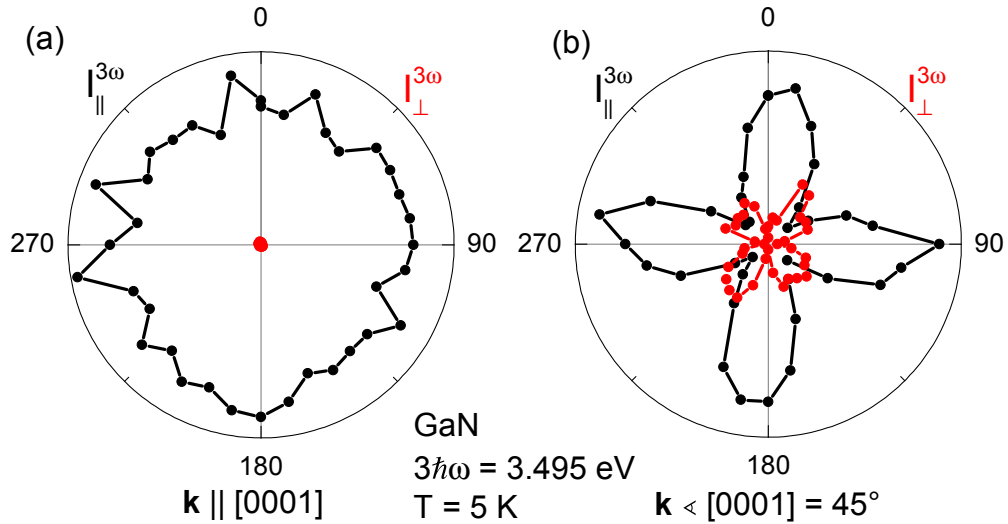
Figure 5.4. – Anisotropy of THG in GaN for two different $\mathbf{k}$ directions. The anisotropies have the same shape on every observed resonance and the presented ones are exemplary anisotropies at the exciton resonance $3\hbar\omega = 3.495\,\mathrm{eV}$. For $\mathbf{k} \parallel [0001]$ the parallel anisotropy $I_\parallel^{3\omega}$ is constant and the crossed $I_\perp^{3\omega}$ is zero. In the tilted geometry $\mathbf{k}\angle[0001] = 45\,^\circ$ both anisotropies have a four-fold shape.

there is only one independent tensor component χ_{xxyy} for χ^{cryst} without a z component as shown in Sec. 2.3.4. The one tensor component allows only one shape for every resonance.

In Fig. 5.4(b) the anisotropy for the tilted geometry $\mathbf{k}\angle[0001] = 45°$ is presented. In the tilted geometry more independent tensor components of χ^{cryst} contribute to the THG and a four-fold shape for both $I_{\parallel}^{3\omega}$ and $I_{\perp}^{3\omega}$ is the result. Again the anisotropy for every resonance is measured, but the intensity is only high enough to detect the anisotropy shape clearly at the exciton resonance in the tilted configuration. The R_n resonances are very weak in the tilted configuration as shown before in the spectra.

There is no $\mathbf{k}$ direction in which crystallographic THG is suppressed, which would be ideal for the investigation of magnetic field induced components. Therefore the $\mathbf{k} \parallel [0001]$ configuration is chosen, because magnetic field induced components should show a different rotational anisotropy than crystallographic contributions and the change of the constant parallel and zero crossed crystallographic anisotropy should be obvious.
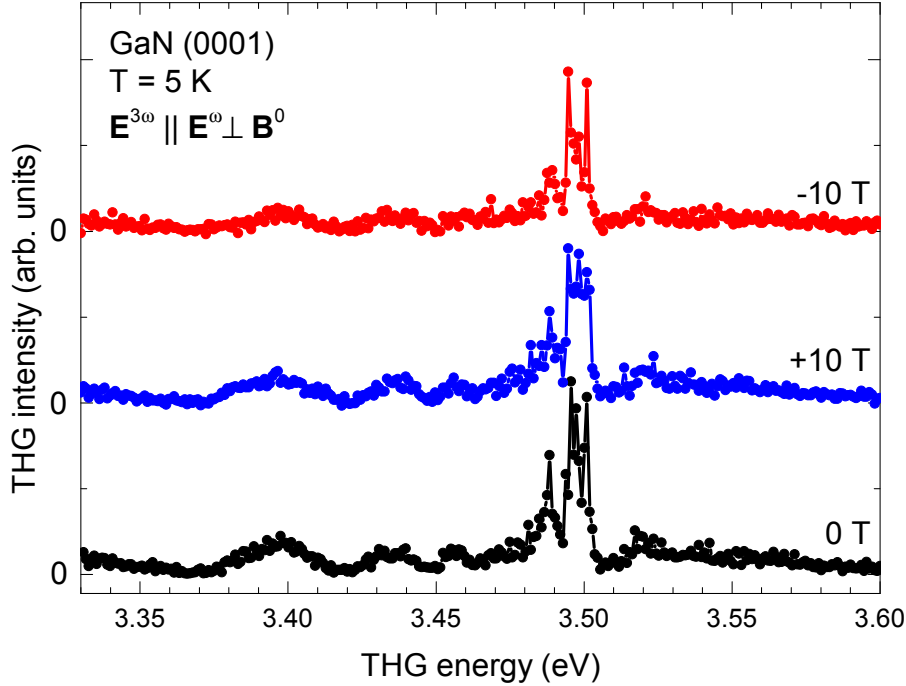
Figure 5.5. – THG spectra in the exciton energy range of GaN for zero field (black dots) and $\pm 10\,\mathrm{T}$ (blue/red dots) in the Voigt geometry. There is no difference between the spectra which can be attributed to the influence of the magnetic field. There is no difference between positive and negative field direction.

In Fig. 5.5 THG spectra for $B^0 = \pm 10\,\mathrm{T}$ are presented. The light polarization for the measurement is $\mathbf{E}^{2\omega} \parallel \mathbf{E}^{\omega}$ at $\varphi = 90°$. As shown in Fig. 5.6 the measurements are the same for every light polarization φ in the parallel configuration. There is no difference between the $B^0 = 0\,\mathrm{T}$ and the $B^0 = \pm 10\,\mathrm{T}$ spectra, which can be attributed to the influence of the external magnetic field. The influence of a magnetic field should be the same for positive and negative field direction. Taking this into account there is no feature which is different with or without a magnetic field, but present for both direction at the same time. Since there is no shift of resonances or increase of intensities from the external

magnetic field, the influence of the external field is investigated by anisotropies, which are another tool for such an investigation.
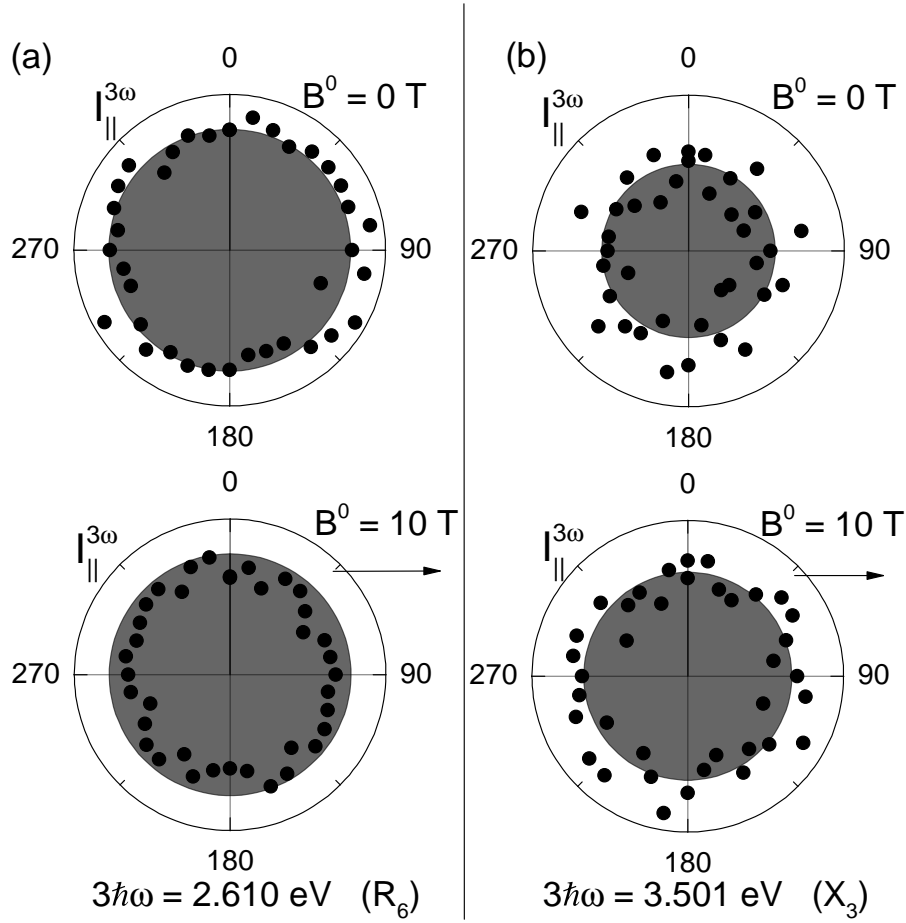
Figure 5.6. – Comparison of the parallel anisotropy of THG in GaN for $\mathbf{k} \parallel$ [0001] with and without a Voigt magnetic field $B^0 = 10\,$T. There is no difference between the spectra. Again all labeled resonances are checked and an exemplary exciton resonance (b) and one of lower energy resonances (a) is presented.

In Fig. 5.6 anisotropies with and without a Voigt magnetic field of $B^0 = 10\,$T are presented. In fact every exciton resonance and every lower resonance was measured. The resonance with the smallest energy $3\hbar\omega = 2.610\,$eV is presented in (a) and the strongest exciton resonance is shown representationally in (b). There is no difference between the rotational anisotropy with or without a magnetic field, which shows that the influence of the magnetic field on the observed states is negligible. The crossed anisotropy $I_{\perp}^{3\omega}$, which is zero for χ^{cryst}, should even reveal small contributions from induced THG, but no signal was found in a magnetic field for any resonance.

At last the temperature dependence of the exciton resonances are presented in Fig. 5.7. They are measured in the $\mathbf{k} \parallel$ [0001] configuration. For $T = 6.5\,$K the spectrum is unchanged from the $T = 5\,$K spectrum presented before in Fig. 5.2. In Sec. 2.2.3 the
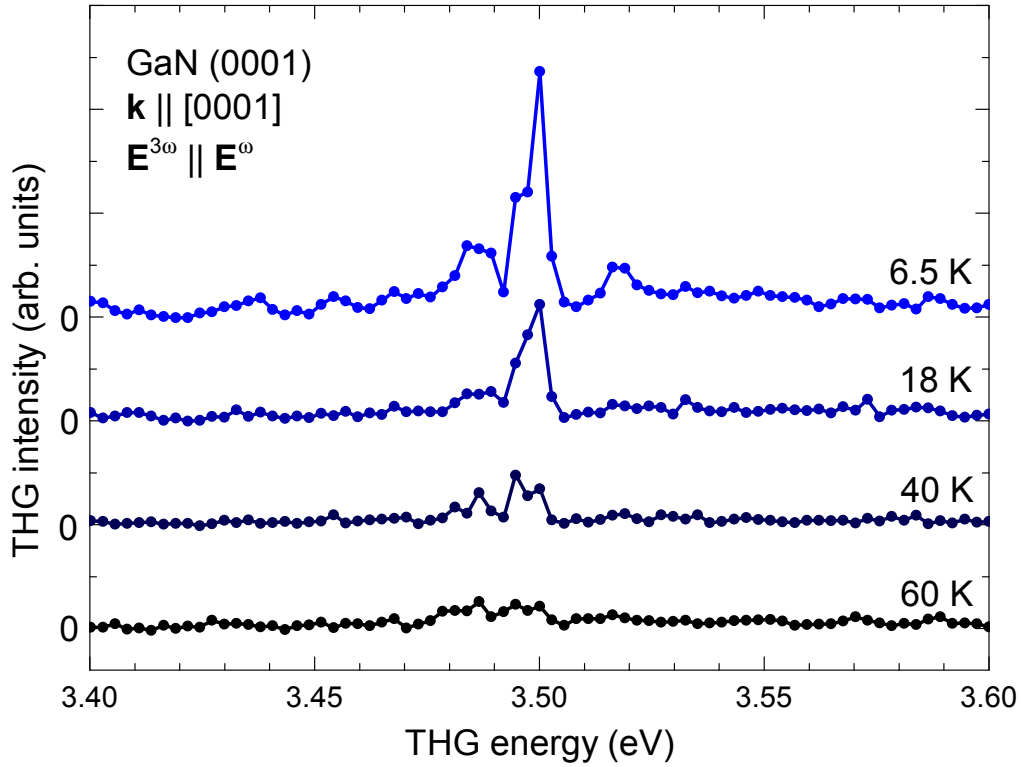
Figure 5.7. – Temperature dependence of the exciton resonances in the THG spectrum in the **k** ∥ [0001] configuration. For increased temperature the intensity of the resonances decreases. No shift of the resonance energy is observed up to $T = 40\,\mathrm{K}$, which is expected from the temperature dependence of the band gap energy. For temperatures $T > 40\,\mathrm{K}$ the intensity is too small to recognize the exciton resonances.

dependence of the GaN band gap on the temperature is shown. For increasing temperatures the intensity of the exciton resonances decreases. At $T = 60\,\mathrm{K}$ the resonances have almost zero intensity. No shift of the resonance could be found for higher temperatures. At $T = 40\,\mathrm{K}$ the shift of the GaN band gap $\Delta E < 0.9\,\mathrm{meV}$ is just below the resolution of about $1\,\mathrm{meV}$ for THG in this wavelength region. It is possible that the shift is not observed, because the resonance intensity becomes too small, before the energy shift is higher than the resolution of the experimental setup.

5.3.2. Discussion

Compared to GaAs, the spectral position of the excitons are not so well-known. The three exciton series from the different valence bands, together with overall shifting of the resonances due to low sample quality, are difficult to assign and are prone to confusion. In Table 5.4 the assigned exciton resonances from various sources are listed.

In the first two sources (#1 and #2) thin layers of GaN on sapphire are used. They should have a similar strain-induced band gap shift as the sample GaN BS2887. The other

Table 5.4. – Energies of the THG resonances in the vicinity of the band gap from different sources, measured on GaN grown by various techniques.

	Source	sample	$A1s$(eV)	$B1s$(eV)	$C1s$(eV)	E_g(eV)	$A2p$(eV)
#1	[90]	$4.2\,\mu\mathrm{m}$	3.485	3.493	3.518	—	—
#2	[98]	$10\,\mu\mathrm{m}$	3.496	3.506	—	3.525	3.518
#3	[57]	$>100\,\mu\mathrm{m}$	3.475	3.482	3.503	3.493	—
#4	[36]	$>100\,\mu\mathrm{m}$	3.477	3.484	3.503	3.505	3.498

two sources #3 and #4 are thick layers [57] and bulk [36] crystals and the values should be closer to those of an undisturbed bulk GaN.

Comparing the X_n resonances from Fig. 5.2 to values presented in the other sources, especially the first two, allows an assignment of resonances in the THG spectrum. The resonance $X_1 = 3.4884\,\mathrm{eV}$ is the $A1s$ exciton. It is close to the reported value for this exciton, especially from source #1. The A exciton series has the lowest energy as it includes holes from the upper most valence band. The next lower energy resonance is $R_1 = 3.455\,\mathrm{eV}$, which is too small to stem from excitons. Not even in the strain free samples #3 and #4 was such a small value found for an exciton resonance. The reason for this resonance and all the smaller ones is addressed later. The next two resonances $X_2 = 3.4965\,\mathrm{eV}$ and $X_3 = 3.5010\,\mathrm{eV}$ are close to each other and are in the region of the $B1s$ exciton. The three photon transition for the incident light interacts with polaritons having the wave vector $\mathbf{k}^\omega + \mathbf{k}^\omega + \mathbf{k}^\omega = 3\mathbf{k}^\omega$ or the reduced wave vector $\mathbf{k}^\omega + \mathbf{k}^\omega - \mathbf{k}^\omega = \mathbf{k}^\omega$. For the B exciton series the polariton dispersion is strong in this region and the two polariton resonances are noticeably shifted relatively to the exciton. This is not observed in the presented sources, because only linear optical techniques for the $1s$ excitons are used (PL, PLE, reflection) where this effect cannot be observed. In the PhD thesis of Schweitzer [99] THG measurements are used to investigate the polaritons in GaN and the same double peak structure with similar splitting of about $\Delta E \approx 5\,\mathrm{meV}$ was found and explained by the mentioned additive and subtractive $\mathbf{k}$ vector summation. The splitting is below the resolution of the setup for the other bands. The last resonance X_4 is close to the $C1s$ exciton. The $C1s$ is formed from the lowest valence band and is close to the band gap (a few meV depending on the source). All the resonances in the exciton region are assigned. The resonances at lower energies are not explained by the excitons and are investigated further. The $2p$ excitons are forbidden for one- and three-photon transitions and have to be measured with other optical techniques.

It turns out that the THG measurements revealed much more insight into the nonlinear optical response from excitons than the SHG measurements. Higher energy per pulse and different optical selection rules allowed the observation of the ground state of each exciton series. The observed energy values are in good agreement with other hetero-epitaxial samples on sapphire. The strain shifts the band gap to higher energy.

The resonances at lower energy presented in Fig. 5.3 were not reported before. They show no difference in the rotational anisotropy to the exciton resonances, which only allows

assignments based on the energy of the resonance. These are compared to known states within the band gap of GaN. The energy of the resonances are listed in Table 5.3.

There is a famous yellow photoluminescence in GaN at about $\hbar\omega \approx 2.2\,\text{eV}$ up to $2.6\,\text{eV}$. It was of high interest as it could only be explained by an unwanted doping, which in turn would explain unexpected electric conduction from allegedly pure GaN [100]. It was shown, that the reason for this PL in the transparency region was indeed unwanted doping with donors and acceptors. The resonance R_6, which stretches from $3\hbar\omega = 2.4\,\text{eV}$ up to $2.8\,\text{eV}$ with many small features, could be connected to the same defects as the yellow PL. In the course of the investigations of the unwanted doping further defects, including point defects, were also found to be a source of photoluminescence in the transparency region. Even small unintentional doping (memory-doping effect) led to a strong resonance around $\hbar\omega \approx 3\,\text{eV}$[101]. The resonances R_5 and R_4 could also be connected to unwanted doping. Finally, it was shown that these transitions exhibit strong nonlinear optical interactions [102], which explains their occurrence in the THG spectra.

For the additional resonances above $3\hbar\omega \geq 3\,\text{eV}$ another growth defect may be the source. Perpendicular to the c axis, layers of the second stable GaN structure (cubic) can emerge in the growth process. Such layers can form especially in the strained region close to the substrate. Cubic GaN has a band gap, which lies at about $E_{\text{g,cubic}} \approx 3.28\,\text{eV}$. This is smaller than in the wurtzite structure and states within the cubic structure could explain some of the resonances. Such a structure is known and even used as a quantum well within the wurtzite GaN. By only using SHG from a small area with many cubic domains in reflection geometry, a mixed wurtzite and cubic anisotropy was observed in SHG spectra [103]. The cubic GaN could also be the reason for the resonances R_5 and R_4.

For the energy region of the resonances R_1 up to R_3 there are no reports about known growth defects or other states with such an energy. In order to verify the proposed defects and investigate the resonances R_1 up to R_3 in more detail, further measurements on samples with intentionally enhanced defects of a certain kind are necessary. Comparing the intensity with the bulk effects of the excitons in the presented measurements, it is surprising, that point defects are only weaker by a factor of three. On the other hand, the intensity of the excitons itself is weaker than in the other semiconductors presented here and they might not be a good point of reference for such an estimation.

5.4. Summary

An epitaxial GaN sample is investigated by SHG and THG broad range spectroscopy. The SHG spectrum exhibits a strong crystallographic background without exciton resonances. The application of a magnetic field does not lead to enhanced SHG in the exciton region. The crystallographic background SHG and lack of MFISH limit the possibilities of SHG spectroscopy on this sample. It should be possible to observe the p excitons in SHG, but they are masked by the intense background.

For THG no crystallographic background is found. This is the same situation as in GaAs, where THG also shows no crystallographic background. Instead, excitons for each

of the three valence bands lead to enhanced THG, which is a sign of good sample quality, as the exciton states would otherwise be disturbed. The energies correspond to reported values in GaN on sapphire with a blue shifted band gap from strain.
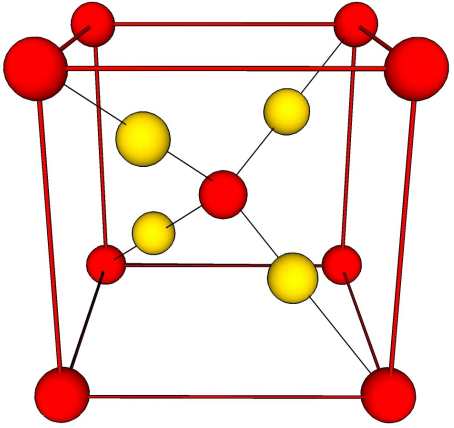
Many more regions of enhanced THG are unexpectedly found below the exciton energy. Rotational anisotropies are measured for each resonance. For these resonances possible growth defect states within GaN are proposed. In the future comparisons with intentionally enhanced growth defects could reveal the origin for each resonance. In addition to the magnetic field, which showed little influence on the observed states, electric field enhanced SHG and THG could be used, as it was shown to increase oscillator strength in GaN, but only for a single wavelength [104].

6. Cuprous Oxide (Cu$_2$O)

6.1. Introduction

Cuprous oxide is the fundamental oxide of copper and therefore also called copper(I) oxide. Copper(II) oxide (CuO), called cupric oxide, has different properties. Cuprous oxide crystallizes in cubic form with the symmetry group O_{h} ($m\bar{3}m$). The copper ions are on a FCC lattice and the oxygen atoms are on a BCC lattice, which are shifted along the body diagonal. It has a lattice constant of $a = 4.27$Å [53]. This structure typically cleaves along the (111) face, but (001) faces, like in other semiconductors, are also possible. The binding of the atoms has a strong ionic character.

Table 6.1. – Basic parameters of Cu$_2$O and the crystal lattice.

	Cu$_2$O
Symmetry	O_{h}
Lattice	FCC/BCC
Centrosymmetric	Yes
Band gap (T $= 0$ K)	2.172 eV
Band gap (T $= 300$ K)	2.137 eV
Exciton binding energy	98 meV
Samples	natural bulk crystal
Refractive index ($T = 5$ K)	$n(1.016\,\mathrm{eV}) \approx 2.57 \quad n(2.033\,\mathrm{eV}) \approx 3.02$
Measurements	SHG and PLE

The O_{h} group is centrosymmetric and parity is not only a good approximation at the Γ point like in GaAs, but is a good quantum number, which has to be conserved. Therefore the second order susceptibility $\chi^{(2)}_{\mathrm{ED}} = 0$ is zero for all components. No ED SHG is possible for any resonance. Only higher order processes can lead to SHG. Even in linear optics Cu$_2$O has unusual properties. The even parity valence band leads to different selection rules compared to other semiconductors. A one-photon ED band-band transition to the lowest conduction band is forbidden. All excitons with an even parity envelope are also

ED forbidden. Only states with an additional odd parity contribution are ED allowed. These are typically p type excitons or transitions involving an odd parity phonon.

The first observation of SHG from the yellow $1s$ exciton, despite the centrosymmetric structure of Cu_2O, was reported by Shen [39]. It is explained by a two-photon ED transition to the exciton and an EQ transition from the exciton. The EQ has specific selection rules and SHG is only possible for certain **k** directions. In another report by Kono et al. [33] SHG was found for the **k** $\parallel$ [001] direction. In this direction SHG is not possible by the EQ transition. The two-photon ED transition can only excite Γ_{5z}^+ states, whereas an EQ transition only couples to Γ_{5x}^+ and Γ_{5y}^+. A cross relaxation between the three degenerated states could lead to TPA-PL which, in this case, is similar to SHG. This was ruled out by applying a magnetic field, which lifts the degeneracy between the three states. Still SHG from each state was observed. This rules TPA-PL out, because without degeneracy TPA-PL cannot be confused with SHG as it has another wavelength. In Sec. 6.2.1 other crystal directions with forbidden EQ SHG are investigated for SHG with and without a magnetic field.

In Sec. 6.3 the influence of a magnetic field on exciton resonances with $n \geq 2$ are investigated. In this region the s and p excitons are close to each other. This is an ideal system to investigate the magneto-Stark effect, because in a centrosymmetric structure a magnetic field should only enhance SHG through this mechanism and other mixing mechanisms are forbidden due to parity. It was found to be the source for MFISH in ZnO [31], which is not centrosymmetric, but it was still possible to identify the magneto-Stark effect among other mixing mechanism. In Cu_2O the magneto-Stark effect promises to be the only source of MFISH from $n > 1$ yellow excitons where the exciton states have only a small splitting $\Delta_{3s/3p} = 0.6\,\mathrm{meV}$ and the oscillator strength between the states is high.

6.2. SHG from the 1s yellow orthoexciton

6.2.1. SHG in forbidden configurations

In Fig. 6.1 SHG spectra in the vicinity of the $1s$ orthoexciton are presented. Each measurement was done in a normal incidence geometry on one of the crystal faces of sample H28. The **k** vector lies in a different crystal direction for each measurement. All the spectra show no crystallographic background, but a resonance at $2\hbar\omega = 2.033\,\mathrm{eV}$ with a FWHM of about $\Delta_{\mathrm{FWHM}} \approx 1\,\mathrm{meV}$. This is at the energy of the yellow $1s$ orthoexciton $E_{1s} = 2.033\,\mathrm{eV}$.

The lack of crystallographic SHG is expected in a centrosymmetric crystal, since ED SHG is forbidden and higher order transitions are typically weak for non-resonant SHG. The resonances for **k** $\parallel$ [111] and **k** $\parallel$ [11$\overline{2}$] are expected from EQ SHG. In the direction **k** $\parallel$ [1$\overline{1}$0] even the EQ SHG is forbidden as shown in Sec. 2.3.4. It has a higher intensity in the presented measurements compared to the other directions. The intensity is at least of the same order, even after taking a possible difference from better alignment into account (after turning the crystal). This rules out higher order transitions as the source for SHG, since they are orders of magnitude weaker. To investigate this resonance in more detail
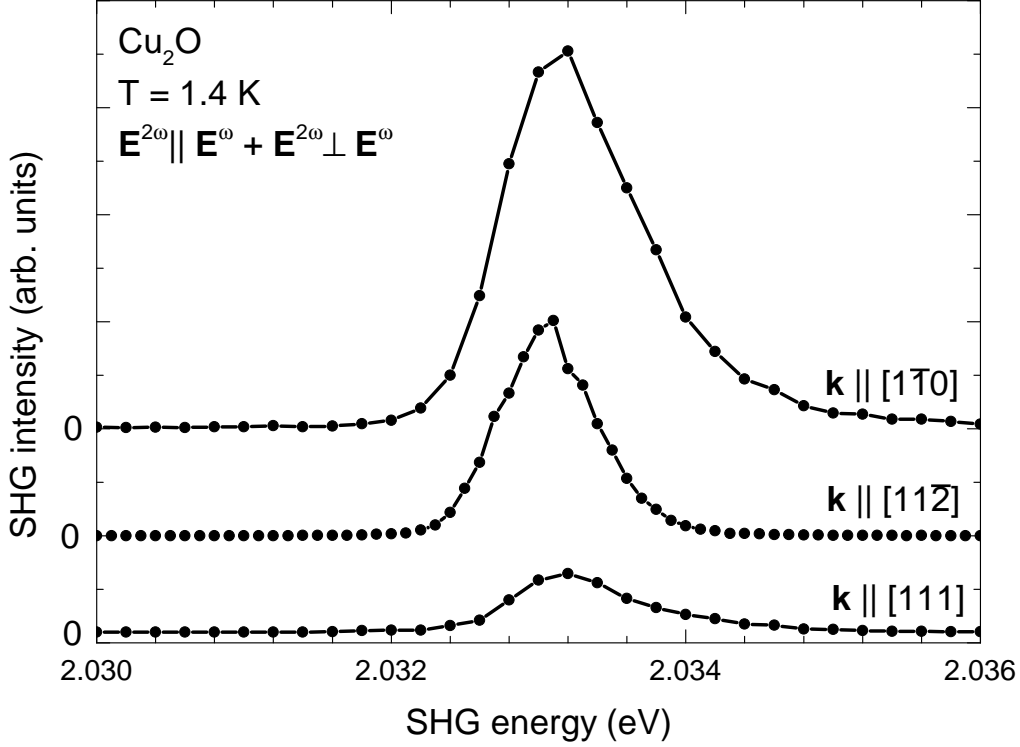
Figure 6.1. – SHG spectra in the region of the yellow $1s$ exciton for different wave vector directions. For none of the directions non-resonant SHG is observed, but in each direction there is a sharp resonance at the energy $E_{1s} = 2.033\,\text{eV}$ of the $1s$ exciton with a FWHM of about $\Delta_{\text{FWHM}} \approx 1\,\text{meV}$.

its rotational anisotropy is presented next.

In Fig. 6.2 the rotational anisotropy of the incident two-photon transition $I_{\text{In}}^{2\omega}$ and the following one-photon transition $I_{\text{Out}}^{2\omega}$ for $\mathbf{k} \parallel [1\bar{1}0]$ are presented. In Fig. 6.2(a) the same $\mathbf{k} \parallel [1\bar{1}0]$ direction as in the spectra is presented. In Fig. 6.2(b) the wave vector is antiparallel in comparison to (a), which helps to identify the crystal axis. The fundamental crystal direction in which the light polarization lies is noted on the scale. The incident two-photon transition (black dots) has a maximum for $\mathbf{E}^{\omega} \parallel [110]$ and a minimum for $\mathbf{E}^{\omega} \parallel [001]$ as is expected from the two-photon ED transition, which is calculated in Sec. 2.3.4. The one-photon transition $I_{\text{Out}}^{2\omega}$ has a minimum for $\mathbf{E} \parallel [110]$ and a local minimum for $\mathbf{E} \parallel [001]$. The vanishing intensity for $\mathbf{E} \parallel [110]$ is expected from the calculations. The directions $\mathbf{E} \parallel [111]$, $\mathbf{E} \parallel [11\bar{2}]$, and $\mathbf{E} \parallel [001]$ are all allowed for the $1s$ orthoexciton states lying parallel to the $\mathbf{k}$ vector. The detailed rotational anisotropy is not given by the calculations, but a signal, which is only zero for $\mathbf{E} \parallel [110]$ and allowed for other polarizations, fits the model from Sec. 2.3.4 well.

In Fig. 6.3 the anisotropies for normal incidence on all three crystal directions is presented. The anisotropy for the $\mathbf{k} \parallel [1\bar{1}0]$ direction is a combination of the absorption and emission polarization dependencies 6.2 in this direction. The shaded area is not an EQ SHG model, which predicts zero intensity for this direction, but just the expected intensity
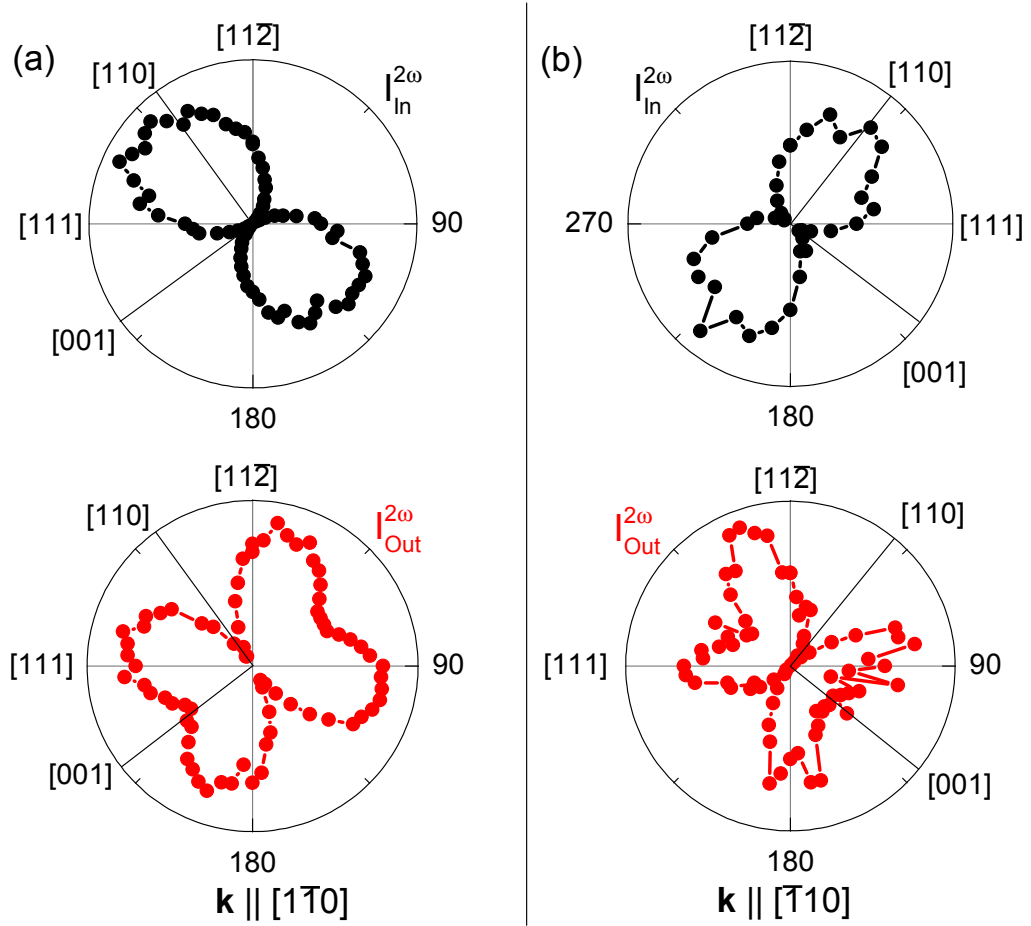
Figure 6.2. – Rotational anisotropy of the 1*s* orthoexciton in **k** ∥ [1$\bar{1}$0] direction. Black dots represent $I_{\mathrm{In}}^{2\omega}$ measurements and red dots $I_{\mathrm{Out}}^{2\omega}$. Additionally to the φ angles the most important crystal directions in which the light polarization lies are noted. (a) Measurements in the same direction as the spectra for **k** ∥ [1$\bar{1}$0]. (b) Measurements with **k** antiparallel compared to (a).

$I_{\parallel}^{2\omega}$ and $I_{\parallel}^{2\omega}$, which can be calculated from $I_{\mathrm{In}}^{2\omega}$ and $I_{\mathrm{Out}}^{2\omega}$, as presented in Fig. 6.2. EQ SHG is allowed for the other directions and can be modeled by the equation from Sec. 2.3.4. In these directions the shaded areas are the model calculations, which do not have to be fitted, since only a single anisotropy shape is expected for these directions and these shapes are scaled to the measurements.

For **k** ∥ [111] the expected six-fold anisotropy is found and fits the model well. That the intensity does not reach zero in between the maxima could stem from additional TPA-PL to the EQ SHG. The measured anisotropy for **k** ∥ [11$\bar{2}$] in Fig. 6.3(c) does not fit to the model calculations. The observed anisotropy only has a small angular dependence in contrast to the expected shapes (shaded area). The observed signal could be a mixture of EQ SHG and TPA-PL. In order to suppress TPA-PL, a diaphragm was added to the experimental setup after the sample. This was used to suppress any light which is not
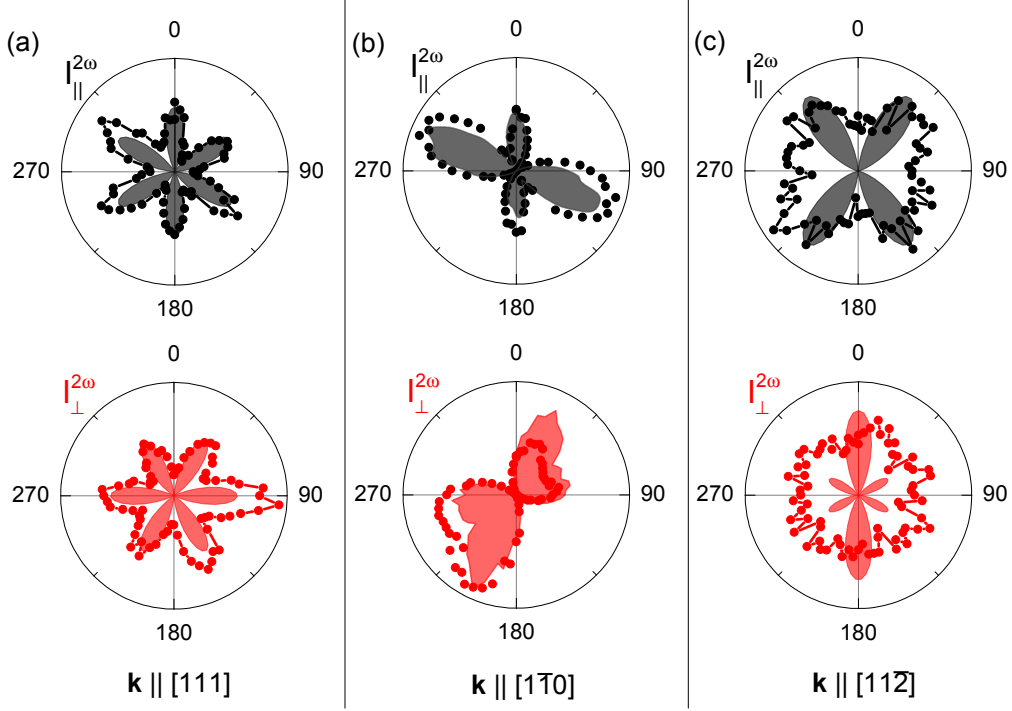
Figure 6.3. – Each polar graph represents an anisotropy for a specific k direction for the parallel $I_{\parallel}^{2\omega}$ configuration (black dots) and the crossed $I_{\perp}^{2\omega}$ configuration. (a) For $\mathbf{k} \parallel [111]$ both configurations have the from EQ SHG expected six-fold shape. (b) For the $\mathbf{k} \parallel [1\bar{1}0]$ direction both configurations are a combination of the incident two-photon transition and emitted one-photon transition presented in Fig. 6.2. The shaded areas are derived from combining the two transitions. (c) For the $\mathbf{k} \parallel [11\bar{2}]$ direction the anisotropy has only a small angular dependence and is not in good agreement with the expected shape.

overlapping with the laser light, but the directed nature of a quadrupole transitions could reduce the efficiency of this technique. In Fig. 6.4 TPA-PL spectra for the $\mathbf{k} \parallel [1\bar{1}0]$ direction are presented. The excitation energy $2\hbar\omega = 2.033\,\text{eV}$ is resonant for TPA of the $1s$ orthoexciton. The top line is measured in a polarization configuration in which the signal has maximum intensity, which is $\varphi = 135\,^\circ$ for the laser light and $\varphi = 95\,^\circ$ for the PL light as shown in Fig. 6.2. On the linear scale only the exciton and a very small transition at $\hbar\omega = 2.020\,\text{eV}$ are observed. Choosing a PL polarization of $\mathbf{E}^{2\omega}\angle\mathbf{E}^{\omega} = 125\,^\circ$ (bottom line) suppresses the strong $1s$ exciton line and reveals further features in the spectrum. The strongest one is the Γ_3 phonon line at $\hbar\omega = 2.02\,\text{eV}$. This is a strong relaxation channel for the $1s$ orthoexciton, in which the Γ_3 phonon is emitted simultaneously to a photon with reduced energy. It has a characteristic shape, with a tail on the high energy side and a sharp drop of intensity at the low energy side. Several other phonon lines, like the Γ_5 phonon, can also be assigned [72]. The resonances below $2.010\,\text{eV}$ are bound states, similar to the ones in GaAs.
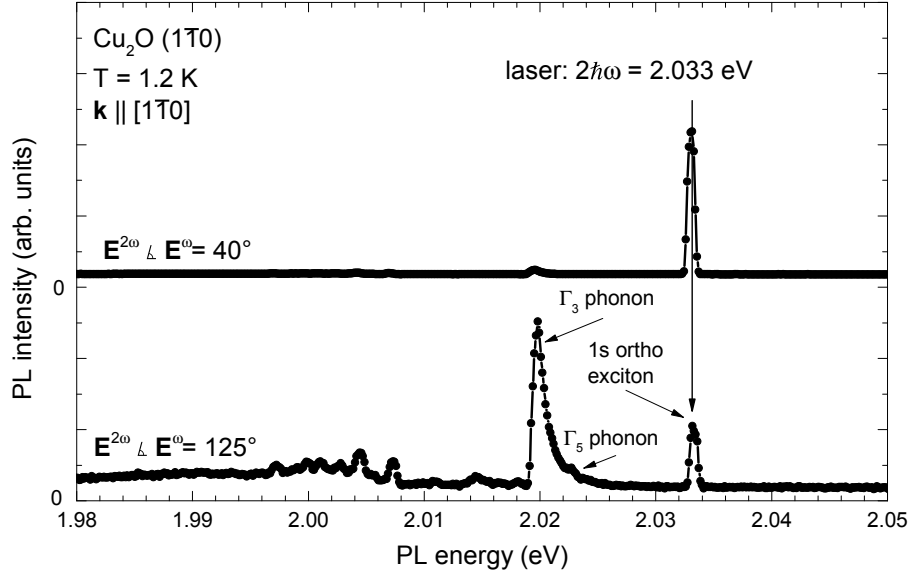
Figure 6.4. – TPA-PL spectra of the $1s$ orthoexciton. For polarization combinations in which the intensity of the $1s$ exciton is maximal ($\mathbf{E}^{2\omega} \angle \mathbf{E}^{\omega} = 40\,^{\circ}$) the exciton dominates the spectrum. In configurations in which the intensity of the $1s$ exciton is minimal ($\mathbf{E}^{2\omega} \angle \mathbf{E}^{\omega} = 125\,^{\circ}$) further transitions can be observed. Near $\hbar\omega \approx 2.02\,\mathrm{eV}$ are the Γ_3 and Γ_5 phonon lines, with a characteristic asymmetric shape. Below $\hbar\omega < 2.01\,\mathrm{eV}$ are bound excitons from impurities.

6.2.2. The 1s exciton in a magnetic field

A Voigt magnetic field is applied to the sample in order to further investigate the observed signal in the $\mathbf{k} \parallel [1\bar{1}0]$ direction. The magnetic field lifts the degeneracy of the three $1s$ exciton states. In this case the relaxation between the states can be distinguished from SHG, since the PL is no longer resonant, but stems from a lower lying state. From TPA measurements it is known that, depending on the field direction (Faraday/Voigt), the three states can be distinguished [73]. In Fig. 6.5 the splitting of the $1s$ exciton in a magnetic field is observed. In a magnetic field the exciton splits into the three $m = 0, \pm 1$ states as explained in Sec. 2.2.4. The $m = \pm 1$ states are observed in the magnetic field direction $\mathbf{B} \perp \mathbf{k}$. These observed energies are in good agreement with the calculation in Sec. 2.2.4.

In Fig. 6.6 the magnetic field induced SHG of the $1s$ orthoexciton for $\mathbf{k} \parallel [1\bar{1}0]$ is presented. The measurement in Voigt geometry was shown before in Fig. 6.5. Only a single resonance is observed in the Faraday geometry, which lies in between the $m = \pm 1$ states of the exciton. It has to stem from the $m = 0$ state. The observed resonance does not stem from ED, EQ, or MD transitions in the $\mathbf{k} \parallel [1\bar{1}0]$ configuration and the selection rules leading to SHG from the $m = \pm 1,0$ states are not known. The $m = 0$ resonance has an increased linewidth of $\Delta_{\mathrm{FWHM}} \approx 1\,\mathrm{meV}$ compared to the $m = \pm 1$ states with $\Delta_{\mathrm{FWHM}} \approx 0.5\,\mathrm{meV}$.

For the explanation of SHG in the unexpected direction $\mathbf{k} \parallel [1\bar{1}0]$ the relaxation between the different states of the $1s$ orthoexciton plays an important role. Without a magnetic
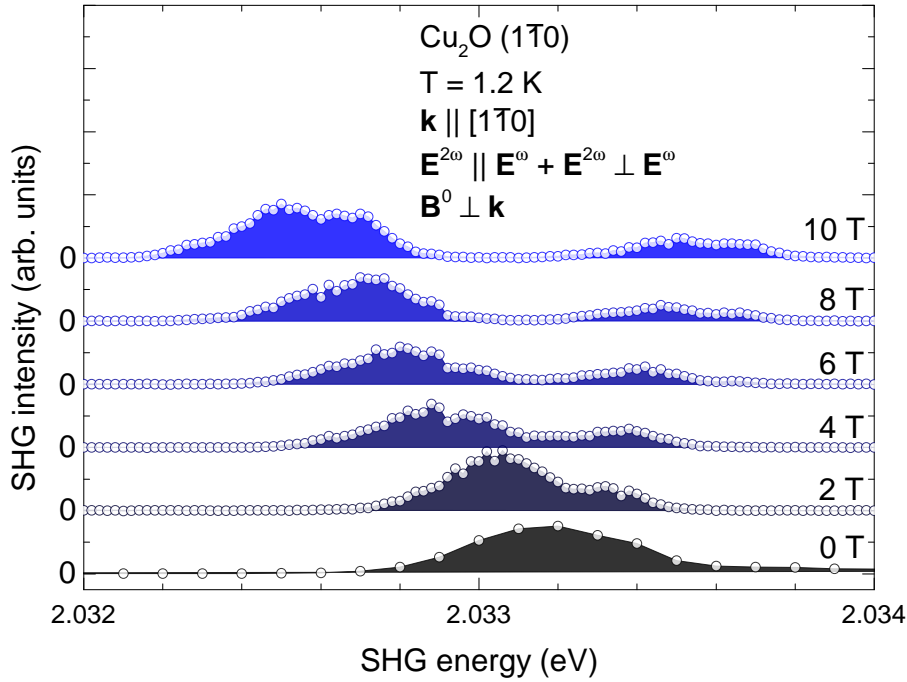
Figure 6.5. – SHG spectra for $\mathbf{k} \parallel [1\bar{1}0]$ in a Voigt magnetic field. For increasing field strength the $m = \pm 1$ components of the $1s$ orthoexciton are shifted by the Zeeman effect. The intensity of the lines does not change in the magnetic field and the integrated intensity grows about 20% in a magnetic field of $B = 10\,\mathrm{T}$.

field the states are nearly degenerated and cannot be resolved. In a magnetic field, however, it is possible to distinguish the three states because of the Zeeman splitting. In Fig. 6.7 measurements in a Voigt magnetic field $B^0 = 10\,\mathrm{T}$ are presented, in which the light from the crystal is spectrally resolved for different excitation wavelength. For the two-photon excitation wavelength $2\hbar\omega = 2.0332\,\mathrm{eV}$ both $m = \pm 1$ states lead to SHG at the same time. The high and low energy tails of the laser line reach both states. The $m = 0$ state is resonant to the two-photon excitation, but is not observed. For $2\hbar\omega = 2.0328\,\mathrm{eV}$ the lower exciton state is resonant to the two-photon transition and is the only source of SHG in the spectrum. The flat top shape of the resonance stems from a saturation of the CCD. Only the high energy exciton state is resonant for $2\hbar\omega = 2.0334\,\mathrm{eV}$ excitation. Still it is possible to observe the low energy resonance at $\hbar\omega = 2.0328\,\mathrm{eV}$. This could be caused by relaxation from excited $m = +1$ states, or again from the low energy tail of the laser linewidth.

In Fig. 6.8 SHG spectra for different magnetic field configurations in the $\mathbf{k} \parallel [111]$ direction are presented. For Voigt and Faraday geometry only the $m = \pm 1$ states are observed. The $m = 0$ state is not observed for any magnetic field direction in the $\mathbf{k} \parallel [111]$ direction in contrast to the $\mathbf{k} \parallel [1\bar{1}0]$ direction.

In every measurement of the $m = \pm 1$ states in a magnetic field the resonant SHG from the $m = +1$ state has a smaller maximum intensity compared to the $m = -1$ resonance. In Fig. 6.8 both magnetic field directions $B^0 = \pm 10\,\mathrm{T}$ are compared for the
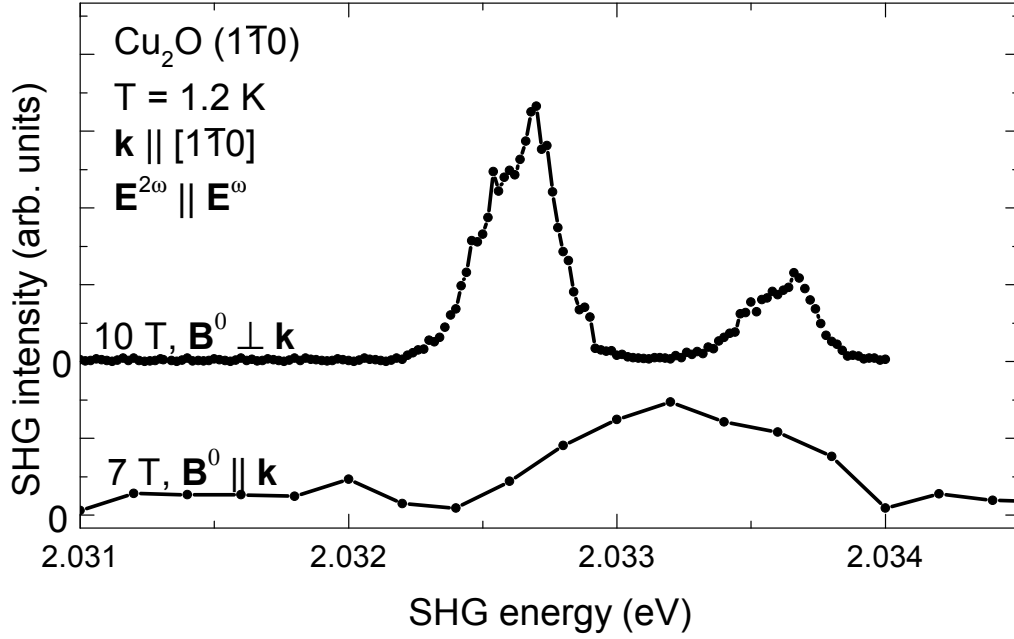
Figure 6.6. – In this graph two SHG measurements in an external magnetic field in the $\mathbf{k} \parallel [1\bar{1}0]$ configuration are shown. In a Voigt magnetic field $\mathbf{B}^0 \perp \mathbf{k}$ the splitting of the $m = \pm 1$ is found as it was shown before. In the Faraday configuration $\mathbf{B}^0 \parallel \mathbf{k}$ the $m = 0$ component is observed, which lies in between the $m = \pm 1$ states. It has an increased FWHM $\Delta_{\mathrm{FWHM}} = 1\,\mathrm{meV}$ compared to $\Delta_{\mathrm{FWHM}} = 0.5\,\mathrm{meV}$ of the $m = \pm 1$ resonances.

Voigt configuration and in both cases the $m = -1$ resonance is stronger.

At the top of Fig. 6.8 anisotropies for $B^0 = -10\,\mathrm{T}$ in the Voigt configuration are presented for both resonances. Both parallel anisotropies have a two-fold shape with an intensity maximum perpendicular to the magnetic field and both crossed anisotropies have a two-fold shape parallel to the magnetic field. The anisotropies for the $m = -1$ resonance has a clear shape, whereas the $m = +1$ resonance has additional features. The intensity maxima of the $m = +1$ resonance have shoulders or additional smaller maxima at about $\varphi \approx 45\,^\circ$ and $\varphi \approx 135\,^\circ$. With the additional smaller maxima the $m = +1$ anisotropy can also be interpreted as six-fold, which could be connected to the six-fold shape of the $1s$ orthoexciton resonance anisotropy without a magnetic field, which was presented in Fig. 6.3.

6.2.3. Discussion

In this section the SHG from the $1s$ orthoexciton in Cu₂O is presented. The first observation of SHG from this exciton resonance by Shen [39] was explained by EQ SHG. Only a few limited polarization congurations were compared in the report. In Sec. 6.2.1 all the rotational anisotropies for $\mathbf{k} \parallel [111]$ are presented. In fact they show the expected six-fold shape, which was calculated from the EQ susceptibility in Sec. 2.3.4.
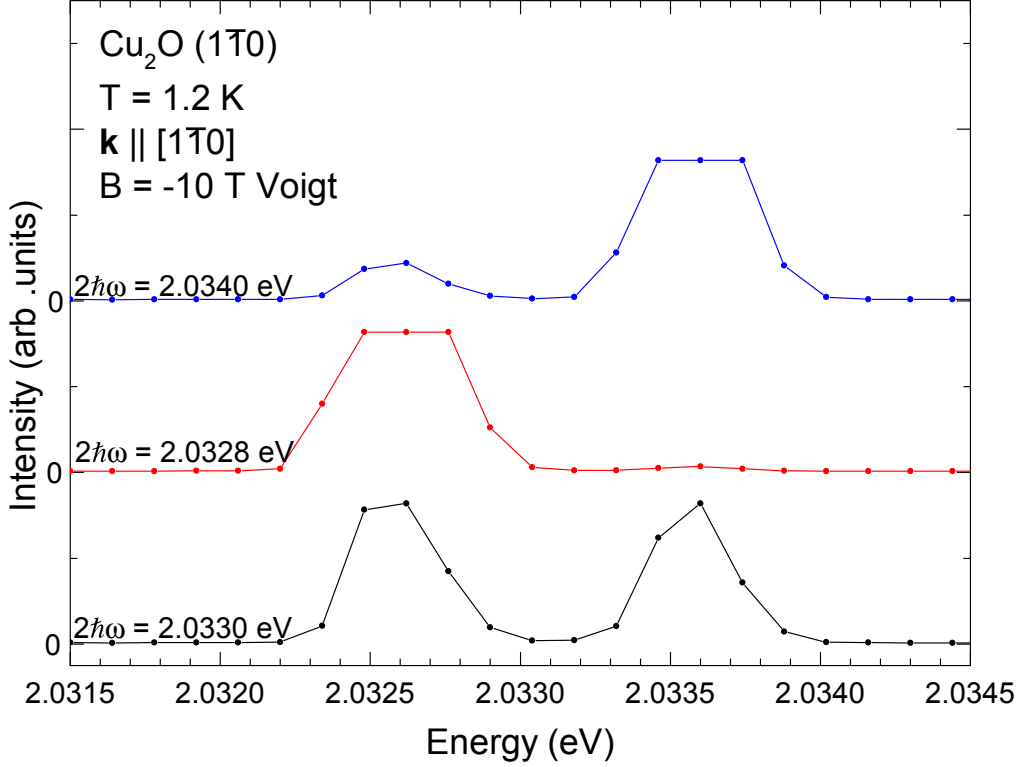
Figure 6.7. – Emission spectra in the **k** ∥ [1$\bar{1}$0] configuration for different fixed two-photon excitation wavelengths in a Voigt magnetic field $B^0 = 10\,\text{T}$. For excitation at $2\hbar\omega = 2.0332\,\text{eV}$ just in between the $m = \pm 1$ 1s exciton states both states lead to SHG. For excitation at $2\hbar\omega = 2.0328\,\text{eV}$ (red dots) and $2\hbar\omega = 2.0334\,\text{eV}$ (blue dots) on one of the exciton states respectively only the one state leads to SHG. For $2\hbar\omega = 2.0334\,\text{eV}$ (blue dots) also the lower lying resonance is observed. The flat top profile of the resonances stems from saturation of the CCD chip.

A possible explanation for the observed signal is resonant TPA-PL with an intermediate relaxation between the different 1s orthoexciton states. This is supported by the TPA-PL measurement in Fig. 6.4, which showed emission from the Γ_5 phonon and bound exciton states under a two-photon excitation of the 1s orthoexciton. The emission from the lower lying states is only possible due to the generation of excitons in addition to the parametric SHG process. To investigate this mechanism the rotational anisotropy of the incident and the emitted transition are presented separately in Fig. 6.2. The incident two-photon transition is in good agreement with a two-photon ED transition. The EQ one-photon transition has a more complicated shape, but the main features are in good agreement with the expected anisotropy of the EQ transition. Although these measurements support the TPA-PL mechanism, further investigations in a magnetic field reveal a more complicated situation.

The observation of SHG from the 1s orthoexciton in the **k** ∥ [001] direction by Kono et al. [33] cannot be explained by the same EQ mechanism. The susceptibility calculations
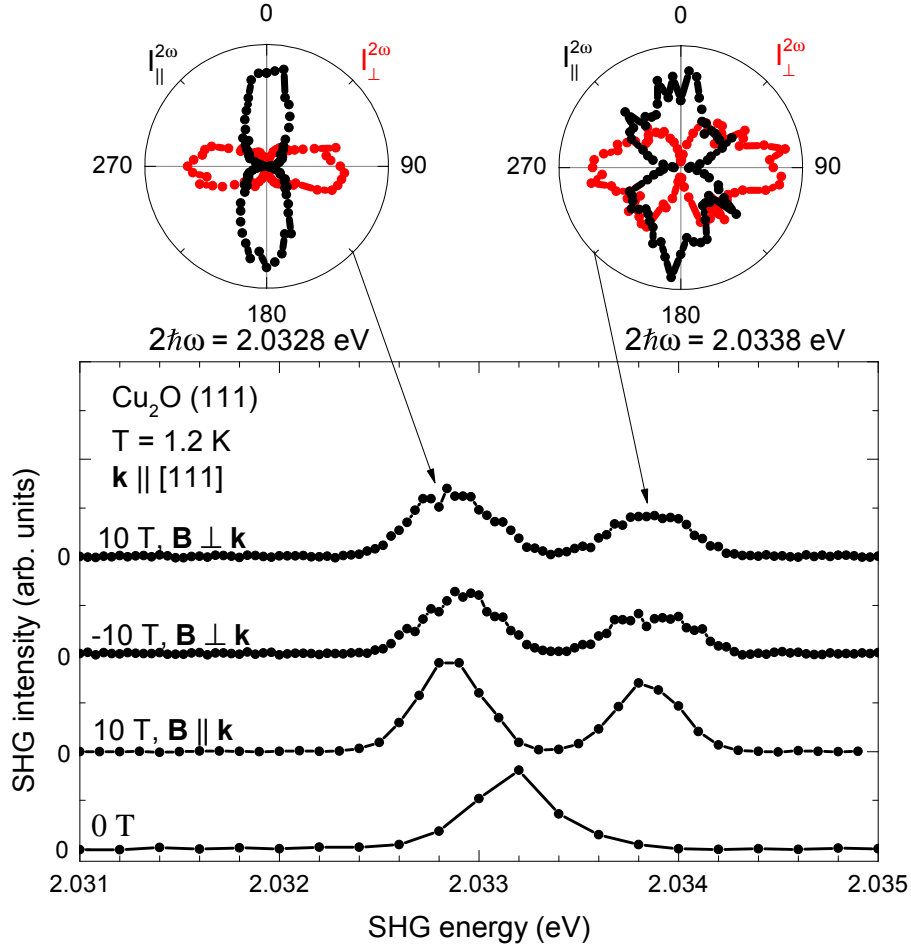
Figure 6.8. – (a) SHG spectra in the **k** ∥ [111] direction for different magnetic field configurations. The $B^0 = 0\,\mathrm{T}$ spectra was shown and discussed before in Fig. 6.1 and is presented for comparison. For Faraday and Voigt configuration resonant SHG from the $m = \pm 1$ states of the 1s orthoexciton is observed. For none of the configurations the $m = 0$ exciton state is observed in contrast to the **k** ∥ [1$\bar{1}$0] direction. Anisotropies for both resonances in the Voigt configuration are presented. Both parallel anisotropies are two-fold perpendicular to the magnetic field and both crossed anisotropies are parallel to the magnetic field. The anisotropy for $m = -1$ has a clear two-fold shape, whereas the $m = +1$ anisotropy has a additional small features.

show that EQ SHG is forbidden in this direction as shown in Sec. 2.3.4. Calculating the specific selection rules for the transition revealed that a two-photon ED process is only allowed to the Γ_x^5 and Γ_y^5 states whereas the one-photon EQ transition only couples to the Γ_z^5 states. This direction is not investigated in this thesis, because it would be prone to error to align the **k** ∥ [001] direction for the crystal cut of sample H28. Instead the **k** ∥ [1$\bar{1}$0] direction is investigated. EQ SHG is also forbidden in this direction as shown in Sec. 2.3.4. In this case the one-photon EQ transition couples only to the $\Gamma_{[111]}^5$ states

and the two-photon transition couples only to the perpendicular states $\Gamma^5_{[1\bar{1}0]}$ and $\Gamma^5_{[11\bar{2}]}$. Again, SHG is found in the forbidden direction.

In order to test the proposed resonant TPA-PL mechanism a magnetic field is applied in Voigt configuration. The magnetic field splits the three $1s$ orthoexciton states into the three not degenerated $m = \pm 1,0$ states. In this case TPA-PL is not resonant anymore, because a relaxation between the states leads to a shift of the PL. Nevertheless resonant SHG is found for all three states in the $\mathbf{k} \parallel [1\bar{1}0]$ direction with a Voigt or Faraday magnetic field. These resonances cannot be explained by TPA-PL, because the degeneracy is lifted. The same was found by Kono et al. [33] for the $\mathbf{k} \parallel [001]$ direction. In Fig. 6.7 the cross relaxation of the different states in a magnetic field is investigated. The excitation of the $m = +1$ state revealed a small relaxation to the $m = -1$ resonance. There is no sign of cross relaxation to the $m = 0$ state. These measurements do not support the TPA-PL mechanism.

In [33] the admixture of the $1s$ exciton from the green series is proposed as a mechanism for the observed SHG, but it has a distance of over $\Delta E > 100\,\mathrm{meV}$ to the yellow $1s$ exciton. Both series also have similar selection rules as all the involved bands have the same parity and it is not clear how the admixture would give rise to SHG. Most probably, still another mechanism is involved in the observed signal. A common feature of every measurement can be found in a magnetic field, which showed the $m = \pm 1$ states. In every case the $m = +1$ state has a smaller intensity compared to the $m = -1$ resonance. This was observed for all three crystal directions $\mathbf{k} \parallel [111]$, $\mathbf{k} \parallel [1\bar{1}0]$, and $\mathbf{k} \parallel [11\bar{2}]$. This could either stem from an interaction of the $m = \pm 1$ with another state or the splitting in a magnetic field leading to an uneven distribution of oscillator strength between the states.

6.3. Magnetic-field-induced SHG of the yellow exciton series

6.3.1. The 1s paraexciton

SHG from the $1s$ orthoexciton was presented in the last section despite the forbidden one-photon ED transitions in the centrosymmetric Cu_2O. Due to an observation of the $m = 0$ states of the $1s$ orthoexciton in SHG spectra, it is expected that the admixture of the ortho and paraexciton states in a magnetic field some of the EQ oscillator strength is transferred to the otherwise forbidden paraexciton as explained in Sec. 2.2.4.

In Fig. 6.9 SHG measurements on the $1s$ paraexciton are presented. The laser is tuned resonant to the two-photon transition to the paraexciton $2\hbar\omega = 2.0206\,\mathrm{eV}$. Without a magnetic field (black dots) no resonance is observed. A minor feature at $\hbar\omega = 2.020\,\mathrm{eV}$ could stem from SHG of optical components in the setup, since a high integration time $t_{\mathrm{int}} = 20\,\mathrm{s}$ is used for the measurements. In a Voigt magnetic field of $B^0 = 10\,\mathrm{T}$ a SHG resonance at the paraexciton energy is observed.

Additionally, measurements of the relaxation from the three $1s$ orthoexciton states to the paraexciton were made. For these measurements the laser is tuned to the two-photon resonance of the $m = \pm 1,0$ states of the $1s$ orthoexciton and the PL from the paraexciton is detected. It turns out that the resolution of the experimental setup is not high enough
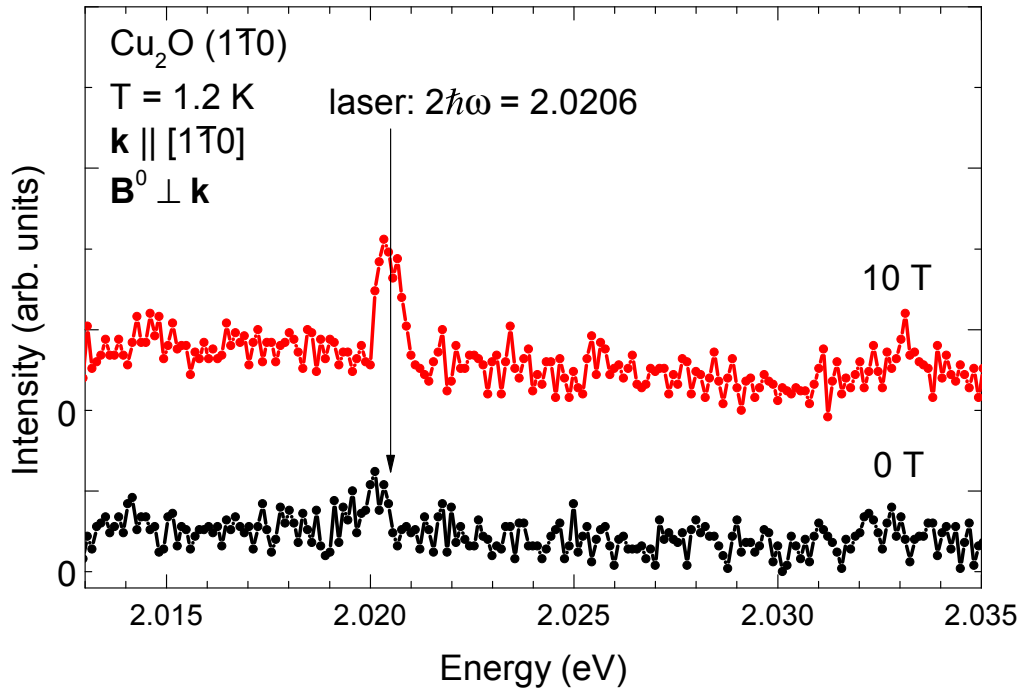
Figure 6.9. – Resonant SHG from the $1s$ paraexciton in a magnetic field. In the **k** ∥ [1$\bar{1}$0] configuration the laser light is tuned resonant to the two-photon transition to the $1s$ paraexciton $2\hbar\omega = 2.0206\,\text{eV}$. Without a magnetic field $B^0 = 0\,\text{T}$ (black dots) no SHG is detected. For $B^0 = 10\,\text{T}$ (red dots) SHG is found at the paraexciton resonance.

for this measurement, due to the rich phonon assisted transitions from the orthoexciton. Especially the Γ_3 phonon assisted transition from the orthoexciton presented in Fig. 6.4 is very intense and close to the paraexciton energy, which makes an observation of the paraexciton difficult.

6.3.2. MFISH of the yellow exciton series

In this section MFISH measurements in the energy range of the yellow $n \geq 2$ excitons are presented. Although the $2s$ and $3s$ states have the same selection rules as the $1s$ exciton, it is not expected to observe them without a magnetic field. The oscillator strength for $n \geq 2$ is much smaller than for the $1s$ exciton and even in noncentrosymmetric materials with ED transitions it is difficult to observe $n \geq 2$ excitons without an additional perturbation.

In Fig. 6.10(a) SHG spectra in a Voigt magnetic field are presented. No SHG in this region is found without a magnetic field (black dots). At $B^0 = 6\,\text{T}$ there are two resonances in the spectra. The first resonance is at $2\hbar\omega = 2.155\,\text{eV}$, which is the energy of the $2s$ yellow exciton $E_{2s} = 2.1544\,\text{eV}$. The second resonance at $2\hbar\omega = 2.161\,\text{eV}$ is at the energy of the $E_{3s} = 2.1603\,\text{eV}$ or $E_{3p} = 2.1609\,\text{eV}$ yellow exciton. The two exciton states are too close to each other to be resolved with certainty. At higher magnetic field strength $B^0 > 8\,\text{T}$ the resonance at $2\hbar\omega = 2.155\,\text{eV}$ vanishes and a third resonance at
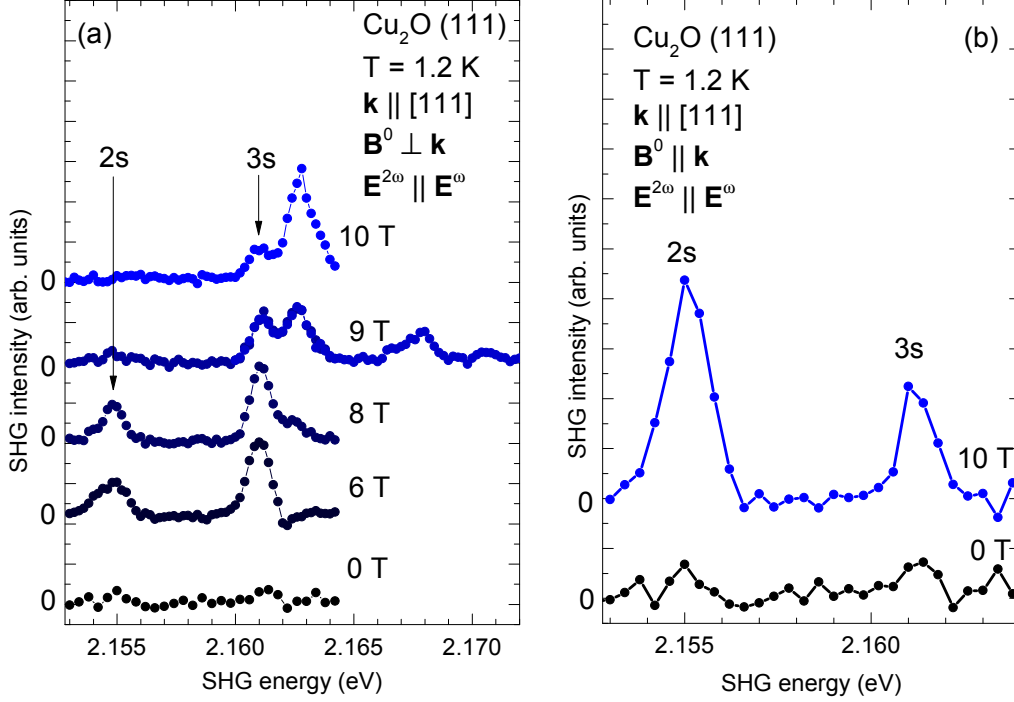
Figure 6.10. – MFISH spectra in the energy range of $n = 2$ and $n = 3$ yellow excitons in the $\mathbf{k} \parallel [111]$ configuration. Without a magnetic field no SHG is detected in this energy range (black dots). (a) In a Voigt magnetic field (blue dots) exciton resonances arise in the spectrum. At $B^0 = 6\,\mathrm{T}$ resonant SHG is at the energy of the $2s$ and $3s/3p$ exciton. At higher field strength these lines vanish and a resonance near the $3d$ state is found. For $B^0 = 9\,\mathrm{T}$ the spectrum covers the $n = 4$ energy range where the different angular momentum states cannot be resolved. (b) In a Faraday magnetic field (blue dots) of $B^0 = 10\,\mathrm{T}$ resonant SHG arises at the $2s$ and $3s/3p$ excitons. The maximum intensity in the spectrum at $B^0 = 10\,\mathrm{T}$ is about the same for Faraday and Voigt geometry.

$2\hbar\omega = 2.163\,\mathrm{eV}$ turns up, which seems to exchange oscillator strength with the second resonance at $2\hbar\omega = 2.161\,\mathrm{eV}$. The third resonance is close to the $E_{3d} = 2.1630\,\mathrm{eV}$ exciton. For $B^0 = 9\,\mathrm{T}$ the higher energy region is also included in the spectrum. There are further resonances, but at this energy the exciton states are so close, that it is difficult to assign them. They are in the vicinity of the $n = 4$ states.

For the found MFISH in Voigt geometry the magneto-Stark effect, which was introduced in Sec. 2.2.4, is a possible mechanism. In order to test for the magneto-Stark effect, measurements in a Faraday magnetic field are made, because the magneto-Stark effect should not be present for $\mathbf{B}^0 \parallel \mathbf{k}$. In Fig. 6.10(b) MFISH spectra in a Faraday magnetic field are presented. Two resonances at $2\hbar\omega = 2.155\,\mathrm{eV}$ and $2.161\,\mathrm{eV}$ are in the spectrum. These are the energies of the $2s$ and $3s$ yellow excitons. In contrast to the Voigt magnetic field only two resonances are found up to $B^0 = 10\,\mathrm{T}$. The intensity of the MFISH is about the same for both field directions. The $2s$ resonance in the Faraday geometry has about the same intensity as the $3p/3d$ resonance in Voigt geometry.

6.3.3. Discussion

The application of a magnetic field gives rise to SHG from the $1s$ paraexciton. The admixture of the $m = 0$ orthoexciton to the paraexciton leads to enhanced oscillator strength for the paraexciton. It is surprising that the SHG is strong enough to be detected, because the selection rules are not in favor of SHG of this exciton state. In fact, it is observed in the $\mathbf{k} \parallel [1\bar{1}0]$ configuration, in which not even SHG from the orthoexciton is expected. In order to understand the microscopic mechanism for SHG of the $1s$ paraexciton, it is first necessary to understand the mechanism of SHG of the orthoexciton in the forbidden direction. The oscillator strength of this mechanism is transferred to the paraexciton through the admixture in a magnetic field as explained in Sec. 2.2.4.

No crystallographic SHG is found in the region of yellow excitons with $n \geq 2$. This is not surprising, since the oscillator strength for $n \geq 2$ states is smaller than for the $1s$, which itself is weak due to the forbidden one-photon ED transition. The application of a Voigt magnetic field up to $B^0 = 6\,\mathrm{T}$ gives rise to SHG at the energy of the $2s$ and $3s/3p$ exciton as shown in Fig. 6.10. For a higher field strength the behavior is more complex and an additional resonance near the $3d$ state is found. The increase of SHG at the excitons is not expected, since the $1s$ exciton gains no oscillator strength in a magnetic field as shown in Fig. 6.5. A difference of the $1s$ yellow exciton to the $n \geq 2$ excitons is, that it has a higher binding energy and is far away from other excitons. The $3s$, $3p$ and $3d$ states are close to each other, which could lead to admixture. Especially the one-photon ED allowed $3p$ exciton would lead to SHG when it is admixed with the two-photon ED allowed $3s$ exciton. This is only possible through the magneto-Stark effect in a centrosymmetric system. The magneto-Stark effect should only mix the excitons in a Voigt magnetic field, but Fig. 6.10(b) shows that the resonances also appear in the Faraday configuration, which rules out the magneto-Stark effect as the main mechanism. The $3d$ states on the other hand have the same parity as the $3s$ states and they are admixed in a magnetic field, but since they have the same parity it is not expected that this admixture gives rise to SHG. The $3s/3d$ admixture could explain the complex change of intensity between the two resonances for high magnetic field strength.

The situation for the yellow $2s$ exciton is similar to that of the $3s$ exciton. The $2s$ yellow exciton is very close to the $1s$ green exciton, but the $1s$ green exciton has the same parity as the $2s$ yellow exciton and an admixture should not lead to enhanced SHG. The admixture of the $2p$ exciton via the magneto-Stark effect is possible, but can be ruled out as a mechanism due to the measurements in Faraday geometry.

The responsible mechanism for the MFISH in Cu$_2$O is not clear. A few possible mechanisms can be ruled out with the measurements in this section. Another possibility is the enhancement of phase matching, due to the influence of a magnetic field on the polariton dispersion, like it was proposed for the increase of THG in GaAs in Sec. 4.3.4. Since sample Cu$_2$O H28 is a thick bulk crystal, increased phase matching would have a strong influence, because the laser light has a long path through the crystal. A possible mechanism has to be in line with the complex change of intensity in a Voigt magnetic field and the different changes in a Faraday magnetic field.

6.4. Summary

Although the excitons Cu_2O have been extensively studied over the last decades, the found SHG in this chapter revealed several unexpected mechanisms leading to SHG. SHG is found in the EQ forbidden $\mathbf{k} \parallel [1\bar{1}0]$ direction even without a magnetic field. The application of a magnetic field leads to a splitting of the three degenerated orthoexciton states and each one is observed separately in SHG spectra. Comparing the SHG intensity between the forbidden and allowed directions reveals, that the SHG is at least as intense in the forbidden direction as in the allowed one. The found SHG cannot simply be attributed to higher order transitions. Several proposed mechanisms for this SHG could be ruled out by the measurements, but the right mechanism is still to be found.

The observation of SHG from the paraexciton in a magnetic field was demonstrated. This was expected from the admixture of the $m = 0$ orthoexciton states. The intensity of SHG from the paraexciton is very small, since it gains only a small amount of oscillator strength from the already weak EQ transitions through the admixture.

The MFISH from $n \geq 2$ excitons is demonstrated in Sec. 6.3.2. It was expected that the magneto-Stark effect could lead to enhanced SHG for these excitons. The increased SHG is in fact found, but the magneto-Stark effect is ruled out by measurements in a Faraday magnetic field.

It is overall interesting that the intensively investigated yellow exciton series in Cu_2O showed several unexpected SHG resonances at the exciton energies. In order to investigate the proposed influence of polaritons it is necessary to perform further measurements.

7. Summary and outlook

The measurements reported in this thesis provide insight into the role of excitons in SHG and THG near the band gap of the well known semiconductors GaAs, GaN, and Cu_2O. The influence of the temperature, electric fields, magnetic fields, and wave vector direction on the found nonlinearities are investigated. The strong electric dipole SHG of excitons is forbidden by optical selection rules in most cases, due to parity conservation. Only the application of an external electric or magnetic field leads to resonant electric dipole SHG from the excitons, because different exciton states become admixed in the external field. THG on the other hand is often allowed by the electric dipole selection rules where the influence of an external field is more complex.

The influence of an electric field on SHG and THG from excitons in GaAs is investigated. The spectral dependence and rotational anisotropy of resonant SHG and THG from the $1s$ exciton in an electric field is measured. The rotational anisotropies are modeled with susceptibility calculations. A microscopic model based on the Stark effect for the SHG and THG field dependence is presented.

A strong increase of resonant THG from excitons in GaAs in a magnetic field by 175 times at $B^0 = 10\,\mathrm{T}$ has been found. It was not expected and is not yet fully understood. Additional white light reflection, TPA-PL, and 3PA-PL measurements in a magnetic field helped to rule out several possible mechanisms. This can be explained phenomenologically by improved phase-matching conditions, due to exciton-polariton effects, which details a subject for further investigations. The microscopic mechanism, which is most probably related to the complex MFISH spectrum of GaAs, needs further clarification.

Cu_2O is a classic semiconductor for the exciton spectroscopy. It is known that electric quadrupole SHG from the yellow $1s$ orthoexciton can be observed in specific geometries. It is shown in this thesis that SHG can be observed even in the electric quadrupole SHG forbidden $\mathbf{k} \parallel [1\bar{1}0]$ direction. Through the application of a magnetic field all three degenerated $1s$ orthoexciton states are observed separately. SHG measurements allow us to observe the effect of the redistribution of the exciton oscillator strength from the $1s$ orthoexciton to the $1s$ paraexciton, which is observed in SHG spectroscopy for the first time. The application of a magnetic field also gives rise to exciton resonances for $n \geq 2$ states. Only the magneto-Stark effect is expected to lead to the mixing of exciton states in a centrosymmetric material such as Cu_2O. The magneto-Stark effect could be ruled out as the only mechanism responsible for the observed SHG of the $n \geq 2$ states.

In GaN the $1s$ exciton from all three exciton series is found in crystallographic THG. Additionally, the spectral feature of several defects and impurities of GaN were observed in THG spectra.

Measurements on the indirect band gap semiconductor Si presented in Sec. A.2 show

that it is possible to investigate the direct band-band transitions at the Γ point with THG in transmission geometry, even in a system with an indirect band gap, since the fundamental laser light energy can be tuned to the transparency region of the material.

The possibility of SHG from states near an indirect band gap is investigated in SiC, because the band gap energy lies in the spectral range of the experimental setup in contrast to Si. Existing reports showed that it is possible to have phonon assisted SHG, which is necessary for the investigation of an indirect band gap, but specific phonons had to be created optically [105]. Neither in SiC 4H nor 6H resonant enhanced SHG is found near the band gap in the measurements presented in Sec. A.3. Only non-resonant SHG is possible in the transparency region.

The presented electric and magnetic field induced measurements can also be applied to other semiconductors to investigate SHG and THG from excitons. Finding and understanding optical frequency conversion processes in semiconductors will remain an important field of research for the integration of optics into semiconductor technology.

Appendices

A. Indirect band gap semiconductors

A.1. Introduction

In this chapter SHG from the indirect band gap semiconductors Si and SiC are presented. Si has a diamond cubic lattice structure with O_h ($m\bar{3}m$) symmetry. The Si atoms are ordered on two FCC lattices, which are shifted along the cubic space diagonal. It is the most common semiconductor for technological applications and almost every computer chip is made from Si. The indirect band gap leads to a poor performance of optics in Si. A great effort is made to find solutions for the integration of Si with optical technology. For non-linear optics the centrosymmetric structure additionally reduces the non-linear interaction with light. All $\chi^{(2)}$ effects (SHG, parametric down-conversion, sum-frequency generation) are forbidden in the ED approximation.

For a long time SHG was only found in reflection geometry from strained interfaces [106, 107] or tailored photonic crystals [108]. Recently, SHG from a strained Si waveguide was found. THG on the other hand is allowed in Si and has been found in reflection from interfaces [109] and micro-cavities [110].

Both hexagonal SiC structures belong to the C_{6V} ($6mm$) group. It is a very hard material, which is used for several abrasive and cutting tools. For technological applications it is mainly known as a material for high power electrical switching devices. As shown in Sec. 2.2.3 hexagonal SiC has an indirect band gap energy of about $3\,\mathrm{eV}$, which is in contrast to Si within the spectral range of the experimental setup. This is exploited to investigate SHG near an indirect band gap.

A.2. Silicon (Si)

In Fig. A.1 THG spectra of Si in the $\mathbf{k} \parallel$ [111] configuration, which is normal incidence on the sample, are presented. Two resonances are in the spectrum at $3\hbar\omega = 3.48\,\mathrm{eV}$ and $3\hbar\omega = 3.51\,\mathrm{eV}$. One of these resonances is close to the direct band-band transition at $E_\Gamma = 3.46\,\mathrm{eV}$. Between $3\hbar\omega = 3.3\,\mathrm{eV}$ and $3.4\,\mathrm{eV}$ the intensity of the fundamental light is too small for THG, because of the OPO efficiency at this wavelength as explained in Sec. 3.1. The inset shows the rotational anisotropy at $3\hbar\omega = 3.51\,\mathrm{eV}$. The parallel anisotropy $I_\parallel^{3\omega}$ is constant and the crossed anisotropy $I_\perp^{3\omega}$ is four-fold.

The energy region of the band gap $E_\mathrm{g}(T = 5\,\mathrm{K}) = 1.170\,\mathrm{eV}$ is not accessible by the experimental setup. Optical harmonic generation in the energy range of an indirect band gap is investigated in SiC in the next section. Also SHG of Si near the band gap was investigated, but as expected from the centrosymmetric structure no SHG was observed.
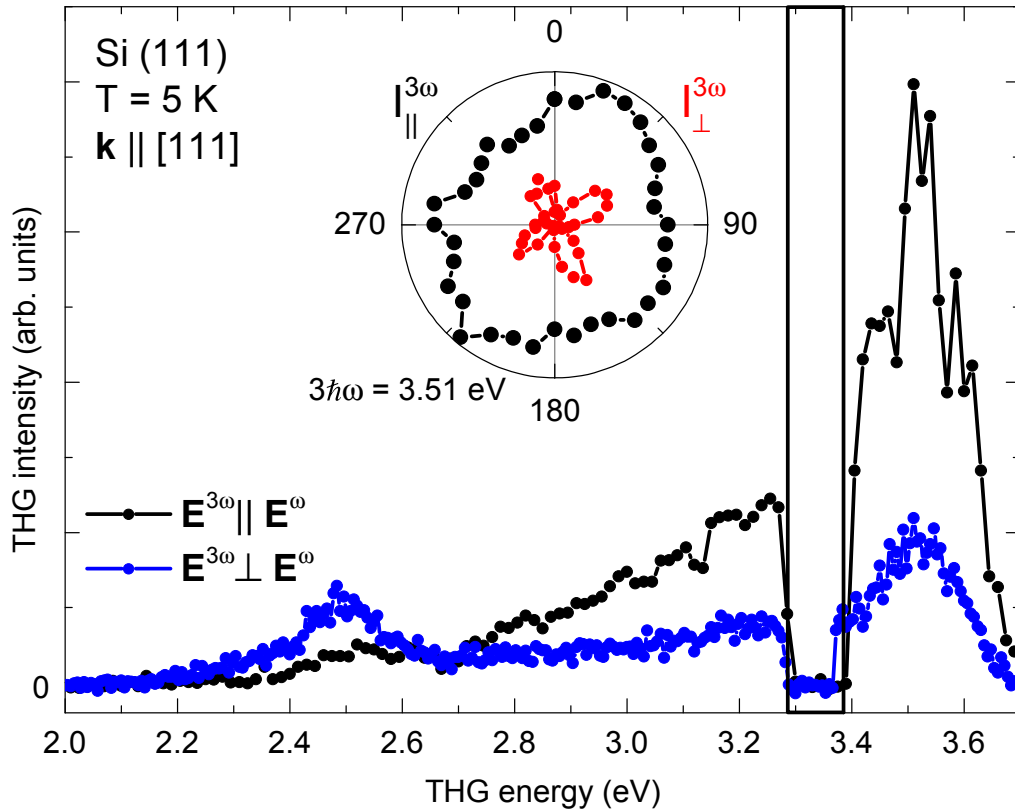
Figure A.1. – THG spectrum of Si in the **k** ∥ [111] direction. There is a strong resonance at $3\hbar\omega = 3.51\,\mathrm{eV}$ near the direct band-band transition and a smaller resonance at $3\hbar\omega = 2.5\,\mathrm{eV}$. In the spectral range between $3.3\,\mathrm{eV}$ and $3.4\,\mathrm{eV}$ (black box) the SHG intensity is zero, because the fundamental light intensity from the laser is too small for THG. The inset shows the rotational anisotropy for $3\hbar\omega = 3.51\,\mathrm{eV}$. The parallel anisotropy $I_{\parallel}^{3\omega}$ is constant and the crossed anisotropy $I_{\perp}^{3\omega}$ is four-fold.

A.3. Silicon Carbide (SiC)

In Fig. A.2 broad range SHG spectra of sample SiC6H are presented. As expected from the second order susceptibility $\chi^{(2)}$ in C_{6v} introduced in Sec. 2.3.4, no ED SHG is allowed for **k** ∥ [0001] (black dots). Only a small SHG intensity from higher order transitions is found, which is presented (for SiC 4H) in Fig. A.3. In a tilted geometry $\mathbf{k}\angle[0001] = 45°$ (blue dots) the spectrum is dominated by non-resonant crystallographic SHG. It has about 30 times more intensity than the SHG in the **k** ∥ [0001] configuration. The spectrum shows similar features as the crystallographic SHG in GaAs presented in Fig. 4.3. The strong oscillations of SHG intensity below the band gap stem from reflections in the sample. The refractive index of SiC 6H is rather high $n(\omega) > 2.5$ in the wavelength region of the fundamental and SHG light, which leads to reflections at the surface of the sample. Above the band gap the SHG light is reabsorbed from band-band transitions to the indirect band gap and the SHG intensity is reduced. The spectrum for SiC 4H shows the same feature

and wave vector direction dependence, which is not surprising as it belongs to the same symmetry group C_{6v}.
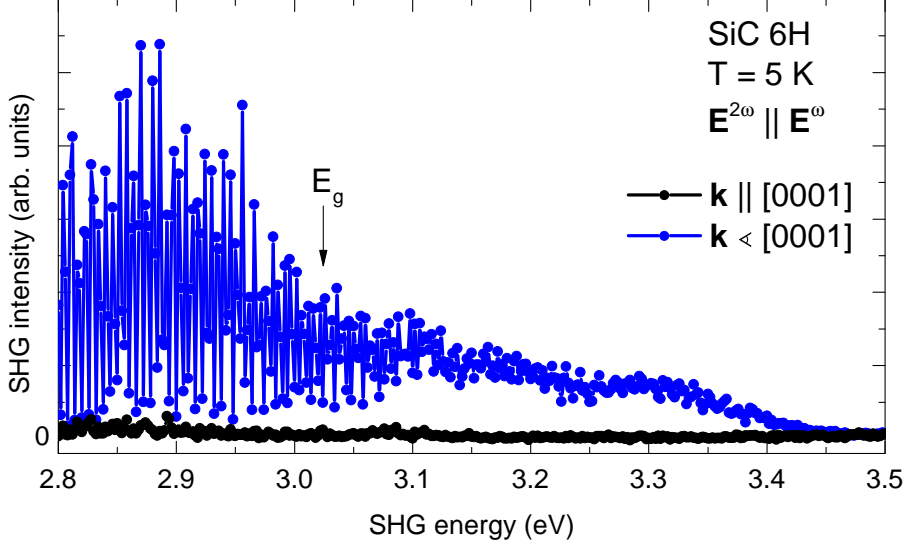
Figure A.2. – Broad range SHG spectra of SiC 6H in the vicinity of the band gap (black arrow). For normal incidence $\mathbf{k} \parallel$ [0001] (black dots) the SHG intensity is very small. For tilted incidence $\mathbf{k}\angle[0001] = 45\,^{\circ}$ (blue dots) there is non-resonant crystallographic SHG in the spectrum, which is 30 times more intense than for normal incidence. Below the band gap the intensity is high and oscillating. Above the band gap the intensity decreases until it vanishes near $2\hbar\omega \approx 3.5\,\mathrm{eV}$.

The normal incidence geometry $\mathbf{k} \parallel$ [0001] is ideal to investigate magnetic field induced effects, because the crystallographic SHG is close to zero and does not overpower MFISH. In Fig. A.3 (black dots) the spectrum of SiC 4H is presented. On this scale of intensity small features are found in the spectrum, which are much smaller than the ED SHG in the tilted geometry presented in Fig. A.2. The small features in the spectrum stem from higher order transitions, since ED SHG is forbidden in this geometry. It is most probable that the features are not connected to crystal states, but are connected to the already mentioned reflections in the sample, which could lead to an enhancement of higher order SHG. The application of a Voigt magnetic field $B^0 = 7\,\mathrm{T}$ does not lead to MFISH. Only small changes in the spectrum can be made out, which are addressed in the Discussion section.

In Fig. A.4 the rotational anisotropies for SiC 4H are presented. For $\mathbf{k} \parallel$ [0001] the anisotropy has the typical six-fold shape for SHG in normal incidence on a hexagonal lattice. Since ED SHG is forbidden in this geometry it has to stem from higher order transitions. The six-fold shape verifies, that the detected SHG in $\mathbf{k} \parallel$ [0001] in Fig. A.3 does not stem from a small misalignment, but from higher order transitions. The six-fold shape is found above and below the band gap for SHG. The rotational anisotropies for a tilted sample about the x axis with $\Theta \approx 45\,^{\circ}$ presented in Fig. A.4 (b,c) clearly have a different shape. The parallel intensity $I_{\parallel}^{2\omega}$ is two-fold with an intensity maximum at
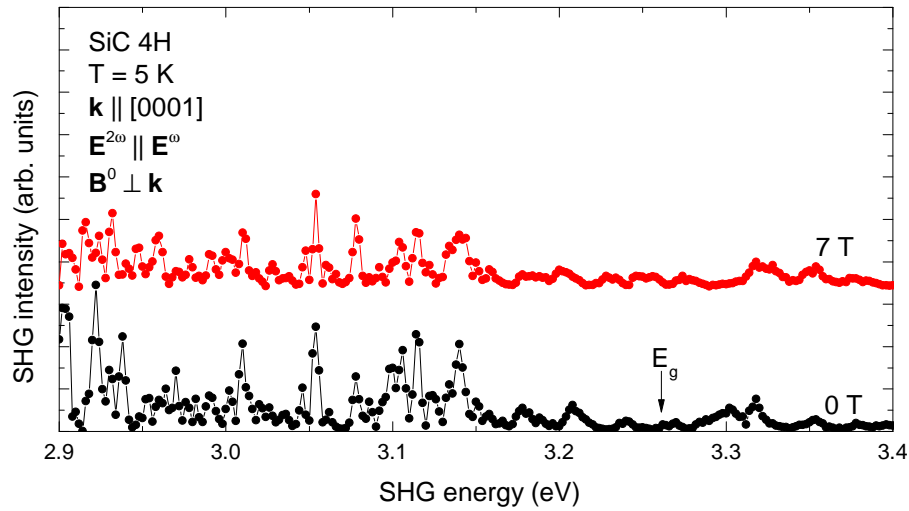
Figure A.3. – Broad range SHG spectra for SiC 4H in the vicinity of the band gap. Without a magnetic field (black dots) several small features are in the spectrum. The application of a magnetic field $B^0 = 7\,\mathrm{T}$ in Voigt geometry (blue dots) reveals only small differences. No induced SHG is found.

$\varphi = 90°$, which lies along the c axis. The crossed anisotropy is four-fold $I_\perp^{2\omega}$ and its exact shape depends on the wavelength. At $2\hbar\omega = 3.32\,\mathrm{eV}$ two of the intensity maxima are stronger than the other two. At $2\hbar\omega = 3.15\,\mathrm{eV}$ the maxima all have the same intensity.
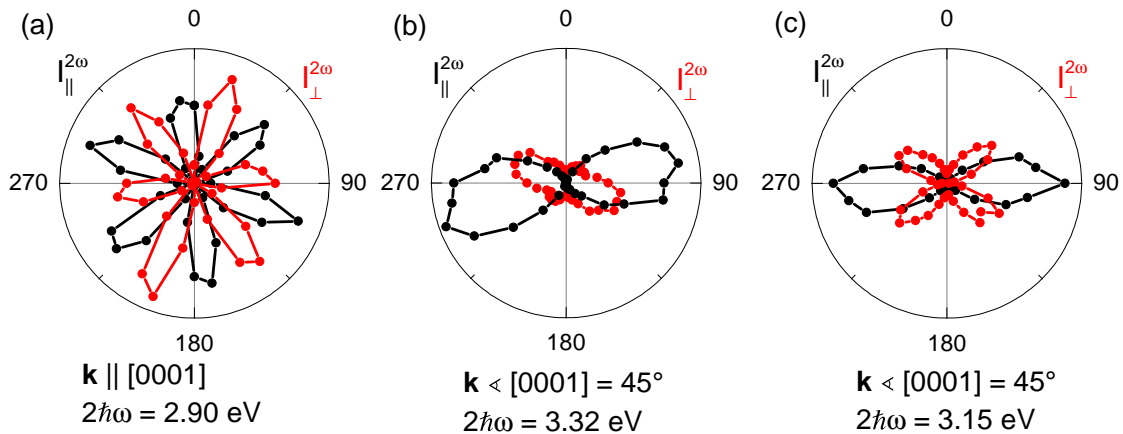
Figure A.4. – Rotational anisotropies of SiC 4H. (a) For $\mathbf{k} \parallel [0001]$ the anisotropy has the typical six-fold shape for normal incidence on a hexagonal structure. (b,c) For a tilting about the x axis with $\Theta \approx 45°$ the parallel intensity $I_\parallel^{2\omega}$ is two-fold along $\varphi = 90°$. The crossed intensity $I_\perp^{2\omega}$ is four-fold. Depending on the wavelength the intensity maxima are different. In (b) the maxima for the crossed intensity at $\varphi = 45°$ and $\varphi = 125°$ are smaller than the other two.

A.4. Discussion

The measurements in Si presented in Fig. A.1 show that it is possible to investigate states near the direct band-band transition at the Γ point with $E_\Gamma = 3.4\,\text{eV}$, despite the small indirect band gap of $1.17\,\text{eV}$. Typically, these states were only investigated in reflection geometry, because the light from the direct transition is reabsorbed by states at the band gap. THG makes it possible to choose a fundamental wavelength in the transparency region, while investigating direct band-band transitions. A strong increase of THG is found at $3\hbar\omega = 3.5\,\text{eV}$, which is close to the direct band-band transition. A smaller intensity maximum at $3\hbar\omega = 2.5\,\text{eV}$ is well below E_Γ. It could stem from crystal defects as unwanted doping or lattice defects, similar to the found resonances in GaN in Fig. 5.3.

In SiC it is possible to investigate SHG near the indirect band gap with the experimental setup used for the investigations. The crystallographic SHG of SiC 4H and SiC 6H is similar to GaAs. For specific geometries $\mathbf{k} \parallel [0001]$ no ED SHG is allowed and only a small SHG intensity from higher order transitions is found. For a tilted geometry non-resonant ED SHG is found, which is reabsorbed above the band gap.

In the $\mathbf{k} \parallel [0001]$ geometry a Voigt magnetic field does not lead to MFISH near the band gap. This is somewhat expected, because states near the indirect band gap cannot contribute to SHG, because the SHG transitions are nearly vertical in the band structure. There is an existing report about phonon assisted SHG [105], but it was done with specific phonons which were excited by an infrared laser. In the presented measurements on SiC there is no sign of resonant SHG from states near the band gap, which can only be reached with phonon assisted transitions. The small influence of a magnetic field on the SHG spectrum presented in Fig. A.3 probably stems from changes of the refractive index from the magnetic field. This changes the phase-matching conditions for SHG and influences the spectrum.

B. From perturbation theory to susceptibility

In order to derive Eq. (2.9) perturbation theory is used to calculatee the influence of the electric light field $\mathbf{V}$ on the atomic wave function $\mathbf{H}_0$ [7].

$$\mathbf{H} = \mathbf{H}_0 + \lambda \mathbf{V} \tag{B.1}$$

The parameter λ is necessary for perturbation theory and can range from 0 to 1 in order to vary the strength of the perturbation. The value $\lambda = 1$ represents the actual situation. The wave function, which solves Schroedinger's equation, can be expanded into a power series in terms of λ

$$\Psi = \Psi^{(0)} + \lambda \Psi^{(1)} + \lambda^2 \Psi^{(2)} + \dots . \tag{B.2}$$

Each of the wave functions can be expressed in terms of the probability $a_m^{(N)}$ of being in a particular eigenstate. The probability of being in a higher order state by the perturbation $\mathbf{V}$ can be seen in analogy to the classical case of introducing harmonics due to a strong light field of an incident wave.

$$\Psi^{(N)} = \sum_l a_l^{(N)} u_l e^{i\omega_i t} \tag{B.3}$$

In this equation u_l is the part of the wave function which is not time dependent. By using Schroedinger's equation, a general description for $a_n^{(N)}$ can be derived:

$$a_m^{(N)}(t) = (i\hbar)^{-1} \sum_l \int_{-\infty}^{t} dt' \langle u_m | \mathbf{V} | u_l \rangle a_l^{(N-1)}(t') e^{i\omega_{ml} t'} \tag{B.4}$$

The probability of order N is related to all probabilities of lower order in this equation. In the lowest order the atom is known to be in the ground state $a_n^{(0)} = \delta_{ng}$. The highest order used in this thesis is necessary for THG. These can be derived successively from Eq. (B.4). Additionally, the general perturbation $\mathbf{V}$ will be specified to the ED transition moment as it is the strongest contribution. Other transitions can be calculated in the same manner.

$$\mu_{ml} = \int u_m^* \boldsymbol{\mu} u_l d^3 r \tag{B.5}$$

Now the probabilities up to third order can be derived successively:

$$a_{\mathrm{f}}^{(1)}(t) = \frac{1}{\hbar} \sum_{\mathrm{p}} \frac{\boldsymbol{\mu}_{\mathrm{fg}} \cdot \mathbf{E}(\omega_{\mathrm{p}})}{\omega_{\mathrm{mg}} - \omega_{\mathrm{p}}} \mathrm{e}^{i(\omega_{\mathrm{fg}} - \omega_{\mathrm{p}})t} \tag{B.6a}$$

$$a_{\mathrm{f}}^{(2)}(t) = \frac{1}{\hbar^2} \sum_{\mathrm{pq}} \sum_{\mathrm{m}} \frac{[\boldsymbol{\mu}_{\mathrm{fm}} \cdot \mathbf{E}(\omega_{\mathrm{q}})] [\boldsymbol{\mu}_{\mathrm{mg}} \cdot \mathbf{E}(\omega_{\mathrm{p}})]}{(\omega_{\mathrm{fg}} - \omega_{\mathrm{p}} - \omega_{\mathrm{q}}) (\omega_{\mathrm{mg}} - \omega_{\mathrm{p}})} \mathrm{e}^{i(\omega_{\mathrm{fg}} - \omega_{\mathrm{p}} - \omega_{\mathrm{q}})t} \tag{B.6b}$$

$$a_{\mathrm{f}}^{(3)}(t) = \frac{1}{\hbar^3} \sum_{\mathrm{pqr}} \sum_{\mathrm{mn}} \frac{[\boldsymbol{\mu}_{\mathrm{fm}} \cdot \mathbf{E}(\omega_{\mathrm{r}})] [\boldsymbol{\mu}_{\mathrm{nm}} \cdot \mathbf{E}(\omega_{\mathrm{q}})] [\boldsymbol{\mu}_{\mathrm{mg}} \cdot \mathbf{E}(\omega_{\mathrm{p}})]}{(\omega_{\mathrm{fg}} - \omega_{\mathrm{p}} - \omega_{\mathrm{q}} - \omega_{\mathrm{r}}) (\omega_{\mathrm{ng}} - \omega_{\mathrm{p}} - \omega_{\mathrm{q}}) (\omega_{\mathrm{mg}} - \omega_{\mathrm{p}})} \tag{B.6c}$$

With these probabilities the perturbation of the eigenstates of the system by an incident light field can be calculated. For non linear optics the influence of the electric dipole moment is most important. These dipole moments can radiate photons of higher frequency when they are excited by the incident photons, as it was shown in the classical approach. The first order polarization $\langle \mathbf{P}^{(1)} \rangle = \langle\,\Psi^{(0)}\,|\,\boldsymbol{\mu}\,|\,\Psi^{(1)}\,\rangle + \langle\,\Psi^{(1)}\,|\,\boldsymbol{\mu}\,|\,\Psi^{(0)}\,\rangle$ leads to the linear susceptibility $\chi_{\mathrm{ij}}^{(1)}(\omega_{\mathrm{p}})$ via the relation $P_{\mathrm{i}}^{(1)}(\omega_{\mathrm{p}}) = \sum_{\mathrm{j}} \chi_{\mathrm{ij}}^{(1)} E_{\mathrm{j}}(\omega_p)$. This susceptibility can finally be rewritten into the complex index of refraction, which covers many well-known linear optical effects. For SHG the second order polarization is important.

$$\left\langle \mathbf{P}^{(2)} \right\rangle = \left\langle\,\Psi^{(0)}\,\middle|\,\boldsymbol{\mu}\,\middle|\,\Psi^{(2)}\,\right\rangle + \left\langle\,\Psi^{(1)}\,\middle|\,\boldsymbol{\mu}\,\middle|\,\Psi^{(1)}\,\right\rangle + \left\langle\,\Psi^{(2)}\,\middle|\,\boldsymbol{\mu}\,\middle|\,\Psi^{(0)}\,\right\rangle \tag{B.7}$$

Plugging in the perturbed wave functions and using the definition of the second order susceptibility:

$$P_{\mathrm{i}}^{(2)} = \sum_{\mathrm{jk}} \sum_{(\mathrm{pq})} \chi_{\mathrm{ijk}}^{(2)}(\omega_{\mathrm{p}} + \omega_{\mathrm{q}}, \omega_{\mathrm{q}}, \omega_{\mathrm{p}}) E_{\mathrm{j}}(\omega_{\mathrm{q}}) E_{\mathrm{k}}(\omega_{\mathrm{p}}) \tag{B.8}$$

allows one to write down the second order susceptibility

$$\chi_{\mathrm{ijk}}^{(2)}(\omega_{\mathrm{p}} + \omega_{\mathrm{q}}, \omega_{\mathrm{q}}, \omega_{\mathrm{p}}) = \frac{N}{\hbar^2} \mathbb{P} \sum_{\mathrm{mn}} \left(\frac{\boldsymbol{\mu}_{\mathrm{gf}}^{\mathrm{i}} \boldsymbol{\mu}_{\mathrm{fm}}^{\mathrm{j}} \boldsymbol{\mu}_{\mathrm{mg}}^{\mathrm{k}}}{(\omega_{\mathrm{fg}} - \omega_{\mathrm{p}} - \omega_{\mathrm{q}}) (\omega_{\mathrm{mg}} - \omega_{\mathrm{p}})} + \right.$$
$$\frac{\boldsymbol{\mu}_{\mathrm{gf}}^{\mathrm{j}} \boldsymbol{\mu}_{\mathrm{fm}}^{\mathrm{i}} \boldsymbol{\mu}_{\mathrm{mg}}^{\mathrm{k}}}{\left(\omega_{\mathrm{fg}}^{*} + \omega_{\mathrm{q}}\right) (\omega_{\mathrm{mg}} - \omega_{\mathrm{p}})} +$$
$$\left. \frac{\boldsymbol{\mu}_{\mathrm{gf}}^{\mathrm{j}} \boldsymbol{\mu}_{\mathrm{fm}}^{\mathrm{k}} \boldsymbol{\mu}_{\mathrm{mg}}^{\mathrm{i}}}{\left(\omega_{\mathrm{fg}}^{*} + \omega_{\mathrm{q}}\right) \left(\omega_{\mathrm{mg}}^{*} + \omega_{\mathrm{p}} + \omega_{\mathrm{q}}\right)} \right) \tag{B.9}$$

in terms of the dipole transition moments $\boldsymbol{\mu}$ and light frequencies ω. The permutation operator $\mathbb{P}$ includes all (both) permutations of ω_{p} and ω_{q} and N is the density of the participating atoms. In principle, it is possible to calculate the exact value for $\chi_{\mathrm{ijk}}^{(2)}$ at this point. The precision of such a calculation depends on the description of the undisturbed wave functions. The band structure has to be known in the case of a semiconductor. In most cases the wave functions of the full band structure is not completely understood, as computations are very complex. In many cases it is sufficient to understand the ground state and states close to ω_{ng}. In the case of a semiconductor and near visible light this

is the valence band and conduction band. This is done for EuTe and it yields a good approximation of the nonlinear optical response of the material [38].
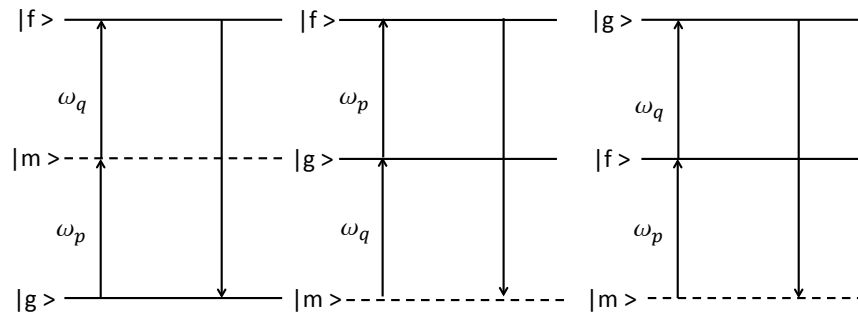
Figure B.1. – Visualization of the transitions included in Eq. (B.9). The states $|f\rangle$ and $|g\rangle$ are undisturbed crystal states in SHG spectroscopy and $|m\rangle$ are mixed light matter states which are reached by virtual transitions. (Similar to Boyd Fig. 3.2.2 [7])

In order to get Eq. (2.9), which is used to describe the measurements, a few simplifications have to be made. The full description of the second order susceptibility B.9 is not needed for SHG. In the SHG spectroscopy a singe wavelength ω is incident on the crystal and only 2ω is detected. Therefore the denominator is reduced by $\omega_{\mathrm{p}} = \omega_{\mathrm{q}} = \omega$ and $\omega_{\mathrm{ng}} = 2\omega_{\mathrm{p}} = 2\omega$. Instead of assuming every frequency to be complex, the frequencies are real and an imaginary damping term $i\Gamma$ takes the linewidth of the final state into account. It is also rewritten in terms of energy, because the energy levels of a semiconductor are the main focus. The first transition in Fig. B.1 describes the SHG from the measurement section. The mechanism responsible for SHG in semiconductors is a virtual transition from the ground state $|g\rangle$ to the final state $|f\rangle$. The state of interest is the final state and therefore its energy is introduced into the equation $\hbar\omega_{\mathrm{gf}} = \mathbf{E}_{\mathrm{f}}$. This is valid, because the ground state in semiconductors is usually the top of the valence band and is defined as the zero energy position. The important susceptibility parameters are rather the states and external fields than the frequencies $\chi^{(2)}_{\mathrm{ijk}}(\omega_{\mathrm{p}} + \omega_{\mathrm{q}},\omega_{\mathrm{q}},\omega_{\mathrm{p}}) \Rightarrow \chi^{(2)}_{\mathrm{ijk}}(\mathbf{E}_{\mathrm{f}},\mathbf{k}_{\mathrm{f}},\mathbf{B}^0,\mathbf{E}^0)$.

Bibliography

[1] P. A. Franken, A. E. Hill, C. W. Peters, and G. Weinreich, "*Generation of Optical Harmonics*," Phys. Rev. Lett. **7**, 118 (1961).

[2] E. Garmire and A. Kost, *Semiconductors and Semimetals* (Academic Press, 1998).

[3] D. A. Kleinman, "*Theory of Second Harmonic Generation of Light*," Phys. Rev. **128**, 1761–1775 (1962).

[4] S. Colin, E. Contesse, P. L. Boudec, G. Stephan, and F. Sanchez, "*Evidence of a saturable-absorption effect in heavily erbium-doped fibers*," Opt. Lett. **21**, 1987–1989 (1996).

[5] R. Singh, "*C. V. Raman and the Discovery of the Raman Effect*," Physics in Perspective **4**, 399–420 (2002).

[6] G. H. C. New and J. F. Ward, "*Optical Third-Harmonic Generation in Gases*," Phys. Rev. Lett. **19**, 556–559 (1967).

[7] R. W. Boyd, *Nonlinear optics* (Academic Press, 1992).

[8] Y. R. Shen, *The Principles of Nonlinear Optics* (Wiley, 2002).

[9] D. Fröhlich, "*Two- and three-photon spectroscopy in solids*," Physica Scripta **1991**, 125 (1991).

[10] N. Bloemberg, *Nonlinear Optics* (Benjamin, 1965).

[11] M. Fiebig, "*Revival of the magnetoelectric effect*," J. Phys. D: Appl. Phys. **38**, R123–R152 (2005).

[12] K. B. Eisenthal, "*Liquid Interfaces Probed by Second-Harmonic and Sum-Frequency Spectroscopy*," Chem. Rev. **96**, 1343–1360 (1996).

[13] S.-n. Zhu, Y.-y. Zhu, and N.-b. Ming, "*Quasi-Phase-Matched Third-Harmonic Generation in a Quasi-Periodic Optical Superlattice*," Science **278**, 843–846 (1997).

[14] V. Berger, "*Nonlinear Photonic Crystals*," Phys. Rev. Lett. **81**, 4136–4139 (1998).

[15] D. Eaton, "*Nonlinear Optical-Materials*," Science **253**, 281–287 (1991).

[16] W. Zipfel, R. Williams, R. Christie, A. Nikitin, B. Hyman, and W. Webb, "*Live tissue intrinsic emission microscopy using multiphoton-excited native fluorescence and second harmonic generation,*" Proceedings of the National Academy of Sciences of the United States of America **100**, 7075–7080 (2003).

[17] L. T. Cheng, W. Tam, S. H. Stevenson, G. R. Meredith, G. Rikken, and S. R. Marder, "*Experimental investigations of organic molecular nonlinear optical polarizabilities. 1. Methods and results on benzene and stilbene derivatives,*" J. Phys. Chem. **95**, 10631–10643 (1991).

[18] P. J. Campagnola and L. M. Loew, "*Second-harmonic imaging microscopy for visualizing biomolecular arrays in cells, tissues and organisms.*" Nat. Biotechnol. **21**, 1356 – 1360 (2003).

[19] H. R. Philipp and H. Ehrenreich, "*Optical Properties of Semiconductors,*" Phys. Rev. **129**, 1550–1560 (1963).

[20] M. Fiebig, V. V. Pavlov, and R. V. Pisarev, "*Second-harmonic generation as a tool for studying electronic and magnetic structures of crystals: review,*" J. Opt. Soc. Am. B **22**, 96–118 (2005).

[21] Osram AG, (2014), http://www.osram-os.com/.

[22] S. Harris, "*Tunable optical parametric oscillators,*" Proceedings of the IEEE **57**, 2096–2113 (1969).

[23] D. C. Edelstein, E. S. Wachman, and C. L. Tang, "*Broadly tunable high repetition rate femtosecond optical parametric oscillator.*" Appl. Phys. Lett. **54**, 1728 (1989).

[24] M. Fejer, G. Magel, D. H. Jundt, and R. Byer, "*Quasi-phase-matched second harmonic generation: tuning and tolerances,*" Quantum Electronics, IEEE Journal of **28**, 2631–2654 (1992).

[25] M. Houe and P. D. Townsend, "*An introduction to methods of periodic poling for second-harmonic generation,*" J. Phys. D: Appl. Phys. **28**, 1747 (1995).

[26] B. Brecht, A. Eckstein, A. Christ, H. Suche, and C. Silberhorn, "*From quantum pulse gate to quantum pulse shaper-engineered frequency conversion in nonlinear optical waveguides,*" New Journal of Physics **13**, 065029 (2011).

[27] H. P. Wagner, M. Kühnelt, W. Langbein, and J. M. Hvam, "*Dispersion of the second-order nonlinear susceptibility in ZnTe, ZnSe, and ZnS,*" Phys. Rev. B **58**, 10494–10501 (1998).

[28] S. Bergfeld and W. Daum, "*Second-Harmonic Generation in GaAs: Experiment versus Theoretical Predictions of chi(2),*" Phys. Rev. Lett. **90**, 036801 (2003).

[29] J. L. P. Hughes and J. E. Sipe, "*Calculation of second-order optical response in semiconductors*," Phys. Rev. B **53**, 10751–10763 (1996).

[30] J. E. Sipe and E. Ghahramani, "*Nonlinear optical response of semiconductors in the independent-particle approximation*," Phys. Rev. B **48**, 11705–11722 (1993).

[31] M. Lafrentz, D. Brunne, A. V. Rodina, V. V. Pavlov, R. V. Pisarev, D. R. Yakovlev, A. Bakin, and M. Bayer, "*Second-harmonic generation spectroscopy of excitons in ZnO*," Phys. Rev. B **88**, 235207 (2013).

[32] V. V. Pavlov, A. M. Kalashnikova, R. V. Pisarev, I. Sänger, D. R. Yakovlev, and M. Bayer, "*Magnetic-Field-Induced Second-Harmonic Generation in Semiconductor GaAs*," Phys. Rev. Lett. **94**, 157404 (2005).

[33] S. Kono and N. Nagasawa, "*Two-photon resonant emissions of 1s ortho-excitons in Cu_2O in a magnetic field*," J. Lumin. **76-7**, 86–89 (1998), 11th International Conference on Dynamical Processes in Excited States of Solids, Mittelberg, Austria, Jul 20-24, 1997.

[34] J. L. Shay, "*Temperature Dependence of the Energy Gap in GaAs*," Phys. Rev. B **4**, 1385–1386 (1971).

[35] I. Sänger, D. R. Yakovlev, B. Kaminski, R. V. Pisarev, V. V. Pavlov, and M. Bayer, "*Orbital quantization of electronic states in a magnetic field as the origin of second-harmonic generation in diamagnetic semiconductors*," Phys. Rev. B **74**, 165208 (2006).

[36] K. Reimann, M. Steube, D. Fröhlich, and S. Clarke, "*Exciton binding energies and band gaps in GaN bulk crystals*," J. Cryst. Growth **189-190**, 652 – 655 (1998).

[37] C. Klingshirn, *Semiconductor Optics* (Springer, 2007).

[38] B. Kaminski, M. Lafrentz, R. V. Pisarev, D. R. Yakovlev, V. V. Pavlov, V. A. Lukoshkin, A. B. Henriques, G. Springholz, G. Bauer, E. Abramof, P. H. O. Rappl, and M. Bayer, "*Optical second harmonic generation in the centrosymmetric magnetic semiconductors EuTe and EuSe*," Phys. Rev. B **81**, 155201 (2010).

[39] M. Y. Shen, S. Koyama, M. Saito, T. Goto, and N. Kuroda, "*Second-harmonic generation resonant to the 1S orthoexciton level of cuprous oxide*," Phys. Rev. B **53**, 13477–13481 (1996).

[40] J. Wildenauer, "*Generation of the ninth, eleventh, and fifteenth harmonics of iodine laser radiation*," J. Appl. Phys. **62**, 41–48 (1987).

[41] J. D. Jackson, *Classical Electrodynamics* (J. Wiley & Sons, New York, 1962).

[42] M. Bass, P. A. Franken, and J. F. Ward, "*Optical Rectification*," Phys. Rev. **138**, A534–A542 (1965).

[43] P. D. Maker, R. W. Terhune, M. Nisenoff, and C. M. Savage, "*Effects of Dispersion and Focusing on the Production of Optical Harmonics*," Phys. Rev. Lett. **8**, 21–22 (1962).

[44] M. Lafrentz, D. Brunne, B. Kaminski, V. V. Pavlov, A. B. Henriques, R. V. Pisarev, D. R. Yakovlev, G. Springholz, G. Bauer, E. Abramof, P. H. O. Rappl, and M. Bayer, "*Optical third-harmonic spectroscopy of the magnetic semiconductor EuTe*," Phys. Rev. B **82**, 235206 (2010).

[45] J. Frenkel, "*On the Transformation of light into Heat in Solids. I*," Phys. Rev. **37**, 17–44 (1931).

[46] G. H. Wannier, "*The Structure of Electronic Excitation Levels in Insulating Crystals*," Phys. Rev. **52**, 191–197 (1937).

[47] N. Ashcroft and N. Mermin, *Solid State Physics* (Saunders College, Philadelphia, 1976).

[48] S. W. K. Hartmut Haug, *Quantum Theory of the Optical and Electronic Properties of Semiconductors*, 4th ed. (World Scientific, 2004).

[49] J. J. Hopfield, "*Theory of the Contribution of Excitons to the Complex Dielectric Constant of Crystals*," Phys. Rev. **112**, 1555–1567 (1958).

[50] A. Quattropani, L. Andreani, and F. Bassani, "*Quantum theory of polaritons with spatial dispersion: Exact solutions*," Il Nuovo Cimento D **7**, 55–69 (1986).

[51] I. I. Rabi, "*On the Process of Space Quantization*," Phys. Rev. **49**, 324–328 (1936).

[52] T. Kurosawa, "*Polarization Waves in Solids*," J. Phys. Soc. Jpn. **16**, 1298–1308 (1961).

[53] R. Börnstein and H. H. Landolt, *Landolt-Börnstein, Numerical Data and Functional Relationships, New Series, Group III*, Vol. 41 (Springer, Berlin, 2001).

[54] J. S. Michaelis, K. Unterrainer, E. Gornik, and E. Bauser, "*Electric and magnetic dipole two-photon absorption in semiconductors*," Phys. Rev. B **54**, 7917–7920 (1996).

[55] S. I. Gubarev, T. Ruf, M. Cardona, and K. Ploog, "*Magnetoluminescence of GaAs in the quasiclassical limit*," Phys. Rev. B **48**, 1647–1658 (1993).

[56] V. Bougrov, M. Levinshtein, S. Rumyantsev, and A. Zubrilov, *Properties of Advanced SemiconductorMaterials GaN, AlN, InN, BN, SiC, SiGe* (Wiley & Sons, 2001).

[57] B. Monemar, "*Fundamental energy gap of GaN from photoluminescence excitation spectra*," Phys. Rev. B **10**, 676–681 (1974).

[58] R. G. Waters, F. H. Pollak, R. H. Bruce, and H. Z. Cummins, "*Effects of uniaxial stress on excitons in Cu_2O,*" Phys. Rev. B **21**, 1665–1675 (1980).

[59] H. Matsumoto, K. Saito, M. Hasuo, S. Kono, and N. Nagasawa, "*Revived interest on yellow-exciton series in Cu_2O: An experimental aspect,*" Solid State Commun. **97**, 125 – 129 (1996).

[60] A. Daunois, J. Deiss, and B. Meyer, "*Spectrophotometric study of the blue and violet absorption of Cu2O.*" J. Phys. France **27**, 142–146 (1966).

[61] J. Grun, M. Sieskind, and S. Nikitine, "*Low-temperature determination of the oscillator strength of Cu_2O lines of the green series.*" J. Phys. Radium **22**, 176–178 (1961).

[62] T. Tayagaki, A. Mysyrowicz, and M. Kuwata-Gonokami, "*The Yellow Excitonic Series of Cu_2O Revisited by Lyman Spectroscopy,*" J. Phys. Soc. Jpn. **74**, 1423–1426 (2005).

[63] G. B. H. von Högersthal, G. Dasbach, D. Fröhlich, M. Kulka, H. Stolz, and M. Bayer, "*Dynamic band gap shifts and magneto-absorption of Cu_2O,*" J. Lumin. **112**, 25 – 29 (2005), 6th International Conference on Excitonic Processes in Condensed Matter (EXCON '04).

[64] C. Uihlein, D. Fröhlich, and R. Kenklies, "*Investigation of exciton fine structure in Cu_2O,*" Phys. Rev. B **23**, 2731–2740 (1981).

[65] W. Bludau, A. Onton, and W. Heinke, "*Temperature dependence of the band gap of silicon,*" J. Appl. Phys. **45**, 1846–1848 (1974).

[66] C. Persson and U. Lindefelt, "*Dependence of energy gaps and effective masses on atomic positions in hexagonal SiC,*" Journal of Applied Physics **86**, 5036–5039 (1999).

[67] C. Persson and U. Lindefelt, "*Relativistic band structure calculation of cubic and hexagonal SiC polytypes,*" Journal of Applied Physics **82**, 5496–5508 (1997).

[68] W. Choyke, W. and L. Patrick, "*Absorption and reflection measurements on cubic SiC,*" Bulletin of the american physical society **14**, 417 (1969).

[69] T. S. Moss, "*Optical Absorption Edge in GaAs and Its Dependence on Electric Field,*" J. Appl. Phys. **32**, 2136–2139 (1961).

[70] J. S. Blakemore, *Gallium Arsenide: A Reprint Volume (Key Papers in Physics)* (Amer Inst of Physics Publ Srvs, 1987).

[71] C. J. Johnson, G. H. Sherman, and R. Weil, "*Far Infrared Measurement of the Dielectric Properties of GaAs and CdTe at 300 K and 8 K,*" Appl. Opt. **8**, 1667–1671 (1969).

[72] G. Baldassarri Höger von Högersthal, D. Fröhlich, M. Kulka, T. Auer, M. Bayer, and H. Stolz, "*Acoustic and optical phonon scattering of the 1S yellow orthoexciton in Cu2O*," Phys. Rev. B **73**, 035202 (2006).

[73] D. Fröhlich and R. Kenklies, "*Polarization Dependence of Two-Photon Magnetoab-sorption of the 1S Exciton in Cu_2O*," Phys. Stat. Sol. (b) **111**, 247–253 (1982).

[74] J. Brandt, D. Fröhlich, C. Sandfort, M. Bayer, H. Stolz, and N. Naka, "*Ultranarrow Optical Absorption and Two-Phonon Excitation Spectroscopy of Cu_2O Paraexcitons in a High Magnetic Field*," Phys. Rev. Lett. **99**, 217403 (2007).

[75] I. Sänger, Magnetic-Field-Induced Second Harmonic Generation in Semiconducers and Insulators, Ph.D. thesis, TU Dortmund (2006).

[76] J. Jerphagnon and S. K. Kurtz, "*Maker Fringes: A Detailed Comparison of Theory and Experiment for Isotropic and Uniaxial Crystals*," Journal of Applied Physics **41**, 1667–1681 (1970).

[77] M. Bass, C. DeCusatis, J. Enoch, V. Lakshminarayanan, G. Li, C. MacDonald, V. Mahajan, and E. Van Stryland, *Handbook of Optics, Third Edition Volume IV: Optical Properties of Materials, Nonlinear Optics, Quantum Optics (set)*, Handbook of Optics (Mcgraw-hill, 2009).

[78] U. Fano, "*Effects of Configuration Interaction on Intensities and Phase Shifts*," Phys. Rev. **124**, 1866–1878 (1961).

[79] M. Göppert-Mayer, "*Über Elementarakte mit zwei Quantensprüngen*," Annalen der Physik **401**, 273–294 (1931).

[80] J. J. Hopfield, J. M. Worlock, and K. Park, "*Two-Quantum Absorption Spectrum of KI*," Phys. Rev. Lett. **11**, 414–417 (1963).

[81] G. D. Mahan, "*Theory of Two-Photon Spectroscopy in Solids*," Phys. Rev. **170**, 825–838 (1968).

[82] S. V. Popov, Y. P. Svirko, and N. I. Zheludev, *Susceptibility Tensors for Nonlinear Optics* (Institute of Physics Publishers, Philadelphia, 1995).

[83] R. R. Birss, *Symmetry and Magnetism* (North-Holland Pub. Co., 1967).

[84] L. Hanke and D. Fröhlich, "Spin scattering of 1s orthoexcitons in cu₂o," Solid State Communications **116**, 621 – 624 (2000).

[85] GWU, premiScan brochure (2007).

[86] Princeton Instruments, Pixis256 datasheet (2010).

[87] Jobyn Ivon, Specifications brochure: Gratings for HR460 (2013).

[88] B. B. Krichevtsov, V. V. Pavlov, R. V. Pisarev, and V. N. Gridnev, "*Magnetoelec-tric Spectroscopy of Electronic Transitions in Antiferromagnetic Cr_2O_3,*" Phys. Rev. Lett. **76**, 4628–4631 (1996).

[89] R. H. French, H. Müllejans, and D. J. Jones, "*Optical Properties of Aluminum Ox-ide: Determined from Vacuum Ultraviolet and Electron Energy-Loss Spectroscopies,*" J. Am. Ceram. Soc. **81**, 2549–2557 (1998).

[90] W. Shan, R. J. Hauenstein, A. J. Fischer, J. J. Song, W. G. Perry, M. D. Bremser, R. F. Davis, and B. Goldenberg, "*Strain effects on excitonic transitions in GaN: Deformation potentials,*" Phys. Rev. B **54**, 13460–13463 (1996).

[91] G. Stillman, C. Wolfe, and J. Dimmock, "*Hall coefficient factor for polar mode scattering in n-type GaAs,*" J. Phys. Chem. Solids **31**, 1199 – 1204 (1970).

[92] J. S. Blakemore, "*Semiconducting and other major properties of gallium arsenide,*" J. Appl. Phys. **53**, R123–R181 (1982).

[93] C. Neumann, A. Nöthe, and N. O. Lipari, "*Two-photon magnetoabsorption of ZnTe, CdTe, and GaAs,*" Phys. Rev. B **37**, 922–932 (1988).

[94] D. D. Sell, "*Resolved Free-Exciton Transitions in the Optical-Absorption Spectrum of GaAs,*" Phys. Rev. B **6**, 3750–3753 (1972).

[95] W. C. Hurlbut, Y.-S. Lee, K. L. Vodopyanov, P. S. Kuo, and M. M. Fejer, "*Multi-photon absorption and nonlinear refraction of GaAs in the mid-infrared,*" Opt. Lett. **32**, 668–670 (2007).

[96] R. Dingle, D. D. Sell, S. E. Stokowski, and M. Ilegems, "*Absorption, Reflectance, and Luminescence of GaN Epitaxial Layers,*" Phys. Rev. B **4**, 1211–1218 (1971).

[97] V. I. Gavrilenko and R. Q. Wu, "*Second harmonic generation of GaN(0001),*" Phys. Rev. B **65**, 035405 (2001).

[98] C. Merz, M. Kunzer, U. Kaufmann, I. Akasaki, and H. Amano, "*Free and bound excitons in thin wurtzite GaN layers on sapphire,*" Semicond. Sci. Technol. **11**, 712 (1996).

[99] C. Schweitzer, Nichtlineare Spektroskopie an Halbleitern mit grosser Bandlücke, Ph.D. thesis, TU Dortmund (2002).

[100] D. M. Hofmann, D. Kovalev, G. Steude, B. K. Meyer, A. Hoffmann, L. Eckey, R. Heitz, T. Detchprom, H. Amano, and I. Akasaki, "*Properties of the yellow lumi-nescence in undoped GaN epitaxial layers,*" Phys. Rev. B **52**, 16702–16706 (1995).

[101] E. R. Glaser, T. A. Kennedy, K. Doverspike, L. B. Rowland, D. K. Gaskill, J. A. Freitas, M. Asif Khan, D. T. Olson, J. N. Kuznia, and D. K. Wickenden, "*Optically detected magnetic resonance of GaN films grown by organometallic chemical-vapor deposition,*" Phys. Rev. B **51**, 13326–13336 (1995).

[102] Y. Toda, T. Matsubara, R. Morita, M. Yamashita, K. Hoshino, T. Someya, and Y. Arakawa, "*Two-photon absorption and multiphoton-induced photoluminescence of bulk GaN excited below the middle of the band gap*," Appl. Phys. Lett. **82**, 4714–4716 (2003).

[103] S. Juodkazis, A. Galeckas, J. V. Vaitkus, S. Sakai, and H. Misawa, eds., Characterization of GaN layers by second harmonic generation and photoluminescence, Proc. SPIE 4318, Smart Optical Inorganic Structures and Devices, Vol. 4318 (2001).

[104] C.-K. Sun, S.-W. Chu, S.-P. Tai, S. Keller, U. K. Mishra, and S. P. DenBaars, "*Scanning second-harmonic/third-harmonic generation microscopy of gallium nitride*," Appl. Phys. Lett. **77**, 2331–2333 (2000).

[105] I. V. Kityk and B. Sahraoui, "*Phonon-Assisted Second Harmonic Generation in As1-xBixTe3-CaBr2-PbBr2 Glasses*," J. Phys. Chem. B **109**, 3163–3168 (2005), pMID: 16851336.

[106] J. Y. Huang, "*Probing Inhomogeneous Lattice Deformation at Interface of Si(111)/ SiO2 by Optical Second-Harmonic Reflection and Raman Spectroscopy*," Jpn. J. Appl. Phys. **33**, 3878 (1994).

[107] S. V. Govorkov, V. I. Emel'yanov, N. I. Koroteev, G. I. Petrov, I. L. Shumay, V. V. Yakovlev, and R. V. Khokhlov, "*Inhomogeneous deformation of silicon surface layers probed by second-harmonic generation in reflection*," J. Opt. Soc. Am. B **6**, 1117–1124 (1989).

[108] M. Galli, D. Gerace, K. Welna, T. F. Krauss, L. O'Faolain, G. Guizzetti, and L. C. Andreani, "*Low-power continuous-wave generation of visible harmonics in silicon photonic crystal nanocavities*," Opt. Express **18**, 26613–26624 (2010).

[109] C. C. Wang, J. Bomback, W. T. Donlon, C. R. Huo, and J. V. James, "*Optical Third-Harmonic Generation in Reflection from Crystalline and Amorphous Samples of Silicon*," Phys. Rev. Lett. **57**, 1647–1650 (1986).

[110] M. G. Martemyanov, E. M. Kim, T. V. Dolgova, A. A. Fedyanin, O. A. Aktsipetrov, and G. Marowsky, "*Third-harmonic generation in silicon photonic crystals and microcavities*," Phys. Rev. B **70**, 073311 (2004).

List of Figures

List of Tables

Symbols and Abbreviations

J	Angular momentum
a.u.	Arbitrary units
E_g	Band gap energy
BBO	Beta barium borate
a_B	Bohr radius
k_B	Boltzmann constant
CCD	Charge coupled device
ρ	Charge density
$|f\rangle$	Crystal state
Cu_2O	Cuprous oxide
$\mathbf{j}$	Current density
ϵ	Dielectric constant
m_e	Effective mass of conduction band electron
m_h	Effective mass of valence band hole
ϵ_0	Electric constant
$\mathbf{P}$	Electric dipole moment
ED	Electric dipole
EFISH	Electric field induced second-harmonic generation
E^0	Electric field magnitude
$\mathbf{E}^\omega$	Electric field of the laser light
$\mathbf{E}^{2\omega}$	Electric field of the SHG light
$\mathbf{E}^{3\omega}$	Electric field of the THG light
$\mathbf{E}$	Electric field

Q	Electric quadrupole moment
EQ	Electric quadrupole
eV	Electron volt
e_0	Elementary charge
Δ	Energy difference
E	Energy
R_{exc}	Exciton binding energy
E_{exc}^n	Exciton energy in quantum state n
m_{exc}	Exciton mass
F_i	Exciton oscillator strength
k_{exc}	Exciton wave vector
$\mathbf{E}^0$	External electric field
$\mathbf{B}^0$	External magnetic field
$m_{\mathrm{free,e}}$	Free electron mass
ω	Frequency
GaAs	Gallium arsenide
GaN	Gallium nitride
H	Hamiltonian
P_{eff}	Induced polarization
Γ	Irreducible representation
k	Light wave vector magnitude
k	Light wave vector
M	Magnetic dipole moment
MD	Magnetic dipole
MFISH	Magnetic field induced second-harmonic generation
B^0	Magnetic field magnitude
$\mathbf{H}^\omega$	Magnetic field of the laser light

B	Magnetic field
m	Mass
OPO	Optical parametric oscillator
ξ	Oscillator strength proportion between $1s/2p$ and $2s/2p$
μ_0	Permeability
PLE	Photoluminescence excitation
PL	Photoluminescence
KTP	Potassium titanyl phosphate
QM	Quantum mechanics
Ω_{R}	Rabi frequency
μ_{exc}	Reduced exciton mass
n	Refractive index
ϵ_r	Relative permittivity
SHG	Second-harmonic generation
$I^{2\omega}_{\mathrm{Both}}$	SHG intensity for both polarizations
$I^{2\omega}_{\parallel}$	SHG intensity for parallel polarization
$I^{2\omega}_{\perp}$	SHG intensity for perpendicular polarization
SiC	Silicon carbide
Si	Silicon
c	Speed of light (in vacuum)
Δ_{SO}	Split off energy
$\chi^{(n)}$	Susceptibility of order n
T	Temperature
THG	Third-harmonic generation
3PA	Three photon absorption
t	Time
TPA	Two photon absorption
A	Vector potential

List of Publications

[1] M. Lafrentz, D. Brunne, B. Kaminski, V. V. Pavlov, A. B. Henriques, R. V. Pisarev, D. R. Yakovlev, G. Springholz, G. Bauer, E. Abramof, P. H. O. Rappl, and M. Bayer, "*Optical third-harmonic spectroscopy of the magnetic semiconductor EuTe*," *Phys. Rev. B*, vol. 82, p. 235206, Dec 2010.

[2] M. Lafrentz, D. Brunne, B. Kaminski, V. V. Pavlov, R. V. Pisarev, A. B. Henriques, D. R. Yakovlev, G. Springholz, G. Bauer, and M. Bayer, "*Optical third harmonic generation in the magnetic semiconductor EuSe*," *Phys. Rev. B*, vol. 85, p. 035206, Jan 2012.

[3] M. Lafrentz, D. Brunne, B. Kaminski, V. V. Pavlov, A. V. Rodina, R. V. Pisarev, D. R. Yakovlev, A. Bakin, and M. Bayer, "*Magneto-Stark Effect of Excitons as the Origin of Second Harmonic Generation in ZnO*," *Phys. Rev. Lett.*, vol. 110, p. 116402, Mar 2013.

[4] M. Lafrentz, D. Brunne, A. V. Rodina, V. V. Pavlov, R. V. Pisarev, D. R. Yakovlev, A. Bakin, and M. Bayer, "*Second-harmonic generation spectroscopy of excitons in ZnO*," *Phys. Rev. B*, vol. 88, p. 235207, Dec 2013.

Acknowledgements